Vector Sensors and User Based Link Layer QoS

for 5G Wireless Communication Applications

by

Frank Lee James III

A Dissertation Presented in Partial Fulfillment
Of the Requirements for the Degree
Doctor of Philosophy

Approved April 2019 by the
Graduate Supervisory Committee:

Martin Reisslein, Chair
Michael McGarry
Patrick Seeling
Yanchao Zhang

ARIZONA STATE UNIVERSITY

May 2019

ABSTRACT

The commercial semiconductor industry is gearing up for 5G communications in the 28GHz and higher band. In order to maintain the same relative receiver sensitivity, a larger number of antenna elements are required; the larger number of antenna elements is, in turn, driving semiconductor development. The purpose of this paper is to introduce a new method of dividing wireless communication protocols (such as the 802.11a/b/g/n and cellular UMTS MAC protocols) across multiple unreliable communication links using a new link layer communication model in concert with a smart antenna aperture design referred to as Vector Antenna. A vector antenna is a 'smart' antenna system and as any smart antenna aperture, the design inherently requires unique microwave component performance as well as Digital Signal Processing (DSP) capabilities. This performance and these capabilities are further enhanced with a patented wireless protocol stack capability.

ACKNOWLEDGMENTS

I would like to acknowledge Dr. Martin Reisslein for the opportunity to present this dissertation.

To all of those who have helped me over the many years that I have spent pursing higher education. I cannot give back the lost time spent studying over long sleepless nights and the lack of studious attention to the most important elements of life. Thank you.

TABLE OF CONTENTS

Page

LIST OF TABLES

Table Page

Table Page

LIST OF FIGURES

Figure Page

Figure Page

Figure Page

Figure Page

Figure Page

Figure Page

Figure Page

CHAPTER 1

INTRODUCTION

Wireless Technologies such as Wi-Fi and Cellular are converging in the market place. This convergence promotes a need for a different link layer protocol stack technology that better facilitates the convergence of these technologies both from the radio frequency (RF) modulation adaptation perspective as well as from the link layer protocol perspective. This convergence has also driven a desire to increase bandwidth, reduce symmetrically Gaussian noise, reduce insertion loss and increase carrier signal frequency. These performance improvements are addressed utilizing microwave component design, digital signal processing (DSP) and aperture [material and structural] design; both aperture and digital signal processing are required for 'smart' antenna system design. This paper will introduce the use of a new vector antenna technology to improve the performance of modern communication signal sets in concert with massive MIMO, such as those proposed in 5G communication proposals, in concert with a patented link layer routing protocol stack concept.

Wireless Transceiver Design Trends

To maintain the required relative receiver sensitivity, a larger number of antenna elements are required; the larger number of antenna elements is, in turn, driving semiconductor development requirements. 5G communication requirements are increasing the target frequencies up in the millimeter wave frequency range of 24GHz to 86GHz. When operating at frequencies above 10GHz, atmospheric absorption must be considered when selecting a frequency of operation.

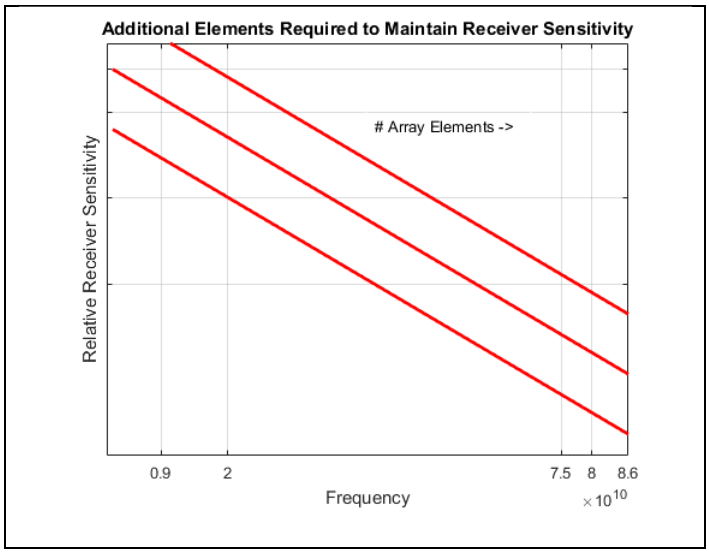

Figure 1. Receiver Sensitivity Drives Larger # of Antenna Elements

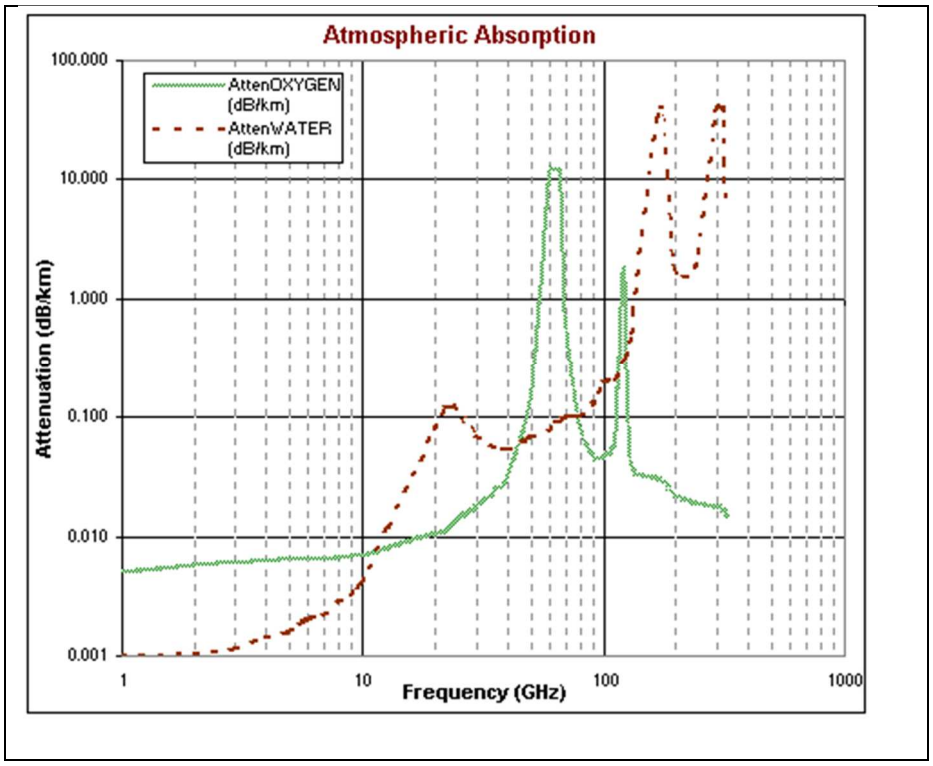

Figure 2 Atmospheric Absorption versus Frequency

Additional antenna elements are enabling Massive Multiple Input Multiple Output (MIMO) system applications that are increasing system performance as well as improving spectral efficiency. Achievable rates are given by a variation of the Shannon-Hartley limit as follows:

$$R \leq \frac{M(BW)}{K} log_2(1 + SINR) \quad (1)$$

M = # of antennas
BW = Bandwidth
K = # of users
SINR = Signal to Interference plus Noise Ratio

All received signals in a discrete-time MIMO signal model:

$$y_i[n] = \sum_{l=-\infty}^{\infty} h_i[l]\, x[n-l] + v_i[n], where\ y[n] = \begin{bmatrix} y_{1[n]} \\ \vdots \\ y_{R_N}[n] \end{bmatrix}, h[n] \tag{2}$$
$$= \begin{bmatrix} h_{1[n]} \\ \vdots \\ h_{R_N}[n] \end{bmatrix}, R_N x N_s$$

$R_N = Number\ of\ elements$
$N_S = Number\ of\ Samples$

$$y[n] = \sum_{l=0}^{N_S-1} H[l]\, x[n-l] + v[n] \tag{3}$$

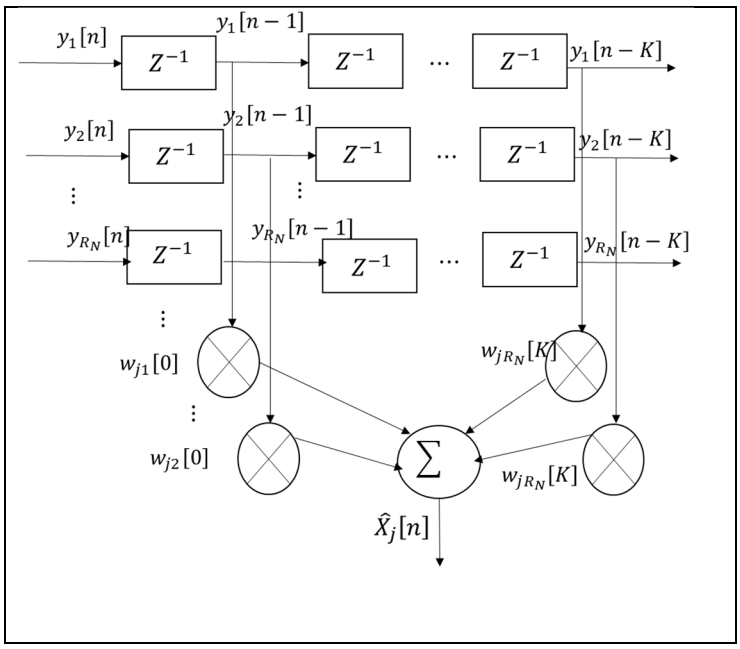

Figure 3 MIMO Channel Equalization

MIMO channel equalization solves $w_j[l], (l = 0 \ldots K)$. The following equation is solved:

$$x_j^*[n-delay] = \sum_{l=0}^{K} w_j^*[l]\, y[n-l] \tag{4}$$

Assuming the knowledge of the channel transform H[0],…,H[L], find $w_j[l]$, $(l = 0 \ldots K)$.

Solve the weights for the following equation:

$$d_j^*[n] = \sum_{l=0}^{K} w_j^*[l]\, H[n-l], where\ n = 0, \ldots, K+L \quad (5)$$

where $w_j[k]\ is\ R_N x1, d_j[k]\ is\ N_t x1, H[n]\ is\ R_N x N_t\ vectors$

$$d_j^*[n] = \sum_{l=0}^{K} w_j^*[l]\, H[n-l], where\ n = 0, \ldots, K+L \quad (6)$$

Machine learning will be used to perform adaptive beamforming based upon cognitive spectral learning. An adaptive FIR filter is a learning system.

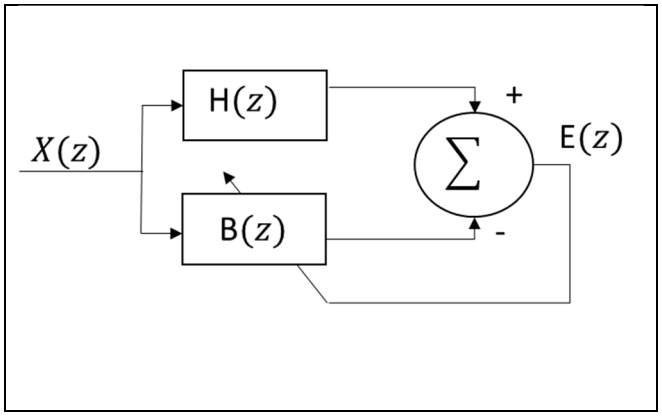

Figure 4 Adaptive Filter is a Learning System

By making the filter B(z) behave like H(z), we adaptively identify the system. This then becomes a learning element for a neural network. By using the adaptive filter technique in the RLS or LMS sense, we match the output to the desired output by changing the weights using a gradient μ.

The following figures of merit relative to antenna gain:

$$Free\ Space\ Loss = \frac{4\pi(Dist.)(Freq.)^2}{c} \tag{7}$$

$$Antenna\ Gain \cong 10\ log_{10}(\#Antenna\ Elements) \tag{8}$$

$$Relative\ Free\ Space\ Loss = 20\ log_{10}\left(\frac{Freq_1}{Freq_2}\right) \tag{9}$$

$$Example: F_1 = 28GHz, F_2 = 5GHz, \qquad Antenna\ Gain \cong 30\ elements$$

As shown in the example above, in order to maintain the same relative receiver sensitivity, extending a 5GHz receiver with one antenna to 28GHz requires ~30 elements.

Sampling and Decimation

The following are ADC/DAC architectural performance characteristics. Generally, there are two types of ADC/DAC designs: Nyquist and oversampling noise shaping data converters. Oversampling in Nyquist type converters improves SNR by reducing the average quantization noise power. The advantage of sigma-delta converters is the use oversampling in conjunction with noise shaping. Higher instantaneous bandwidth is now available which dramatically improves Effective Number of Bits (ENOB) permitting 500MHz of instantaneous bandwidth complex sample rate.

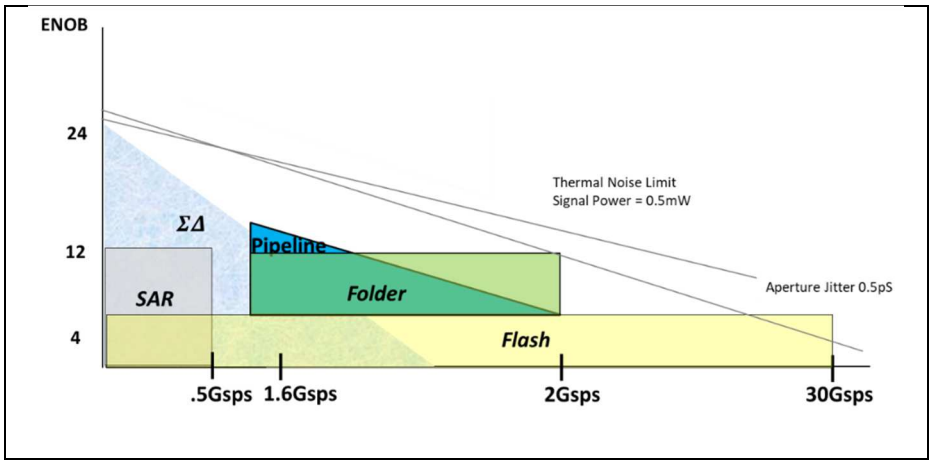

Figure 5. ADC/DAC Architecture Defines Achievable Performance (Garrity, 2016)

The above graph depicts the different data converter design approaches and the limitations associated to the data converter architecture, each architecture type defines the realizable/achievable ENOB. Each architecture continues to invade the territory of the other. Process improvements are pushing up the sampling rates (F_s). Pipeline and Sigma-Delta architecture bandwidths is inherently programmable at the sacrifice of signal to noise ratio (SNR).

$$SNR_{max} := 6.02(n) + 1.76 + 10\,log_{10}(OSR) \tag{10}$$

We gain SNR through by utilizing digital filtering in concert with oversampling. By sampling faster, the quantization noise is spread over a wider band and therefore a gain in SNR is achieved by digitally filter a subset of the instantaneous bandwidth.

$$OSR := \frac{F_s}{2 * BW} \tag{11}$$

When utilizing Nyquist Sampling, SNR_{max} increases by ~3dB per octave (factor of 2) per OSR. As shown in the equation below, as the sampling rate increases sampling

[aperture] jitter limits resolution regardless of signal power (i.e. $\frac{S}{N_o}$). Jitter limits are described by the following equation:

$$T_{RMS(jitter)} := \frac{\sqrt{OSR}}{2\pi F_{in} 10^{\left(\frac{SNR}{20}\right)}} \tag{12}$$

Jitter requirements are very important to ADC and DAC performance. As the sample rate increases, jitter requirements become more critical. Reductions in power come mainly from ADC/DAC architectural breakthroughs and secondarily from IC process advances. Adding on bit of resolution requires at least 4x increase in power:

$$Power\ Factor := \frac{Power}{2F_s SNR^{(2)}}\ Femtojoules \tag{13}$$

In broad band sampling fabric (i.e. 64Gsps), decimation is accomplished by multiple digital down conversion (DDC) stages enabling multiple portions of the entire sampled band to be output per antenna element. Following DDC stages, half band filter stages are provided for further reduction of output bandwidth from ADC sampling fabric. Interpolation logic on DAC fabrics are provided. Wireless communication demands return to zero (RTZ) sampling and interpolation is used to ensure output waveforms are not distorted.

Receiver Design Architectural Characteristics

Aperture jitter causes inaccuracies and/or increases in Digital Signal Processing (DSP) in regard to processing multiple versions of [interfering] signals allowed within narrow band channels channelized by downstream processing firmware/software; such aperture jitter also reduces adjacent channel rejection of Power Spectral Density (PSD) 'spilling'

into narrow band channels (this 'spilling' is referred to as reciprocal mixing). Aperture jitter is generally caused by frequency translation (i.e. mixing). Such translations occur as a function of the number of down converters required in the receiver path. The number of down converters is driven by the frequency of the received signal and the bandwidth of the received signal.

The reciprocal mixing and phase noise problem is described adequately as the maximum allowable phase noise L (in dBc/Hz) that allows the design to achieve the adjacent channel rejection (selectivity) of S (in dB) is given by the following equation:

$$L := C - S - I - 10\,log_{10}(BW) \tag{14}$$

$L \stackrel{\text{def}}{=} Maximum\ allowable\ phase\ noise\ in\ dB$
$C \stackrel{\text{def}}{=} Carrier\ Power\ in\ dB$
$S \stackrel{\text{def}}{=} Adjacent\ channel\ rejection\ in\ dB\ (i.e. Selectivity)$
$I \stackrel{\text{def}}{=} Interference\ Power\ in\ dB$

The interfering signal (I) that is permitted from an adjacent subchannel due to jitter in the mixing signal. All frequency components in the passband (i.e. smaller subchannel sizes) must adhere to this formula.

Receiver Noise Algorithms

Reducing the level of the noise floor to improve the receive sensitivity and improving the Dynamic Range (DR) of the receiver is important. The following equations measure the noise contributions of the Analog Front End (AFE). The cascaded noise figure is expressed through the following equation (Pozar, 2005):

$$F_{cas} := F_1 + \frac{F_2 - 1}{G_1} + \frac{F_3 - 1}{G_1 G_2} + \cdots \quad (15)$$

Receiver noise temperature adds noise to the receiver and reduces dynamic range. The cascaded noise temperature is expressed through the following equation:

$$T_{cas} := T_{e1} + \frac{T_{e2}}{G_1} + \frac{T_{e3}}{G_1 G_2} + \cdots \quad (16)$$

Shot noise is associated with the transfer charge across a PN junction, since it is a Gaussian white process like thermal noise, it can be modeled as an appropriate increase in effective temperatures of the device. Any active Integrated Circuit (IC) exhibits Flicker noise, also called $\frac{1}{f}$ noise, is attributed to random fluctuations of the carrier density in the device. Any non-linearities present will cause $\frac{1}{f}$ noise sidebands around the carrier frequency. Since the background temperatures is uniform, the brightness temperatures is independent of the antenna pattern and equal to the background temperature:

$$T_A := \frac{T_b}{L} + \frac{(L-1)}{L} T_p \quad (17)$$

Example: If the total loss of the antenna apertures is 9dB or L=9dB=7.9433 dimensionless. T_b is the brightness temperatures (example: Ground Noise Temperature $\cong 4K$). This sets the noise level to the input to the receiver.

$$T_S := T_A + T_{LNB} \quad (18)$$

Most RF communication is established through the electromagnetic far-field, Fraunhofer region. The SNR at the input of a receiver is proportional to the antenna's G/T ratio which is defined as the following equation (Balanis, 2009):

$$Polarization\ Loss\ Factor\ (PLF) = |\hat{\rho}_w * \hat{\rho}_a|^2, 0 \leq PLF \leq 1 \tag{19}$$

$$\begin{matrix} Aperture\ Efficiency \\ (Ae): 0 \leq Ae \leq 1\ (Directional\ Antennas), Ae\ >> 1\ (For\ Wire\ Antennas) \end{matrix} \tag{20}$$

$$\frac{P_r}{P_t} = \left(\frac{\lambda}{4\pi R}\right)^2 G_t(\theta_t, \phi_t) G_r(\theta_r, \phi_r) |\hat{\rho}_w * \hat{\rho}_a|^2 \tag{21}$$

$$G/_T := 10\, log_{10}\left(\frac{G_r}{T_s}\right) \tag{22}$$

The above equation is expressed in dB per degree Kelvin and used to express the gain versus symmetrically Gaussian noise generated by the antenna and low-noise block of the receiver. The following equation is used to express the temperature of the antenna and the input to the low-noise block of the receiver:

$$T_E = T_A + (F - 1)T_0 \tag{23}$$

Maximum Distance of Modern Communication Channel

In order for communication to occur, the receiver must synchronize with the transmitter. During initial control channel negotiation, physical layer modulation often utilize PSK using a convolutional encoder with a Viterbi/Trellis decoder. Therefore, it is now possible to then calculate the maximum distance based upon a minimum SNR at the receiver. The following equation is derived from Friis equations and is based upon a

minimum SNR of 0 or 1dB of received power which is the minimum required for these modulated signals with a $P_b = 0.5$. The following curbs below:

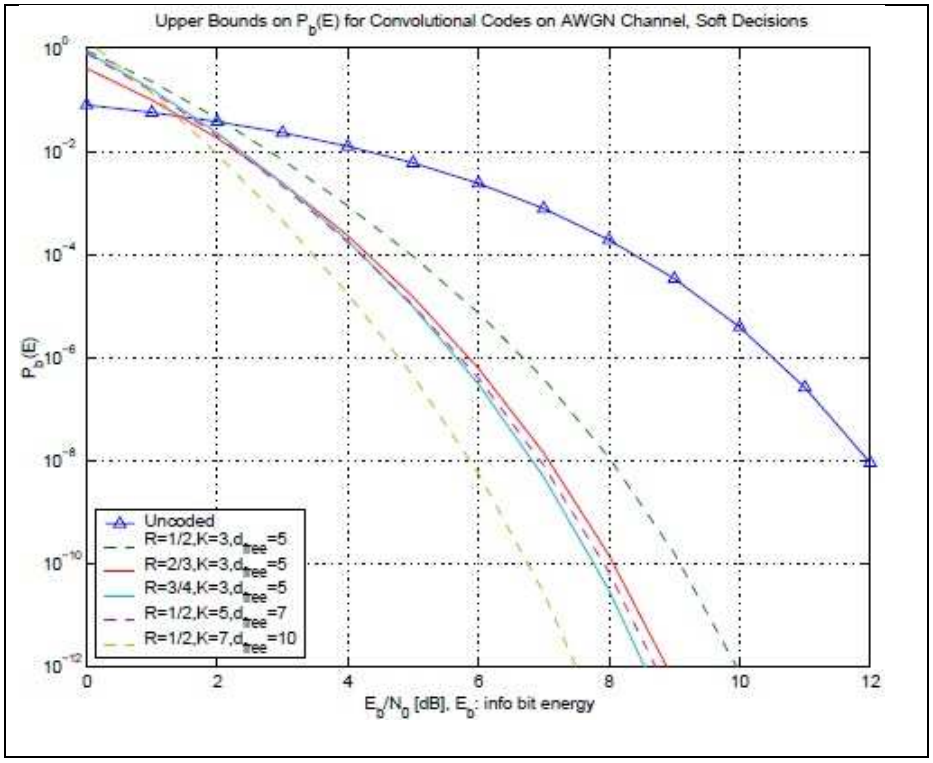

Figure 6. $P_b(E)$ QPSK, Convolutional Encoded, Soft Decision

The maximum bit rate achievable across the link is expressed by the following equation derivation:

$$R_b \cong \frac{\left(S/n_0\right)}{\left(E_b/n_0\right)} \tag{24}$$

The maximum achievable distance for a communication link:

$$R_{max} = \left(\frac{c}{2\pi f}\right)\sqrt{\frac{P_t G_t G_r}{SNR_{req} N_0}} \tag{25}$$

$$N_0 = KT_A BW = N\ (watts) \tag{26}$$

Note: Assuming a noiseless receiver (modify for real world)

$$R_{max} = \left(\frac{c}{2\pi f}\right)\sqrt{\frac{P_t G_t G_r}{SNR_{req} N_0}} \tag{27}$$

$f = Frequency\ of\ carrier$

BW = Bandwidth of signal

$$G_t G_r = Gain\ of\ receiver/transmitter\ apertures\ (dimensionless\ quant.) \tag{28}$$

$$S_0 = SNR_{req} N_0 = P_{min} \tag{29}$$

$$P_{min} = \left(\frac{c}{4\pi f R_{max}}\right)^2 G_t G_r P_t \tag{30}$$

Now solve for the maximum distance:

$$R_{max} = \left(\frac{c}{4\pi f}\right)\sqrt{\frac{P_t G_t G_r}{SNR_{req} N_0}} \tag{31}$$

The derivation above calculating the maximum distance expectation for received signals using the modulation and forward error correction (FEC) defined above. Other modulation and FEC types can be approached in the same fashion. Another important figure of merit is the SNR at the input of the receive antenna is G/T. The equation for G/T is the following (Pozar, 2005):

$$\frac{G}{T} = 10\,log_{10}\left(\frac{G}{T_A}\right) \tag{32}$$

The gain (G) of the receiver over the antenna noise temperature (T_A). Increasing gain minimizes the noise from sources at low elevation angles. These equations are used to calculate the link budget by estimating the relative power to the receiver when using the gain of the receiver:

$$P_r = \frac{G_t G_r \lambda^2}{(4\pi R)^2} P_t\ (Watts) \tag{33}$$

Receive power P_r is the maximum receive power which ignores partial field cancellation caused by multipath, impedance mismatch, polarization mismatch, propagation attenuation effects.

$$A_e = \frac{D\lambda^2}{4\pi}\ ,where\ D\ is\ the\ directivity\ of\ the\ antenna\ pattern \tag{34}$$

For electrically large antennas (such as dishes, horns, etc…) A_e is close to the physical aperture area; however, modern communication devices utilize electrically small apertures (such as dipoles, loops, PIFAs, etc…) are used that have much larger A_e than their physical size. The D in the equation above can be replaced by the effective gain G of the antenna which can take into account the effective loss within the antenna aperture.

$$L_0 = 20\,log_{10}\left(\frac{4\pi R}{\lambda}\right) \tag{35}$$

L_0 is the path loss between the receiver and transmitter. Using the equation above in concert with the Friis equation, a link budget can be derived.

$$L_{(r|t)imp} = -10\,log_{10}(1 - |\Gamma|)^2 \tag{36}$$

The equation above includes a reflection coefficient Γ which is calculated in the following manner:

$$\Gamma = \frac{Z_L - Z_S}{Z_L + Z_S} \tag{37}$$

The following table demonstrates the calculation of the link budget using losses and gains using the equations earlier described.

Table 1
Link Budget Calculation

Transmit Power	P_t
Transmit antenna line loss	$(-)L_t$
Transmit antenna gain	G_t
Path loss (free-space)	$(-)L_0$
Atmospheric attenuation	$(-)L_A$
Receive antenna gain	G_r
Receiver impedance mismatch	$(-)L_{r\text{-}imp}$
Transmitter impedance mismatch	$(-)L_{t\text{-}imp}$
Receive antenna line loss	$(-)L_r$
Total Receive power	P_r

Other losses such as absorption loss depends on the absorption medium and the path length within the medium. As an example, a rain cloud of 10km would produce a 2dB loss. In desert conditions, atmospheric scintillation will add loss. These and other such losses are in addition to those outlined above and are addressed on a case by case basis.

Chapter 2

PROPOSED DESIGN ESTABLISHING MODERN COMMUNICATION CHANNELS

Establishing communications between two mobile devices in the presence of channel distortion is challenging when uncertainty in both the frequency and time domains is combined with further challenges introduced by the frequency drift in the transmitter of the peer and sparse communication time opportunities. In wireless communication, time synchronization is guaranteed by frequent and regular transmission of time information; however, in cases where time information is not readily available a different approach must be used. An exploration of a different approach will be investigated to determine if a common method for transmitter and receiver synchronization can be used. A set of adaptive algorithms that implement techniques to establish a reliable communication channel is accomplished by reducing the frequency and time uncertainty windows and parallelizing adaptive signal detection algorithms, a highly reliable signal acquisition technique is established that enables communication under challenging channel distortion conditions. The performance of this technique will be demonstrated in two areas: signal acquisition and, once signal is detected, signal tracking.

To successfully model establishing a time efficient communication synchronization technique, implemented in the presence of a distorted fading channel model, a fading distribution model must be utilized. Such fading distributions can be modeled using Rayleigh, Ricean, Nakagami or Chi^2 algorithms. Frequency selectivity depends upon the transmission rate; therefore, in a multi-rate system, different # of adaptive filter taps can be used. To address the frequency selectivity of the channel, channel estimation followed

by a reverse filter equalization will be performed. To derive the filter tap coefficients, a training sequence will be used as part of the communication process. The synchronization technique often used to cross correlate the signal to the a-priori known orthogonal code sequence taking into account uncertainty in frequency, time and channel distortion within a very small time requirement. The following block diagram describes an exemplar design which is used in conjunction with the overall receiver design. In such a design signal acquisition is achieved by the following parallelized approach: a convolution operation will be performed on the input signal which is used in detector that utilizes an order Recursive Least Square (RLS) algorithm to adapt the variable control oscillator (VCO). This operation is parallelized to reduce the amount of time required to converge on a cross correlation. The VCO handles the uncertainty in frequency while the detector handles the uncertainty in time. An exemplar detector called a Tong[1] detector is described below. This detector was then improved by use of the order RLS algorithm to accommodate system identification.

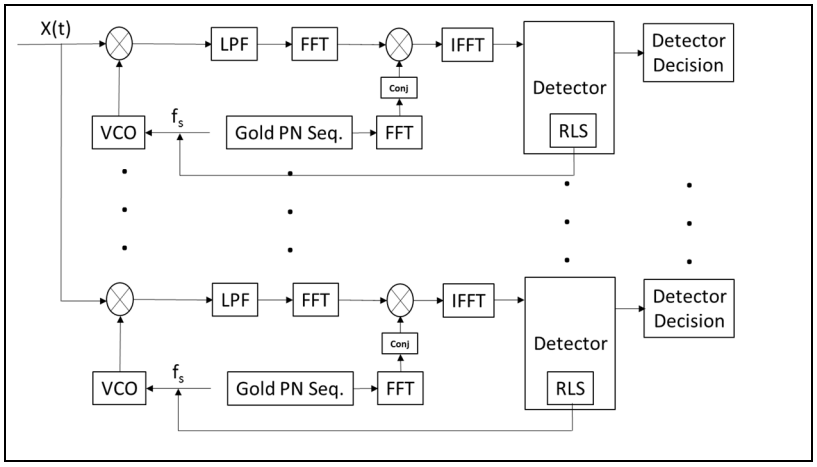

Figure 7. Receiver Synchronization Detection Design

The system diagram above depicts the detection path for the correlation receiver described. This correlation receiver is used to acquire the transmitted signal within a small window of uncertainty in time and frequency. A correlation receiver must implement the equations associated to correlation in a Doppler Environment. The transmitted signal is convolved with the impulse response of the channel; the following description follows in regard to transmit and receive signal in a Doppler environment. An example of the transmitted signal is:

$$Re\left[u(t)e^{j2\pi f_c t}\right] \tag{38}$$

In this scenario the receive signal is:

$$r(t) = \sum_{n=1}^{N} C_n\left[u(t-T_n)e^{j2\pi(f_c+f_{Dn})(t-T_n)}\right] \tag{39}$$

Where T_n represents the multipath delay length that can be derived statistically from several distribution models described earlier. The frequency shift caused by Doppler is as follows:

$$f_{Dn} = f_{max}\cos\theta_n = \frac{\nu}{\lambda_c}\cos\theta_n \tag{40}$$

Where ν is the relative speed between the two peer devices and λ_c is the wavelength of f_c $u(t)$ is the complex baseband signal C_n are channel coefficients (iid: independent, identically distributed). f_{max} is the maximum Doppler frequency shift describing the relative velocity of the time varying impulse response of the channel between the communication peers as represented by $u(t)$ and $r(t)$. The symbol θ_n represents the angle of the n^{th} wave impinging upon the receive antenna with receiver velocity. If we assume θ_n is uniformly distributed (due to high number of reflections) over the angular range$[0, 2\pi]$, the following substitutions can be applied:

$$\theta_n = 2\pi(f_c + f_{Dn})\tau_n$$

$P_\theta(\theta) = \frac{1}{2\pi}$ Uniformly distributed over: $[0, 2\pi]$. (41)

$$C(\tau, t) = \sum_{n=1}^{N} C_n\left[u(t - T_n)e^{j2\pi f_{Dn}}e^{-j\theta_n}\delta(\tau - \tau_n)\right] \quad (42)$$

The following correlation equation is utilized to describe the Doppler spectrum as well as the multipath intensity profile:

$$A_c(\tau, \Delta t) = \int_0^{2\pi} P_\theta(\theta)\, e^{-j2\pi f_{max}\Delta t\, cos\,\theta} \quad (43)$$

Therefore, this leads us to the following Bessel function (order 0):

$$J_0(2\pi\Delta t) = \frac{1}{2\pi}\int_0^{2\pi} e^{-j2\pi f_{Dn}\Delta t} \quad (44)$$

The following Doppler spectrum (scattering function) follows. For a fixed τ, the Doppler spectrum is the Fourier Transform of the Bessel function $J_0(.)$.

$$\Im\{A_c(\tau, \Delta t)\} = \rho_\tau(\tau)\frac{1}{\sqrt{1-\left({}^{f}/_{f_{max}}\right)^2}} \quad (45)$$

To estimate the channel coefficients $\square[n]$, a training sequence is used at the beginning of the transmission to provide a mechanism to provide a mechanism for the receiver to verify the received sequence to the known, a-priori sequence. In this scenario, the channel acts as a Finite Impulse Response (FIR) filter. To account for the frequency selectivity of the channel, we implement equalization, the following equation relates to the discrete time domain representation of the channel:

$$r[n] = \sum_{k=1}^{K} h[n]s[n-k] + w[n] \quad (46)$$

$$w[n] = CN(0, r_w^2)$$ (47)

In the equation above, K represents the channel order and is based upon the transmission rate ($1Ts$) and the "Coherence Time". As the rate of transmission increase, causing the symbol period Ts to decrease, the channel order K increases (i.e. number of channel coefficients). In this model, the FFT point size was limited to one Pseudo-Random Number (PN) period and this point size is equal to the number of coefficient taps calculated during the training sequence period. This correlation receiver mixes the input signal to a reference variable controlled oscillator (VCO) that is used to perform frequency translation on the receive signal. As depicted in the system diagram below, multiple correlation threads are executing in parallel. The Low Pass Filter (LPF) is used to remove the associated frequency spurs that occur as a result of frequency translation. Each correlation thread has a frequency offset that is equivalent to the inverse of a fraction of the chip or symbol time Tc. This symbol period Tc is spread over N parallel receiver paths. The following estimate is performed in the discrete time domain:

$$\hat{h}[m] = \sum_{k=0}^{N} r[k]s[k-m]$$ (48)

Where $[k]$ represents the receive signal and $[k-m]$ represents the training sequence. The following vector equation follows from this equation:

$$\bar{r} = \bar{h} * \bar{s} + \bar{w}$$ (49)

The received signal is convolved with the impulse response of the channel where $\bar{r}$ represents the receive signal, $\bar{\ }$ represents the channel, $\bar{s}$ represents the symbol and $\bar{w}$ represents additive noise.

$$\hat{h}[m] = \sum_{k=0}^{K} h[k] \sum_{l=0}^{N} s[l-k]s[l-m] \tag{50}$$

Where $[l{-}m]$ represents the training sequence and $[l{-}k]$ represents the received symbol. In these equations, we able to recover $[l]$ because $\bar{s}$ comes from a finite alphabet/code book. In this case, the Verterbi algorithm was implemented using a Trellis to model the FIR channel. The goal of this approach is to reduce the Euclidean distance with respect to $[l]$.

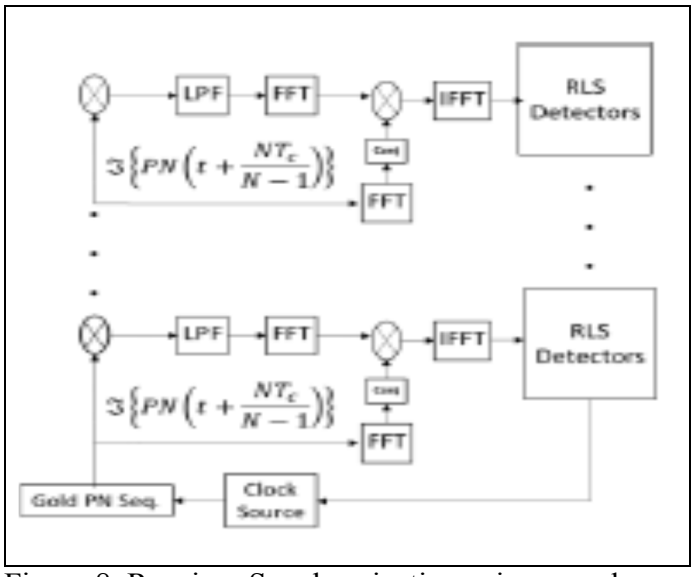

Figure 8. Receiver Synchronization using pseudo-random (PN) Sequence

Use of Parallel Correlators

The transmit path does not require the parallelization required on the receive path; though the transmit path is not depicted in this paper, a reverse filter operation $(z){-}1$ is performed on the transmitted signal data to pre-distort the transmitted signal based upon channel coefficients calculated on the receive path. The goal of this procedure is to counter act the channel distortion detected during the receive operation. The transmission

improvement is limited if there are long time periods between transmissions or if the relative speed between communication devices is too high and is related to what is referred to as the "Coherence Time" of the channel.

The Coherence Time of a channel is the period of time in which the condition of the channel remains static and is proportional to the Doppler environment.

$$Coherence\ Time\ \propto \frac{1}{F_{Max}} \tag{51}$$

Since the Order Recursive Least Square (RLS) algorithm family is closer to the Newton type performance, the following equations were chosen to perform a Recursive Least Square (RLS) to converge to an optimum Wiener solution.

$$\lim_{i\to\infty}\{E[b(i)]\} = b^0 \tag{52}$$

There are numerous advantages with using the order recursive (RLS) algorithm. The RLS is based upon the partitioned structure of the autocorrelation matrix which makes it easier to integrate with time averaged sampling. The RLS algorithm used the partitioned form of the Matrix Inversion Lemma, making partial matrix updates possible reducing overall computational overhead, reducing complexity to $O(L^2)$. The algorithm utilizes the diagonal portion of the Toeplitz matrix and therefore, further reduces algorithm complexity. The RLS algorithm provides better performance by converging much faster than with the LMS approach.

Given an input signal x(n) and a desired signal d(n), the concept is to minimize the error e(n) as expressed by the following system diagram:

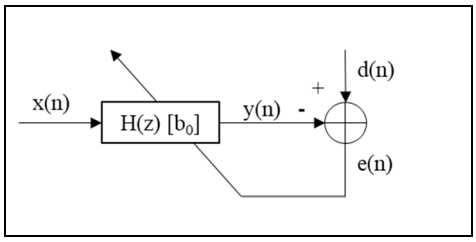

Figure 9. RLS/LMS Error Minimization Convergence

By enabling a hardware architecture that enables faster floating point calculations, we can the utilize the RLS algorithm that is faster when an input is characterized by an autocorrelation with eigenvalue disparity. Each parallel thread is performing a RLS estimation. In this example, each correlator is executing the following thread of calculations:

```
%
% Matlab Code Excerpt
% RLS Algorithm
% L = Est. Order, mu=Step Size
%
FGetFctr=0.999; % Forgetting Factor β
P=eye(L)/mu;
...
xx=X(n:-1:n-L+1);
...
k=FGetFctr^(-1)*P*xx/(1+FGetFctr^(-1)*xx'*P*xx);
yHat=bHat'*xx;
e(iter)=d(n)-yHat;
bHat=bHat+k*conj(e(iter));

P=FGetFctr^(-1)*P-FGetFctr^(-1)*k*xx'*P;
```

Figure 10 Recursive Least Square (RLS) MATAB Equation Exemplar

The following diagram depicts the convergence performance improvement over the use of Least Mean Square (LMS) approach.

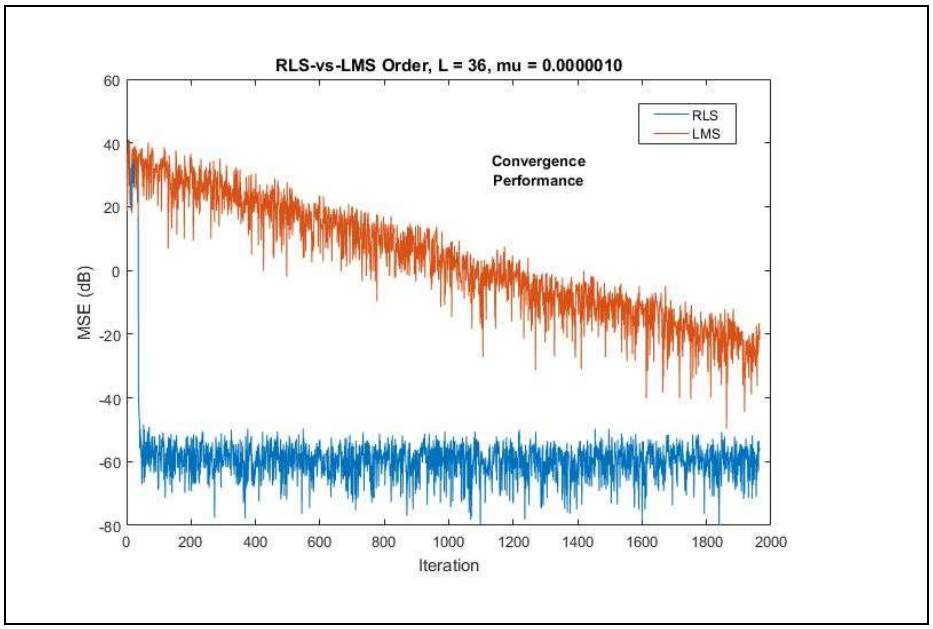

Figure 11. RLS versus LMS Convergence Performance (LMS μ unstable in this example)

Improved Equalization Performance

By mitigating the computational complexity through the use of the Matrix Inversion Lemma (MIL) as well as mitigating numeric instability by using a floating point (with bound definitions), versus a fixed point, implementation in each parallelized thread of execution enables a dramatic improvement in convergence performance. In legacy communication devices, transmitter instability is common and must be dealt with after signal acquisition to ensure message communication is not lost. The following diagram depicts this instability.

Additional issues arise from longer time periods between communication message periods coupled with non-deterministic frequency uncertainty. When this occurs, the signal must be re-acquired using the methods previously described. Once the signal is

acquired, the phase tracker algorithm below implements a time varying Block Modified Covariance Algorithm (BMCA-2) to maintain signal lock.

The following BMCA algorithm is used to perform the time varying simulation:

$$F_y(z) = \frac{1}{(z - \alpha(n)e^{j\theta(n)})^2} \tag{53}$$

Each frequency is time varying note: (n). In order to maintain phase tracking, sample blocks are limited to only four samples. These small sample blocks maintain the frequency response necessary to quickly adjust to transmitter drift as it occurs.

This exemplar system is composed of two adaptive system components: Signal Acquisition and Phase Tracking. As described earlier, the Signal Acquisition adaptive system component performs tasks in parallel to reduce the time required for signal acquisition. To ensure the computational needs of the architecture are achieved the following, parallelized, processing fabric is assumed. An array processing capability enables processors to work in parallel autonomously.

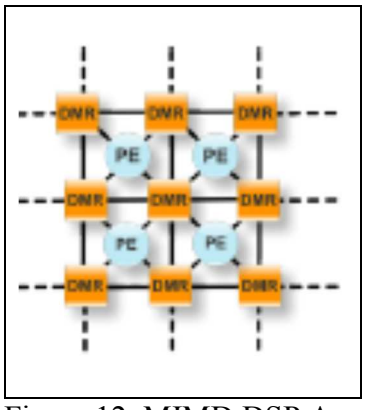

Figure 12. MIMD DSP Array Concept (Efficient Floating Point Performance)

An example of such architecture enables a Multiple Instruction Multiple Data (MIMD) implementation (as defined by Flynn's taxonomy) that enables complete parallelization architecture which is not possible with a Single Instruction Multiple Data (SIMD) architecture provided by a Graphic Processor Unit (GPU). One advantage of this structure is its ability to pipeline the RLS algorithm using Scaled Tangent Rotation (STAR).

By the use of several adaptive techniques on the receiver architecture, the RLS algorithm (in sequential form) is used to orchestrate the detection of the signal during signal acquisition. During detection, equalization also occurs and is demonstrated on the receiver design. Once signal acquisition is achieved, phase tracking is also important and described. Though the use of the RLS algorithm requires the inversion of the autocorrelation matrix, the MIL can aid in reducing this complexity. Additionally, to avoid numeric instability, a floating point implementation is utilized with bounds defined.

Proposed Vector Aperture Design

To increase the performance of 5G wireless communication without requiring extensive changes to the wireless protocol stack, vector antennas will be used to exploit the polarization diversity inherent in these apertures to double the effective bandwidth available between mobile devices and base stations. This exploration will transmit two linearly polarized signals that are spatially and temporally orthogonal with an OFDM

modulated signal that is more resilient to multipath effects that utilize a circularly polarized signals with opposite spins. In the receive direction, the polarization state can be estimated without an antenna that is polarization sensitive. The improved capability of deriving the Direction of Arrival (DoA) using all six field components comprised of $E(\theta, \emptyset, r)$ and $H(\theta, \emptyset, r)$ will enhance how the system adapts to device density distribution at each transceiver spatially distributed (discussed in the link layer design portion of this document). In addition, the DOA information can then be used to increase the directionality of the transmitted signal. The transmitted signal is directed towards the arrived signal by calculating an instantaneous direction without suffering from spatial ambiguity caused by uniform and non-uniform planar arrays such as 2-dimensional planar arrays.

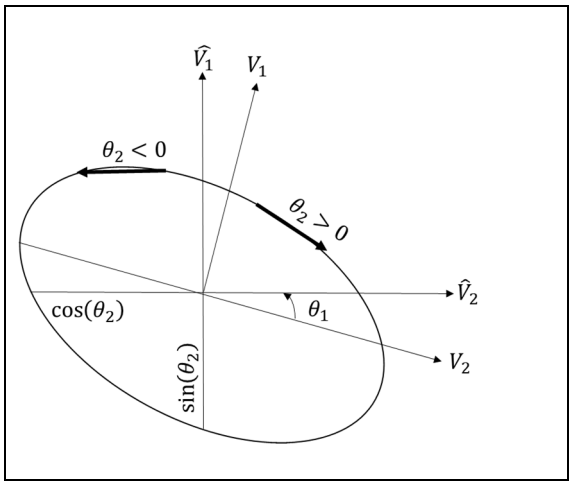

Figure 13. Vector Antenna Polarization Plot (Nehorai, 1994)

By using a vector sensor in addition to the super resolution direction finding algorithm such as MVDR, MUSIC or ESPRIT. The vector sensor must search two polarization state parameters (γ, η) in addition to the two angle parameters$(\theta, \emptyset)$. This polarization

state search and the adapted angular response techniques is solved by a generalized eigenvalue problem of the form:

$$Yv = \lambda Xv \tag{54}$$

The use of λ in this equation corresponds to the eigenvalues of the decomposition and v the associated eigenvectors. In MATLAB, the [V,λ] = eig(Y,X) and can be easily solved mathematically. The pseudo spectrums for minimum variance distortionless response (MVDR as proposed by Capon in 1967) and multiple signal classification (MUSIC) are as follows:

$$P_{MVDR}(\theta,\phi) = \frac{v_{vs}^H(\theta,\phi)v_{vs}(\theta,\phi)}{v_{vs}^H(\theta,\phi)R_{xx}^{-1}v_{vs}(\theta,\phi)} \tag{55}$$

$$P_{MUSIC}(\theta,\phi) = \frac{v_{vs}^H(\theta,\phi)v_{vs}(\theta,\phi)}{v_{vs}^H(\theta,\phi)E_N E_N^H v_{vs}(\theta,\phi)} \tag{56}$$

$v_{vs}(\theta,\phi)$ is the steering vector for a single vector sensor. For the receiver with an unknown polarization state, a maximization of the eigenvalue λ_{max} is performed over the P_{MVDR} or P_{MUSIC} pseudo spectrums to determine the correct polarization. Once this is derived, the individual polarization parameters (γ,η) can be solved:

$$\gamma = tan^{-1}\left|\frac{P_{max}(1)}{P_{max}(2)}\right| \; and \; \eta = \angle\left(\frac{P_{max}(1)}{P_{max}(2)}\right) = \angle P_{max}(1) - \angle P_{max}(2) \tag{57}$$

A vector version of the P_{MVDR} or P_{MUSIC} pseudo spectrum can be used to create a two dimensional surface: $10\,log_{10}(\theta,\phi)$, elevation angle θ and azimuth angle ϕ. The maximum peak of the two dimensional surface of the pseudo-spectrum for a single signal

arriving at (θ, ϕ); using this peak, the associated eigenvector is used to estimate the polarization parameters(γ, η).

Vector sensors exploit their spatial and polarization diversity of incident signals by weighing the complex electromagnetic field components as opposed to the traditional spatial derivation utilized by uniform planar arrays. By using the steering vector $v_{vs}(\theta_d, \phi_d, \gamma_d, \eta_d)$ where (θ_d, ϕ_d) is the arrival angle and (γ_d, η_d) is the polarization. Using the dummy variable $\xi_d = (\theta_d, \phi_d, \gamma_d, \eta_d)$, the beam pattern $\rho(\xi_d, \xi_i)$ is then the response of the vector sensor $v_{vs}(\xi_d)$ when steered toward ξ_d (Gross, 2015).

$$\rho(\xi_d, \xi_i) = \frac{|v_{vs}(\xi_d)^H v_{vs}(\xi_i)|^2}{4} \tag{58}$$

The maximum directivity is achieved when $\xi_d = \xi_i$ and is normalized to unity when the equation above reaches it maximum. The quality measurement of the estimate is described using the Cramer Rao Lower Bound (CRLB). To derive the CRLB for the arriving angles (θ, ϕ) and the unwanted parameters polarization state (γ, η), the equation is as follows (Gross, 2015):

$$J = \begin{bmatrix} J_{(\theta,\emptyset)(\theta,\emptyset)} & J_{(\theta,\emptyset)(\gamma,\eta)} \\ J_{(\gamma,\eta)(\theta,\emptyset)} & J_{(\gamma,\eta)(\gamma,\eta)} \end{bmatrix} \tag{59}$$

$$C(\theta, \emptyset) = \begin{bmatrix} C_{(\theta\theta)} & C_{(\theta\emptyset)} \\ C_{(\emptyset\theta)} & C_{(\emptyset\emptyset)} \end{bmatrix} = \left[J_{(\theta,\emptyset)(\theta,\emptyset)} - J_{(\theta,\emptyset)(\gamma,\eta)} {J^{-1}}_{(\gamma,\eta)(\gamma,\eta)} J_{(\gamma,\eta)(\theta,\emptyset)} \right] \tag{60}$$

To derive the CRLB $(\theta, \emptyset)$, the signal power $\sigma_s^2 = 1$ is unity and the associated noise power is derived using the following equation (Nehorai, 1994) (Gross, 2015):

$$\sigma_N^2 = \frac{\sigma_s^2}{10^{\frac{SNR}{10}}} \tag{61}$$

By steering beams towards mobile devices using the DOA information from received signals, one can utilize the MUSIC algorithm, known as the root-MUSIC algorithm which utilizes the roots of a polynomial in the denominator to derive the MUSIC pseudo-spectrum.

$$P_{RMUSIC} = \frac{1}{|\bar{s}(\theta)^H \bar{Q} \bar{s}(\theta)|}\ ,\ \bar{Q}_l = \sum_{l=M+1}^{M-1} A_l e^{-jkdl\sin\theta}\ ,roots(\ \bar{Q}_l) \tag{62}$$

$$AoA's = -sin^{-1}\left(\frac{roots(\ \bar{Q}_l)}{\pi}\right)\left(\frac{180}{\pi}\right) \tag{63}$$

The root-MUSIC approach is used to improve the performance of DOA estimates while reducing the computational requirements of the algorithm.

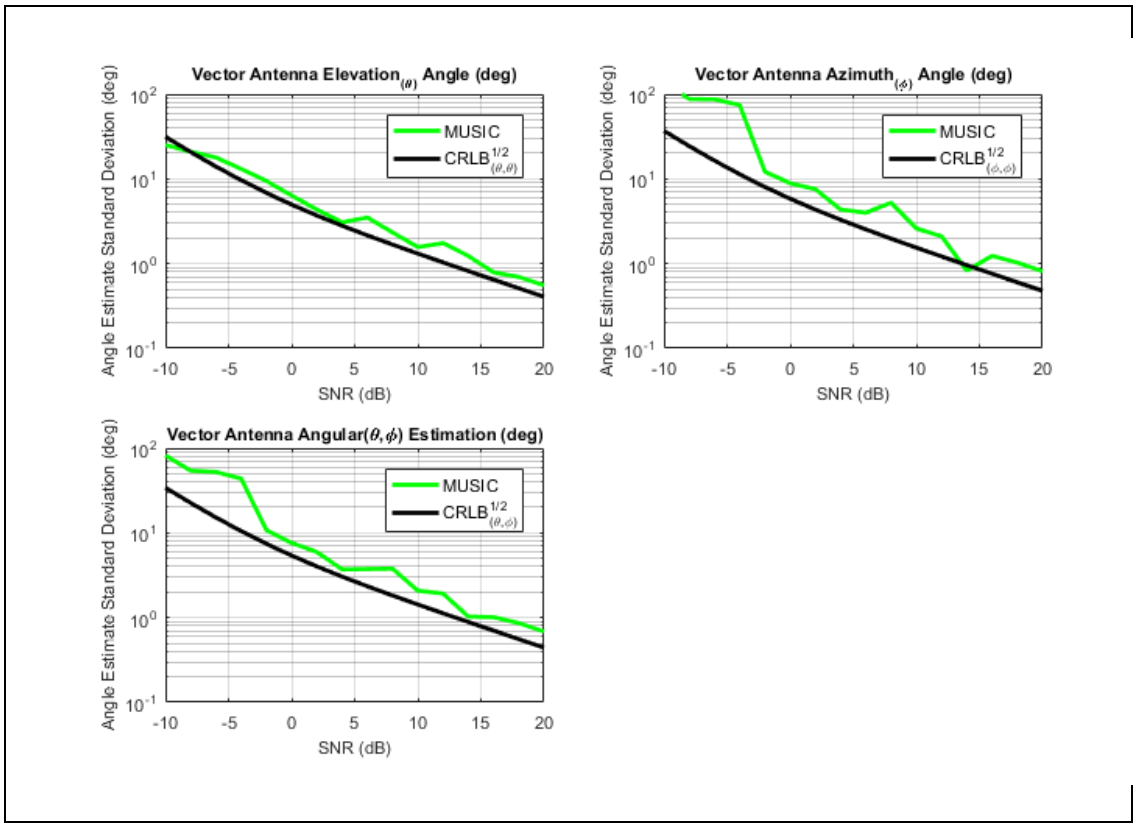

Figure 14. Vector Antenna MUSIC Performance

As the SNR increases, the signal averaging and correlation provided by MUSIC converges to the CRLB standard deviation estimation accuracy; however, under high signal correlation the MUSIC algorithm performance degrades significantly. Subject to a uniform linear array or vector array, SNR, signal correlation and time averaging the use of root-MUSIC improves the performance of the traditional MUSIC algorithm. The vector sensor provides six vector measurements in a single antenna aperture with full polarization sensitivity and diversity. It provides two dimensional angle of arrival (AoA) and polarization state estimation with a single vector sensor and a single time snapshot. Vector sensors are more accurate than spatially displayed arrays of the same footprint with no spatial under sampling ambiguities caused by grating lobes. No synchronization

required between separate sensors due to all elements are collocated with superior co-channel/co-direction interference mitigation performance. Since the array elements of the vector antenna has three elements (x, y, z) in both the E and H fields given the antenna system a wide field of view and outstanding low frequency performance (~6GHz or less). The performance is defined by the achievable SNR as defined the Friis radio link equation.

The goal of the vector antenna design is to create an adaptive smart antenna system that can automatically adapt signal transmission and reception based upon the achievable power spectral density (PSD) by individual mobile devices which is often associated to their spatial distribution. Additionally, the design goal is direct the main beam toward the signal of interest (SOI) and direct nulls towards signal interferers. Though references to mathematical equations that describe transceiver design have been provided earlier in this document, the focus of this analysis will be on results that can be qualitatively measured and to what extent do elements [within a vector antenna] interfere or couple with each other in a vector antenna as well as an array of such antennas. The largest challenge is to overcome in the design of the vector antenna are the effects of mutual coupling between the antenna elements. (In other words, some of the signal on one of the six elements will be re-radiation from the other five elements.) The objective of this analysis is to enhance knowledge in regard to the effects of mutual coupling, what they are and how can they be mitigated practically. The focus of this analysis will be on results that can be quantitatively measured, specifically when a signal is directed towards an antenna element. To achieve maximum energy transfer from the electromagnetic field to the

antenna element, the element impedance should match such that the response is equal in magnitude and phase to the reflected wave in an antenna array to minimize reflected energy (Allen & Diamond, 1966). The impedance is measured in the presence of coupled waves which depend upon the excitation as well as the distance between antenna elements; therefore, the impedance selected is optimum only for a particular frequency and spatial separation. The radiation efficiency of an array of antenna elements vary with the frequency range of operation; a plane wave incident on a receiving array causes current to flow on the element(s), the element(s) retransmit energy into space and into adjacent antennas (Balanis, 2009). This retransmitted complex energy adds to the wave directly incident from space. The total input energy to each antenna from an incident wave is the sum of the wave and those coupled from other antennas. Again, the energy from these coupled elements is dependent upon their relative position. The total amount of energy absorbed and reradiated from one element depends upon the impedance match at all other elements. Additionally, to achieve maximum extraction of energy, a terminating, closely matched impedance of the elements is selected to minimize the retransmission of energy to space. Reciprocity dictates that the impedance based upon the placement and excitation of the other elements is the same as the impedance on the transmit path of the array element. Because of mutual coupling, it is clear that array efficiency will vary depending upon the frequency of transceiver signals.

The following basic parameters of measurement of this, or any, antenna starts with the directivity and gain which is calculated as follows (Balanis, 2009):

$$Rad.Intensity: U(\theta,\phi) = U_\theta(\theta,\phi) + U_\phi(\theta,\phi)\,, U_\theta \propto |E_\theta|^2, U_\phi \propto \left|E_\phi\right|^2 \qquad (64)$$

$$Part.\,Directivities\; D(\theta,\phi) = D_\theta(\theta,\phi) + D_\phi(\theta,\phi)\,, D_\theta = \frac{4\pi U_\theta}{P_{rad}}, D_\phi = \frac{4\pi U_\phi}{P_{rad}} \quad (65)$$

$$P_{rad} = U_{max}\Omega_A\,, where\; \Omega_A = \frac{4\pi}{D_0} \quad (66)$$

$$Directivity\;(D) = \frac{U(\theta,\phi)}{U_0} = \frac{4\pi U(\theta,\phi)}{P_{rad}}, where\; D_{max} = \frac{4\pi U_{max}}{P_{rad}} \quad (67)$$

$$Gain\;(G) = \frac{4\pi U(\theta,\phi)}{P_{in}}, where\; P_{in} = \frac{P_{rad}}{e_{cd}} = \frac{P_{rad}}{e_c e_d}:\;\; G(\theta,\phi) = e_{cd}D(\theta,\phi) \quad (68)$$

Absolute gain accounts for the reflection efficiency coefficient when an antenna element is connected to a transmission line. The reflection efficiency coefficient and absolute gain are calculated as follows:

$$\Gamma = \frac{(Z_{in} - Z_O)}{(Z_{in} + Z_O)}, e_r = (1 - |\Gamma|^2)\,, e_o = e_{cd}(1 - |\Gamma|^2) \quad (69)$$
$$Z_{in} = Aperture\; input\; impedance$$
$$Z_O = Characteristic\; impedance\; of\; the\; transmission\; line$$

$$Absolute\; Gain\;(G_{abs}) = e_r e_c e_d \frac{4\pi U(\theta,\phi)}{P_{rad}}, where\; G_{abs}(\theta,\phi) = e_0 D(\theta,\phi) \quad (70)$$
$$e_c = Conduction\; efficiency$$
$$e_d = Dielectric\; efficiency$$

U is a far field parameter that is defined as the power radiated from an aperture per unit solid angle.

$$U = r^2 W_{rad}\,, where\; U = Radiation\; intensity \quad (71)$$
$$W_{rad} = Radiation\; density$$
$$r = Distance$$

$$W_{rad}(r,\theta,\phi) = \frac{U(\theta,\phi)}{r^2}\ , where\ W_{rad} \propto \frac{1}{r^2} \tag{72}$$
$W_{rad} = Radiation\ density$
$r = Distance$

Another figure of merit is called beam efficiency and is used a measure of quality of receive and transmit apertures. The beam efficiency (BE) is defined as the following:

$$BE = \frac{\int_0^{2\pi}\int_0^{\theta_c} U(\theta,\phi)\sin\theta\, d\theta d\phi}{\int_0^{2\pi}\int_0^{\pi} U(\theta,\phi)\sin\theta\, d\theta d\phi}\ , where\ \theta_c = cone\ angle \tag{73}$$
$\theta_c = angle\ of\ 1st\ null/minimum$

A very important figure of merit is the pattern and impedance bandwidths. The pattern of the vector antenna can vary greatly based upon aperture design. The proposed design is based upon the use of a either a set of Vivaldi antenna elements or a set of monopole/dipole elements that are orthogonally arranged around the x, y and z axis. As the term bandwidth suggests, both the pattern and the impedance are frequency dependent. The impedance bandwidth is comprised of the input impedance and the antenna radiation efficiency. The pattern bandwidth is comprised of the following components (Balanis, 2009):

Table 2
Pattern Bandwidth Figures of Merit

Pattern Metric
Beam direction
Directivity/Gain
Beamwidth
Polarization

As beamwidth goes up, directivity decreases. The previously discussed parameters influence the performance of the antenna array design by varying its reflection

coefficients, element impedance and overall antenna pattern. The following is a diagram of the mutual coupling between antennas co-located:

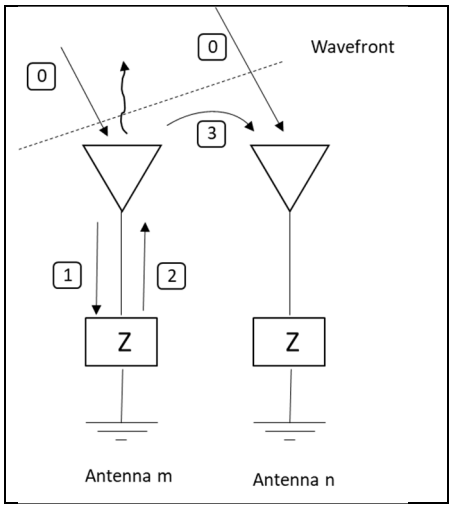

Figure 15 Mutual Coupling Diagram (Two Elements)

Array impedance changes as a function of scan angle and frequency. The vector antenna below describes the x, y and z axis for either the E or H field. The other field (not depicted) is orthogonal to this field.

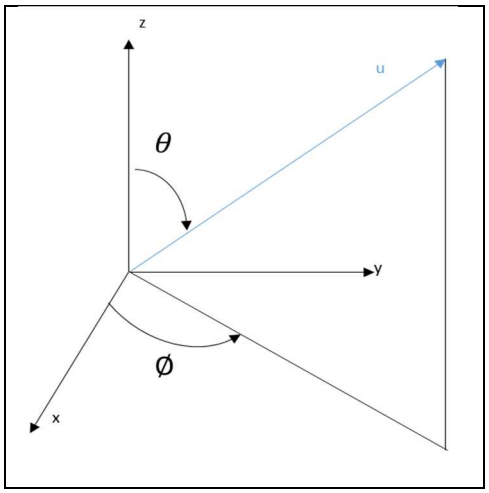

Figure 16. Vector Antenna Poynting Vector (Nehorai, 1994)
(Polarization depicted in Figure 13)

$$\bar{u} = \begin{bmatrix} cos\,\phi\, sin\,\theta \\ sin\,\phi\, sin\,\theta \\ cos\,\theta \end{bmatrix} \tag{74}$$

$$\bar{u} \times \bar{E}(t) = -\eta \bar{H}(t) \tag{75}$$

$$Y_E(t) = \bar{E}(t) + N_E(t) \tag{76}$$

By substitution of Maxwell's equation, we get the following:

$$Y_H(t) = \bar{u} \times \bar{E}(t) + N_E(t) \tag{77}$$

Estimation of $\bar{u}$ is derived from reducing measurement noise through averaging:

$$\bar{S} = \frac{1}{N} \sum_{t=1}^{N} Re[y_E(t) \times \bar{y}_H(t)]\,, where\ \bar{u} = \frac{\bar{S}}{\|\bar{S}\|} \tag{78}$$

$$E(t) = Q\bar{\gamma}(t)\,, where\ \bar{\gamma}(t) = transmitted\ signal \tag{79}$$

$\mu = \begin{bmatrix} cos\,\phi\, sin\,\theta \\ sin\,\phi\, sin\,\theta \\ cos\,\theta \end{bmatrix}$, vector pointing toward target source (Figure 16) (80)

$$\rho = e^{-j\frac{freq}{c(VApos)\mu}}\,, Phase\ diff.between\ elements,\ relative\ VA_{pos} = [x, y, z] \tag{81}$$

VA_{pos} is a matrix which contains the relative (to each other) vector antenna locations on each axis x, y, and z.

$$Q = \begin{bmatrix} cos\,\phi\, cos\,\theta & sin\,\phi \\ sin\,\phi\, cos\,\theta & cos\,\phi \\ -sin\,\theta & 0 \\ -sin\,\phi & cos\,\phi\, cos\,\theta \\ cos\,\phi & sin\,\phi\, cos\,\theta \\ 0 & sin\,\theta \end{bmatrix} \tag{82}$$

$$V_s = \rho \otimes \mu \, , (Tensor\ product)\ Steering\ vector \tag{83}$$

Polarization phase difference P_0 between (γ, η) of the incoming signal using the following equation:

$$P_0 = \left[sin(\gamma) e^{j\eta \frac{\pi}{180}} \quad cos(\gamma) \right] \tag{84}$$

Compute covariance matrix R_{xx} for the vector antenna antenna (sized by six elements, one for each dimension):

$$x = QP_0S + N_0, where\ R_{xx} = \frac{xx^T}{Columns(x)} \tag{85}$$

$$R_{xx} = \frac{xx^T}{Columns(x)} \, , finally\ R_{xx} = \frac{R_{xx}}{trace(R_{xx})} \tag{86}$$

Calculate the eigenvalues and eigenvectors using Jacobi rotations by determining the roots of the following equation:

$$R_{xx} \cdot V = \lambda V, where\ V = eigenvectors, and\ \lambda = eigenvalues \tag{87}$$

$$det|R_{xx} - \lambda I| = 0, \qquad where\ V = eigenvectors, and\ \lambda = eigenvalues \tag{88}$$

Since the of the covariance matrix order is six, one element for each dimension (i.e. $E(\theta, \phi, r)\ and\ H(\theta, \phi, r)$), the Jacobi method is sufficiently efficient and simpler to implement than other approaches such as the inverse iteration method. Once the eigenvectors V is obtained, we have obtained the noise subspace E_n:

$$E_n = V(:, 1:n) \tag{89}$$

$$G_1 = V_s^T E_n E_n^T V_s \, , and \; G_2 = V_s^T V_s \tag{90}$$

Calculate eigenvalues and eigenvectors for matrices G_1 and G_2 (i.e. $G_1V = G_2V*\lambda$). Extract elements of diagonal matrix λ and take the maximum eigenvalue λ and eigenvector V.

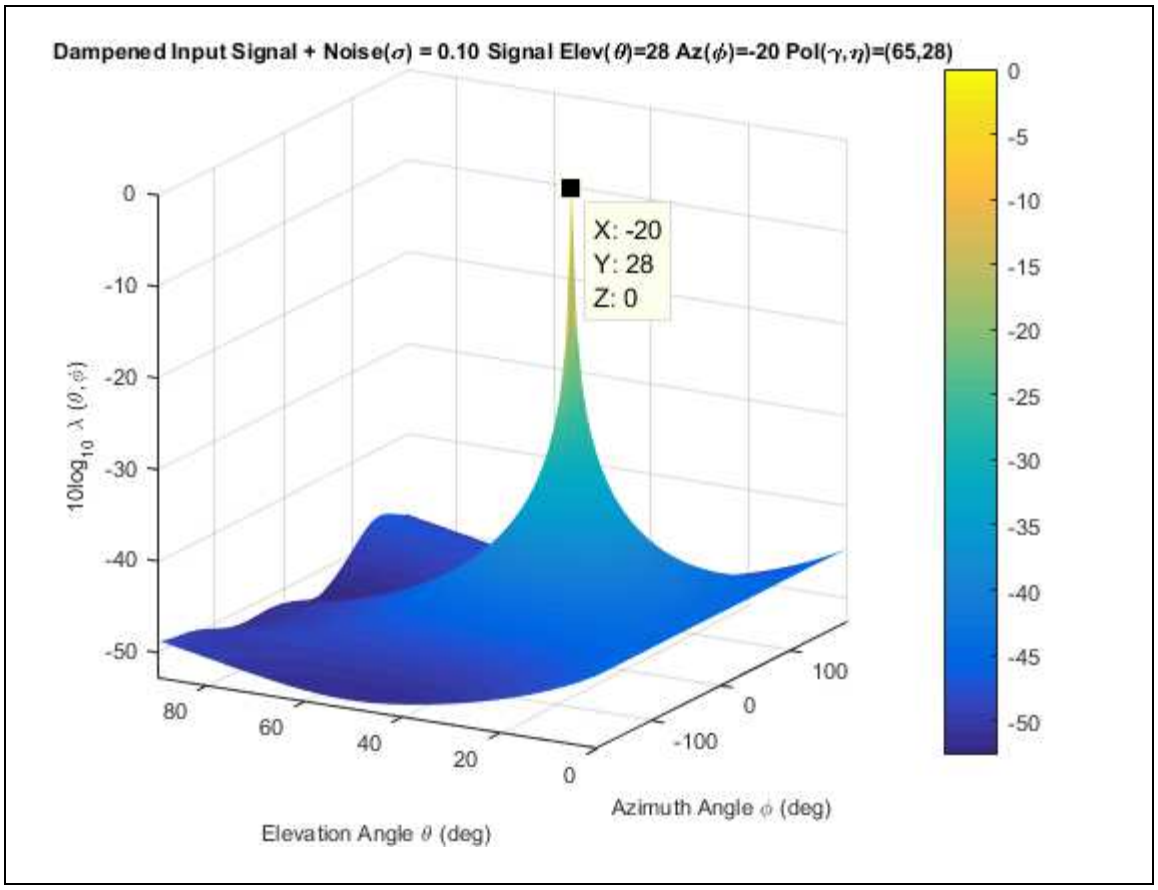

Figure 17 Vector Antenna DOA Estimate Using MUSIC

The overall receive and transmit capabilities can be derived by calculating the link margin. The following Friis radio link equation describes how much power is received by the receive antenna:

$$P_r = \frac{G_t G_r \lambda^2}{(4\pi R)^2} P_t \, W \tag{91}$$

This equation describes the maximum amount receive power and is frequency dependent as described by the use of the wavelength λ. The parameters related to $G_t G_r$ are dimensionless and are dependent upon the directivity aperture pattern given the angle of reception. Since a vector antenna does not have high gain, receive design is a key factor in the performance of the vector antenna. The better the receiver sensitivity (i.e. low cascaded noise figure, high transceiver gain, etc...), the better the performance of the vector antenna design. Polarization mismatch, atmospheric attenuation and multipath effects reduce the performance of the vector antenna. An obvious outcome of the equation above, is that the receive power is inversely proportional to distance:

$$P_r \propto= \frac{1}{(R)^2} \tag{92}$$

The link margin can be calculated using the following equation and is equation form of the table reference (Table 1).

$$P_r = P_t - L_t + G_t - L_0 - L_A + G_r - L_r \tag{93}$$

Other losses (L), such as impedance mismatch can also be added to the equation above. The noise power N_0 is the following:

$$N_0 = kT, Example\ (@300K/80.33F) = 4.1(10)^{-21}\, W/_{Hz} = -203.9dBW \tag{94}$$

Therefore, the receive power to noise ratio $\frac{P_r}{N_0}$:

$$\frac{P_r}{N_0} = P_r dB - (N_0)dB = \rho\left(\frac{dB}{Hz}\right) \tag{95}$$

Spatially Diverse Arrays

As a comparison, the typical direction of arrival (DOA) algorithms as well as proper combining of received signals for [digital] signal processing rely upon what can be referred to as an array correlation matrix, steering matrix or covariance matrix. The following diagram depicts this concept:

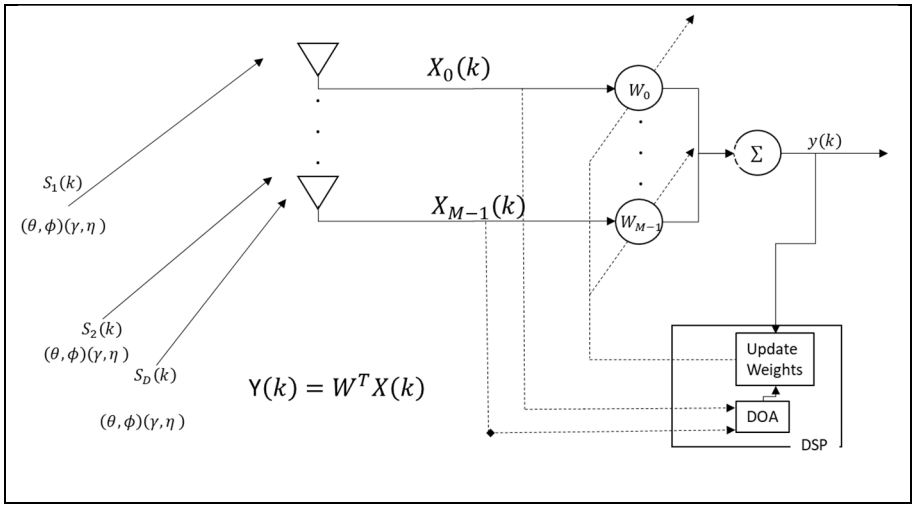

Figure 18 M-Element DOA and (SOI) Receiver Diagram

$$X(k) = A_D(k)S_D^T(k) + N(k) \tag{96}$$

Where steering vector A(k) is a M x D matrix for each (θ) direction of arrival.

Therefore, the spatial covariance matrix R_{xx} is calculated as follows:

$$R_{xx} = AE[SS^H]A^H + E[NN^H] \tag{97}$$

$$R_{xx} = AR_{SS}A^H + R_{NN}$$

Spatially diverse arrays are depicted below. As is the case with the steering vector A(k), their weights are frequency dependent. In practical applications, this matrix is indexed and calibrated over the intended frequency range so that each angle of arrival can be calculated.

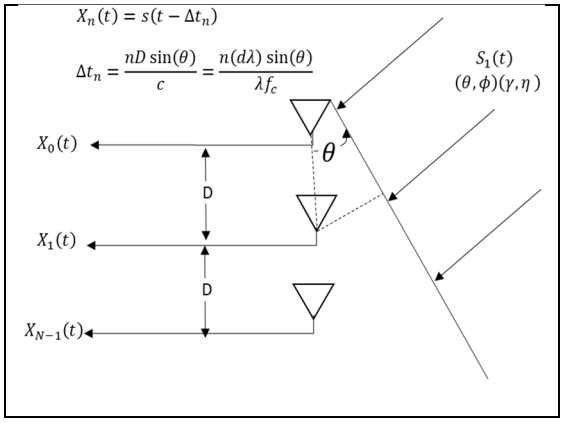

Figure 19 Uniform Linear Array (ULA) Example

The following equations relate frequency to angles of arrival, these equations have the following Vandermonde matrix structure:

$$\begin{bmatrix} x_0[k] \\ x_1[k] \\ \vdots \\ x_{N-1}[k] \end{bmatrix} = \begin{bmatrix} 1 & 1 & \cdots & 1 \\ e^{-j\omega_0} & e^{-j\omega_1} & \cdots & e^{-j\omega_{r-1}} \\ e^{-j2\omega_0} & \vdots & \ddots & \vdots \\ e^{-j(N-1)\omega_0} & \cdots & \cdots & e^{-j(N-1)\omega_{r-1}} \end{bmatrix} \begin{bmatrix} S_0[k] \\ S_1[k] \\ \vdots \\ S_{r-1}[k] \end{bmatrix} + \begin{bmatrix} V_0[k] \\ V_1[k] \\ \vdots \\ V_{N-1}[k] \end{bmatrix} \quad (98)$$

$\omega_i = 2\pi d\, sin(\theta_i)\,, where\ A_n(\theta_i) = e^{-jn\omega_0}, and\ V\ is\ the\ noise\ sample$

In this example, spectral estimation algorithms (such as MUSIC, ESPIRIT, etc…) are used to estimate ω_i and DOAs are then estimated by solving for θ_i.

The previous paragraphs demonstrate an understanding of DOA estimation using uniform linear arrays as well as Vector apertures. This study focuses on the performance of Vector apertures utilizing root-MUSIC and ESPIRIT spectral estimation. The following diagram depicts the use of adaptive digital signal processing to perform adaptive beam forming that permits the null of interfering signals or accentuating beans in the direction of particular signals of interest (SOI).

From a beamforming perspective, MUSIC is utilized to identify signal direction and polarization within a subspace orthogonal to beam forming array noise subspace. Eigenmodes of array sample vectors are found by factoring the estimated observed signal covariance matrix $\bar{\bar{R}}_{yy}$:

$$\bar{\bar{R}}_{yy} = \bar{\bar{E}}\bar{\bar{\Lambda}}\bar{\bar{E}}^T \qquad \bar{\bar{\Lambda}} = \begin{bmatrix} \lambda_1 & \cdots & 0 \\ \vdots & \ddots & \vdots \\ 0 & \cdots & \lambda N_x N_y \end{bmatrix}, where\ \bar{\bar{E}} = [e_1 \quad \dots \quad e_2 N_x N_y] \tag{99}$$

$\bar{\bar{\Lambda}}$ is a diagonal matrix of positive real eigenvalues, each of which is the energy in an observed signal mode. $\bar{\bar{E}}$ is a column matrix of eigenvectors that are orthonormal and span the observed signal space. During the formulation of MUSIC when formulating the signal subspace, signal amplitude is lost because the power signal information does not enter the minimization of the magnitude of the error vector. This minimization is accomplished by maximizing the vector's inverse length squared over all signal

propagation directions and polarizations. However, once the directions and polarization within the signal subspace are established, the signal amplitudes can be estimated by forming the beam weights for these directions. The precision of this signal maximization process depends on the MUSIC functional's parametric M dimensional landscape (i.e. the functional $\frac{1}{\left|\frac{1}{\Delta S(n)}\right|^2}$ viewed as a function of NM variables), where M is the number of incoherent received signals, a total of M unique local maxima are identifiable and N is the number of aperture elements. The degree of precision available in identifying the parameters for each maximum depends on the functional peakedness, which in turn depends on the second derivative of the MUSIC function with respect to each of the N peakedness parameters (i.e. polarization, direction, etc…). The signal power does not affect the MUSIC functional maximization, rather the SNR for the M presumed signals affects the subspace eigenvector determination via the eigenvector decomposition, and thus nonlinearity affects the determination of the signal directions and polarizations. A high SNR (10dB or higher) for each signal is needed to reliably separate the signal and noise subspaces.

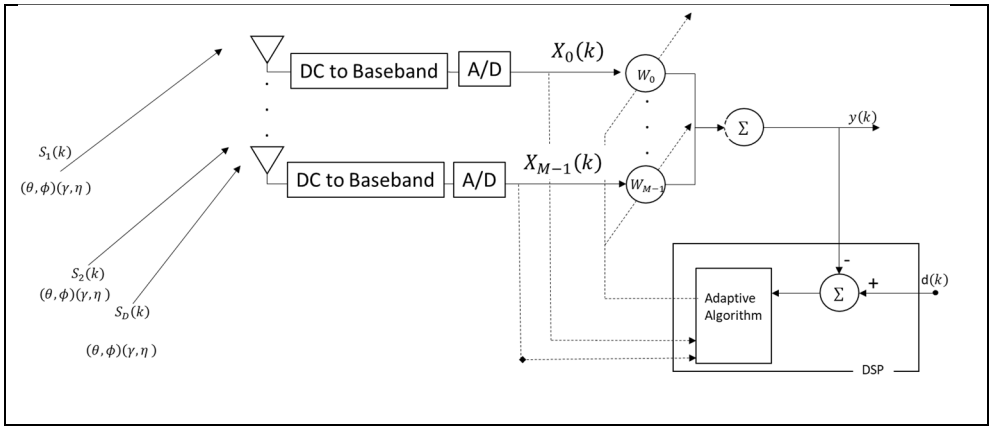

Figure 20 Adaptive Beam Forming Algorithm (DC=Down Conversion)

The following algorithm is the Least Mean Square (LMS) approach to adapting the beam pattern to desired pattern. Desired beam forming patterns are very similar to a Finite Impulse Response (FIR) filter patterns using windows to reduce the side lobe levels.

$$W_{k+1} = W_k + 2\mu x_k(d_k - x_k^T w_k) \tag{100}$$

$$H(f) = \frac{1}{N}\sum_{n=0}^{N-1} w_n e^{-j\omega n} \ , where\ \omega = 2\pi f \tag{101}$$

$$W(\theta) = \frac{1}{N}\sum_{n=0}^{N-1} w_n e^{-j\omega_s n} \ , where\ \omega_s = 2\pi d sin\,\theta \tag{102}$$

The difference in the two equations is the spatial frequency ω_s. ω_s varies as $sin\,\theta$ while ω varies directly as frequency f. The coefficients of a FIR filter is analogous to design the complex weights of a beam former in a uniform linear array. Also, windowing techniques used in FIR filter design can also be used in the design of beam patterns. Sidelobe levels of beam formers can be lowered by multiplying beam pattern with window types such as Hamming or Chebyschev (see Dolph-Chebyshev).

Block Least Mean Square (BLMS)

The implementation of the Block Least Mean Square (BLMS) algorithm in both the time and frequency domains is now described. The following demonstrates a comparison between the LMS approach and the BLMS algorithms in the time and frequency domains. All converge to the Weiner Solution (Spanias, 2009):

$$\lim_{i\to\infty}\{E[b(i)]\} = b^0 \tag{103}$$

The following plots utilize colored noise as defined below to demonstrate that the same answers are obtain with or without the presence of colored noise.

Periodogram:

$$R_{xx}(e^{j\Omega}) = E\left[\frac{1}{2M+1}\left|\sum_{n=-M}^{M} x(n)e^{-jn\Omega}\right|^2\right] \qquad \text{x(n)=1,2,-1 n=\{0,1,2\}} \tag{104}$$

$$R_{xx}(e^{j\Omega}) = \left|1 + 2e^{-i\Omega} - e^{-i\Omega}\right|^2 \tag{105}$$

The following examples are a plot of the LMS algorithm performance to be used as reference for comparison to the additional plots in regard to the BLMS algorithms. The following plot demonstrates a perfect system identification. The estimation is a perfect overlay.

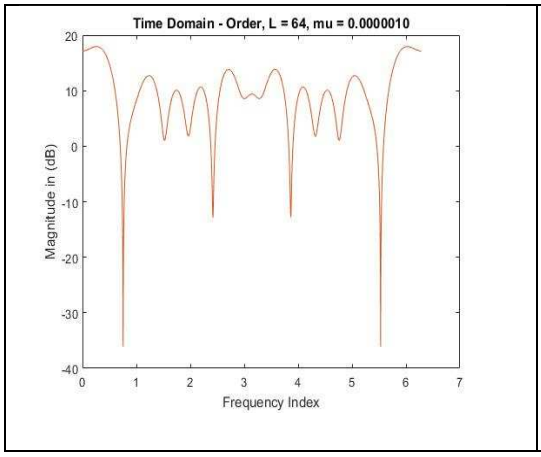

Figure 21 No Overlap (S=N)

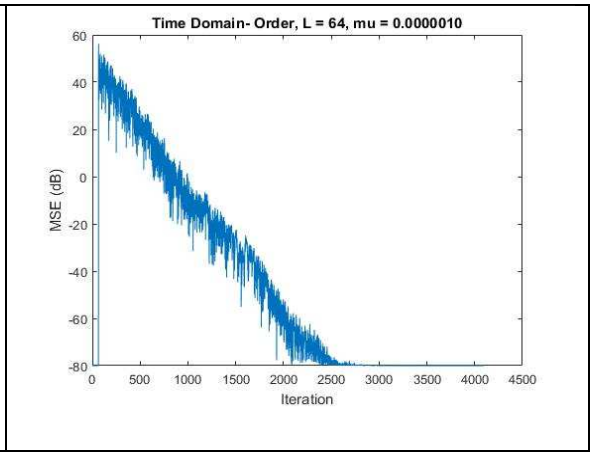

Figure 22 LMS Performance (S=N)

The Mean Square Error Plot versus iteration plot demonstrates the convergence of the algorithm. The [time domain] BLMS algorithm is described by the following state diagram, equations and the plots follow.

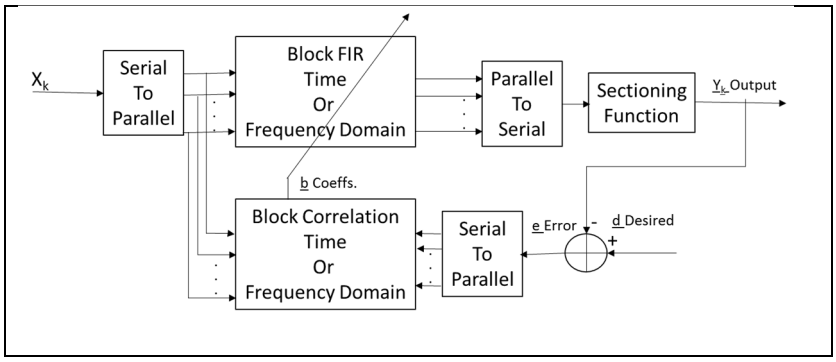

Figure 23 Implementation of Block LMS Algorithm

The algorithm above is composed of the following elements:

The following Input Matrix N x (L + 1):

$$x_B(i) = \begin{bmatrix} x(iS) & \cdots & x(iS-L) \\ \vdots & \ddots & \vdots \\ x(iS+N-1) & \cdots & x(iS+N-L+1) \end{bmatrix} \tag{106}$$

The following is the Error Matrix (N x 1):

$$\begin{bmatrix} e(iS) \\ \vdots \\ e(iS+N-1) \end{bmatrix} \tag{107}$$

$$= \begin{bmatrix} d(iS) \\ \vdots \\ d(iS+N-1) \end{bmatrix}$$

$$- \begin{bmatrix} x(iS) & \cdots & x(iS-L) \\ \vdots & \ddots & \vdots \\ x(iS+N-1) & \cdots & x(iS+N-L+1) \end{bmatrix} \begin{bmatrix} b_0(i) \\ \vdots \\ b_L(i) \end{bmatrix}$$

The following is the block update equation:

$$\begin{bmatrix} \widehat{b_0}(i) \\ \vdots \\ \widehat{b_L}(i) \end{bmatrix} \tag{108}$$

$$= \begin{bmatrix} \widehat{b_0}(i) \\ \vdots \\ \widehat{b_L}(i) \end{bmatrix} - 2\mu \begin{bmatrix} x(iS) & \cdots & x(iS-L) \\ \vdots & \ddots & \vdots \\ x(iS+N-1) & \cdots & x(iS+N-L+1) \end{bmatrix}_B^T \begin{bmatrix} e(iS) \\ \vdots \\ e(iS+N-1) \end{bmatrix}$$

The following is an example simulation of a Finite Impulse Response (FIR) the simulation of the time domain BLMS algorithm:

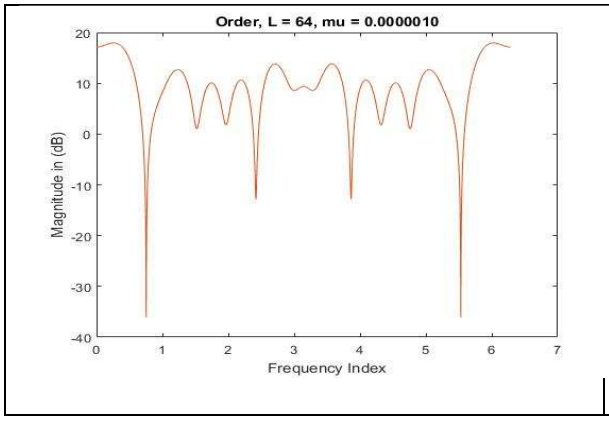

Figure 24 No Overlap (S=N)

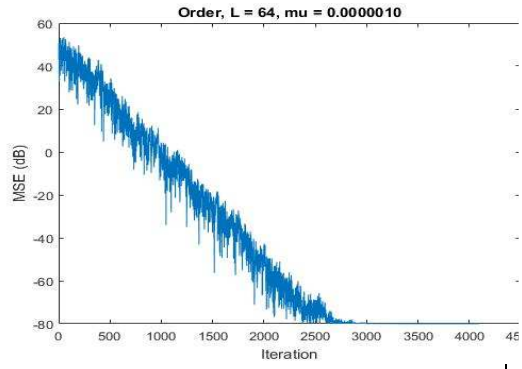

Figure 25 MSE No Overlap (S=N)

The convergence plot above (Figure 25Figure 24) will smooth out if the block size is larger. As was the case in the LMS reference plot above, the [time domain] BLMS estimation above is a perfect overlay. The following is the Mean Square Error Plot versus iteration plot which demonstrates the convergence of the BLMS algorithm:

This Mean Square Error (MSE) plot (of the BLMS algorithm) is identical to the LMS plot. Closely related, the Normalized Energy Estimation (NEE) double precision plot of

the BLMS [time domain] algorithm is described below. The following is the state diagram for the BLMS algorithm:

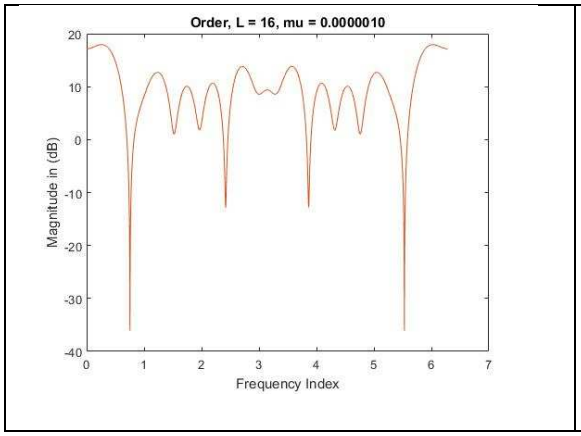

Figure 26 No Overlap (S=N)

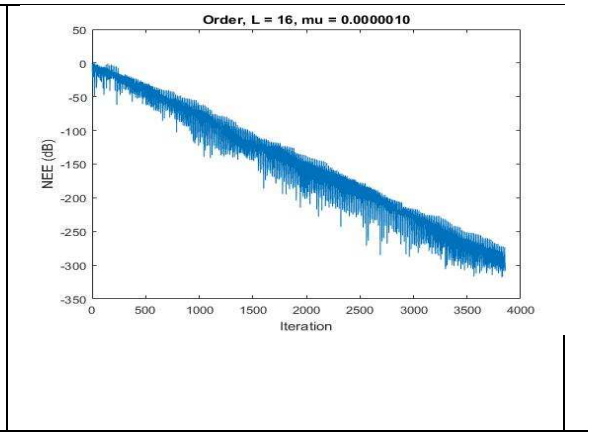

Figure 27 No Overlap (S=N), NEE Plot

The plot of the BLMS estimation as well as the NEE plot are displayed above for the BLMS algorithm using double precision with a filter order of L=16. As was the case when plotting the adaptive filter order L=64, the plot of the adaptive filter for order L=16 is displayed below. The plot of the convergence using the NEE algorithm is plotted above using double precision variables to calculate the NEE (in dB).

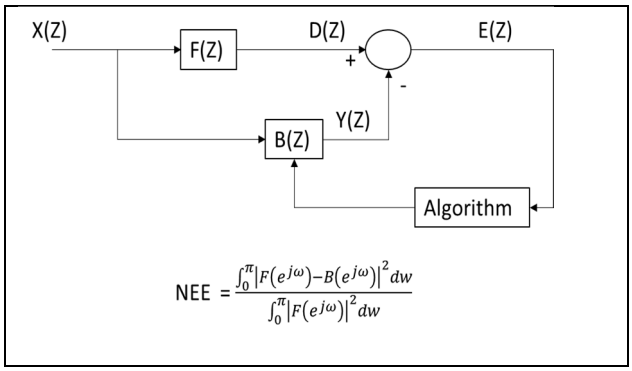

Figure 28 NEE Algorithm Block Diagram

Frequency Domain BLMS

As is the case of with the BLMS time domain algorithm, the frequency domain BLMS is a block type algorithm. All signals are transformed to the frequency domain. All

multiplies are convolutions in the time domain and therefore reduces the complexity. The FFT computations used in the BLMS frequency domain algorithm is $log_2(N)$ while the convolution approach in the time domain represents computation complexity of $log_2(N^2)$.

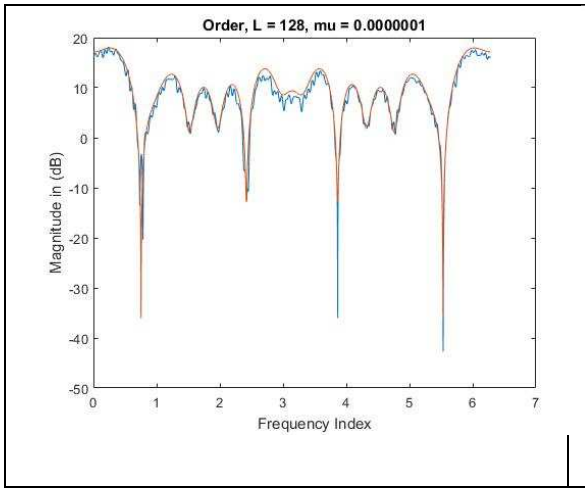

Figure 29 No Overlap (S=N)

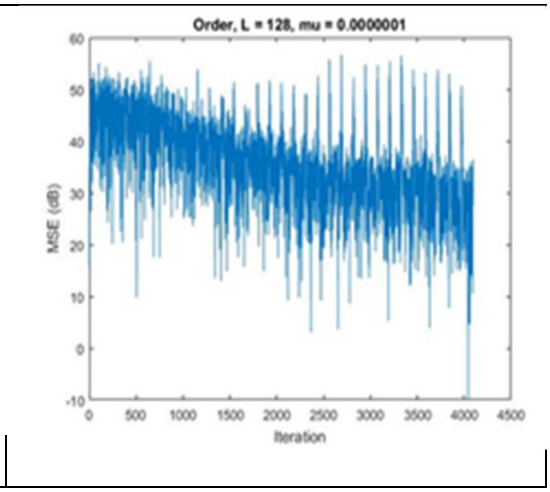

Figure 30 (S=N), Noisy MSE Plot

The plot below describes a convergence of a BLMS algorithm that utilizes the circular convolution, a suboptimal algorithm, therefore the convergence is limited to approximately ~20dB. The plot below shows the suboptimal performance (i.e. spikes in the mean square error (MSE) plot). The following is the NEE plot with an adaptive filter of order L=64:

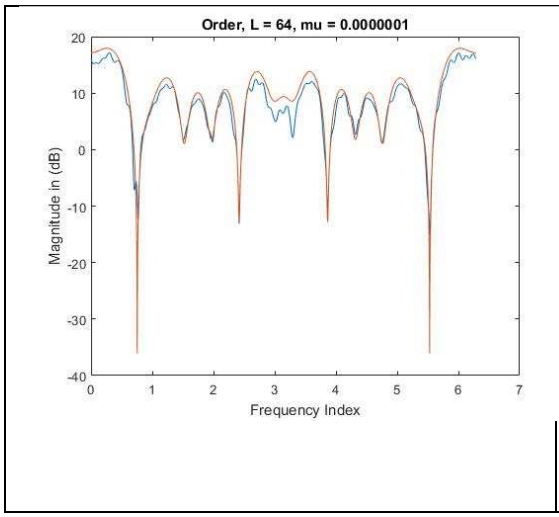

Figure 31 No Overlap (S=N)

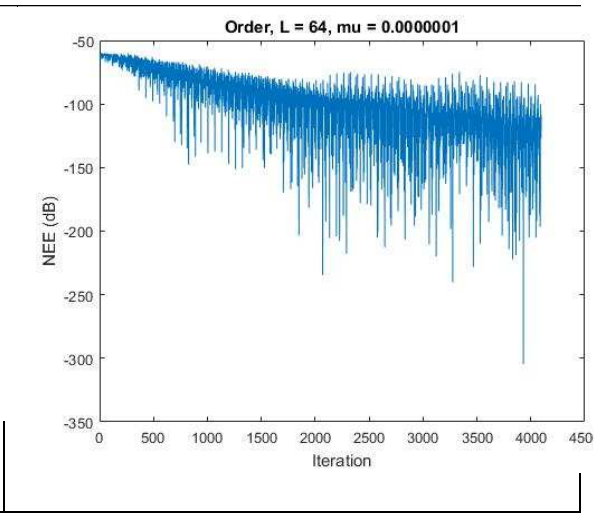

Figure 32 Noisy NEE Plot, No Overlap (S=N)

As was in the previous plots this BLMS plot in the frequency domain using the circular convolution method; therefore, the estimation is noisy and though still provides a decreasing NEE (NEE was plotted instead of MSE) every iteration. No overlap was used. The previous plots demonstrate the why the use of RLS, and the overlap and save method are preferred for adaptive beam forming techniques.

Overlap and Save

The following approach was implemented using linear convolution (instead of circular convolution) to implement frequency domain adaptive filter operations. This was accomplished by doubling the block sizes and using the overlap and save method. This implementation is described in the following diagrams and MATLAB code excerpts.

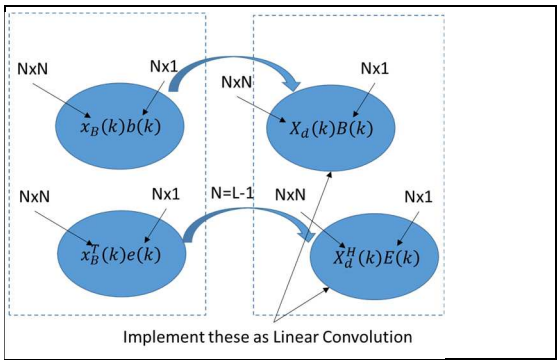

Figure 33 Overlap and Save Using Linear Convolution

$$\mathrm{X}(k) = \begin{bmatrix} X_k(0) \\ \vdots \\ X_k(2N-1) \end{bmatrix} = FFT \begin{bmatrix} x(k) \\ \vdots \\ x(kS+2N-1) \end{bmatrix} \tag{109}$$

$$\mathrm{D}(k) = \begin{bmatrix} D_k(0) \\ \vdots \\ D_k(2N-1) \end{bmatrix} = FFT \begin{bmatrix} d(kS) \\ \vdots \\ d(kS+2N-1) \end{bmatrix}$$

$$\mathrm{E}(k) = \begin{bmatrix} E_k(0) \\ \vdots \\ E_k(2N-1) \end{bmatrix} = FFT \begin{bmatrix} e(kS) \\ \vdots \\ e(kS+2N-1) \end{bmatrix} \tag{110}$$

$$\mathrm{B}(k) = \begin{bmatrix} B_k(0) \\ \vdots \\ B_k(2N-1) \end{bmatrix} = FFT \begin{bmatrix} b(k) \\ \vdots \\ b_{N-1}(k) \\ \vdots \\ 0 \end{bmatrix} \tag{111}$$

Zero padded coefficient block
=>
Overlap & Save, Zero pad impulse response

The following overlap and save function is then performed in the following manner:

$$\mathrm{X}(k) = \begin{bmatrix} X_k(0) \\ \vdots \\ X_k(2N-1) \end{bmatrix} = FFT \begin{bmatrix} x(k) \\ \vdots \\ x(kS+2N-1) \end{bmatrix} \tag{112}$$

$$X_d(k) = \begin{bmatrix} X_k(0) & & 0 \\ & \ddots & \\ 0 & & X_k(2N-1) \end{bmatrix}$$

The following equation is the multiplication of the input diagonal matrix with the coefficients to form the output Y of the adaptive filter in the frequency domain:

$$Y(k) = X_d(k)B(k) \tag{113}$$

To remove the circular convolution effects, we then take the inverse Fourier transform of the output Y and save only the last N points of this transform output and the calculate the error vector:

$$\overline{yk} = FFT^{-1}\{Y(k)\}$$
$$\overline{yz} = yk\left([N+1]: len\left(\overline{yk}\right)\right) \quad (114)$$
$$\bar{e} = D(index)[1:N,1] - \overline{yz}\ , where\ index = m^{th}\ block$$
$$\overline{ek} = [zeros(1,N)\ \bar{e}.'\ ]$$
$$\bar{E}_Z = FFT\{\overline{ek}\}$$

The gradient is calculated using the pre-padded Ez error vector and the diagonal input matrix Xd. We then only utilize the first N points of the inverse Fourier transform output. We then perform a 2N Fourier transform of the first N point output of the inverse Fourier transform by zero padding the input to the Fourier transform thereby obtaining Gz'. Gz' was constrained by zero padding.

$$\bar{G}_z = -2X_d'(k)\,\overline{E}z$$
$$\bar{G}_i = FFT^{-1}\{\bar{G}_z\} \quad (115)$$
$$\overline{gz} = [\bar{G}_i(1:N,1).'\ zeros(1,N)].'$$
$$\bar{\bar{G}}_z = FFT\{\overline{gz}\}\ ,\ \text{where}\ \bar{\bar{G}}_z = \text{Gradient}$$

Finally, the error vector is calculated in the frequency domain based upon the output of the update equation.

$$\bar{E}_z = \overline{D}_Z - \bar{X}_d\bar{B}_Z$$
$$e_Z = FFT^{-1}\{\bar{E}_Z\} \quad (116)$$

The convergence and estimation is then plotted with the following results. I have included MATLAB code that allows for a change the input signal sample to further adjust the overlap of the input vector. Though this overlap has nothing to do with the overlap & save operation, it does aid in the in the overlap of samples of the input matrix.

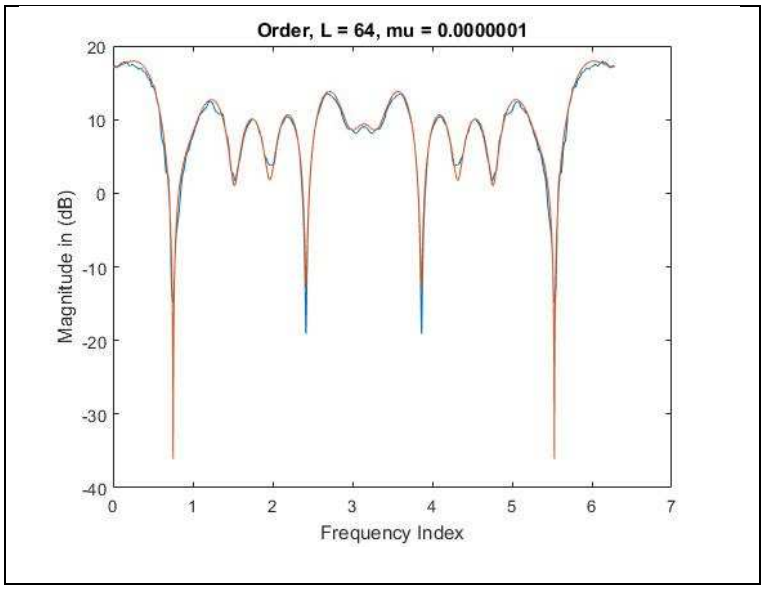

Figure 34 Overlap and Save with Order L = 64

The following is a normalized convergence factor that demonstrates the reduction in convergence noise by implementing a μ_k that is averaged across the frequency bins per block. The normalization equation is given below:

$$\mu_k(i) = \frac{\alpha}{1 + \frac{2}{I}\sum_{i=k-I}^{k}|X_k(i)|^2}, where\ \alpha = 0.5, I = 10 \tag{117}$$

The following are the resultant performance curves. Note that increasing order improves the performance of each algorithm, but increases the number of iterations required to converge. This algorithm entirely consistent and can be erratic.

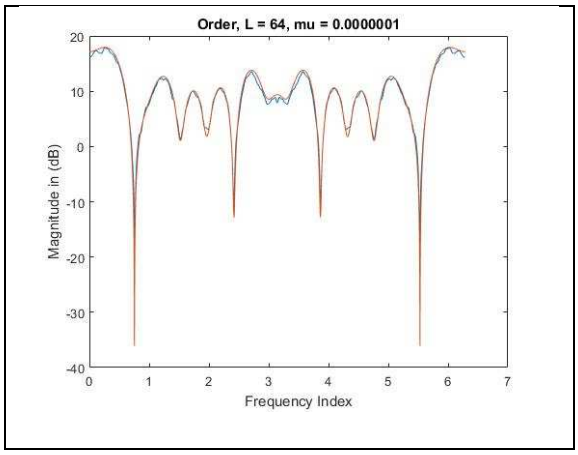

Figure 35 Normalized Impulse Response Performance (Order L=64)

The concept of Block Least Mean Square in both the frequency domain and the time domains have been described. In both cases, these algorithms converge to the mean (i.e. wiener solution). In the time domain, the structure of the input matrix aids in the convolution operation. In the frequency domain, multiplications are the same as convolution in the time domain. By performing adaptive filter operations in the frequency domain, computational complexity is reduced. In order to obtain a proper BLMS output in the frequency domain, one must utilize linear convolution. Linear convolution is achieved by using either overlap and add or overlap and save. In this report, I implemented the overlap and save method; this required the implementation of linear convolution enabled by doubling the size of the input blocks and the FFT's and appropriately pre-padding or padding matrices to eventually calculate the gradient. Though all plots were noisy, even the Normalized Error Estimates. To improve performance a Recursive Least Square (RLS) implementation should be performed. Ideally, for better performance (i.e. less estimate noise) a line RLS should be performed utilizing the following step size (see Figure 11):

Note: $\mu_i(n) = \frac{\alpha}{2E[|X_i(n)|^2]}$

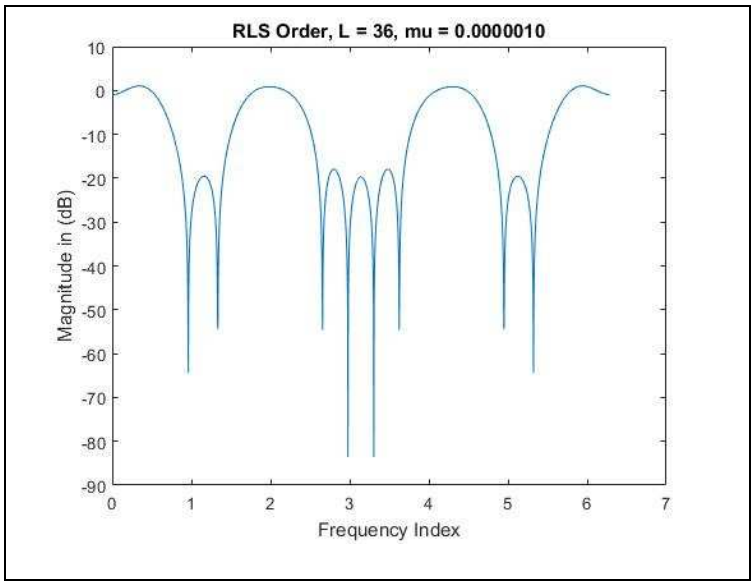

Figure 36 Exemplar impulse Response to Fit (RLS Example)

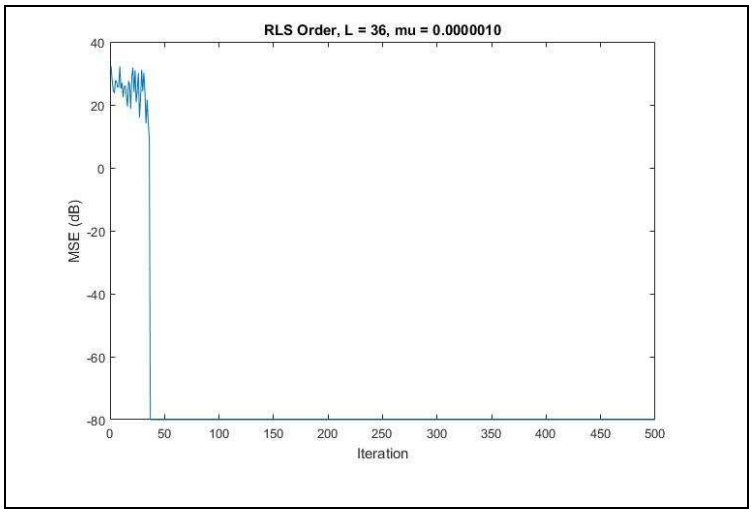

Figure 37 RLS Mean Square Error (MSE) Performance

Further, in the presence of non-stationary data, convergence is affected by block size and the degree of overlap. To calculate the Recursive Least Square (RLS) beam pattern, on a uniform or non-uniform (Dolph-Chebyshev) linear array the following equations must be implemented:

$$K_{n+1} = \frac{\beta^{-1} R_{xx}^{-1}(n) x_{n+1}}{1 + \beta^{-1} x_{n+1}^{T} R_{xx}^{-1}(n) x_{n+1}} \tag{118}$$

$$\hat{e}_{n+1} = d_{n+1} - b^{T}(n) x_{n+1} \tag{119}$$

$$b_{n+1} = b_n + K_{n+1} \hat{e}_{n+1} \tag{120}$$

$$R_{xx}^{-1}(n+1) = \beta^{-1} R_{xx}^{-1}(n) - \beta^{-1} K_{n+1} x_{n+1}^{T} R_{xx}^{-1}(n) \tag{121}$$

The following are antenna patterns for two linear arrays of eight element combinations. The steering weights are adjusted adaptively to match the following patterns (Balanis, 2009):

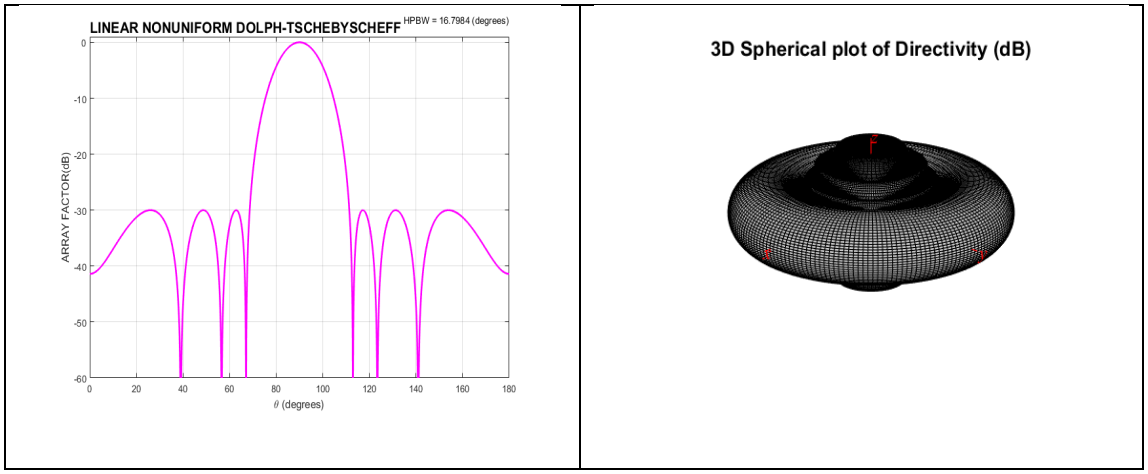

Figure 38 Eight Element (Non-Uniform: Dolph-Tschebyshev) Linear Array (Low Sidelobes)

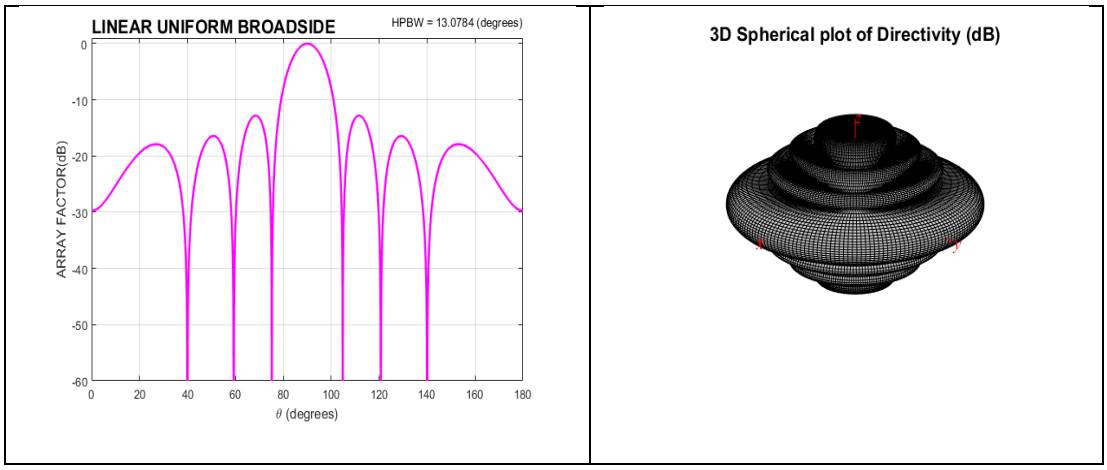

Figure 39 Eight Element Uniform Linear Array (Higher Sidelobes)

By implementing an adaptive recursive least square (RLS) algorithm, the patterns described in the two figures above are achieved with the least number of calculations utilizing floating point calculations. Floating point calculations prevents algorithm singularities, ensuring stable algorithm execution and fast convergence that is closer to the Newton multi-dimensional case. This will be used to perform beam forming using a Vector aperture.

Microwave Design Approach

The goal is to introduce a set of modular design, development and fabrication concepts utilizing heterogeneous technologies that reduce non-recurring engineering (NRE) cost. The use of materials such as Silicon© and/or Polystrata© materials provide the basis for the development of modular analog and digital circuits which can be referred to as chiplets. Monolithic designs can be made modular utilizing interposer technologies to create reusable chiplets.

Interposer technologies enable the integration of heterogeneous materials such as HEMT, PHEMT, InP, GaN and Si CMOS. Si interposers enable the integration of multiple chips within the same Si package. Si interposer technology enables I/O interfaces between chips to be utilized without the use of ESD protection circuits and therefore reduces the power draw and impedance thereby improving overall chip performance. Si interposers enables the finer pitch for increased densities. Silicon© and Polystrata© interposer technology supports isolation, lower loss and larger footprints where the coefficient of thermal expansion (CTE) is well matched to Rodgers© printed circuit board (PCB) material.

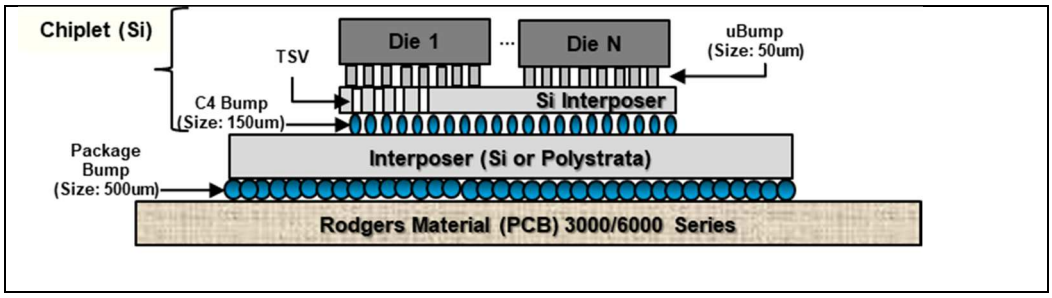

Figure 40 Proposed Chiplet Stack up (2.5 Interposing Technology)

This enables applications such as millimeter wave, microwave, beamforming, software define radio (SDR), satellite communications and radar applications. Numerous chiplets can be developed and reused across numerous PCB designs thereby reducing NRE costs. Chiplets represent multiple semiconductor chips that are combined together to create reusable analog or digital tiles that can be placed on numerous PCB designs.

Chiplets can combine microwave component combinations that are designed with well-matched impedances. Additionally, chiplets containing digital component combinations

can also be created such as ADC, DAC, and processing architecture. Chiplets, due to the small distance between chips, drive smaller signal levels leveraging a combination of complementary metal-oxide semiconductor (CMOS) and current mode logic to use voltage level thresholds that do not require impedance match requirements chip to chip. The interposing technology used by chiplets also enable 3D integration using FinFET technology nodes such as 5nm, 7nm, 14nm, and 16nm technology. Through the use of digital design tools, issues such as corner effects and proximity effects dominate error that do occur during the synthesis process. One example is the derivation of the corner models for the analog portion of a digital circuit. The electrical performance of a device is expressed in the following table:

Table 3
Model Properties and Associated Considerations (EEE 627, Fall 2016)

Simulation Model	Model Classification	Properties	Considerations
BSIM3 BSIM4	V_{TH} Based	Widely used, but outdated Singularity at V_{DS}=0 causes issues w/ mixers, charge switching (in circuit design) Unphysically moderate inversion, asymmetric capacitances Region boundaries inaccurate	Analog conductance/capacitance problems around simulation regions Problems with inversion low power designs Analog CMOS for V_{DS} charge changes discontinuously as charge changes between source and drain
EKV2.8 EKV3.0 BSIM6	Inversion Charge Based	Improved simulation of high frequency circuits Considers EM effects of signal lines and passives	Improves upon model inaccuracies experienced in V_{TH} based modeling
PSP	Surface Potential Based	Symmetric Linearization Future Vision	Best for analog model 2/3-D process and device simulation

The implication in the analog domain, $\frac{\partial e_p}{\partial p_i}$ varies with e_p and geometry, bias and analog circuit topology as well as the fact that e_p is important for every analog circuit. In the digital domain, worst and bast case corner models are adequate and therefore less sensitive to these variances. Most of the problems occur in in analog modeling when developing in 3D FinFET technology.

$$\delta_{e_p} = \sum_i \frac{\partial e_p}{\partial p_i} \delta_{pi} \tag{122}$$

e_p = Electrical Performance (device or circuit)

p_i =Physical process parameter

The following will describe the technical design details of a radio transceiver design and how Chiplet and transposer technology is applied to modularize the design of a radio. The use of ultra-low noise GaAs based, 0.2 and 0.25 pseudomorphic High Electron Mobility Transistor (pHEMT) technology provided by Avago technologies enables the design of microwave components such as low noise amplifiers (LNA), mixers, oscillators and filters. The noise figure for 0.2 micron gates enable a noise figure of < 1dB with a frequency range that spans .5 and 12GHz and is a key technology in the development of smart vector antenna systems.

The noise figure of the receiver chain is set by the 1st components (see equation 9) in the receiver chain such as a band pass filter (BPF) and/or a Low Noise Amplifier (LNA). The noise figure of a two port, low noise, amplifier is the following:

$$F = F_{min} + \frac{R_N}{G_S}|Y_S - Y_{OPT}|^2 \quad (123)$$

F_{min} = Minimum noise figure of transistor

$Y_S = G_s + jB_s\ (source\ admittance)$

$Y_{OPT} = (optimum\ src\ admittance) F = F_{min}$

$R_N = Equivalent\ noise\ resistance\ of\ transistor$

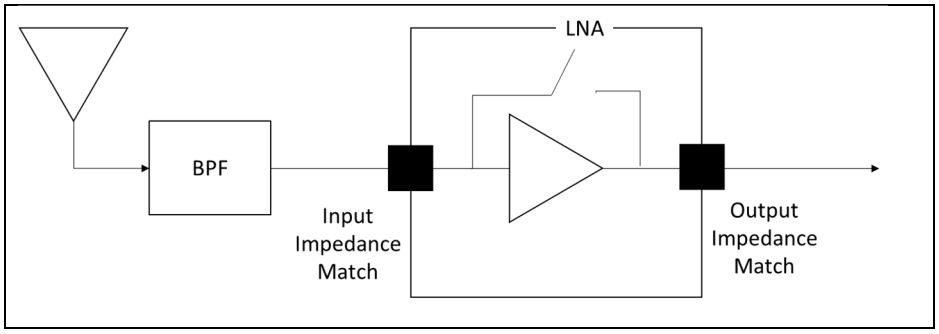

Figure 41 Receiver Front-End Diagram (Typical)

In the figure above, the band pass filter (BPF) and the LNA set the noise figure for the entire receiver chain. Using pHEMT technology, a noise figure < 1dB is possible by using the device S- and noise parameters in the design assuming a bias condition of Vds = 3.0 V and Id = 20 mA. By utilizing component size of 0402 using the Avago Tech VMMK-1225 Low Noise E-PHEMT and Rogers RO4003™ substrate (20 mil thickness with 1/2 ounce electrodeposited copper cladding on both sides). To investigate the feasibility of such a design, the following are the parameters for the 3V, 20mA E-pHEMT, VMMK-1225 technology from 2GHz to 17GHz. This along with high performance passive components from Murata.

Typical Noise Parameters

Freq	Fmin	Γ opt	Γ opt	Rn/50	Ga
GHz	dB	Mag.	Ang.		dB
2	0.14	0.783	16.4	0.19	20.73
3	0.21	0.704	23.4	0.18	19.33
4	0.29	0.632	30.9	0.18	18.03
5	0.37	0.565	39.1	0.17	16.85
6	0.45	0.505	48	0.16	15.77
7	0.53	0.45	57.4	0.15	14.81
8	0.61	0.402	67.6	0.14	13.95
9	0.68	0.359	78.3	0.13	13.21
10	0.76	0.322	89.7	0.12	12.57
11	0.84	0.291	101.7	0.11	12.04
12	0.92	0.266	114.3	0.11	11.62
13	1	0.247	127.6	0.1	11.31
14	1.08	0.234	141.5	0.09	11.12
15	1.15	0.227	156	0.09	11.03
16	1.23	0.226	171.2	0.09	11.05
17	1.31	0.231	-173	0.09	11.18

Note:
1. S-parameters are measured in 50 Ohm test environment.

Figure 42 VMMK-1225 technology Capabilities from 2GHz to 17GHz

The design approach to the LNA depicted in Figure 41, the optimum design technique is to derive intersection between noise circle and gain circle to determine the appropriate 'L' matching network for the broadband frequency range of operation. In the following example, for high speed multi-media wireless communication link at 5.8GHz, the optimum design parameter occurs at the intersection between the gain & noise circles on the smith chart occur. The following Smith Chart performance demonstrates an optimum design point.

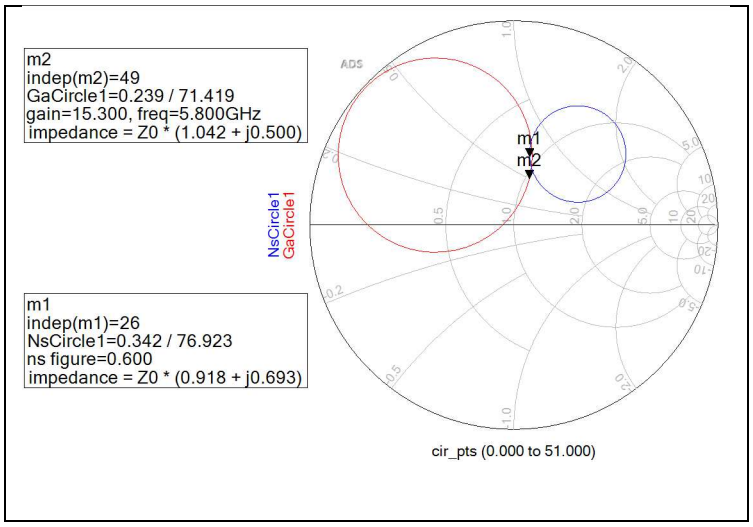

Figure 43 Smith Chart LNA Design @ 5.8GHz

The following plot describes the output of the low noise amplifier (LNA). The following design schematic utilized the VMMK-1225 Low Noise E-PHEMT transistor technology.

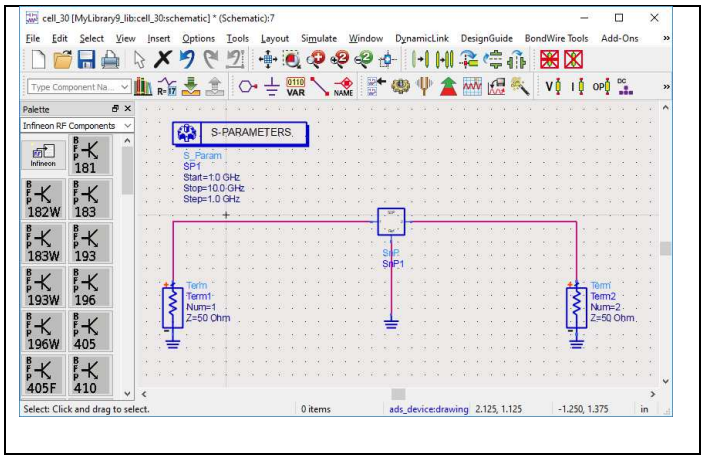

Figure 44 Keysight Advanced Design System (ADS) Simplified Circuit

Figure 45 Broadband P-HEMT LNA Performance Curve

Based upon the Rogers 4003 material used for the design of this Low Noise Amplifier (LNA), the following plots describe the expected performance as a function of frequency. Based upon V_{ds} = 1V, I_{ds} = 20mA, and V_{gs} = 0.6V. V_{DD} = 5V, the bias resistance is the following:

$$R_{bias} = \frac{(5-1)}{20E-3} = 250\Omega \tag{124}$$

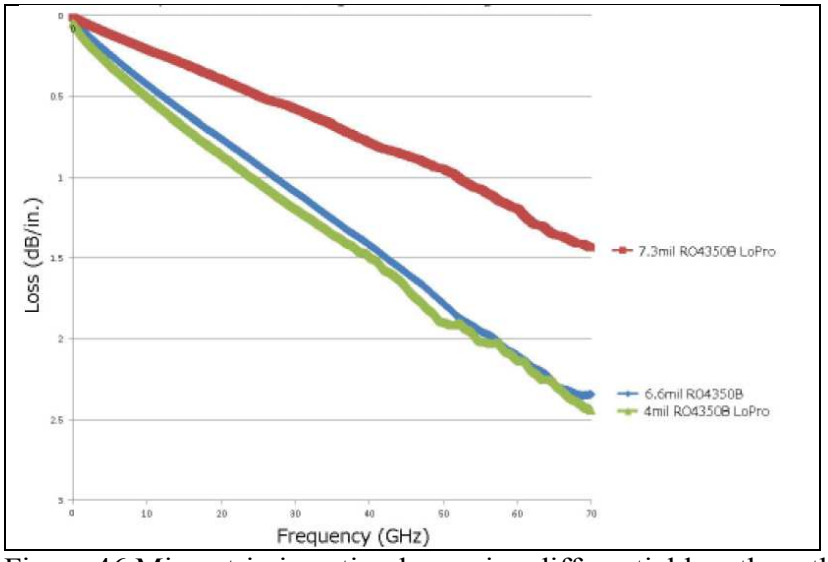

Figure 46 Microstrip insertion loss using differential length method (Rogers Corporation R04000©)

This model will required adjustment of substrate lengths to meet the gain requirements (i.e. Design the LNA at the ADS schematic level to achieve over the frequency range of 1 to 10GHz, a noise figure that is less than 1.2 dB, and $\geq$ 13.0 dB of transducer gain with no more than $\pm$ 0.25 dB gain ripple in a 50 ohm system). All components in this design will utilize passives with size 0402.

Chapter 3

NEW MULTI-NODAL WIRELESS COMMUNICATION SYSTEM METHOD

(Multi-nodal wireless communication systems and methods,

US Patent 9,717,088, Granted July 25, 2017.)

The RF characteristics of Wi-Fi devices commonly utilize an omni-like directional antennas. Multiple antennas on these devices are controlled separately to transmit separate spatially diverse streams. WiFi device modulation techniques such as the use of Complementary Code Key (CCK) in concert with Quadrature Phase Shift Keying (QPSK) for 802.11b, CCK and Orthogonal Frequency Division Multiplexing (OFDM) in concert with Quadrature Amplitude Modulation (QAM) (e.g. 16 or 64 QAM) or Phase Shift Keying (PSK) (.e.g. BPSK or QPSK) are both used for 802.11g, OFDM with QAM or PSK used on each subcarrier is only used for 802.11a, 802.11n (max. 64 QAM, rate 5/6) utilizes OFDM in concert with QAM and PSK modulation techniques, and lastly 802.11ac which can utilize 256 QAM (rates 3/4 and 5/6) with use of MIMO to perform spatial diversity between multiple OFDM user streams using much smaller cell sizes. Further research in the use of Alamouti space-time block coding (STBC) is planned to identify the achievable gain in 5G millimeter frequency ranges.

Management support interfaces for Wi-Fi devices are defined by the Telecommunications Management Network (TMN) model which encourage protocol support for different layers of a network infrastructure. Simple Network Management Protocol (SNMP) is the predominant protocol in national provider networks today.

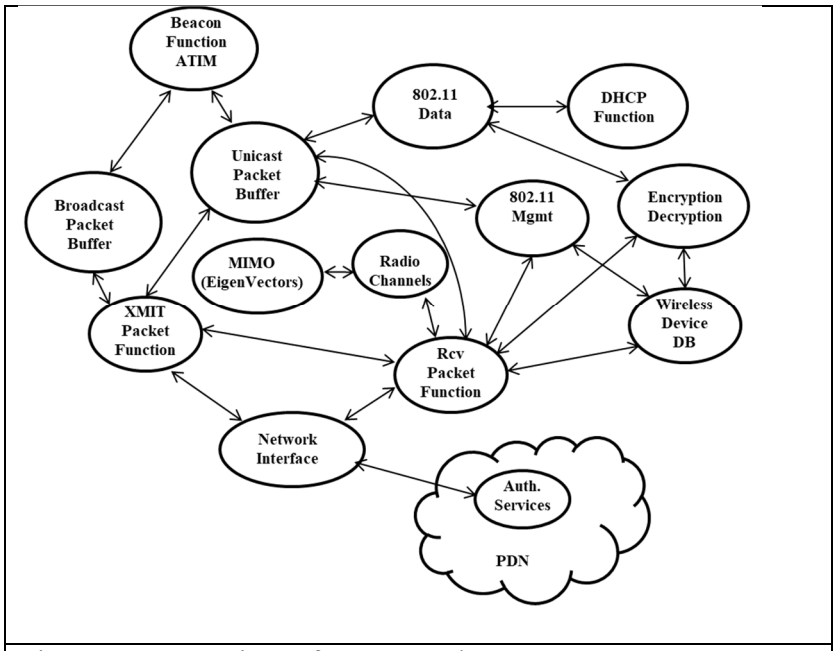

Figure 47. Overview of 802.11 Subsystems

Cellular Technology

Background: Cellular base stations, as is the case with Wi-Fi base stations, are located across the country in proximity to cellular towers. Often these towers are visible in close proximity to interstates, highways, and neighborhoods; these towers are found (sometimes camouflaged) in areas where RF coverage is needed. These towers are commonly referred as "cell towers" and often are equipped with dipole antennas so as to reduce impedance mismatch between the receiver and the antenna (impedance mismatch causes Voltage Standing Wave Ratio (VSWR) which is a measure of reflected voltage) that causes transmitter and receiver signal distortion. As with the case with WiFi, transceivers are located behind antenna elements. The following depicts the high level structure of the cellular subsystems involved with 2G, 3G and 4G network devices.

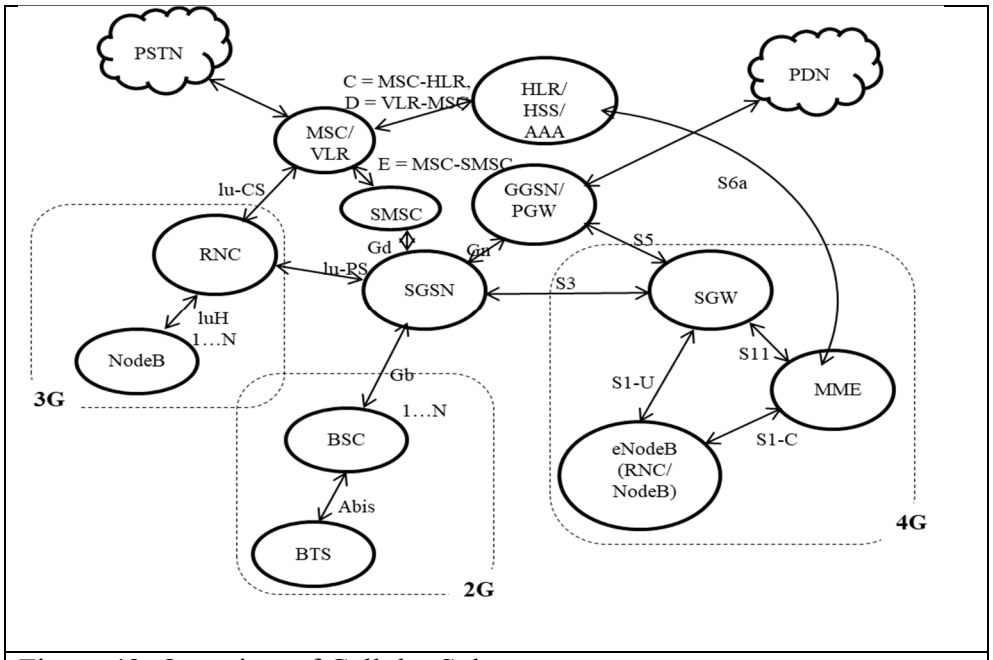

Figure 48. Overview of Cellular Subsystems

Wireless Technology Not Considered

Other wireless protocols include Bluetooth, 802.11z, 802.11p (MS-Aloha) and Wi-Fi-Direct; however, these protocols are not used to support a large number of users simultaneously. This paper is only focused on systems that can support a large user population.

Cellular and Wi-Fi System Comparison

Wi-Fi RF cell coverage sizes are limited by their higher frequency (2.4GHz and 5GHz versus 900MHz), limited allowed power transmission interference from other devices in this unlicensed band (though somewhat mitigated by its modulation technique), and more importantly by their link layer communication specification. Unlike cellular communication, Wi-Fi communication devices specify a link layer communication model

based upon a CSMA/CA format. The CSMA/CA format is not as effective multiple access protocol as is the case with TDMA or CDMA technologies. Though Wi-Fi can close links at longer distances, greater amplification and antenna directivity is required as well as cooperative changes to the Wi-Fi link layer timing specifications. Example: DIFS is the amount of time a station must sense a clear radio before beginning a new transmission sequence. Note that a node can format and buffer a data frame to be transmitted during this time interval. SIFS is the amount of time a station must wait before sending or beginning to receive a RTS, CTS or ACK frame, note that the SIFS time includes the amount of time to format the ACK frame to be transmitted; this is possible since only the first portion of the data frame (e.g. BSSID) is used in the ACK message. PIFS is the DIFS for the access point in a special access method known as Point Coordination Function. The times are defined such that the RTS, CTS, and ACK frames are given a higher priority (ie once a packet transmission sequence has begun, the station holds onto the channel until it is finished). Without 802.11 RTS/CTS handshaking the following time periods are observed.

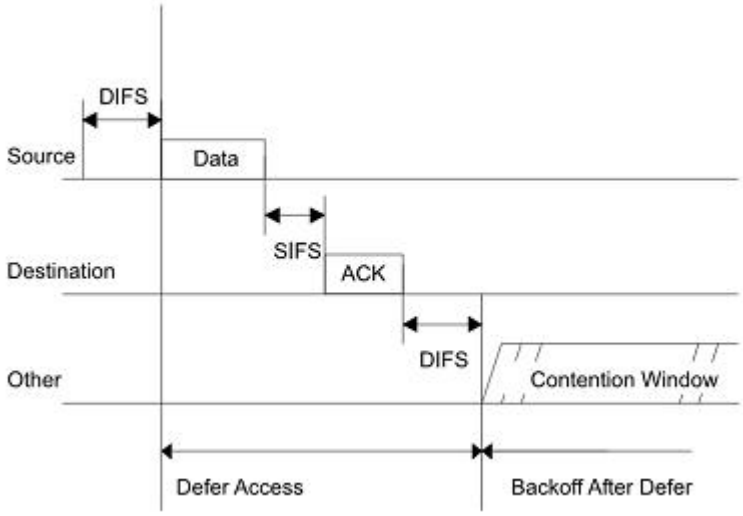

Figure 49. 802.11 MAC Layer Communication Note: No RTC/CTS handshake depicted in diagram above. (Airstream, 2014)

IEEE mandates the following timing for 802.11a:

- Time Slot = 9 µs
- SIFS = 16 µs

$$DIFS_{802.11a} = SIFS + 2\,x\,Time\,Slot = 34\ \mu s \quad (125)$$

IEEE mandates the following timing for 802.11b:

- Time Slot = 20 µs
- SIFS = 10 µs
- PIFS = SIFS + Time Slot = 30 µs

$$DIFS_{802.11b} = SIFS + 2\,x\,Time\,Slot = 50\ \mu s \quad (126)$$

IEEE mandates the following timing for 802.11g:

- Time Slot = 9 µs
- SIFS = 10 µs

$$DIFS_{802.11g} = SIFS + 2\,x\,Time\,Slot = 28\ \mu s \quad (127)$$

Sender procedure: Wait DIFS, Send Data, Wait SIFS, Listen for and receive ACK (until maximum ACK timeout), Repeat

Receiver Procedure: Listen for and receive Data,Wait SIFS, Send ACK, Wait DIFS

Given this link layer communication protocol, the destination must start constructing the ACK message once the first part of the data message has been received. Once it has been determined that the data message was received without error, an ACK message may be transmitted. The following is the timing calculation for sending the ACK message:

$$\tau\_total = \tau\_ACK\ (+\ \tau\_SIFS\ ) \tag{128}$$

$\tau_{total} = Total\ Time$

$\tau_{ACK} = Transmission\ of\ ACK\ message$

$\tau_{SIFS} = Short\ Interframe\ Spacing$

With the speed of light $3x10^8\ m/sec$, a 802.11 ACK transmission can travel a distance of 300 $m/usec$. Assuming a normal transmission of an ACK message, the receiver could be no greater than 3 km (given the speed of light, a nice number) away or 10 usec. If ACK timeout was increased (to say 19 usec), the maximum slot time for a point to multi-point communication environment is equal to the slot time. For 802.11b the slot time of 20 usec equates to a maximum distance of 6 km. Other wireless standards have similar limitations but the distances are shorter.

Cellular requirements to address cellular reselection within greater cell sizes (> 1Km), though is possible with some cellular protocols, requires special configuration of the cellular chipsets to accomplish. 802.11, due to the CSMA/CA protocol requirements is much harder to accomplish unless it is a point to point connection. Figure 49 describes the general cellular reselection process as defined by the 2G specification (3G specification includes neighbor list evaluation -not depicted here).

By observing the parameters in our cellular transmission cellular devices will choose a base station over other base stations in the area (even though there is a mismatch Power Spectral Density (PSD) may be less than others). See Chapter 3 for additional information. This is important because it implies that the number of cellular devices connected to a specific cellular base station can be control with the use of parameters transmitted in the Broadcast Channel (BCCH).

Unlike 802.11 devices, assuming sufficient transmit power and sufficient receive sensitivity; a base station can attract distant devices in the same manner. Though many 3G/4G chipsets (i.e. Mindspeed) have a time limitation (~1Km distance) in regard to how long they will wait for a response from a peer device, however chipsets can be programmed to deal with devices at greater distances > ~1Km by configuring the chipset to only respond to devices within a circular area with a diameter of ~1Km 'distance of interest' for distances > 1Km, ignoring devices that are not within that area of interest.

Wi-Fi and cellular devices used in hot spots (locations that represent extensions to the Internet) use link layer protocols to control access to the Wireless Local Area Network (WLAN) and ultimately to the Wide Area Network (WAN). Both wireless technologies form a LAN environment where IP addresses with a subnet designation are delivered to individual devices for data access. Cellular devices utilize IP addresses primarily for data access, but with Long Term Evolution will use these services for using voice services as well. These addresses are then allowed access to the WAN through a network process referred to as Network Address Translation (NAT). During normal operation each device initiates a data connection and delivers network frames that are transmitted to the backbone network of a service provider through a network gateway. The network gateway provides the NAT service that is used to proxy IP network requests to the WAN. Wi-Fi and cellular devices used in an enterprise environment may not utilize NAT, but rather be assigned IP addresses distributed by a router or server that supplies Dynamic Host Configuration Protocol (DHCP) for the enterprise network.

Link layer network technology can be used to facilitate adaptation to legacy network infrastructure, adaptation to new network backhauls, QoS of wired integration points within a legacy or new Wide Area Network (WAN) entry point. QoS of wireless technology that utilizes techniques such as MIMO and virtual roaming (discussed later). As the performance at the edge of the network continues to increase, more demands will be made on the network infrastructure to perform QoS functions nearer to the edge of the network.

This paper will focus on the use of a centralized communication controller that will control link layer communication between radios and the communication controller for the purpose of load balancing between radio nodes, automated discovery of new radio nodes, QoS in regard to RF communication channels, authentication, cryptography, and virtual roaming. This paper is structured into the following sections: Wired integration with existing networks, 802.11a/b/g/n, Cellular 3G/4G technology and Ethernet / Fiber optic communication with a focus on link layer communication. These areas will be evaluated as it relates to the Open Systems Interconnection (OSI) model starting at the physical layer and moving to the Link Layer.

CHAPTER 4

PROPOSED WIRELESS SYSTEM DESIGN

The new aspects of the following design depicted in Figure 50 entail the following attributes:

1. High performance roaming and autonomous distribution of wireless devices.
2. The measurement of Power Spectral Density across multiple RF cells to determine the best integration of 802.11 and cellular backhaul systems while performing intelligent frequency distribution across adjacent cells.
3. Integration of WiFi and cellular backhaul networks to utilize the same network topology.
4. Cognitive adaptation of Digital Signal Processing (DSP) parameters based upon empirical measurement of RF environmental parameters.
5. The ability to prioritize frames based upon link layer behavior.
6. The use of security encryption utilizing random numbers that are generated from a system with a sufficient amount of entropy (to be quantified later).

The wireless system design follows the paradigm that the radios are simply radio interfaces that simply communicate as commanded by a regional communication controller. The radio interfaces are comprised of a radio (with a transmitter and receiver), a very small processor, memory resources and an Ethernet interface. These radios can communicate Cellular Frequencies utilizing W-CDMA using a 5MHz channel bandwidth or the radios can communicate Wi-Fi with 22 and 25 MHz channel bandwidth. 802.11n can utilize 20Mhz or 40Mhz channel bandwidths. LTE (using OFDMA/SC-FDMA)

comprised of channel bandwidths of 1.4, 3, 5, 10, 15 and 20 Mhz. LTE clients are communicated a mask that indicates the OFDMA subcarrier(s) to be used in the uplink transmission.

The radios are preconfigured with real time link layer messages that are required to support real-time communication messages while all non real-time messages are sent to the regional communication controller where the message can be characterized and where an appropriate response can be constructed. The link layer messages will be characterized per technology so that subsystem functions can be clearly identified and aspects of the design can be described adequately.

Elements of this new innovation relating to both structure and operation can best be understood by referring to the following diagrams and their descriptions.
This is a system of radios and their use in a large network. This new link layer communication design is implemented using the Ethernet technology (MAC header, the VLAN header, and a proprietary layer 2 protocol header) to implement communication features that implement features 1 thru 6 above as well as specialized hardware that processes wireless link layer functions and communication, classification of network frames (wired and wireless), queuing and routing of frames, encryption/decryption of frames, and network buffer management. Though most wireless systems provide adaptive features, these features are not implemented with cognitive feedback from a RF and network environment that is not visible to the device. The design depicted in Figure 50

describes the overall hardware functions implemented on the cell controller that support these new features.

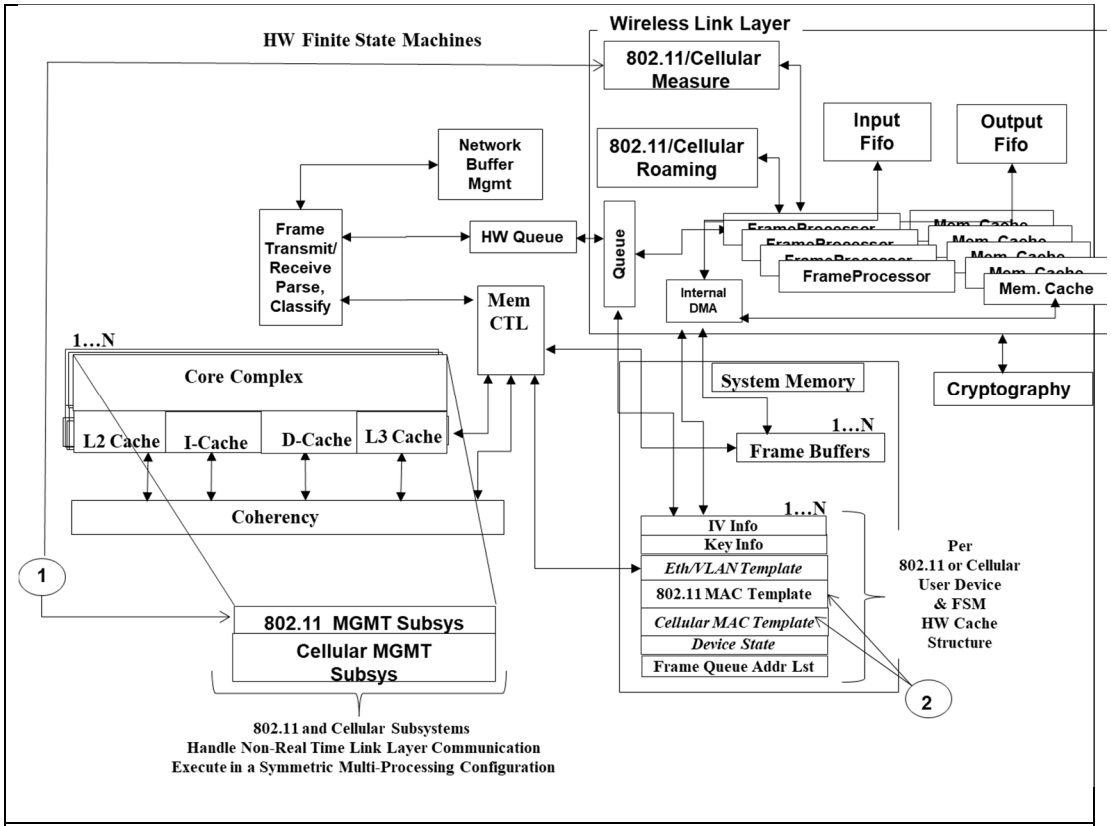

Figure 50. Proposed System Architecture

By communicating the TMSI, IMSI, and TLLI between different cellular base stations within the same cell controller, the system is able to improve the speed at which a device changes from one Location Area Code (LAC) to another. This is because the normal sequence of messages required to move from one cell to another is no longer required. This dramatically improves the performance of the Location Area Update process in cellular networks. As all of the existing cellular technologies implement this portion of the specification as it is required when moving from one cellular coverage area to another. Additionally, if the TMSI & TLLI are ensured to be unique across all cell

controllers, then this information can be moved in between interconnected cell controllers thus improving performance further.

This new wireless system design is based upon the concept of splitting the wireless Media Access Control (MAC) across interconnected cell controllers using specialized hardware that process non-real time portions of the wireless MAC protocol as well as handle high speed frame processing for wireless devices under its control. These cell controllers make "intelligent" decisions based upon feedback from multiple radios within a physical area. The wireless system design is comprised of hardware systems that are connected utilizing unreliable communication media (Ethernet) but could utilize other forms of unreliable communication such as satellite and wireless bridges as long as the required communication delay does not violate time constraints imposed by the MAC layer communication required between a central communication controller and radio that communicates the wireless MAC protocol. Such a system needs to be capable of providing ubiquitous RF coverage across many desperate physical locations as well as be capable of integrating into existing, legacy network topologies that may be strictly based upon wired communication technologies. The wireless system design utilizes RF transmitters and receivers that perform real time data communication to devices. These devices are typically mobile; however, they can also include stationary devices such as desktop computers. The major components of the hardware system are comprised of the following components:

The overall system topology looks deceptively simple (see Figure 51). This system topology describes the overall top-level architecture. The hardware link layer

communication methods used in the overall system will now be described. The system topology must be adaptable to ensure that the link layer design can be implemented without violating existing cellular and WiFi standards. This introduces a challenge that is addressed in the following manner.

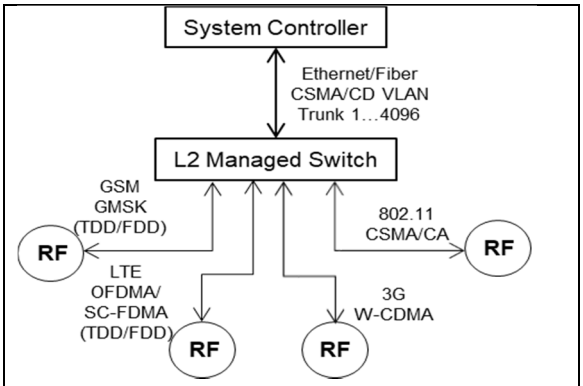

Figure 51. Simplified System Topology

Link Layer Communication Model

The link layer communication model splits both the cellular and the 802.11 MAC protocols across unreliable communication links in a unique way. As depicted in Figure 51, Virtual Local Area Network (VLAN) technology as specified by the IEEE 802.1pq is utilized between the cell controller and the base stations. In doing so, I can prioritize the communication links dynamically. This design approach employs a fourfold advantage.

1. The new link layer communication model can be implemented across an existing wired infrastructure with very low impact to the existing network infrastructure. As an example, a network architect can overlay a completely different IP subnet over an existing wired network infrastructure without changing the existing wired network.

2. Based upon link layer communication behavior, prioritization of wireless frames can be changed dynamically. As an example, if Quality of Service (QoS) parameters

dictate a particular percentage of the system bandwidth, this system design can quickly change the VLAN priority tag to prioritize frames to one RF base station over another RF base station.

3. Unlike autonomous wireless routers and access points, the cell controller has visibility to the RF spectrum where radios exist. This design enables the cell controller to perform cognitive adaptation to the RF environment. Based upon the RF noise temperature, the cell controller can equally distribute mobile devices across the available RF spectrum in a fashion that provides for the greatest network performance. As an example, BER as well as neighboring cell information transmitted by the RF base station can be communicated back to the cell controller. Neighbor cell information can be communicated in the form of Power Spectral Density (PSD) calculations (this is covered in a later section). The cell controller can make a dynamic decision to send data frames across a different RF base station, in essence the device is now communicating with a different RF base station without awareness by the mobile device. This is a form of a cognitive adaptation based upon BER.

4. The integration of cellular and WiFi stacks provides the ability for cellular and WiFi devices to utilize the same backhaul network infrastructure. This provides relief of the cellular systems in regard to bandwidth utilization and improves the use of unoccupied bandwidth on the backhaul network infrastructure.

The link layer design includes adapters for both WiFi and cellular technologies. 802.11 technology will be discussed first followed by cellular technology. As depicted in Figure 51, the wireless 802.11 MAC is split across unreliable communication links. RT

messages are addressed at the RF base station, while higher level management messages are handled at the cell controller.

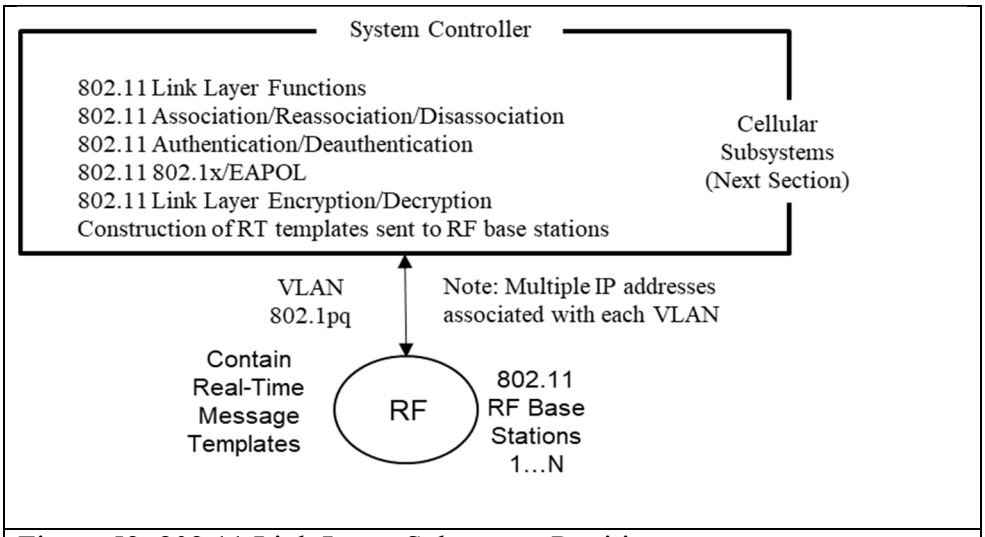

Figure 52. 802.11 Link Layer Subsystem Partition

The following 802.11 link layer subsystem functions are addressed in the RF base station. The RF base station handles all RT messages. Since Probe Response messages are very similar to Beacon Messages, Beacon Messages are also handled in the RF base station.

Table 4
802.11 Real-Time Messages

1	Beacon/DTIM
2	Probe Response
3	Acknowledgements
4	RTS/CTS (If Enabled)

Templates for these messages are sent by the cell controller to the RF base station for purposes of transmission to their RF coverage area. When cells overlap, these messages can also be forwarded by other RF base stations in the coverage area. A measure of the received power (E_b/N_o) can be made and a decision in regard to which RF base station should ultimately respond to later Association requests can be calculated. The following diagram depicts an 802.11 example:

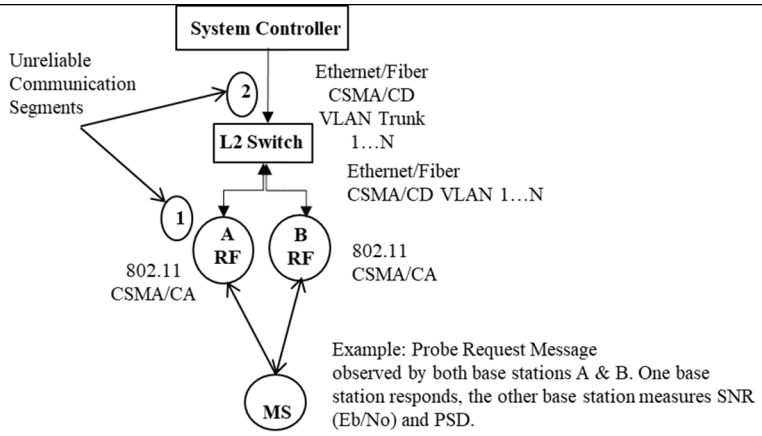

Figure 53. Probe Response Exemplar

On Ethernet there are two distinct delays: propagation delay and transmission delay. The following equation describes the nodal delay, the delay per node in an Ethernet network.

$$d_{nodal} = d_{proc} + d_{queue} + d_{trans} + d_{prop} \quad (129)$$

The velocity of an electromagnetic wave through a copper media is approximately $V_{Copper} = 2.1 * 10^8$. Though base transmission rate has no bearing on propagation delay, base rate directly affects transmission rate d_{trans}. Assuming full duplex Ethernet operation $d_{trans} = .512\ usec$ for a 64 byte frame. A probe request, including a proprietary header, can be no less than this size; therefore, round trip (RT) delay of $2*d_{trans} = 1.024usec$. Assuming a maximum length of 100 meters, $d_{prop} = .4762usec$ with a round trip delay of $2*d_{prop} = .9524usec$. Ignoring $d_{queue} and\ d_{proc}$ for a moment, one RT segment is $1.976usec$. Adding the segments depicted in Figure 53 we have a $d_{total} = 3.9528usec$. Figure 53 is representative of the minimum network delay between a cell controller and a RF base station; therefore, the 802.11 messages depicted in Table 4 represent messages that must be handled in RT by the RF base station.

Table 5
802.11 Non-Real Time Messages

1	Association/Reassociation/Disassociation
2	Authentication/Deauthentication
3	802.1x, EAPOL, etc…
4	802.11 Data Messages

WiFi messages listed in Table 5 are handled by the cell controller which manages messages from all devices in a large regional area. These messages provide for a centralized management of all 802.11 devices in the area as well as provide for the accurate application of Quality of Service (QoS) between individual wireless networks

since all data frame are sent through the cell controller. For example, if a network identifier (e.g. SSID) is suppose to have available 60% of the available bandwidth while another network identifier is suppose to have available 40% of the available band, the bandwidth between the two networks can be arbitrated in RT instantaneously since the cell controller has full access to all traffic being delivered to the whole network prior to be distributed to individual RF base stations in the regional areas.

Cellular Link Layer MAC

There are many system design differences between the different cellular technologies (e.g. 2G/GSM, 3G/UMTS, 3G/CDMA2000, 4G/LTE). Cellular vendors have changed their subsystem designs to improve access speeds, coverage, and reduce cost to deployment. I will focus on cellular subsystems that intersect GSM, 3G/UMTS, and 4G/LTE cellular link layer subsystem functions. Unlike WiFi devices, cellular provider networks have routinely (out of necessity) split their link layer communication across unreliable communication links (e.g. Ethernet/Fiber).

Table 6
Example Cellular UMTS Messages (Wikipedia, 2014)

MOBILITY MANAGEMENT (MM) MESSAGES	RADIO RESOURCE (RR) MESSAGES
imsi detach/attach indication	additional assignment
location updating reject	immediate assignment
location updating request	immediate assignment extended
location updating response	immediate assignment reject
authentication reject	ciphering mode command
authentication request	ciphering mode complete
authentication response	assignment command
identity request	assignment complete
identity response	assignment failure
tmsi reallocation command	handover command

tmsi reallocation complete	handover complete
cm service accept	handover failure
cm service reject	physical information
cm service abort	paging request type 1-3
cm service request	system information type 1-8,2(bis/ter), 5(bis/ter)
cm establishment request	channel mode modify {ack}
Abort	classmark change/enquiry
mm status	measurement report/ frequency redefinition

The cellular link layer communication model is much more distributed; however, there are improvements that can be made. I will outline the link layer communication model changes that integrate WiFi and cellular technologies together as well as improve roaming between the technologies. In addition, I will describe why this approach is superior to other approaches.

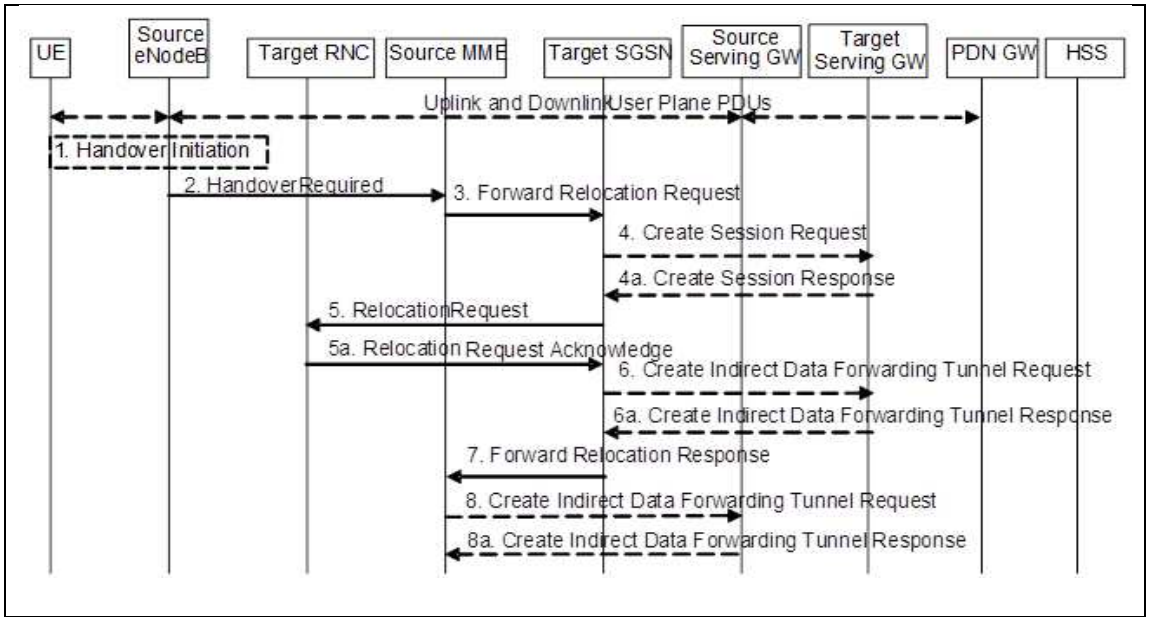

Figure 54. Example Inter-RAT Handover Setup (4G Source to 3G Target Network) (Barton, 2012)

The example above describes the handover setup procedure example between a 4G source to a 3G target network. The end goal is to ensure that when the handover is complete data frames will be sent to the new serving gateway service in this the GGSN 3G service. The Source MME subsystem initiates the Handover resource allocation procedure by sending a Forward Relocation Request (IMSI, Target Identification, CSG ID, CSG Membership Indication, MM Context, PDN Connections, MME Tunnel Endpoint Identifier for Control Plane, MME Address for Control plane, Source to Target Transparent Container, RAN Cause, MS Info Change Reporting Action (if available), CSG Information Reporting Action (if available), UE Time Zone, ISR Supported) message to the target SGSN subsystem of the 3G cellular network. Note that this entire setup process occurs before the User Equipment (UE) has actually "roamed" to the 3G network. Once the setup has completed, the source MME subsystem initiates the handover process by coordinating with the UE by sending a handover command (depicted in Figure 55). The UE responds to the network with a handover complete message to the target RNC subsystem who initiates a message to its SGSN subsystem which then conveys a completion message to the source MME subsystem. The source MME acknowledges the completion message and the SGSN notifies its GGSN service (using a "Modify Bearer" request). Once the GGSN service then notifies the source PGW of the change, data frames are now presented through the new serving 3G gateway (e.g. SGSN and GGSN).

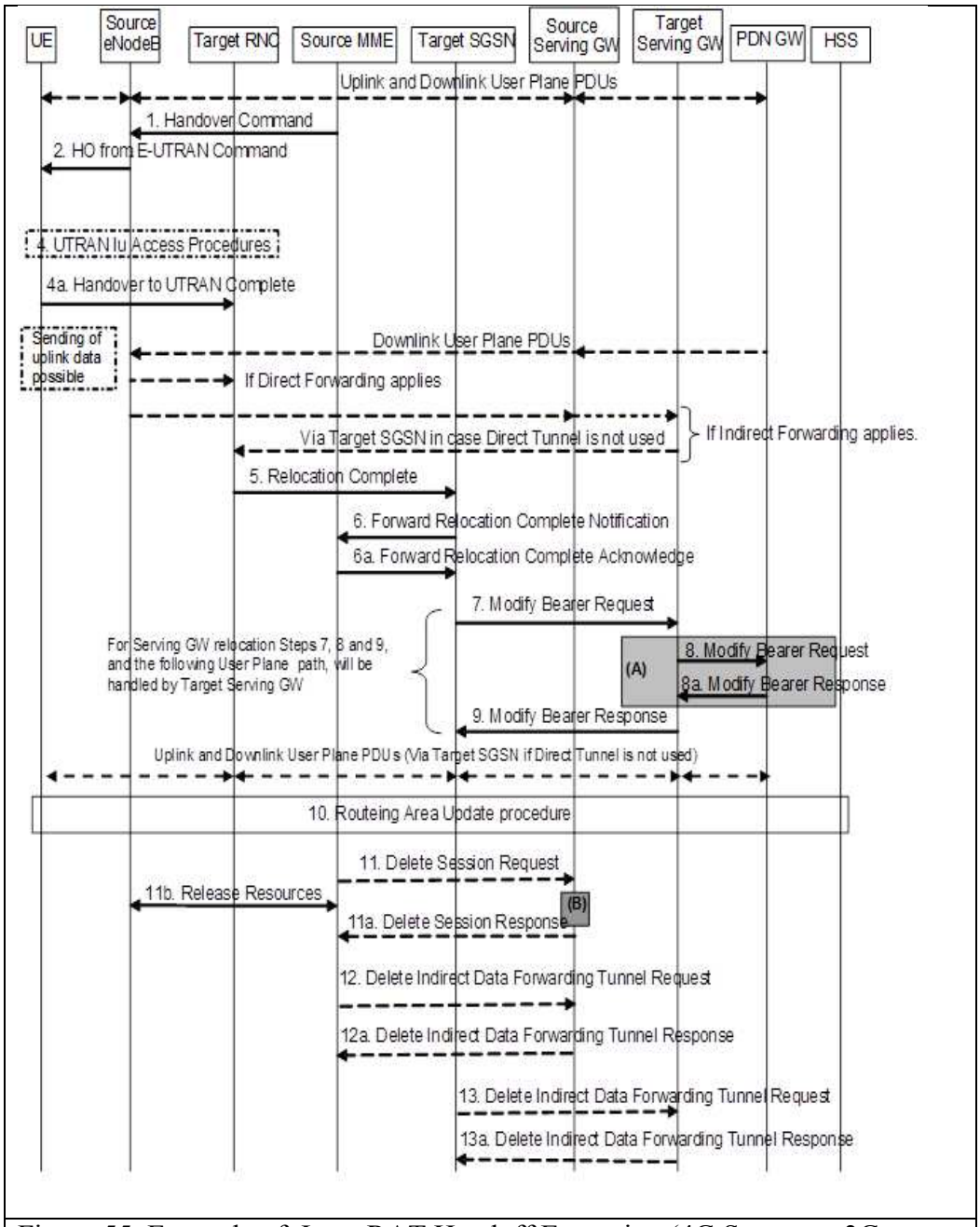

Figure 55. Example of Inter-RAT Handoff Execution (4G Source to 3G Target Network) (Barton, 2012)

Using a cell controller, these subsystems are combined into a single platform that can more quickly execute the roaming examples such as this. Latency is reduced greatly because fewer messages across unreliable communication links are required. A cell

controller would be used to handle large geographic areas. With the use of Fiber channel communication links (assuming the use of repeaters and proper configuration), very low latency and high bandwidth can be achieved.

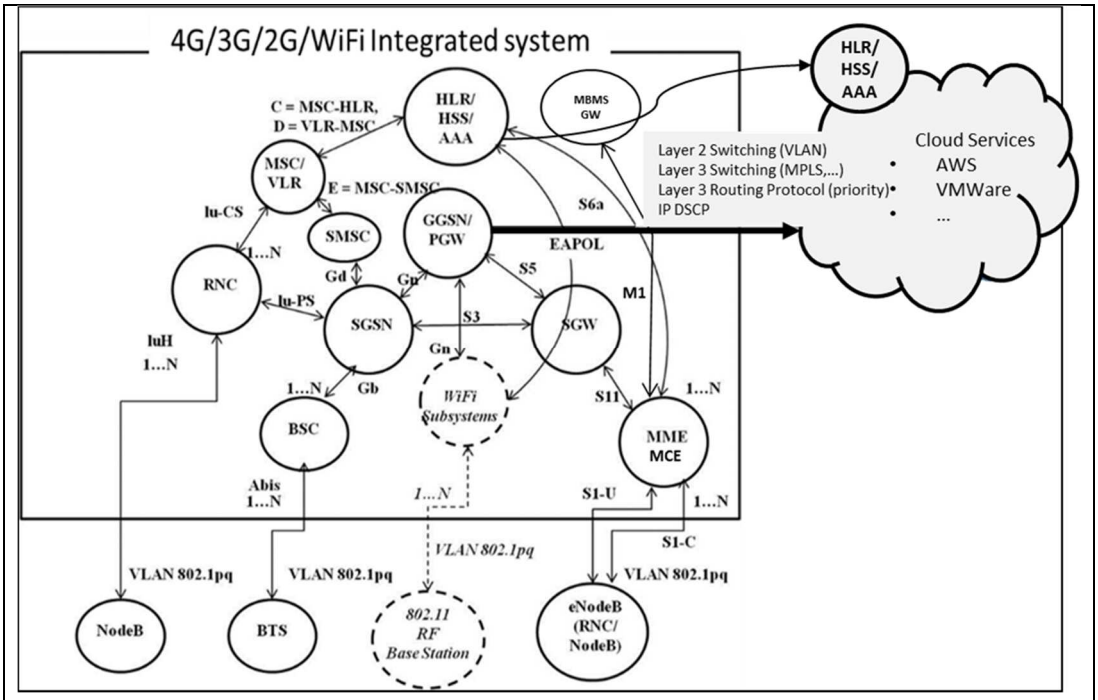

Figure 56. New Cellular Link Layer Topology With Combined 802.11 Subsystems

With the architecture above, the cellular MAC is split between the cell controller and BTS, NodeB, and eNodeB transceivers. Today these cellular subsystems are found in desperate locations across the country. Since these subsystems interact with each other across vast physical locations, very little information is communicated in regard to the RF environment as it relates to BER and RF performance. With this new link layer architecture, cellular coverage can be provided for large geographic areas by the same system controller. In this case a full hardware data path can be applied to handle frame

classification and distribution to the wireless subsystems required to handle this processing as well as gather BER information in regard to RF performance in local areas. This integrated with Wi-Fi capability provides the ability to off load traffic from the cellular network, freeing up cellular bandwidth for other users. By the use of a 802.11 split MAC, we can now provide Authentication and Association credentials directly into the cellular network using Extensible Authentication Protocol of Local Area Network EAPOL. Using the same authentication triplets used between the service provider and the UE, WiFi can be enabled and provide service to cellular UE. Just as is the case with the Packet Gateway (PGW) or the Gateway GPRS Support Node (GGSN), Network Address Translation (NAT) services are provided for IP addresses that are provided for the local area. This service is used to go to the Internet from a UE that is using WiFi instead of the straight cellular services. Because the WiFi base stations can be elevated, and have amplification added for both transmit and receive, it is possible to use WiFi to offload some cellular data traffic.

The link layer communication model has been described for both the 802.11 where the RF MAC is split between a RF base station and the addition of the 802.11 subsystem to cellular subsystems. The point areas where the 802.11 subsystems are integrated will function correctly for all versions (e.g. GSM, UMTS, LTE) of cellular subsystems. In addition, a method of authentication has been described as well as how access to the Wide Area Network (WAN) is provided as is the case with all data services on UE.

Link Layer Hardware

In order to provide the best class of service for the link layer model described in the previous section, the hardware must be designed to support the following features:

Table 7
Sample Link Layer Feature List

1	Link Layer Encryption/Decryption (Cellular & WiFi). Encryption over the wired network.
2	Frame Manager (Classification Engine), Queue Manager, and Data Path Acceleration Architecture (DPAA -Freescale Standard)
3	Fixed format headers sent to wireless base stations
4	Table of all UE required
5	NAT and Proxy ARP provided for all bridged UE (different modes of operation), MAC learning feature to support MAC address transition across Layer 2 switch interfaces.
6	High performance frame processing with little or no intervention with GPP HW
7	Large number of Fiber and Ethernet interfaces available in one unit
8	Security Fuses, secure boot, security monitor (can be connected to tamper detection).
9	Numerous other hardware attributes not relevant for a research paper such as dual power supplies, solid state disks, etc...

The hardware design to support the link layer hardware would start with the design of the SoC. This design would facilitate the use of dedicated hardware state machines that act independently from each other. These hardware state machines are provided instructions in memory that are then loaded into their internal register cache for execution. These instructions facilitate the functions required to support the predefined headers found for both the link layer Ethernet communication as well as the cellular and 802.11 MAC fields. Since most of these fields are based upon configuration parameters that are configured by software, it would the responsibility of the link layer software to

implement the structures that are accessed by the hardware to support this link layer communication.

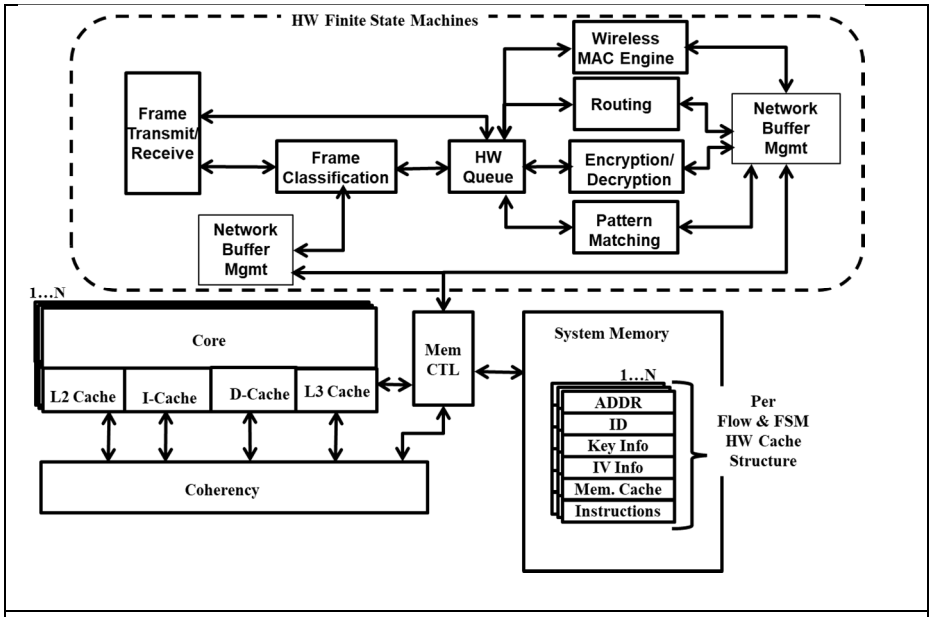

Figure 57. HW State Machines in SoC Architecture

The hardware state machines (as configured by software and depicted in Figure 57) used for frame processing would contain internal register memory that is used to communicate frames to a wireless base station. This internal register memory would be used to construct the proper frame header for a particular device that has been configured. In addition some hardware state machines would also include a hardware internal Direct Memory Address (DMA) engine. When a base station device has properly authenticated itself to the network, the base station MAC address, BSSID, radio MAC address(es), VLAN header information, security key information, and capabilities will be communicated and stored into system memory (not in hardware registers). When a network frame buffer is received from a wireless base station, the hardware frame classification engine would evaluate the source MAC address, VLAN tag information.

Based upon this information it will do further classification to identify the source MAC address of the actual wireless client. The source MAC address would then translate to unique hardware queue ID. A message with the address of the frame and that queue ID would be sent to the hardware queue. This hardware queue is configured to send frames with this queue ID to the security engine for link layer decryption. The security engine returns a specific queue ID after decrypting this frame (based upon its hardware memory cache structure). The hardware queue is configured to send frames with this queue ID to the wireless link layer engine for further processing. As an example, based upon the fields in the 802.11 MAC header, the wireless hardware engine will perform standard operations on the frame starting at the address of the frame. The wireless link layer hardware state machine is specifically designed to understand the 802.11 and UMTS MAC protocols. Using 802.11 as an example, the hardware state machine behavior can be based on the source (radio MAC) address of the sender in the forward direction. If the destination MAC address is that of another wireless device that is managed by this cell controller the frame will be forwarded onto the same queue that other frames from the network in the reverse direction are placed for eventual transmission to the wireless device.

Link layer encryption is based upon cryptographic algorithms verified and validated by the The National Institute of Standards and Technology (NIST). NIST issued the Federal Information Processing Standard (FIPS) Publication 140-2 (FIPS PUB 140-2) is a United States government computer security standard that is used to accredit cryptographic

modules. This publication is titled "Security Requirements for Cryptographic Modules" and was published on May 25, 2001 and was updated on December 3, 2002.

The National Institute of Standards and Technology (NIST) issued the FIPS 140 Publication Series to define requirements and standards for cryptography modules for both hardware and software components developed by technology companies. Federal agencies and departments can validate whether a module, termed a Hardware Security Module, is covered by an existing FIPS 140-1 or FIPS 140-2 certificate which specifies module name, hardware, software, firmware, and/or applet version numbers. Many cryptographic modules are produced by the private sector (and even by the open source) communities for use by the U.S. government and other regulated industries, including financial and health-care institutions, that collect, store, transfer, share, and disseminate sensitive but unclassified (SBU) information.

NIST regulated security programs enforce government and industry cooperation to establish secure systems and networks by developing, managing and promoting security assessment tools, techniques, and services, and supporting programs for testing, evaluation and validation. NIST security programs extend to development and maintenance of security metrics; security evaluation criteria and evaluation methodologies; tests and test methods; security-specific criteria for laboratory accreditation; guidance on the use of evaluated and tested products; research to address assurance methods and system-wide security and assessment methodologies; security

protocol validation activities; and appropriate coordination with assessment-related activities of voluntary industry standards bodies and other assessment regimes.

Annex C of FIPS 140-2 specifies Approved Random Number Generators. Random Number Generators (RNG) are used to generate random content for cryptographic algorithms that require the need of random content such as content required for the generation of IV information for IPSEC or DTLS protocols as two examples.

United States Federal Government standard Federal Information Processing Standard (FIPS) Publication 140-2 (FIPS PUB 140-2) requires verification that each sample produced by a Random Number Generator (RNG) be compared against the immediately preceding sample to verify that the random number generator does not generate the same numeric value twice sequentially; statistically, this would indicate a hardware or software fault rather than a coincidence. FIPS 140-2 specifies that any time a Random Number Generator (RNG) generates a new random number, the generated number is to be compared against a previously generated random number. If the two are the same, the event indicates a hardware (or software) failure rather than by some extraordinary, statistical chance. If the two are the same, an error indication is generated.

In order for any system to be compliant with requirements such as FIPS 140-2, but not perform the check in software, the hardware must enable the security engine utilizing a "bump in the wire" architecture in a mostly-hardware autonomous data path to perform this function. Thus, security can be implemented in separate devices interposed between

devices intended to communicate securely, for example cellular link layer encryption datagram, 802.11 link layer datagram and insecure Internet Protocol (IP) datagrams can be repackaged securely for transport over the public Internet or other unprotected network infrastructure.

The design of a RNG requires the use of hardware design techniques known as "Asynchronous Design". When using asynchronous design techniques to design a RNG subsystem, one must use the instability inherent in relying upon propagation delays in a logic design that vary with temperature, voltage level fluctuation, substrate differences, and register settling time that occur through combinatorial logic designs. These techniques are used to ensure that the RNG subsystem does provide random numbers with sufficient entropy. The following illustrative technique can facilitate random number generator verification, which may be performed without using any microprocessor execution time or specialized hardware.

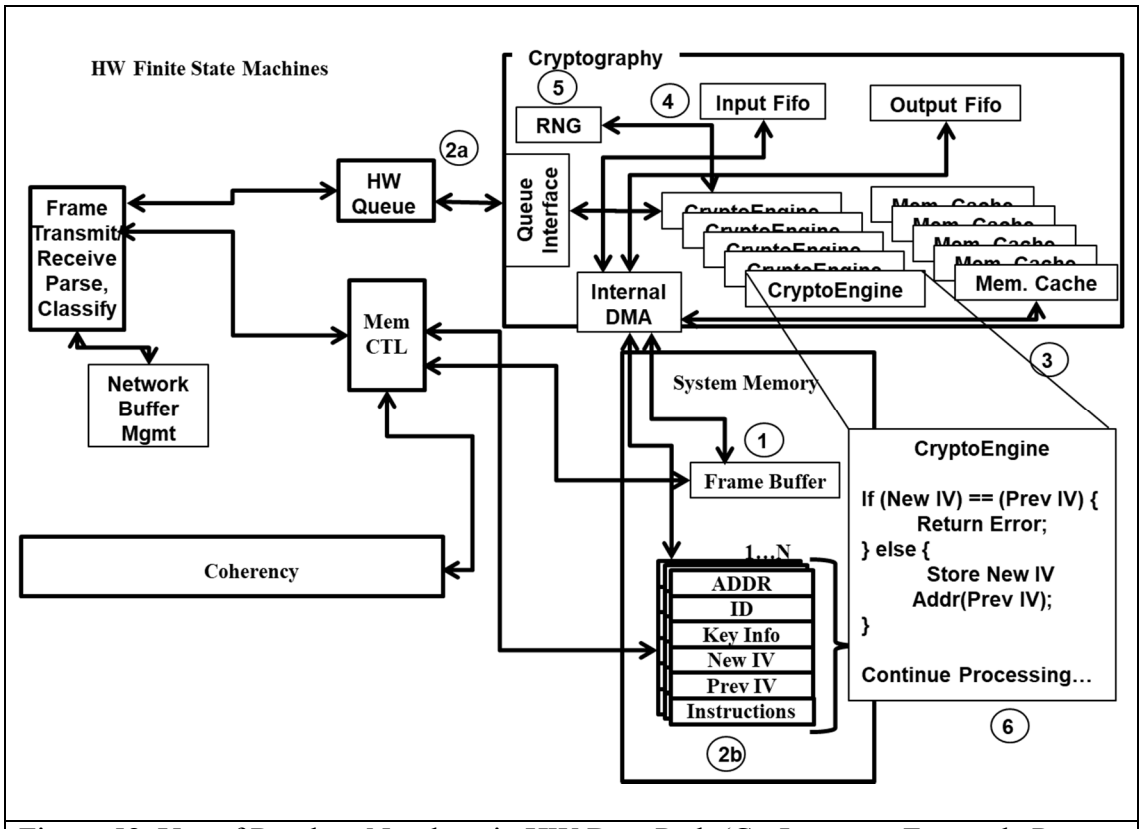

Figure 58. Use of Random Numbers in HW Data Path (Co-Inventor, Freescale Patent : Patent Nbr: 9,158,499)

An input frame that requires encryption is received by the hardware data path and is parsed, stored in system memory (1 in Figure 58) by the hardware receive DMA engine. A message is sent by the frame parser to the HW queue across a hardware bus. This message contains the address of the HW cache associated to the queue ID in system memory (2b in Figure 58). The Queue Interface reads the message in the HW Queue (2a in Figure 58) and alerts the DMA to read the HW memory using the address found in the HW Queue message) and distribute a processing request to a CryptoEngine (3 in Figure 58). The Queue Interface also instructs the DMA to read the Frame Buffer memory using the address found in the HW Queue message (4 in Figure 58). The CryptoEngine requests a random number because it must generate an IV. This IV contains a mask (e.g.

seed) that is XOR'd with the random number (5 in Figure 58). Finally, the CryptoEngine executes its loaded instructions (in its internal memory cache) and checks the newly generated IV to the previous IV. If these IV's are identical, it is indicative of a problem and an error is returned, otherwise the new IV is stored at the address of the previous IV by use of its DMA engine and processing continues normally (6 in Figure 58).
This process illustrates a FIPS compliant hardware design to meet the cryptographic needs of the cell controller.

Link Layer Software

The link layer software is comprised of the following subsystems that interact with the hardware state machines described in the hardware section above. The software must pre-populate the hardware memory of the state machines to accommodate the transmission of frames to wireless device from other wireless devices as well as devices from the WAN side of the network device. Network headers that are used to communicate to the wireless base stations must be pre-populated on a per-flow basis. The following depicts the headers that must be pre-populated. Note that the wireless link layer engine will modify some portions of the header as data moves through the autonomous hardware data path.

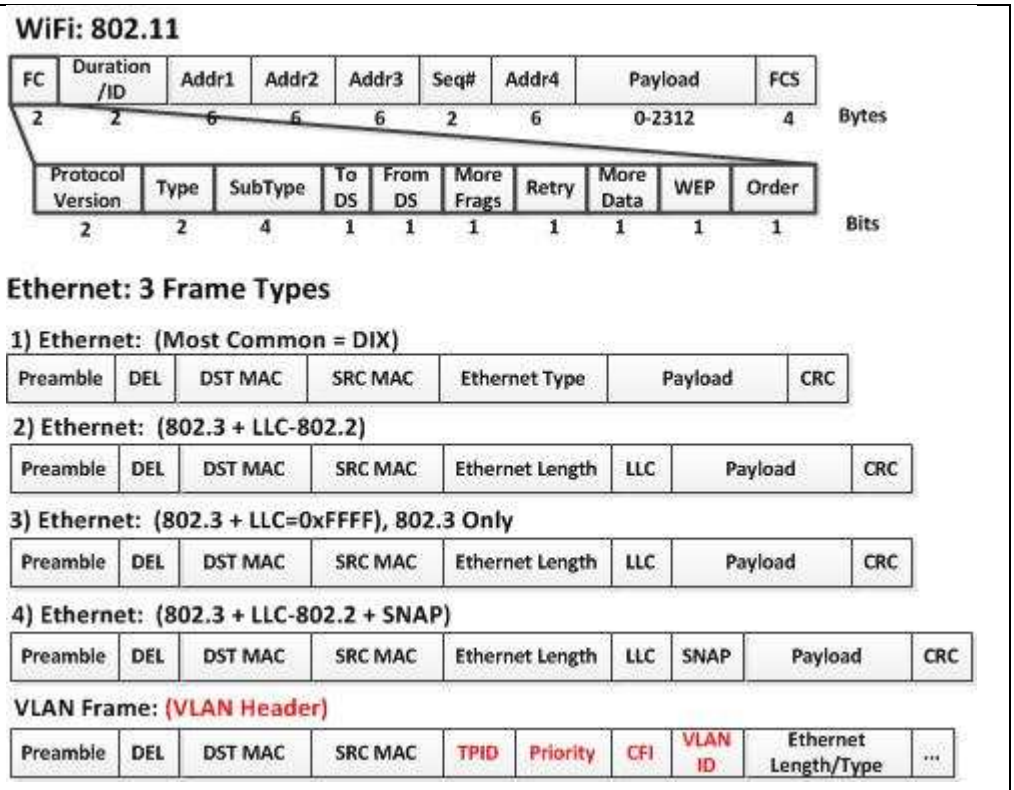

Figure 59. Network Frame Headers that most be pre-populated on a per Flow basis

As described in Figure 57, the wireless link layer engine requires HW memory cache that contains the proper Ethernet, VLAN, Cellular or 802.11 MAC header pre-populated on a per flow basis. This means two per wireless device (1 for the forward direction and 1 for the reverse direction) flow to and from a wireless device. The network header formats described in Figure 59 must be pre-populated in the wireless link layer hardware state machine. This finite state machine (FSM) must also maintain flow control structures between the cell controller and the RF base stations. There are mechanisms in place in regard to the cellular protocol specification; however, on the 802.11 side there are not integrated specifications. The following frame formats are specified to support link layer communication between the RF base stations and the cell controller:

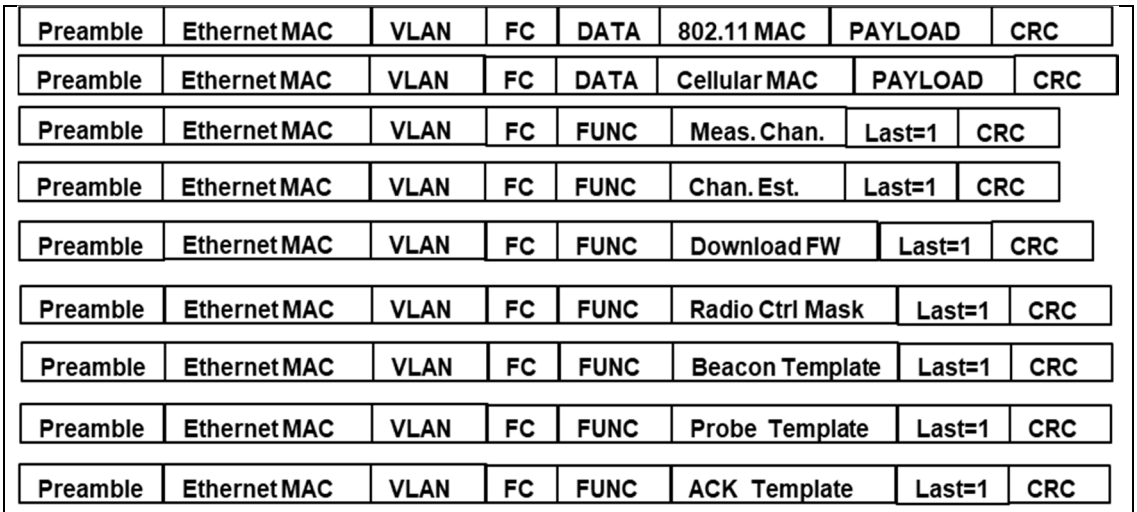

Figure 60. Frame Format Examples

CHAPTER 5

MOBILE AND BASE STATIONS

Wireless State Machines

Cellular and 802.11 devices are constantly measuring the RF environment. As such they are constantly performing neighbor cell power measurements, if sufficient BER rate is sensed by the receiver (where rate adaptation did not improve), a 802.11 client device will initiate its form of cell reselection (issues a 802.11 Reassociation request). On cellular devices this is performed by monitoring all BCCH carriers contained and making one measurement per BCCH carrier. The size of the neighbor cell list (e.g. number of neighboring transmitters), either increases or decreases the amount of time UE spend performing these measurements. Cellular devices initiate the process of cell reselection by a process referred to as Location Area Update (LAU). This process is analogous to the example when in a moving vehicle. The cellular device in your hand will receive a signal from a new tower which will have a different Location Area Code (LAC). This process is repeated as the car continues to move from one tower to the next. This process is sufficient for voice services, while processes referred to as Routing Area Update and MM Attach is required for data services. A cellular device can also request supplementary services such as [no] call waiting, [no] call forwarding, and activate Short Message Service (SMS).

Finite State Machine Behavior

The cell reselection state machine is depicted in Figure 61; he $Dev\_Xmit\_CCCH_{max}$ and the $Cell\_Reselect\_Off$ field values are transmitted on the Broadcast Channel (BCCH) of a cellular base station. In order to distribute the load of cellular devices across cellular base stations, the cell controller can dynamically modify the parameters being transmitted on this channel thereby influencing the state machine of the UE to connect to a different RF base station. For UMTS and LTE UE, the network can also request a cell reselection.

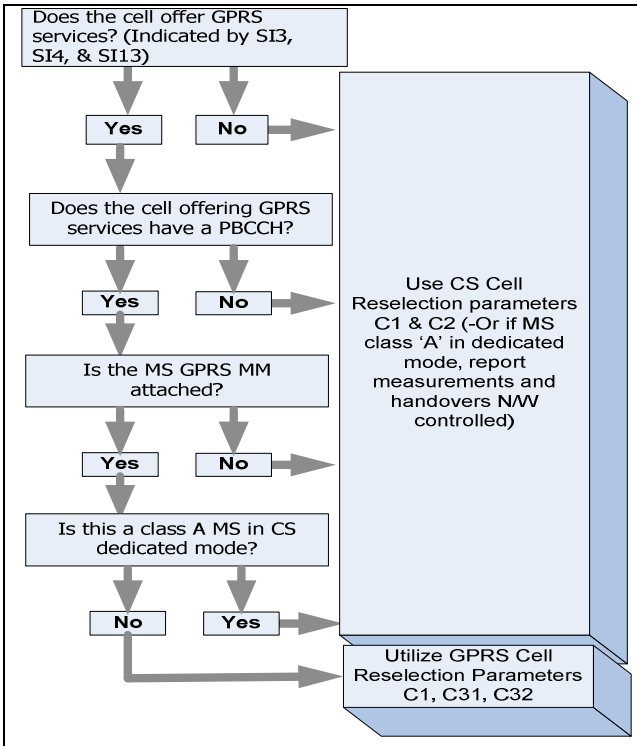

Figure 61. Cellular Cell Reselection Rule Evaluation Process

$$C1 = PSD_{avg} - Dev\_Rx\_Rqd_{min} - max(Dev\_Xmit\_CCCH_{max} - Dev\_Pwr\_Class\ ) \quad (130)$$

PSD_{avg} = Average receive signal level

$Dev\_Rx\_Rqd_{min}$= Minimum PSD_{avg} the MS must receive to access this cell

$Dev\_Xmit\_CCCH_{max}$ = Maximum power the MS is allowed to transmit on the RACH

Dev_Pwr_Class = MS power class

$$C2 = C1 + Cell\_Reselect\_Off - max(Temp_{Off}\ for\ Penalty\_Time) \quad (131)$$

$Cell\_Reselect\_Off$ = dB weighting applied to a cell which may be positive or negative

$Temp_{Off}$ = Positive dB weighting applied to a cell for the time $Penalty\_Time$

$Penalty\_Time$ = Timer set in the MS by the neighbor cell; on it expiry, the $Temp_{Off}$ is removed. $Temp_{Off}$ is only applied to neighbor cells.

In addition, cellular and 802.11 wireless devices also perform rate adaptation based upon sensed BER information. An 802.11 wireless client device normally initiates a Reassociation request, while a cellular device utilizes the LAU procedure as well as manage the cell reselection.

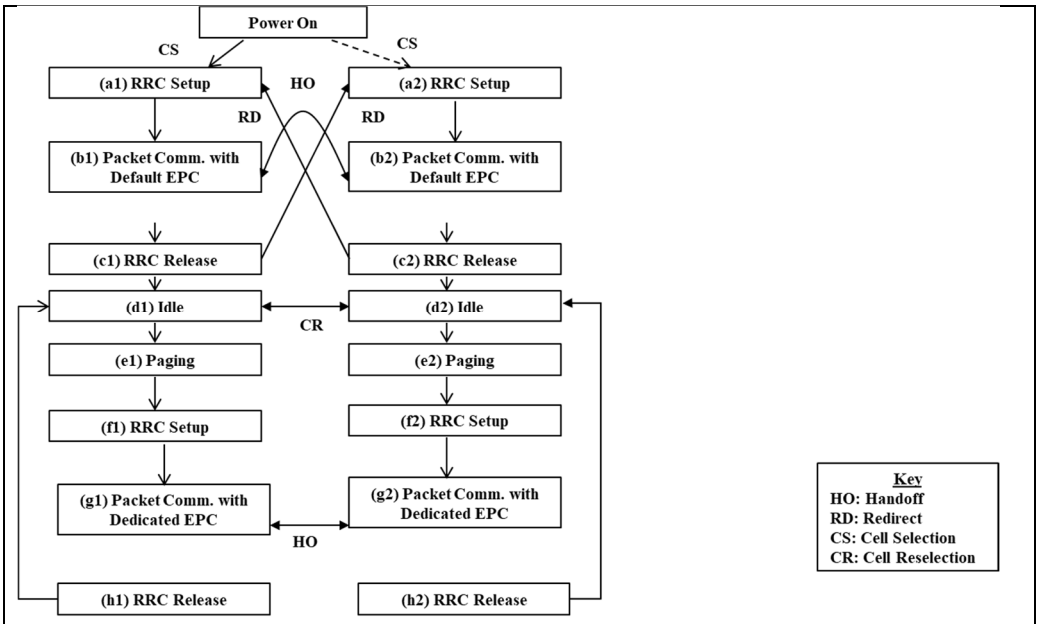

Figure 62 LTE Handset (Basic State Machine Terminology)(ShareTechnote, 2013)

An example LTE cell reselection, initiated by the network side: A UE is in connection with a cell 'A'. The network sends a command to the UE to perform a signal quality measurement on cell 'B' (e.g. UMTS command = "Measurement Control", while LTE command = "RRC Connection Reconfiguration"). The UE performs the measurement and sends the result to Cell 'A'. (e.g. UMTS and LTE = "Measurement Report"). If the controller deems the measurement favorably, the UE is sent a change cell command. (e.g. UMTS command = "Physical Channel Reconfiguration or ActiveSetUpdate", while LTE = "RRC Connection Reconfiguration"). Once the UE changes to cell 'B' successfully, the UE will send a cell change completion message to cell 'B' (e.g. UMTS = "Physical Channel Reconfiguration Complete or ActiveSetUpdateComplete", while LTE = "RRC Connection Reconfiguration Complete"). (ShareTechnote, 2013)

LTE phones presently have two antennas that can be used in a 2x2 MIMO mode. The LTE phone can use one antenna to talk to one tower while using the second antenna to communicate to the second cell tower.

Roaming

In 802.11 roaming to another access point involves sending a 'Reassociation" request to the new access point. This "new" access point was discovered by an outcome of signal strength measurements by the client device. In the 802.11 state machine below, the Reassociation message speeds up the Authentication and Association state change so it more quickly moves to the successfully Authenticated and Associated state. When a wireless device roams, it is important that data transfer is not lost during the process. The MS state machine has an impact on this behavior. When a 802.11 device sends it "ReAssociation" message, it must still properly receive frames from the base station it is presently Associated to. In addition, if the base station it is roaming to does not have direct communication and coordination with the base station it is roaming from the device will be forced to perform a complete Association to the device it is roaming to. With the cell controller link layer approach, the roaming between access points can be seamless. The following state machine diagram depicts the change in the typical state machine behavior of the mobile device.

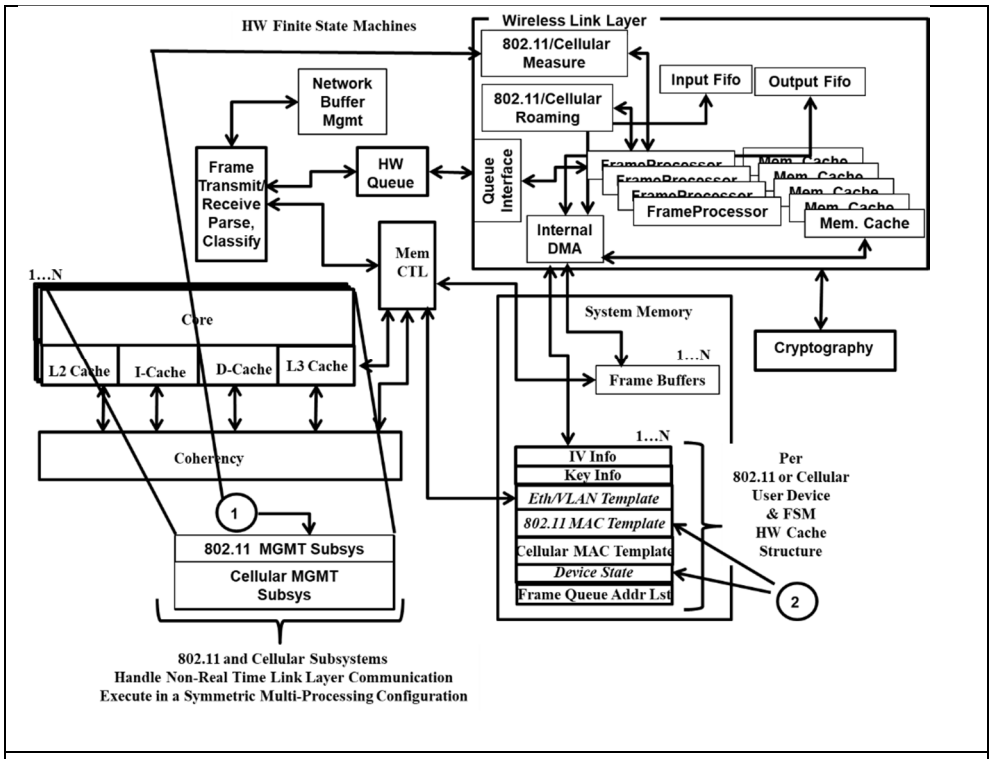

Figure 63. Example of 802.11 Roaming Utilizing Cell Controller Concept

The remote sensing software that manages the hardware link layer (e.g. 802.11/Cellular Measure) RF measurement subsystem either measures that the RF energy from a particular device is actually stronger on a different RF base station that it is presently receiving data or that a Reassociation message is received from that device. In either case, a seamless roaming event is initiated by the software (refer to 1 in Figure 63). This software modifies the per device table managed in memory using the Queue Interface specified above. The Queue Interface is the only hardware entity that can assure the change to this shared memory location is updated atomically without interrupt to other processing flows and to the hardware that is processing the hardware data path. The fields updated are the pre-populated Eth/VLAN header template, the 802.11 MAC to reflect a change to any 802.11 parameters required such as BSSID & RF MAC address

change, and device state (refer to 2 in Figure 63). Note that the Frame Queue Address List (records addresses of all frames to be transmitted to a device), Key and IV information is not modified; therefore, frames queued toward the wireless device will be sent to the new RF base station immediately when the change occurs through 802.1pq link layer communication toward the correct RF base station.

Cellular Roaming

The cell controller commands mobile devices thru their mobile station (MS) to perform a measurement of a neighboring cell. The cellular measurement subsystem is used to continually command a measurement of neighboring RF base stations. Software executing on one or more cores makes a decision based upon signal strength as well as traffic load across the base stations. The cell controller makes it possible to better understand the RF environment in regional areas and to be more responsive to changes in these areas.

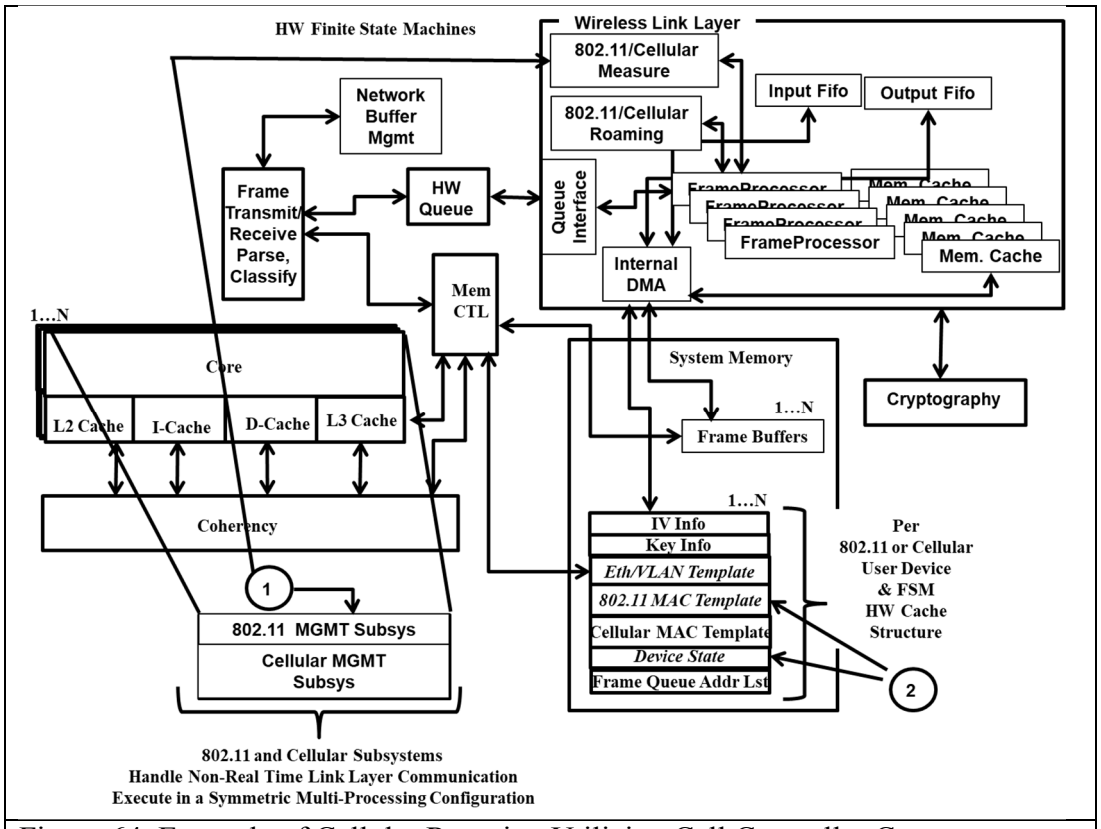

Figure 64. Example of Cellular Roaming Utilizing Cell Controller Concept

Based upon RF measurements roaming is initiated by the software (refer to 1 in Figure 64). This software modifies the per device table managed in memory using the Queue Interface specified above. The Queue Interface is the only hardware entity that can assure the change to this shared memory location is updated atomically without interrupt to other processing flows and to the hardware that is processing the hardware data path. The fields updated are the pre-populated Eth/VLAN header template, the Cellular MAC to reflect the new cellular parameters (Note: TMSI, TLLI, should all remain the same. These identifiers can be globally unique by utilizing the MAC address of the unit for their derivation) and device state (refer to 2 in Figure 64). Note that the Frame Queue Address List (records addresses of all frames to be transmitted to a device), Key (authentication triplet) and IV information is not modified; therefore, frames queued

toward the wireless device will be sent to the new cellular RF base station immediately when the change occurs through 802.1pq link layer communication toward the correct cellular RF base station.

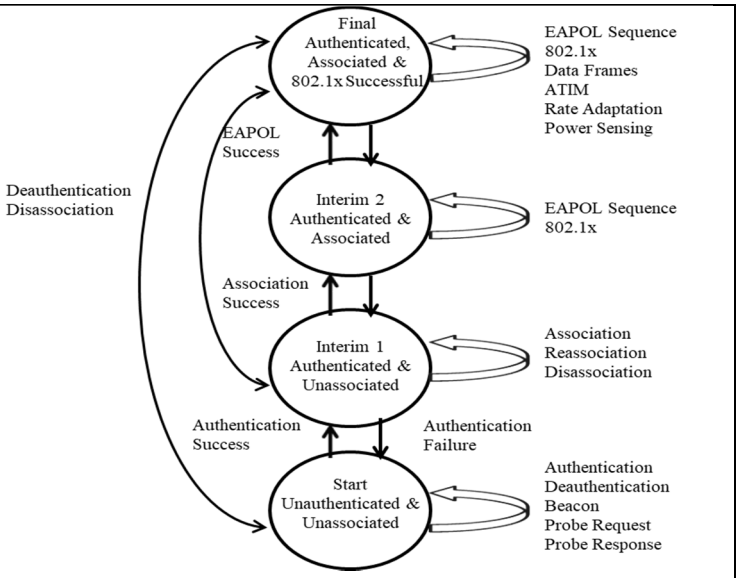

Figure 65. 802.11 Mobile Device State Machine

With the use of MIMO and 802.11ac technology, a 'Reassociation' message is not required when a cell controller can be used to authenticate the user over an existing encrypted channel. The cell controller can make it possible, using link layer command and control, for the neighboring 802.11 RF base station to start communicating with the wireless client (using its second antenna) in a 2x2 MIMO configuration while the wireless client device is still communicating with the other RF base station through the use of the other antenna. The RF base stations would need to be told to not answer on its second antenna for this client device. This is acceptable since the RF base station must transmit ACKs with the BSSID of the network it is associated to. The client device

would not know that the second spatially diverse antenna it was using is on another RF base station. The cell controller would make the decision as to when to complete the full process of 802.11 roaming. This process is identical to the method used by LTE mobile devices. LTE devices can utilize their second antenna in a 2x2 MIMO configuration to interact with multiple base stations simultaneously. This requires only software support for the proper analysis of eigenvectors to be performed on the 802.11 client based upon the concept of having two (very separated) spatially diverse streams possibly on two separate channel frequencies.

Power Spectral Density Estimation

In order for mobile devices to make roaming decisions, these devices must calculate power spectral density. In addition, channel information from a RF base station can be provided to the cell controller to determine and estimate the active signals in the area. An evaluation of PSD and estimation techniques will now be described. To calculate the power of a W-CDMA signal, we must integrate over the entire bandwidth of the signal. For instance, a WCDMA signal based upon the 3GPP WCDMA Frequency Division Duplex (FDD) release 99 Downlink Dedicated Physical Channel (DPCH) with a bandwidth of 5MHz will generate the following Power Spectral Density plot.

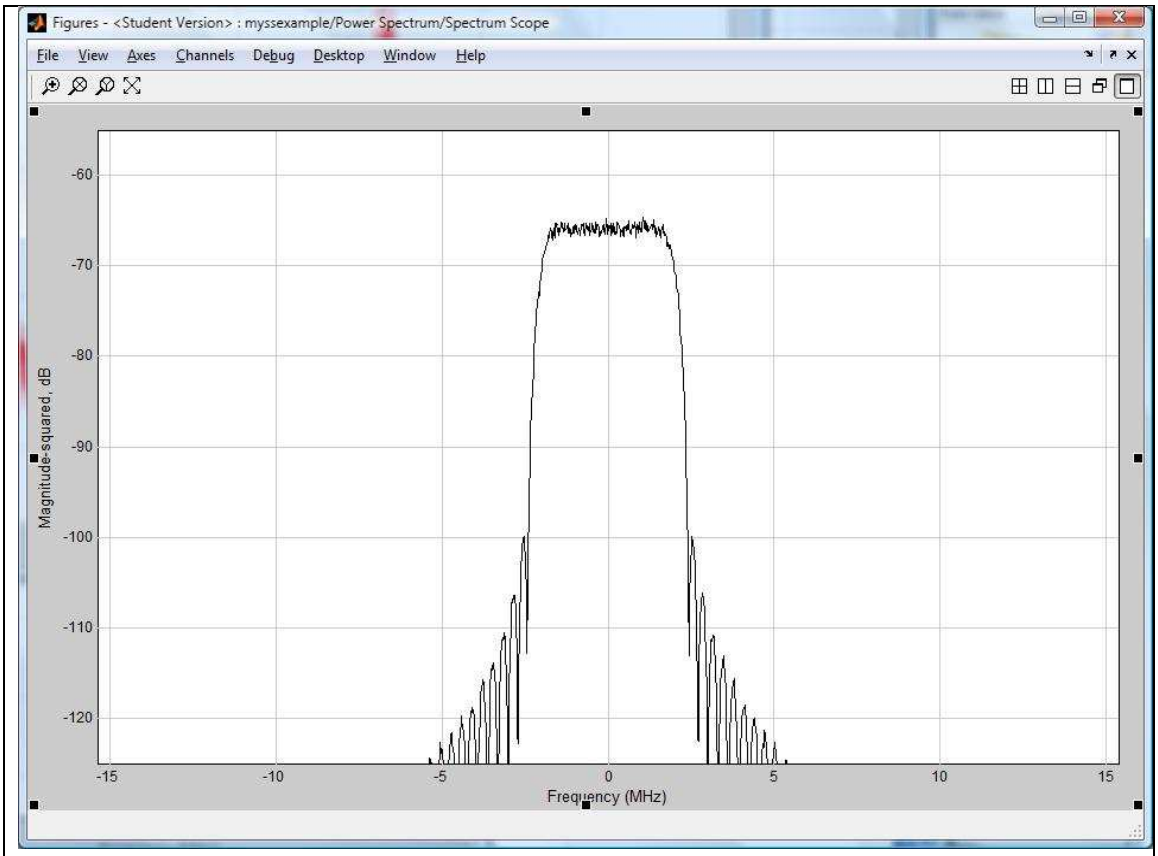

Figure 66. Example Spread Spectrum Tx (5 MHz)

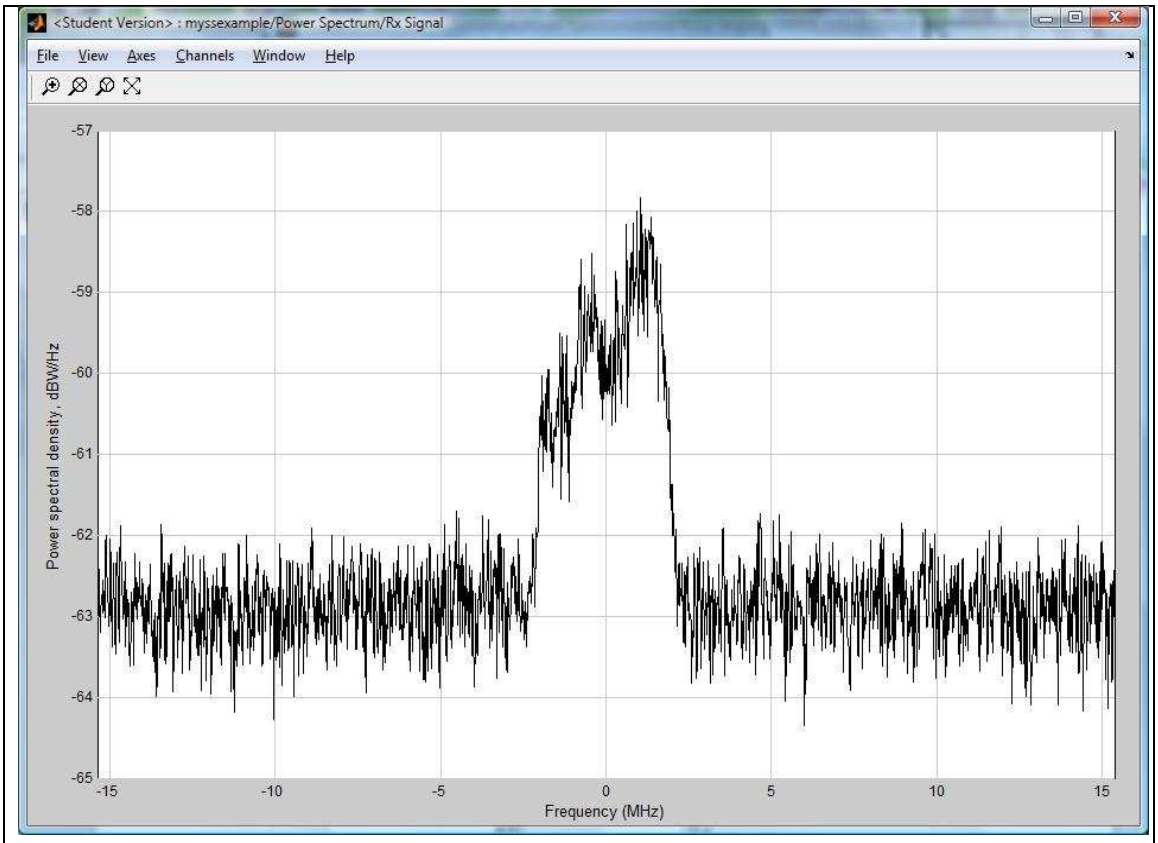

Figure 67. Example Spread Spectrum Rx (5 MHz) Mixed with AWGN

Other signals of interest can be derived from base stations in the area. These base stations can perform signal analysis of the RF environment and report the results of this analysis to the cell controller. Such information can be used to determine why high incidents of BER are reported in specific cell coverage areas. I studied signal estimation and detection methods with the goal to determine the best Power Spectral Density (PSD) estimation method for the derivation of the PSD of sinusoid signals in the presence of white noise utilizing different estimation methods. In order to achieve this goal, I will utilize two general classification methods: non-parametric and parametric methods. Non-parametric methods derive their PSD estimate directly from the input data. Parametric

methods model the data as an output of a linear system driven by White Gaussian Noise (e.g. W.G.N) with a specified variance so system parameters can be estimated. I will utilize two different input levels: Level 1: Three input sinusoids, Level 2: Three input sinusoids and regenerated random noise (for each factor).

I will utilize the following estimation methods as my factors in this experiment: Blackman-Tukey correlogram, Welch Periodogram, Yule-Walker, Burg, Covariance, Modified Covariance, and Multiple Signal Classification (MUSIC). I then utilize the analysis of variance (ANOVA) method to analyze the variance within each estimation method as well as the variances between different estimation methods.

Factors and Factor Ranges

For each estimation method, I will vary the ranges of the factor to best illustrate frequency resolution and derivation of power spectral density. Though I will utilize a Hamming Window for both the correlogram and periodogram estimation methods, the ranges of the factors will be different for both the correlogram and periodogram estimation methods. I will use the following **lag** ranges for the correlogram estimation method as 10, 20, and 70. In the equation below L indicates the **lag** index and is computed using the Discrete Time Fourier Transform (DTFT) of the autocorrelation sequence.

$$P_{xx}(f) = T \sum_{m=-L}^{L} \widehat{r_{xx}}(m) e^{-i2\pi f m T} \tag{132}$$

For the periodogram estimation method, I will use different **shift** adjustments for the analysis window. By utilizing an analysis window, I can cause different overlapping sequences and therefore improve the PSD estimate. In the equation below, n represents the index of the input sample sequence.

$$P(f) = \frac{T}{N}\sum_{n=0}^{N-1} |x\,(n)e^{-i2\pi fnT}|^2 \tag{133}$$

Again, the input sequence can be overlapped (accomplished by utilizing different **shift** adjustments) to improve the power spectral density estimate. I will use the following **shift** adjustments for the periodogram estimation method as 10, 20, and 30.

For the Yule-Walker, Burg, Covariance (& modified covariance), and MUSIC PSD estimation methods, I will utilize model order 5, 15, and 30. The following is the equation used to calculate the Yule-Walker PSD:

$$\tilde{P}_{AR}(f) := \frac{T * var(w)}{|1 + \sum_{k=1}^{p} \tilde{a}_p(k)e^{-j2\pi kfT}|^2} \tag{134}$$

Since the Burg method is an AR process, the following is the equation used to calculate the Burg PSD:

$$\tilde{P}_{AR}(f) := \frac{T * var(w)}{|1 + \sum_{k=1}^{p} \tilde{a}_p(k)e^{-j2\pi kfT}|^2} \tag{135}$$

The value $\tilde{a}_p(k)$ is derived by utilizing a harmonic mean between the forward and backward partial correlation coefficients to calculate the reflection coefficient, $\widehat{K}_p$. Once

these AR parameters are calculated, the PSD estimate is calculated as described in the equation above.

$$\widehat{K}_p := \frac{-2\sum_{n=p+1}^{N} e_{p-1}^{f}[n] e_{p-1}^{b*}[n]}{\sum_{n=p+1}^{N} |e_{p-1}^{f}[n]|^2 + \sum_{n=p+1}^{N} |e_{p-1}^{b}[n]|^2} \tag{136}$$

At each order, P, the variance of the forward and backward linear error prediction is minimized. This calculated utilizing an arithmetic mean:

$$var(fb) := {}^{1}/_{2}\left[{}^{1}/_{N}\sum_{n=p+1}^{N} |e_p^f[n]|^2 + {}^{1}/_{N}\sum_{n=p+1}^{N} |e_p^b[n]|^2\right] \tag{137}$$

Since the Covariance method is also an AR process, the following is the equation used to calculate the Covariance PSD:

$$\tilde{P}_{AR}(f) := \frac{T * var(w)}{|1 + \sum_{k=1}^{p} \tilde{a}_p(k) e^{-j2\pi k f T}|^2} \tag{138}$$

The following is how to compute the covariance matrix of a signal x of time series length N, with maximum lag M:

$$C_{ij} := \left(\frac{1}{N-M}\right)\sum_{k=1}^{N-M} x(k+i)\, x(k+j) \tag{139}$$

and individual elements of R_p:

$$r_p[i,j] := \sum_{k=p+1}^{N} x^*(k-i)x(k-j) + x(n-p+i)x^*(n-p+j). \tag{140}$$

This PSD algorithm minimizes the forward error prediction utilizing least squares to determine AR parameters, $\tilde{a}_p(k)$.

Since the Modified Covariance method is also an AR process, the following is the equation used to calculate the Modified Covariance PSD:

$$\tilde{P}_{AR}(f) := \frac{T * var(w)}{|1 + \sum_{k=1}^{p} \tilde{a}_p(k) e^{-j2\pi k f T}|^2} \tag{141}$$

The following is how to compute the covariance matrix of a signal x of time series length N, with maximum lag M:

$$C_{ij} := (\frac{1}{N-M}) \sum_{k=1}^{N-M} x(k+i)\, x(k+j) \tag{142}$$

and individual elements of R_p:

$$r_p[i,j] := \sum_{k=p+1}^{N} x^*(k-i)x(k-j) + x(n-p+i)x^*(n-p+j). \tag{143}$$

This PSD algorithm minimizes the both the forward error prediction and the backward error prediction utilizing least squares to determine AR parameters, $\tilde{a}_p(k)$.

The 'pseudo' (not true PSD) MUSIC spectrum estimate is derived from the following equation:

$$P_{MUSIC}(f) := \frac{1}{\bar{e}^H(f)(\sum_{k=M+1}^{P+1} \bar{v}_k \bar{v}_k^H)\bar{e}(f)} \tag{144}$$

The power spectral density information is lost when utilizing the MUSIC algorithm; however, it is quite useful in the derivation of the frequency components of signals embedded in white noise. MUSIC makes the assumption that the noise in each channel is uncorrelated making the noise correlation matrix diagonal. This estimation technique

requires advance knowledge of the number of incoming signals or a search for the eigenvalues to determine the number of incoming signals.

Levels

I will input the following signal combinations (Levels):

Table 8
Input Signals for PSD Measurement Tests

1	Signal (3 sinusoids)
2	Signal (3 sinusoids) + AWGN

I will create the noise signal using a randomly generated noise signal in MATLAB, using the" rand()" function.

Measurement

I will measure the magnitude (y-axis) of the three output sinusoids as function of frequency (x-axis) for each factor, range, and input level for a large (10) replicated set of test executions. Random noise is regenerated per replicated test.

Response Variables

The following will be used to as response variables for the tests to be performed.

Table 9
Response Variables (Measured Results)

1	Number of output signal frequencies.
2	Magnitude of each output signal frequency. This is a maximum of three magnitudes per replicated test.

Factors, Factor Levels, and Response Variables

The following sections will describe the Factors, Factor Levels, and Response Variables for each of the following algorithms: Blackman-Tukey correlogram, Welch Periodogram, Yule-Walker, Burg, Covariance, Modified Covariance, and Multiple Signal Classification (MUSIC). I have also included test runs for these algorithms. I will execute and record the results for 5 runs [replicates] for each algorithm.

Blackman-Tukey Test Factors, Factor Levels, and Response Variables

Three input sinusoids at the following frequencies: 10Hz, 11Hz, and 25Hz, with Factor having 3 levels: 10, 20, and 70. Factor: Lag equals variable 'L' as used in the following equation:

$$P_{xx}\ (f) = T \sum_{m=-L}^{L} \widehat{r_{xx}}\ (m) e^{-i2\pi f m T} \tag{145}$$

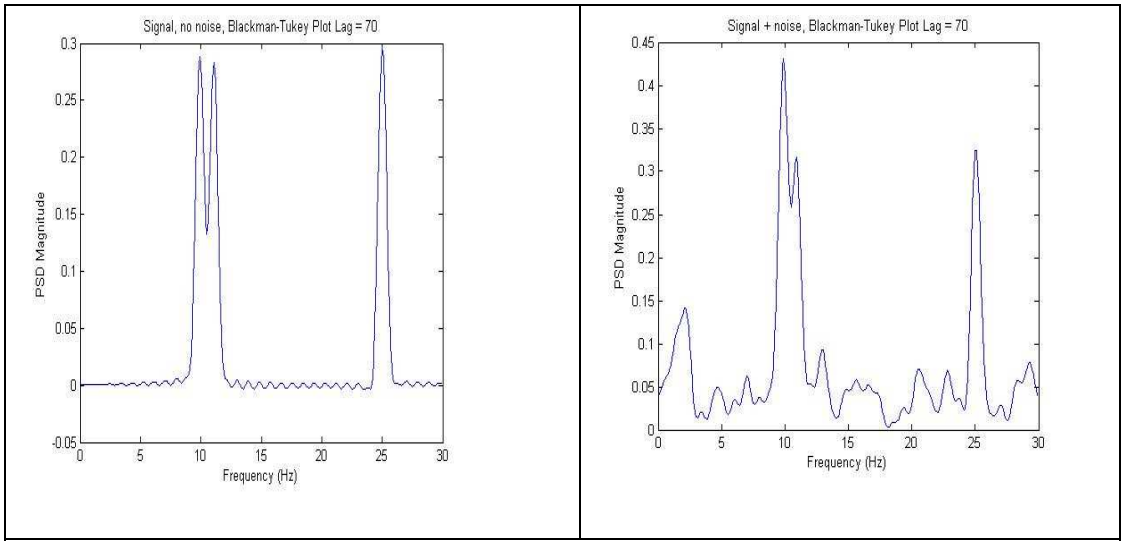

Figure 68. Blackman-Tukey (Signal +no noise, left plot: Signal+noise, right plot), Hamming Window, Lag = 70

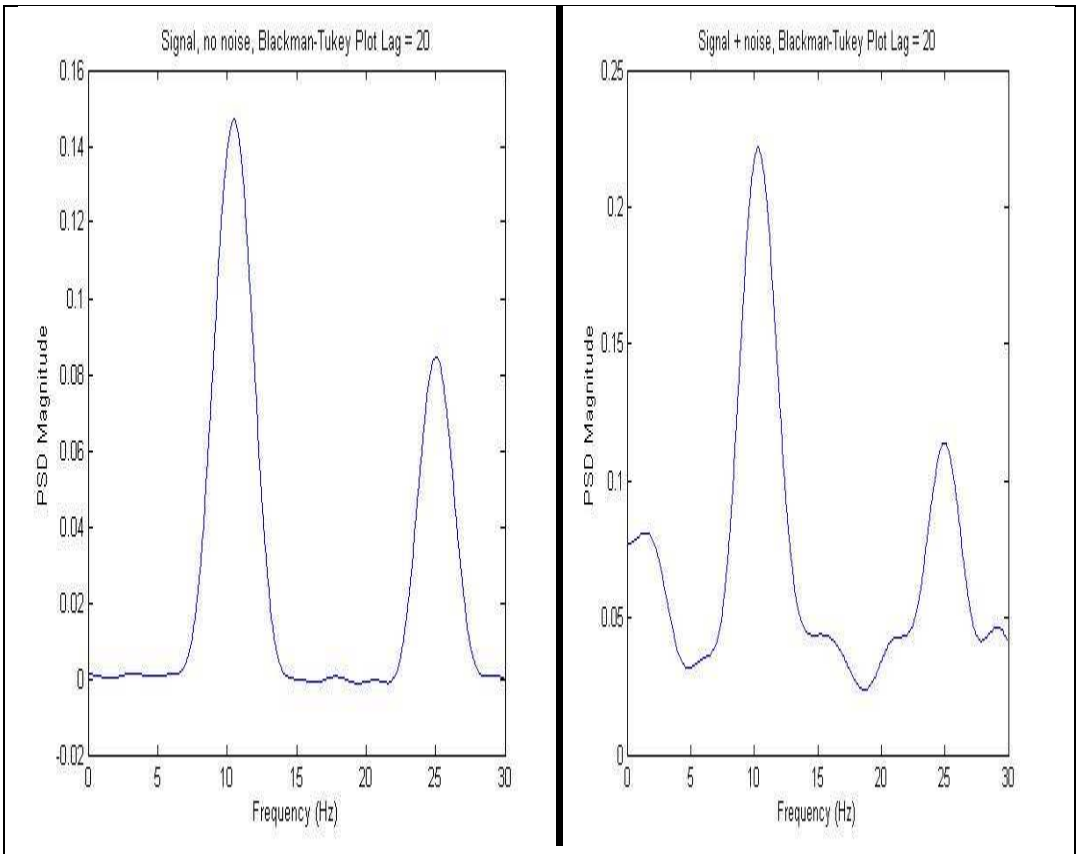

Figure 69. Blackman-Tukey (Signal+no noise, left plot: Signal+noise, right plot), Hamming Window, Lag = 20

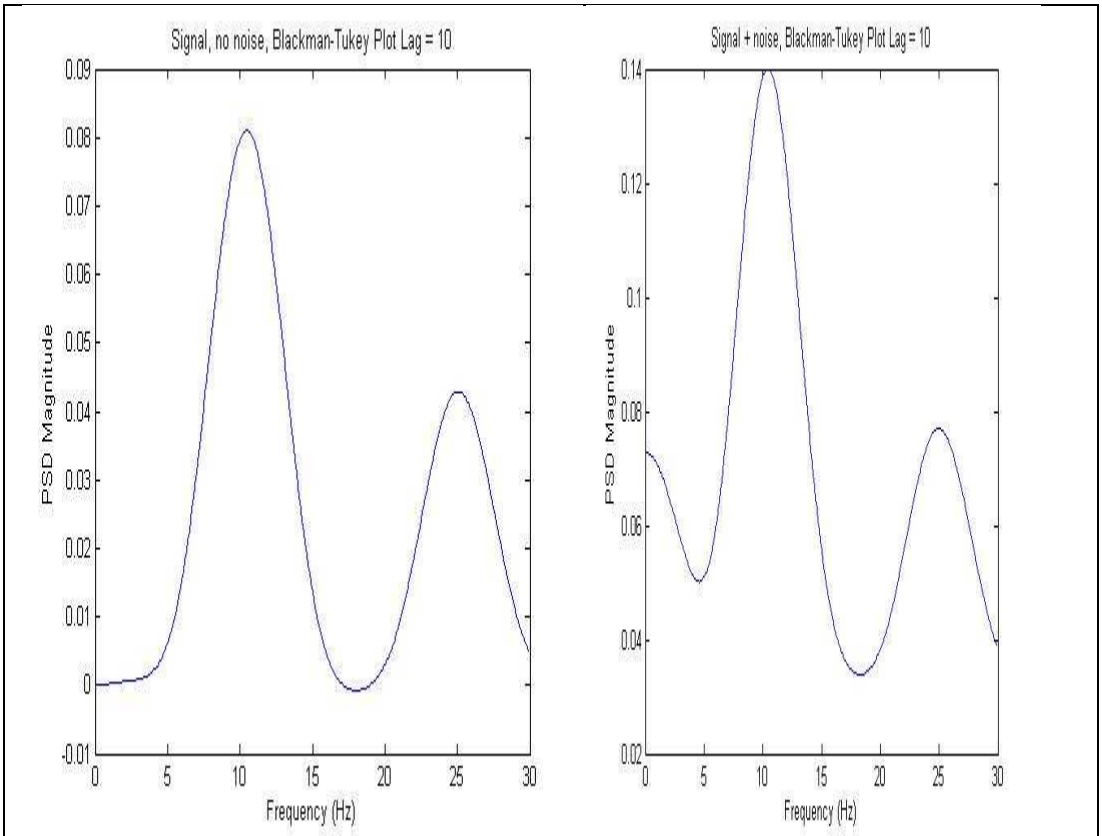

Figure 70. Blackman-Tukey (Signal+no noise, left plot: Signal+noise, right plot), Hamming Window, Lag = 10

Welch Test Factors, Factor Levels, and Response Variables

Three input sinusoids at the following frequencies: 10Hz, 11Hz, and 25Hz, with Factor having 2 levels: Shift Index 10 and 20. Factor: Shift index used in the following equation. The shift index is used to overlap the input sequence $x(n)$ in the equation below.

$$P(f) = \frac{T}{N}\sum_{n=0}^{N-1} |x\,(n)e^{-i2\pi fnT}|^2 \tag{146}$$

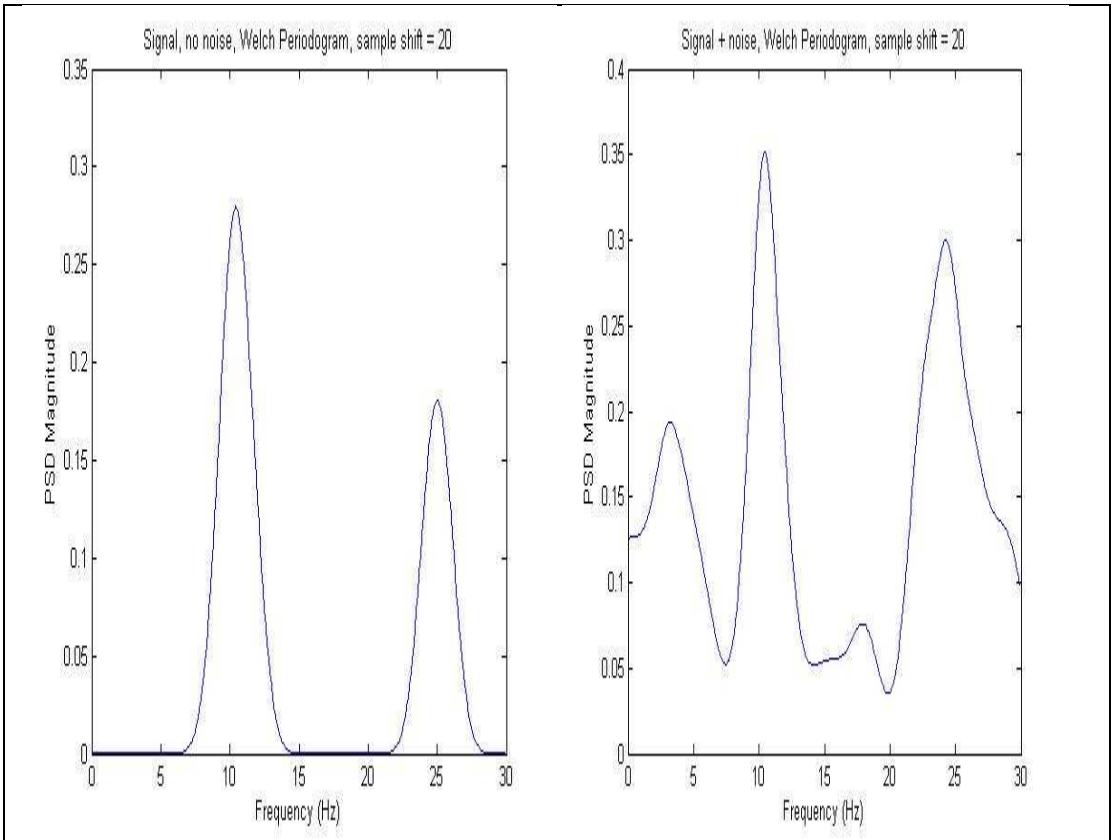

Figure 71. Welch Periodogram (Signal +No Noise, left plot, Signal+Noise, right plot), Hamming Window, Shift = 20

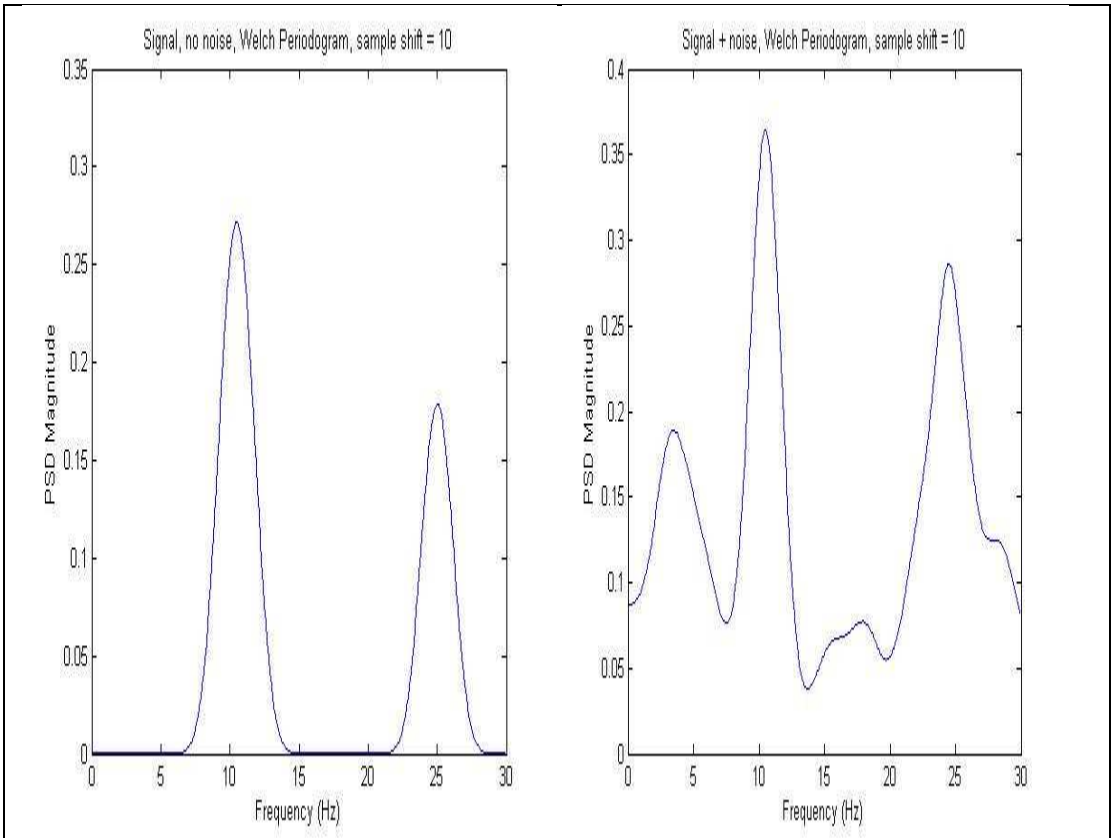

Figure 72. Welch Periodogram (Signal +No Noise, left plot, Signal+Noise, right plot), Hamming Window, Shift = 10

Yule-Walker Test Factors, Factor Levels, and Response Variables

Three input sinusoids at the following frequencies: 10Hz, 11Hz, and 25Hz, with Factor having 3 levels: Model Order 5, 15, and 30. Factor: Model order is used in the following equation. The model order represents the 'p' summation range in the equation below. The following is the equation used to calculate the Yule-Walker PSD:

$$\tilde{P}_{AR}(f) := \frac{T * var(w)}{|1 + \sum_{k=1}^{p} \tilde{a}_p(k) e^{-j2\pi kfT}|^2} \tag{147}$$

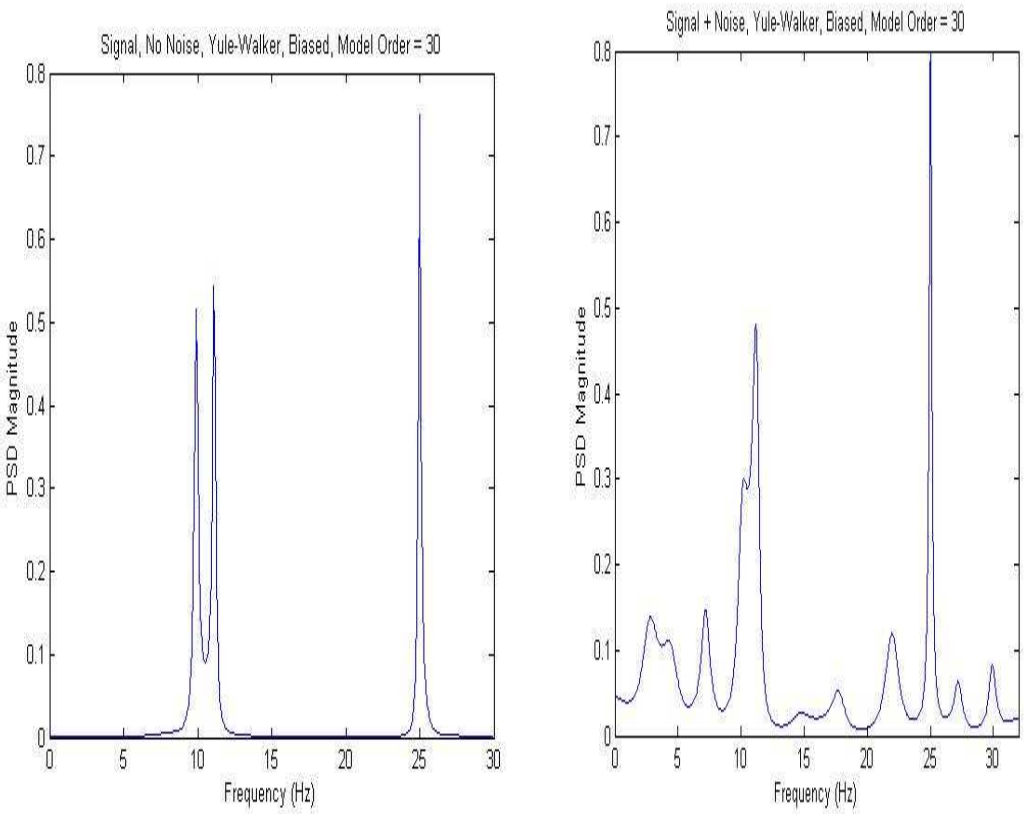

Figure 73. Yule-Walker, (Signal+No Noise, left plot, Signal+Noise, right plot) Biased ACF, Model Order = 30

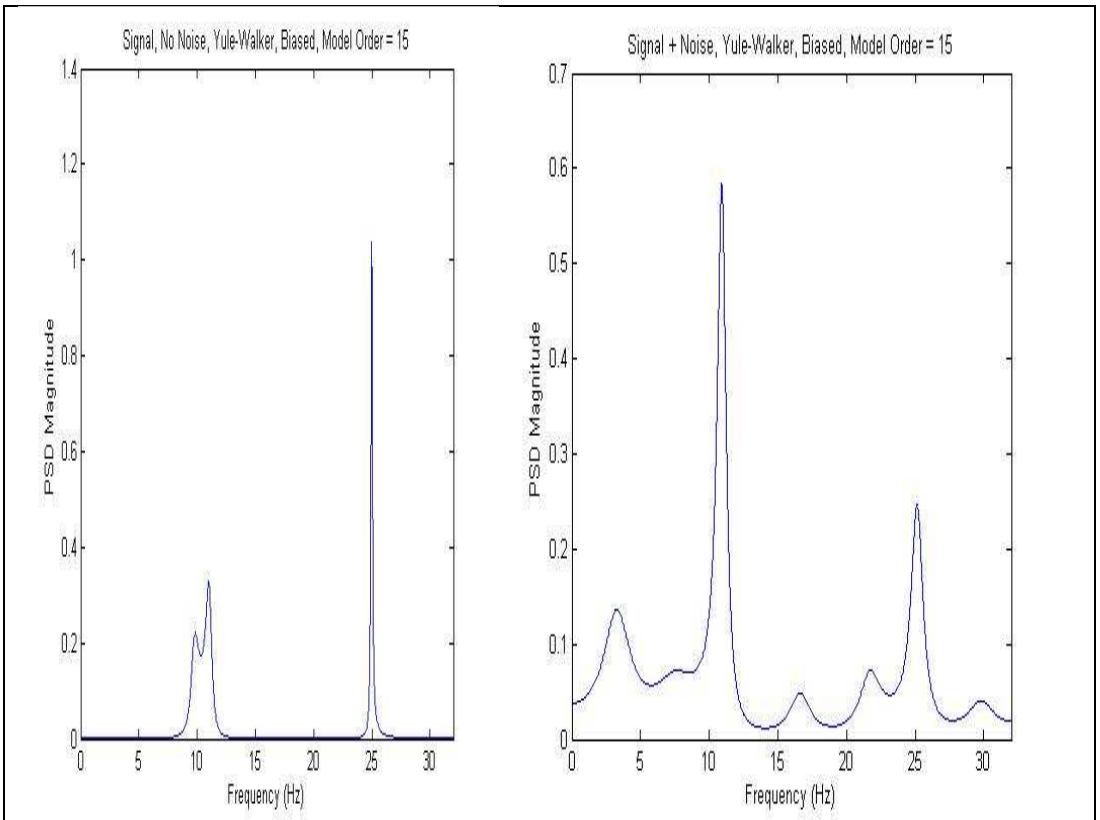

Figure 74. Yule-Walker, (Signal+No Noise, left plot, Signal+Noise, right plot) Biased ACF, Model Order = 15

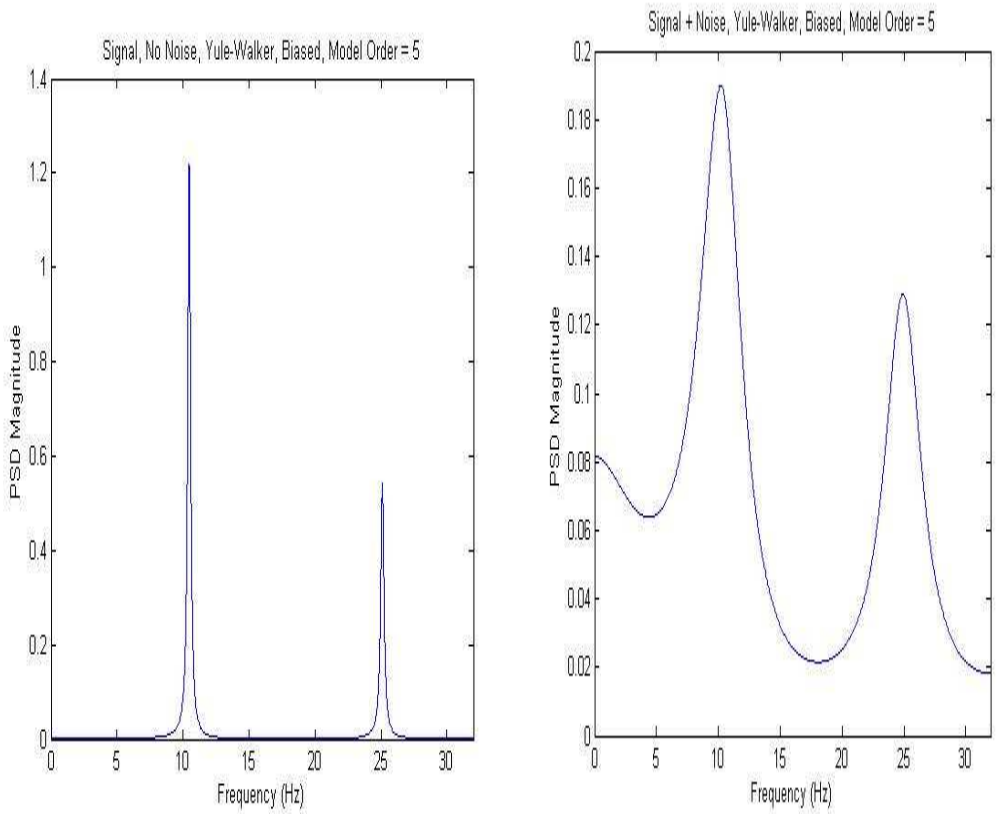

Figure 75. Yule-Walker, (Signal+No Noise, left plot, Signal+Noise, right plot) Biased ACF, Model Order = 5

Burg Test Factors, Factor Levels, and Response Variables

Three input sinusoids at the following frequencies: 10Hz, 11Hz, and 25Hz, with Factor having 3 levels: Model Order 5, 15, and 30. Factor: Model order is used in the following equation. The model order represents the 'p' summation range in the equation below.

$$\tilde{P}_{AR}(f) := \frac{T * var(w)}{|1 + \sum_{k=1}^{p} \tilde{a}_p(k) e^{-j2\pi kfT}|^2} \tag{148}$$

Unlike the Yule-Walker AR process, the value $\tilde{a}_p(k)$ for the Burg PSD estimator, is derived by utilizing a harmonic mean between the forward and backward partial correlation coefficients to calculate the reflection coefficient, $\widehat{K}_p$. Once these AR

parameters are calculated, the PSD estimate is calculated as described in the equation above.

$$\widehat{K}_p := \frac{-2\sum_{n=p+1}^{N} e_{p-1}^{f}[n]e_{p-1}^{b*}[n]}{\sum_{n=p+1}^{N} |e_{p-1}^{f}[n]|^2 + \sum_{n=p+1}^{N} |e_{p-1}^{b}[n]|^2} \tag{149}$$

At each order, P, the variance of the forward and backward linear error prediction is minimized. This calculated utilizing an arithmetic mean:

$$var(fb) := {}^{1}/_{2}\left[{}^{1}/_{N}\sum_{n=p+1}^{N} |e_p^f[n]|^2 + {}^{1}/_{N}\sum_{n=p+1}^{N} |e_p^b[n]|^2\right]$$
$$var(fb) := {}^{1}/_{2}\left[{}^{1}/_{N}\sum_{n=p+1}^{N} |e_p^f[n]|^2 + {}^{1}/_{N}\sum_{n=p+1}^{N} |e_p^b[n]|^2\right] \tag{150}$$

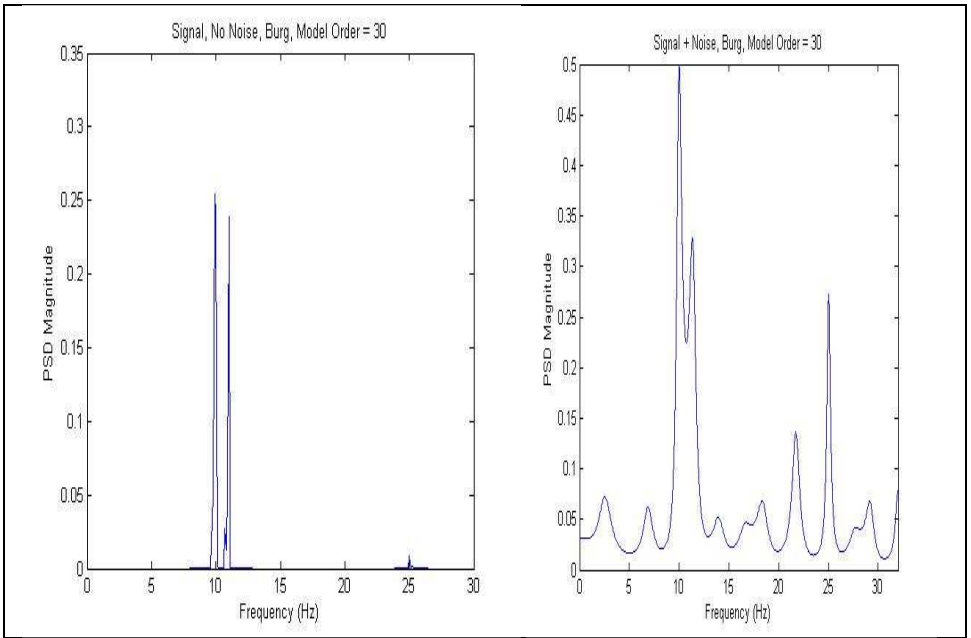

Figure 76. Burg PSD, (Signal+No Noise, left plot, Signal+Noise, right plot), Model Order = 30

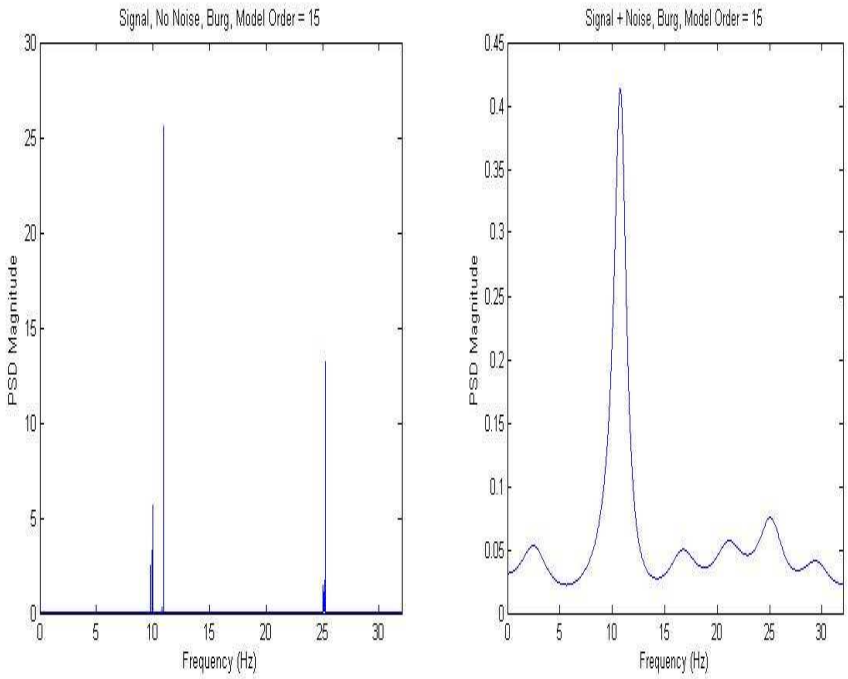

Figure 77. Burg PSD, (Signal+No Noise, left plot, Signal+Noise, right plot), Model Order = 15

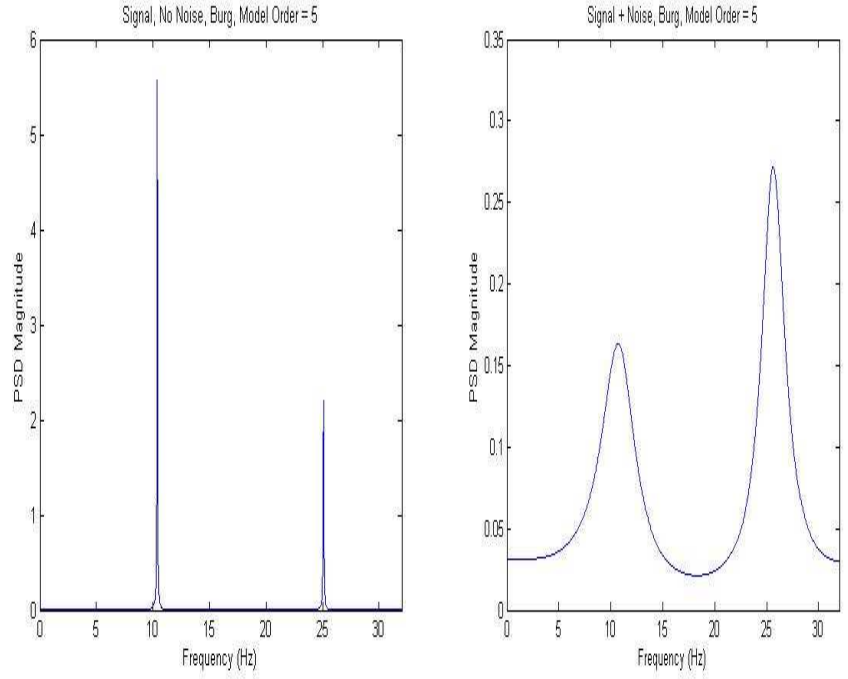

Figure 78. Burg PSD, (Signal+No Noise, left plot, Signal+Noise, right plot), Model Order = 5

Covariance Test Factors, Factor Levels, and Response Variables

Three input sinusoids at the following frequencies: 10Hz, 11Hz, and 25Hz, with Factor having 3 levels: Model Order 5, 15, and 30. Factor: Model order is used in the following equation. The model order represents the 'p' summation range in the equation below.

$$\tilde{P}_{AR}(f) := \frac{T * var(w)}{|1 + \sum_{k=1}^{p} \tilde{a}_p(k) e^{-j2\pi kfT}|^2} \tag{151}$$

Unique to the covariance PSD estimator, the following is used to compute the covariance matrix of a signal x of time series length N, with maximum lag M:

$$C_{ij} := \left(\frac{1}{N-M}\right) \sum_{k=1}^{N-M} x(k + \quad i)\, x(k + \quad j) \tag{152}$$

and individual elements of R_p:

$$r_p[i,j] := \sum_{k=p+1}^{N} x^*(k-i)x(k-j) + x(n-p+i)x^*(n-p+j) \tag{153}$$

This PSD algorithm minimizes the forward error prediction utilizing least squares to determine AR parameters, $\tilde{a}_p(k)$ in the equation above.

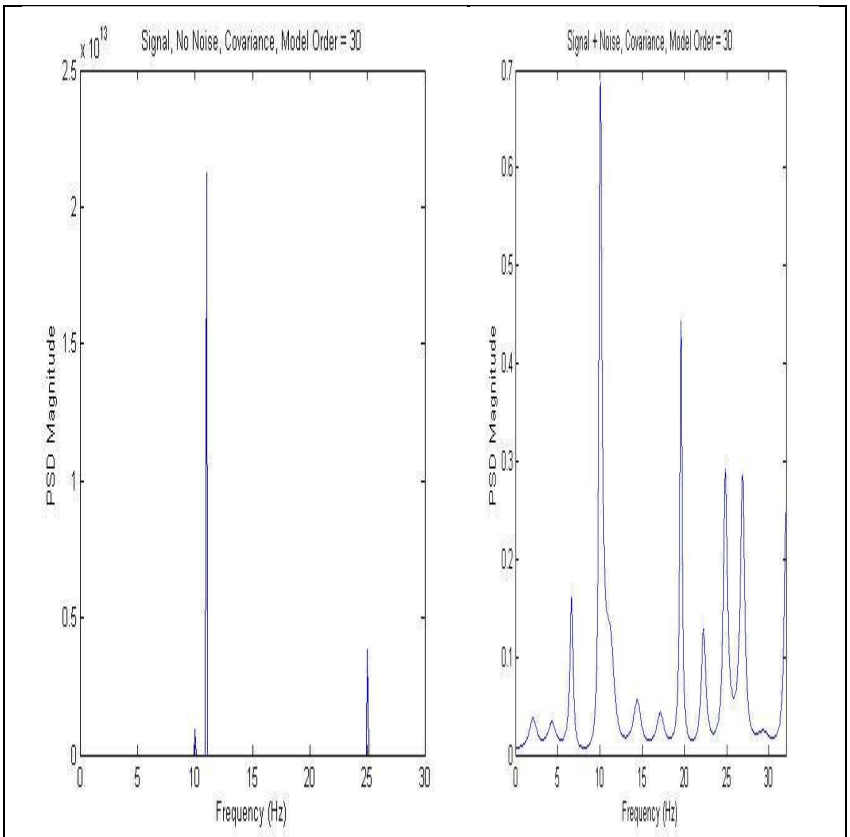

Figure 79. Covariance, (Signal+No Noise, left plot, Signal+Noise, right plot) Model Order = 30

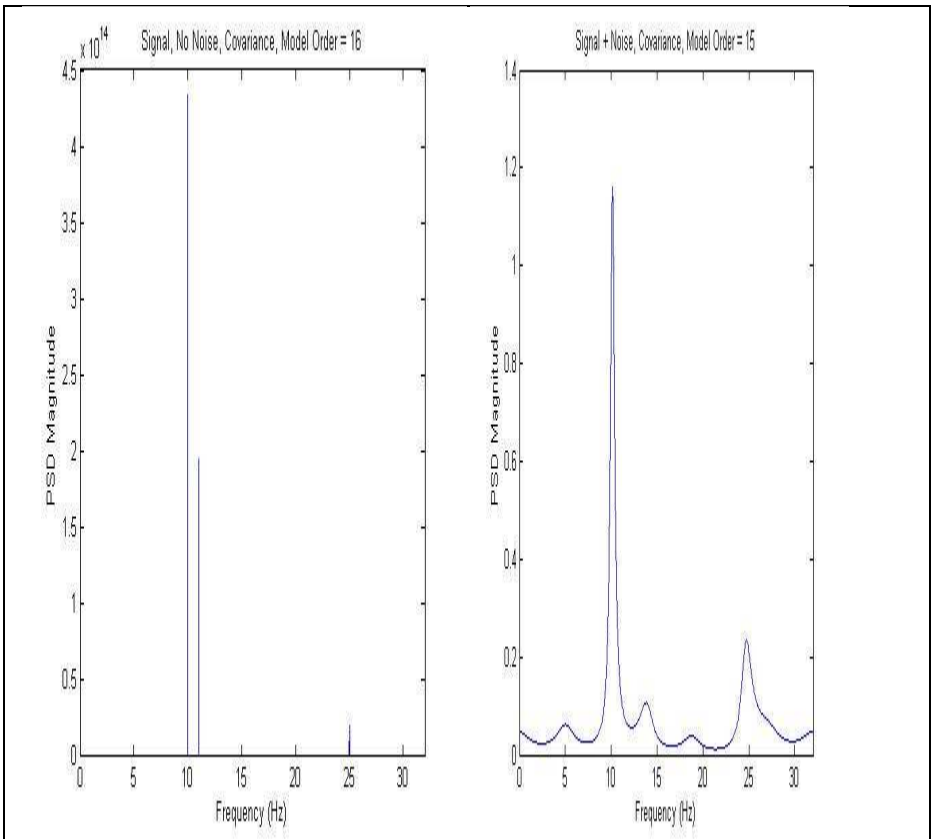

Figure 80. Covariance, (Signal+No Noise, left plot, Signal+Noise, right plot) Model Order = 15

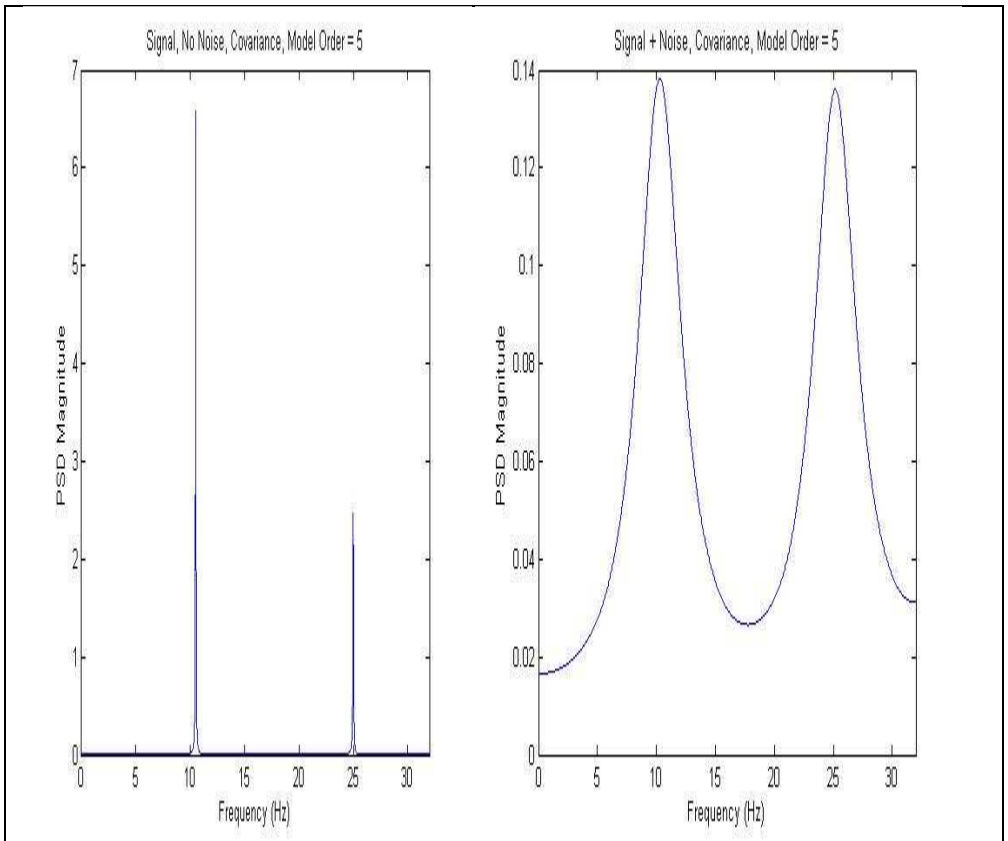

Figure 81. Covariance, (Signal+No Noise, left plot, Signal+Noise, right plot) Model Order = 5

Modified Covariance Test Factors, Factor Levels, and Response Variables

Three input sinusoids at the following frequencies: 10Hz, 11Hz, and 25Hz, with Factor having 3 levels: Model Order 5, 15, and 30. Factor: Model order is used in the following equation. The model order represents the 'p' summation range in the equation below.

$$\tilde{P}_{AR}(f) := \frac{T * var(w)}{|1 + \sum_{k=1}^{p} \tilde{a}_p(k) e^{-j2\pi kfT}|^2} \tag{154}$$

The following is how to compute the covariance matrix of a signal x of time series length N, with maximum lag M:

$$C_{ij} := \left(\frac{1}{N-M}\right) \sum_{k=1}^{N-M} x(k+i)\, x(k+j) \tag{155}$$

and individual elements of R_p:

$$r_p[i,j] := \sum_{k=p+1}^{N} x^*(k - \quad i)x(k-j) + x(n-p+i)x^*(n-p+j). \tag{156}$$

This PSD algorithm minimizes the both the forward error prediction and the backward error prediction utilizing least squares to determine AR parameters, $\tilde{a}_p(k)$ in the above equation.

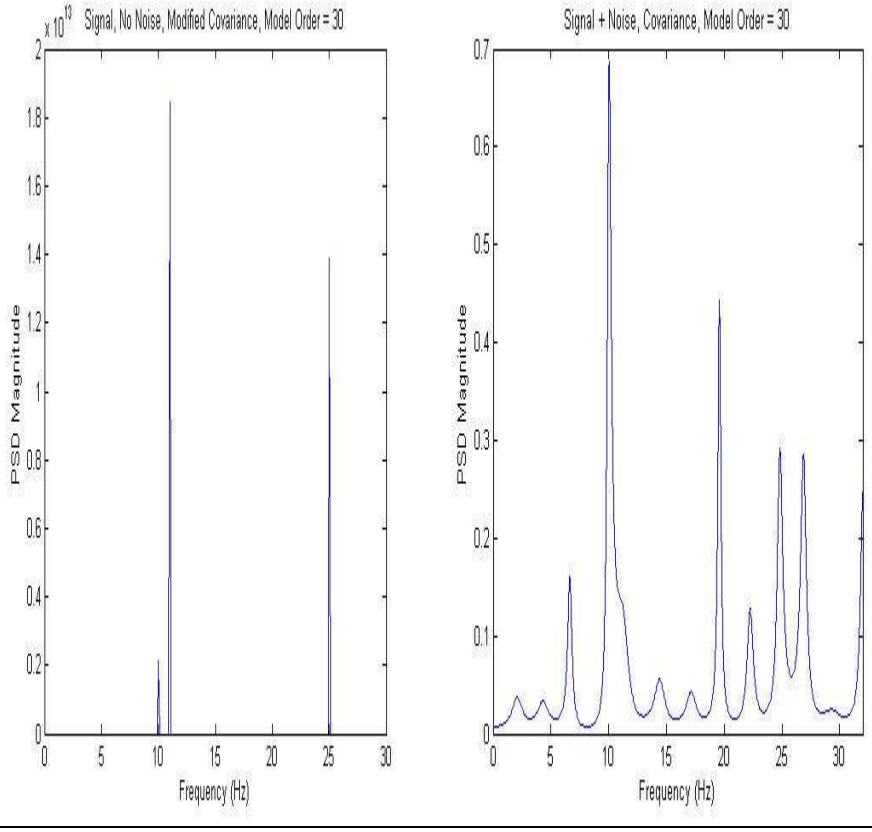

Figure 82. Modified Covariance, (Signal+No Noise, left plot, Signal+Noise, right plot), Model Order = 30

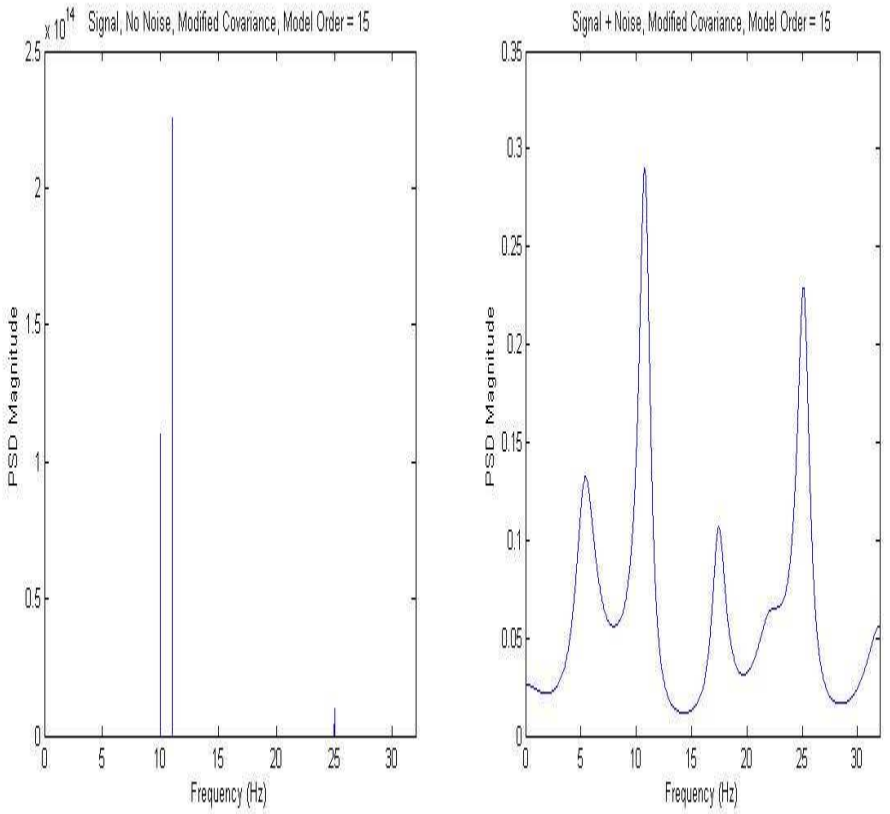

Figure 83. Modified Covariance, (Signal+No Noise, left plot, Signal+Noise, right plot), Model Order = 15

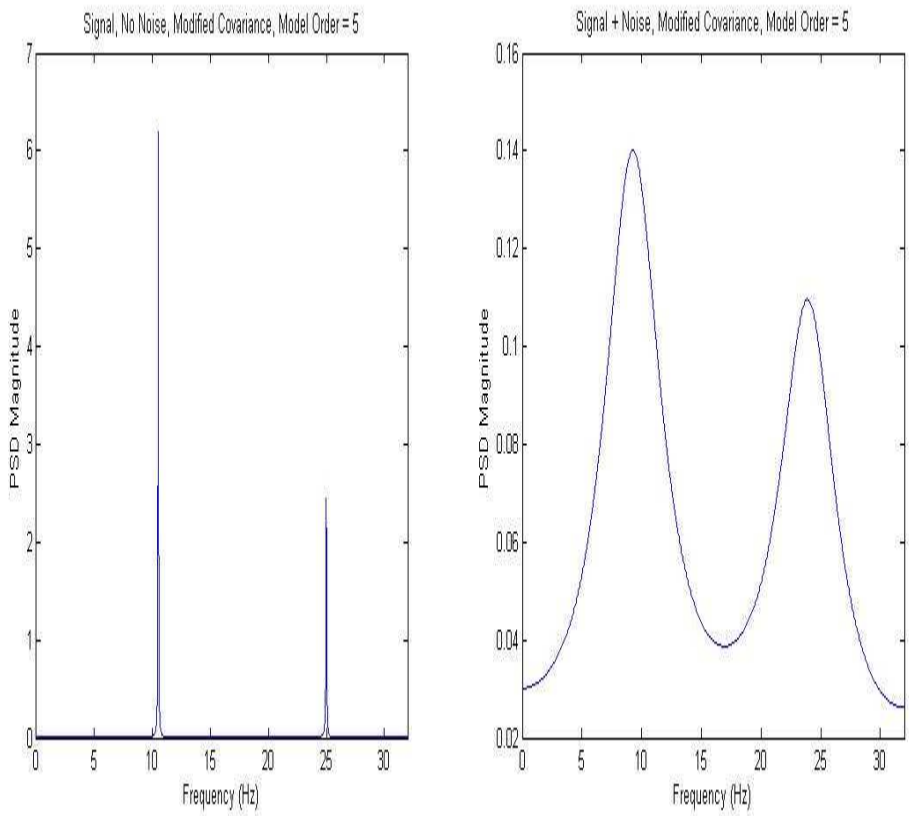

Figure 84. Modified Covariance, (Signal+No Noise, left plot, Signal+Noise, right plot), Model Order = 5

Music Test Factors, Factor Levels, and Response Variables

Three input sinusoids at the following frequencies: 10Hz, 11Hz, and 25Hz, with Factor having 3 levels: Model Order 5, 15, and 30. Factor: Model order is used in the following equation. The model order represents the 'p' summation range in the equation below. The 'pseudo' (not true PSD) MUSIC spectrum estimate is derived from the following equation:

$$P_{MUSIC}(f) := \frac{1}{\bar{e}^H(f)(\sum_{k=M+1}^{P+1} \bar{v}_k \bar{v}_k^H)\bar{e}(f)} \tag{157}$$

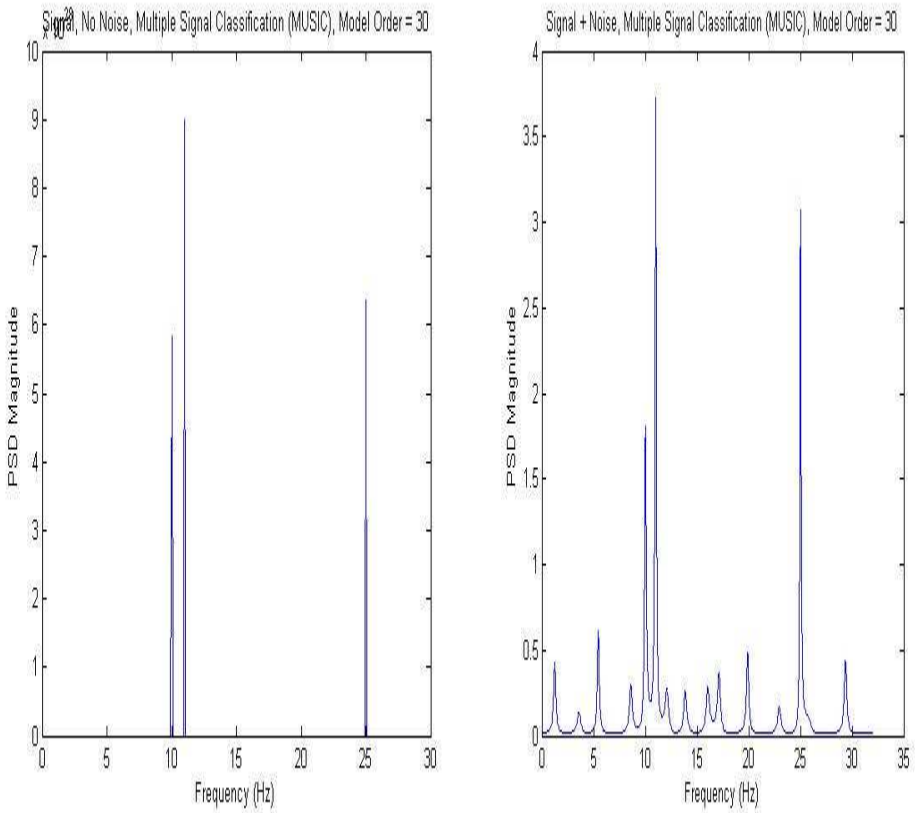

Figure 85. MUSIC PSD, (Signal+No Noise, left plot, Signal+Noise, right plot) Model Order = 30

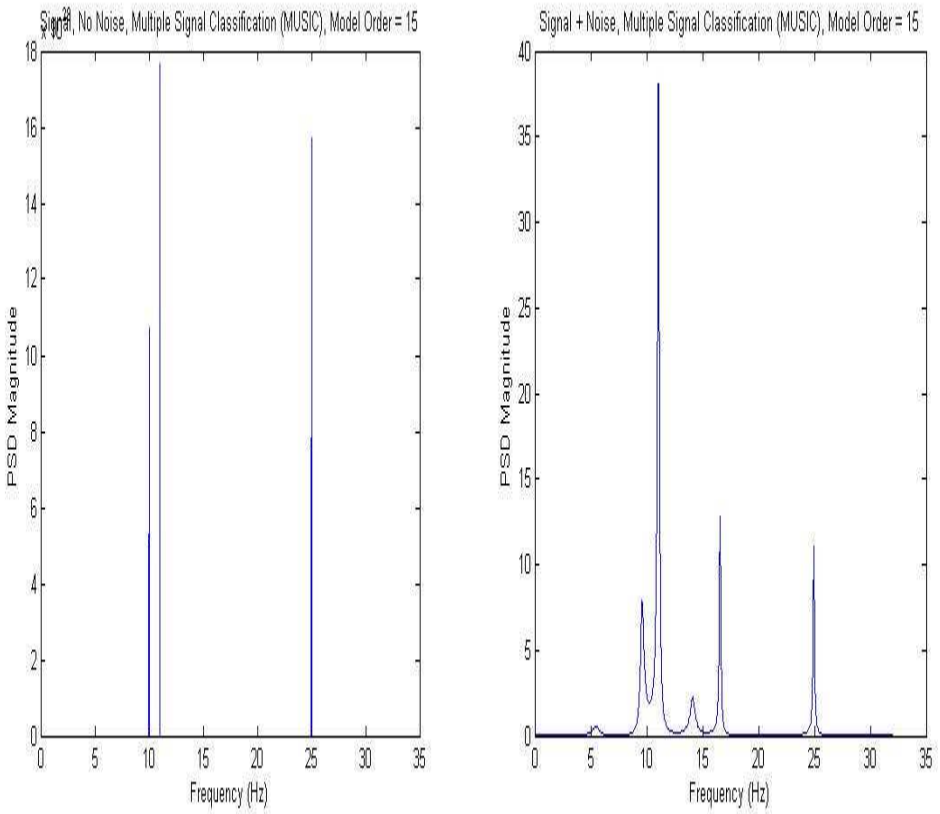

Figure 86. MUSIC PSD, (Signal+No Noise, left plot, Signal+Noise, right plot), Model Order = 15

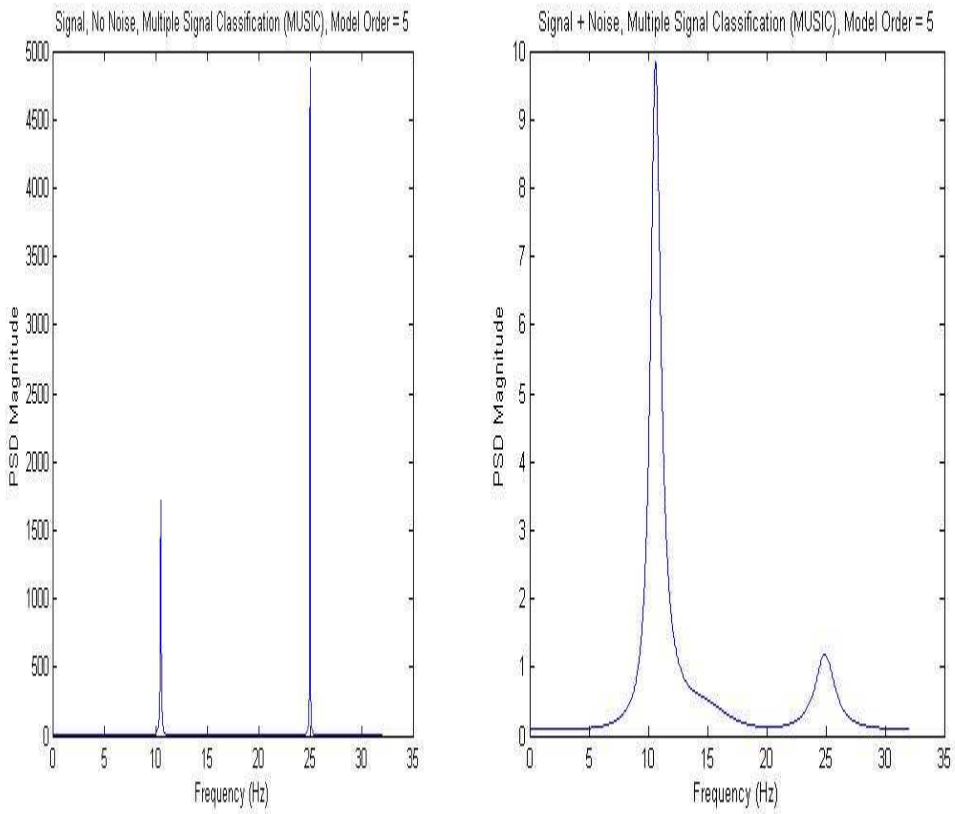

Figure 87. MUSIC PSD, (Signal+No Noise, left plot, Signal+Noise, right plot), Model Order = 5

JMP Results

I model three input signals described above using MATLAB. Each signal was mixed with White Gaussian Noise (WGN) with zero mean. I utilized the following estimation methods as my algorithms in this experiment: Blackman-Tukey correlogram, Welch Periodogram, Yule-Walker, Burg, Covariance, Modified Covariance, and Multiple Signal Classification (MUSIC). I then measured the accuracy of the estimation method using a low, medium, and high resolution factor (pertinent to each algorithm). The goal of this test is determine which estimation algorithm is most accurate given similar resolution factors. The way this is measured is to determine if, when I input three signals mixed with random noise (two signals very close in frequency), that I can accurately estimate the frequency of all three signals on the output. I ran 10 runs with each algorithm using a random estimation model with a low, medium, and resolution factor for each algorithm.

JMP Output Data

The following output data was produced by JMP. I performed several tests to determine if there was any interaction between the main effects: Algorithm and Resolution, as well as, test the variances of each algorithm. I executed a one-way ANOVA, a two-way ANOVA, several means tests, and finally the conclusion drawn from the two-way ANOVA test output.

Algorithm \ Runs	Resolution	1	2	3	4	5	6	7	8	9	10	Mean (u)
Blackman Tukey	High	100	66.67	100	100	66.67	100	100	100	66.7	66.7	86.668
Welch	High	66.67	66.67	33.33	66.67	33.33	66.7	66.7	66.67	66.7	100	63.335
Yule Walker	High	66.67	100	100	100	33.33	100	100	66.67	66.7	66.7	80.001
Burg	High	66.67	66.67	66.67	66.67	66.67	66.7	66.7	33.33	66.7	66.7	63.336
Covariance	High	66.67	100	66.67	33.33	66.67	33.3	100	33.33	66.7	66.7	63.334
Modified Covariance	High	66.67	33.33	33.33	100	100	66.7	33.3	100	100	100	73.333
MUSIC	High	100	33.33	100	100	66.67	66.7	66.7	100	100	66.7	80.001
Blackman Tukey	Medium	66.67	66.67	66.67	66.67	66.67	33.3	66.7	66.67	66.7	66.7	63.336
Welch	Medium	66.67	66.67	33.33	33.33	33.33	66.7	66.7	66.67	66.7	66.7	56.668
Yule Walker	Medium	66.67	66.67	66.67	66.67	66.67	66.7	66.7	33.33	66.7	66.7	63.336
Burg	Medium	66.67	66.67	66.67	66.67	33.33	66.7	66.7	66.67	66.7	66.7	63.336
Covariance	Medium	66.67	66.67	66.67	33.33	66.67	33.3	66.7	66.67	66.7	66.7	60.002
Modified Covariance	Medium	33.33	33.33	66.67	66.67	66.67	66.7	66.7	66.67	66.7	66.7	60.002
MUSIC	Medium	100	33.33	66.67	66.67	33.33	100	66.7	66.67	66.7	100	70.001
Blackman Tukey	Low	66.67	66.67	66.67	66.67	66.67	66.7	33.3	66.67	66.7	66.7	63.336
Welch	Low	66.67	66.67	33.33	33.33	33.33	66.7	66.7	66.67	66.7	66.7	56.668
Yule Walker	Low	66.67	66.67	66.67	66.67	66.67	66.7	66.7	66.67	66.7	66.7	66.67
Burg	Low	66.67	66.67	66.67	66.67	33.33	66.7	66.7	66.67	66.7	66.7	63.336
Covariance	Low	66.67	66.67	66.67	33.33	66.67	66.7	33.3	66.67	66.7	66.7	60.002
Modified Covariance	Low	33.33	0	66.67	66.67	66.67	66.7	66.7	66.67	66.7	33.3	53.335
MUSIC	Low	33.33	66.67	33.33	66.67	33.33	66.7	66.7	66.67	33.3	33.3	50

Figure 88. Output Results (Response) Table

The output response data table above is coded in the following way:

Table 10
Output Response Results (ANOVA)

1	All three signals correctly estimated	100
2	Only two signals correctly estimated	66.67
3	Only one signal correctly estimated	33.33

Each algorithm is listed with its resolution factor level of Low, Medium, or High. We expect to see the best results for each algorithm using the high resolution factor level.

JMP ANOVA (One-Way)

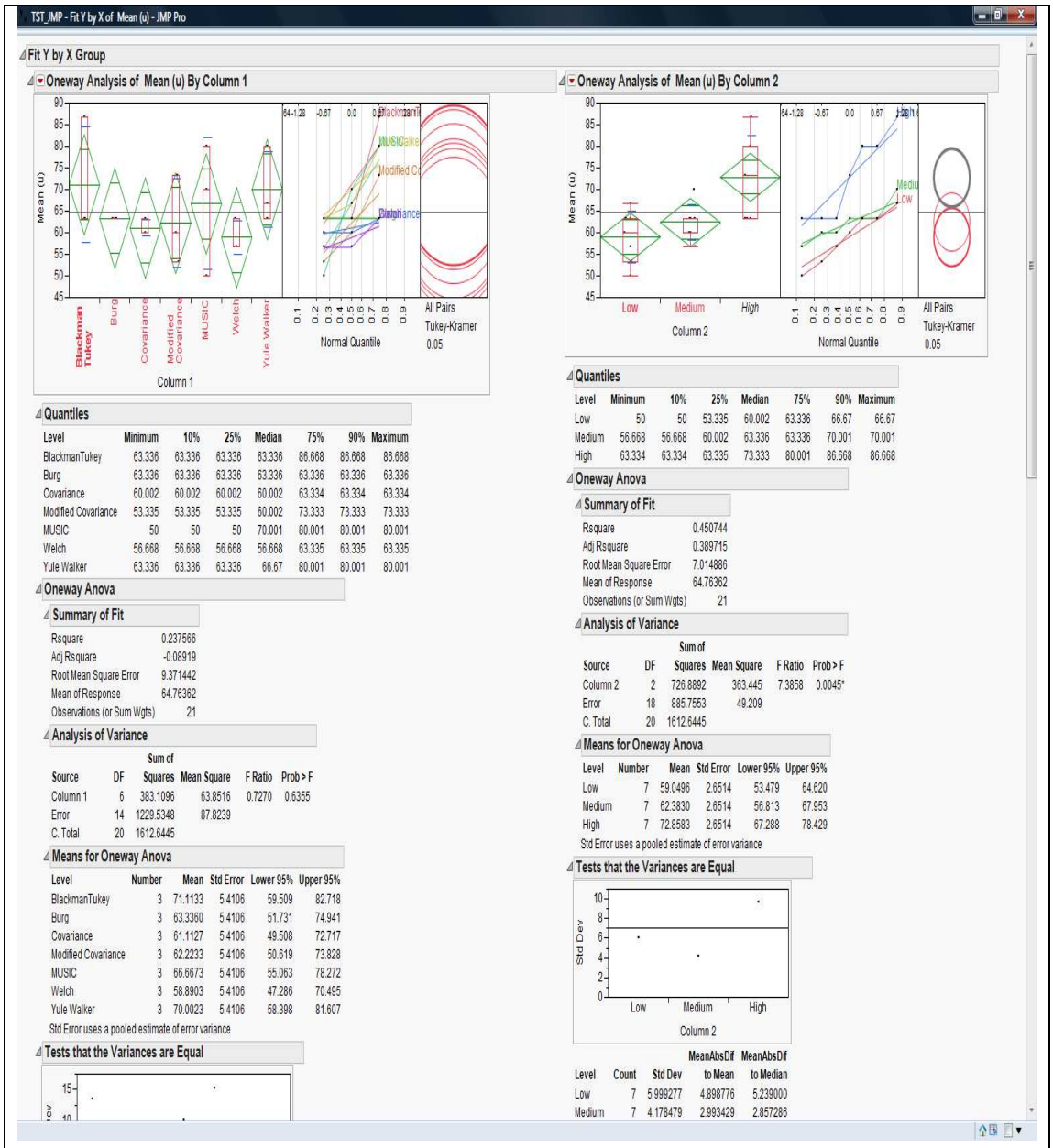

Figure 89. ANOVA analysis of output results (Plot 1: (L) Algorithm vs Mean & Plot 2: (R) Resolution vs Mean)

Response variable = mean output. I compared the mean output to both the algorithm and the resolution of the algorithm model. I should see parallel quantile plots data versus normal distribution. The tilt of each plot line indicates different standard deviations. Also, the distance between the plot lines indicates differences in variances. I do note the variances are different for each algorithm. Additionally, it is clear that the Burg algorithm has the smallest variance. The different quantile box sizes strongly indicate different variances.

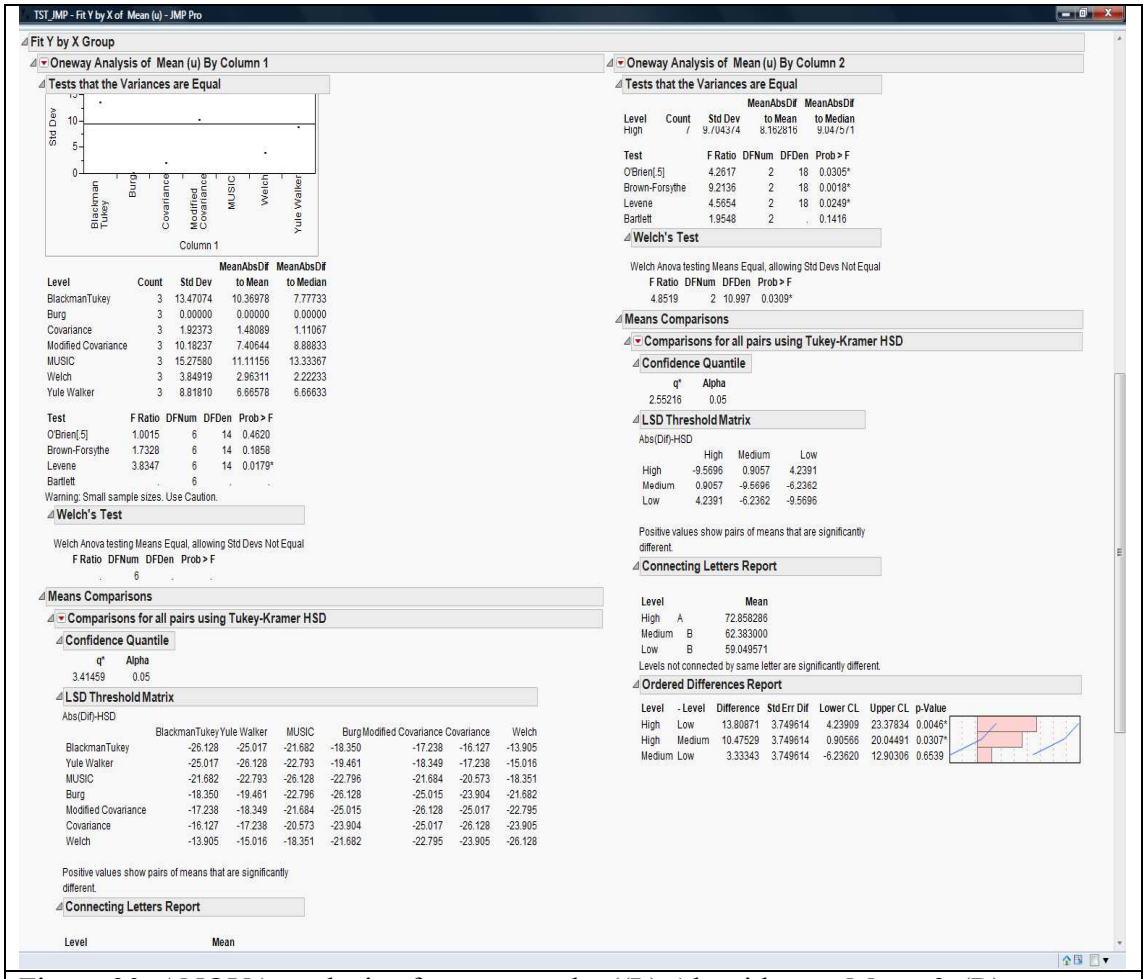

Figure 90. ANOVA analysis of output results ((L) Algorithm vs Mean & (R) Resolution vs Mean)

Differences in variances are confirmed by the difference of variance test whose output is displayed above.

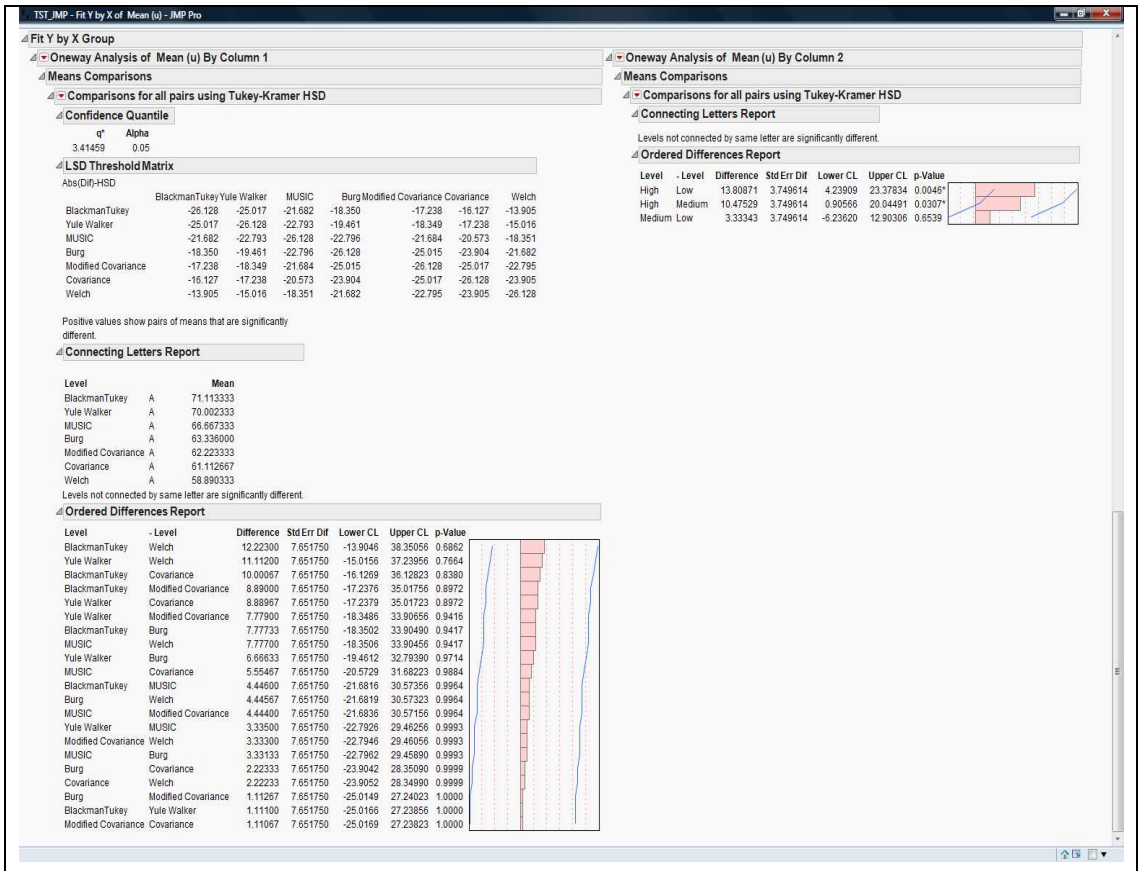

Figure 91. ANOVA analysis of output results ((L) Algorithm vs Mean & (R) Resolution vs Mean) - Continued

The various differences in means are displayed above in the table. Note that the variance for High resolution is quite different from both the low and medium resolution models.

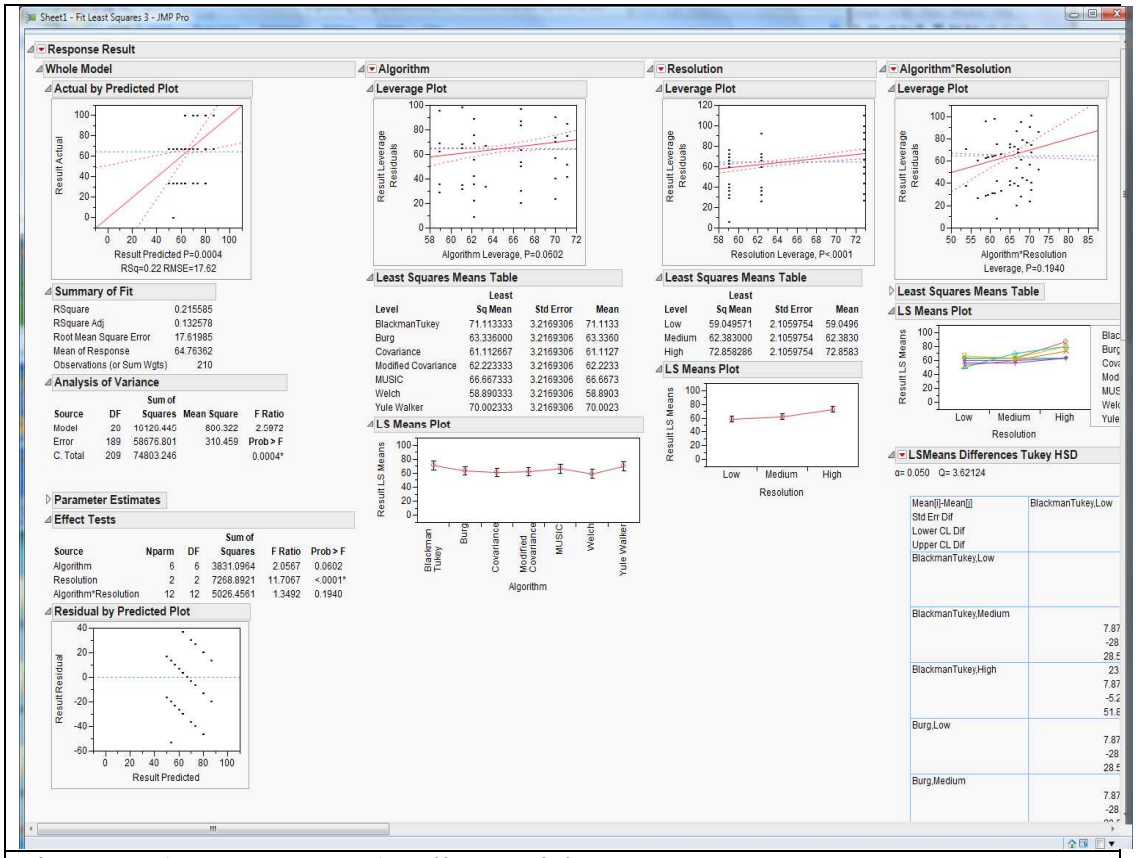

Figure 92. (2-Way ANOVA) Full Factorial

The purpose of this test is to determine any interactions of the main effects. The Main effects: Algorithm and Resolution with their interaction (Algorithm and Resolution). The Least Squares Means plots [in the lower portion of the figure above] indicate that resolution factor (P-Value) is a significant factor. At first glance it would seem there is a significant interaction effect present -plot in lower portion of the 2-Way ANOVA display; however, after review of the Effect Tests, it is clear that the P-Value is only significant for the Resolution factor. There doesn't appear to be a strong interaction effect between factors Algorithm and Resolution.

JMP Results/Conclusion

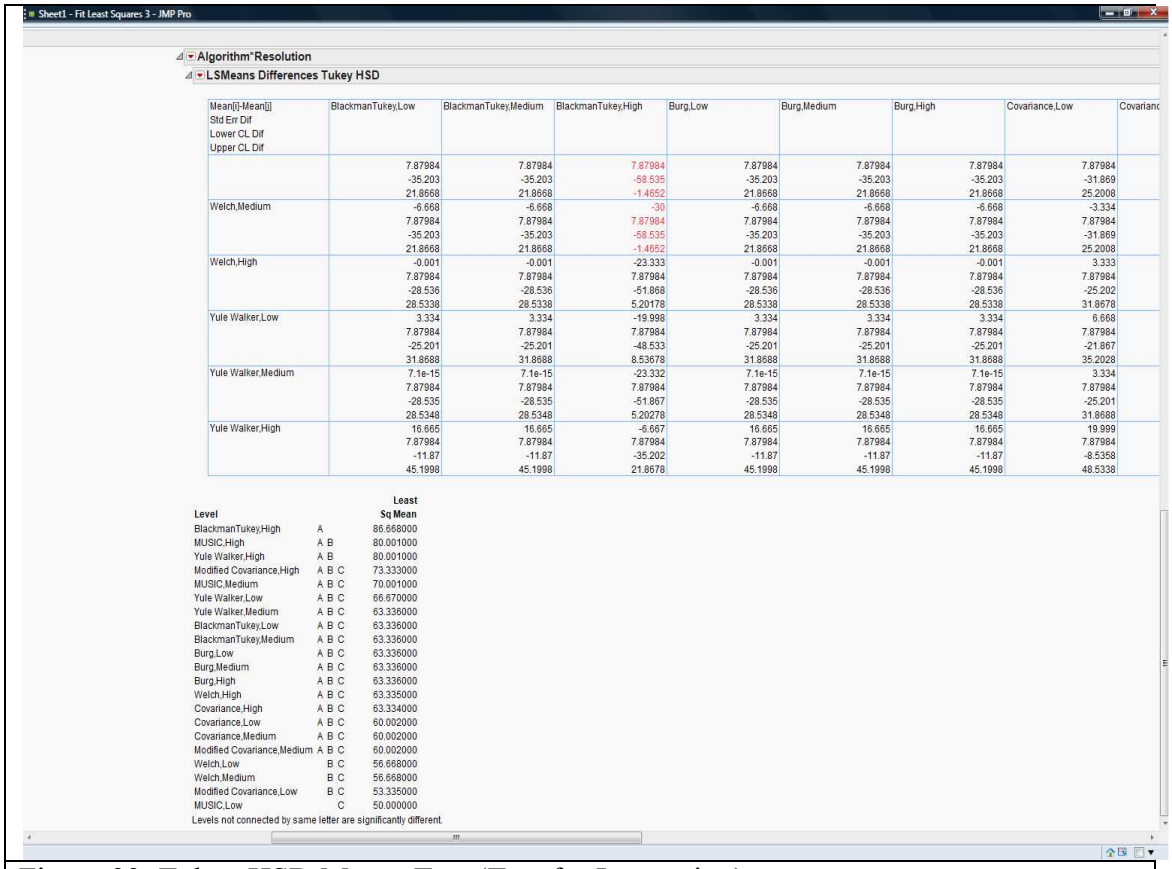

Mean[i]-Mean[j] Std Err Dif Lower CL Dif Upper CL Dif	BlackmanTukey,Low	BlackmanTukey,Medium	BlackmanTukey,High	Burg,Low	Burg,Medium	Burg,High	Covariance,Low	Covarianc
	7.87984 -35.203 21.8668	7.87984 -35.203 21.8668	7.87984 -58.535 -1.4652	7.87984 -35.203 21.8668	7.87984 -35.203 21.8668	7.87984 -35.203 21.8668	7.87984 -31.869 25.2008	
Welch,Medium	-6.668 7.87984 -35.203 21.8668	-6.668 7.87984 -35.203 21.8668	-30 7.87984 -58.535 -1.4652	-6.668 7.87984 -35.203 21.8668	-6.668 7.87984 -35.203 21.8668	-6.668 7.87984 -35.203 21.8668	-3.334 7.87984 -31.869 25.2008	
Welch,High	-0.001 7.87984 -28.536 28.5338	-0.001 7.87984 -28.536 28.5338	-23.333 7.87984 -51.868 5.20178	-0.001 7.87984 -28.536 28.5338	-0.001 7.87984 -28.536 28.5338	-0.001 7.87984 -28.536 28.5338	3.333 7.87984 -25.202 31.8678	
Yule Walker,Low	3.334 7.87984 -25.201 31.8688	3.334 7.87984 -25.201 31.8688	-19.998 7.87984 -48.533 8.53678	3.334 7.87984 -25.201 31.8688	3.334 7.87984 -25.201 31.8688	3.334 7.87984 -25.201 31.8688	6.668 7.87984 -21.867 35.2028	
Yule Walker,Medium	7.1e-15 7.87984 -28.535 28.5348	7.1e-15 7.87984 -28.535 28.5348	-23.332 7.87984 -51.867 5.20278	7.1e-15 7.87984 -28.535 28.5348	7.1e-15 7.87984 -28.535 28.5348	7.1e-15 7.87984 -28.535 28.5348	3.334 7.87984 -25.201 31.8688	
Yule Walker,High	16.665 7.87984 -11.87 45.1998	16.665 7.87984 -11.87 45.1998	-6.667 7.87984 -35.202 21.8678	16.665 7.87984 -11.87 45.1998	16.665 7.87984 -11.87 45.1998	16.665 7.87984 -11.87 45.1998	19.999 7.87984 -8.5358 48.5338	

Level		Least Sq Mean
BlackmanTukey,High	A	86.668000
MUSIC,High	A B	80.001000
Yule Walker,High	A B	80.001000
Modified Covariance,High	A B C	73.333000
MUSIC,Medium	A B C	70.001000
Yule Walker,Low	A B C	66.670000
Yule Walker,Medium	A B C	63.336000
BlackmanTukey,Low	A B C	63.336000
BlackmanTukey,Medium	A B C	63.336000
Burg,Low	A B C	63.336000
Burg,Medium	A B C	63.336000
Burg,High	A B C	63.336000
Welch,High	A B C	63.335000
Covariance,High	A B C	63.334000
Covariance,Low	A B C	60.002000
Covariance,Medium	A B C	60.002000
Modified Covariance,Medium	A B C	60.002000
Welch,Low	B C	56.668000
Welch,Medium	B C	56.668000
Modified Covariance,Low	B C	53.335000
MUSIC,Low	C	50.000000

Levels not connected by same letter are significantly different.

Figure 93. Tukey HSD Means Test (Test for Interaction)

This indicates no strong interaction between Resolution and Algorithm. However, it does suggest the major differences between the Algorithm and Resolution combinations. It indicates that the Blackman Tukey algorithm model and the MUSIC algorithm model when operated utilizing high resolution parameters provide the highest overall mean and therefore the most accurate result of the algorithms tested.

In fact, the estimation accuracy of the algorithms is accurately described above. We can therefore conclude that the best methods to estimate and calculate the PSD for wireless signals are the top two algorithms: the Blackman Tukey using its high resolution factor

and the Yule Walker algorithm using its high resolution factor. Music using its high resolution factor cannot be considered for wireless PSD estimation since the algorithm loses the spectral power components of the signal; it is strictly to be used for estimating frequency components, but not spectral power components. Note that some of the algorithms perform better using their lower resolution factors than other algorithms that are using their highest resolution factors.

CHAPTER 6

SYSTEM DESIGN

The hardware component types of the system design are the 802.11X and cellular base stations and the cell controller. The base stations are comprised of a System on Chip (SoC) that is comprised of symmetric multiprocessing General Purpose Processors (GPP), a number of Digital Signal Processors (DSP), and a number of RF receive and transmit chains. Both the transmitter and receiver will have an antenna. The receiver may have a (e.g. Low Noise Amplifier) a matched filter on the front end as well as an Analog to Digital Converter (ADC), the transmitter will have a Digital to Analog Converter (DAC) and may have a LNA along with an impedance matching circuit to ensure VSWR is not produced. The focus on the design of the base station is to ensure the design allows for a continual evolution in regard to the physical modulation techniques. The design needs to be capable of adapting to changes in the modulation techniques. The design also must ensure that the receive sensitivity is sufficient to receive the minimum desired signal. The receive sensitivity can be defined as the minimum desired signal power above the noise floor of the receiver as defined by the following equation:

$$Pwr_{min} = NoiseFloor_{rcvr} + SNR_{desired} \tag{158}$$

System-On-Chip (SoC) designs now include GPP and a number of DSPs are typical. Often these designs do include an FPGA, however, some implementations are now focusing on DSP arrays such as those provided by Picochip (now Mindspeed) and Coherent Logix (HyperX). In these cases, small FPGAs are used for I/O multiplexing

only while all DSP functions are performed in software on DSP arrays (27nm technology) fully integrated with DSP tools such as MATLAB and SIMULINK.
The cell controller is comprised of specialized hardware that is designed to perform high performance network frame processing and will be designed to handle > 40Gbs encrypted link layer network traffic. In order for the cell controller to handle encrypted network traffic at this rate, it must have a hardware based data path. The hardware data path requires the following functions:

Classification of network frames. This is required so that frames with encrypted traffic can be characterized based upon the source MAC address of the mobile device that transmitted the frame as well as any relevant network headers such as VLAN tags. Once classification is performed, the address of the received frame must be distributed to a cryptography engine for decryption as well as pre and post processing engines. The following packet walkthrough is an example of an architecture where majority of frame processing is off-loaded from GPP and GPU cores within a SoC.

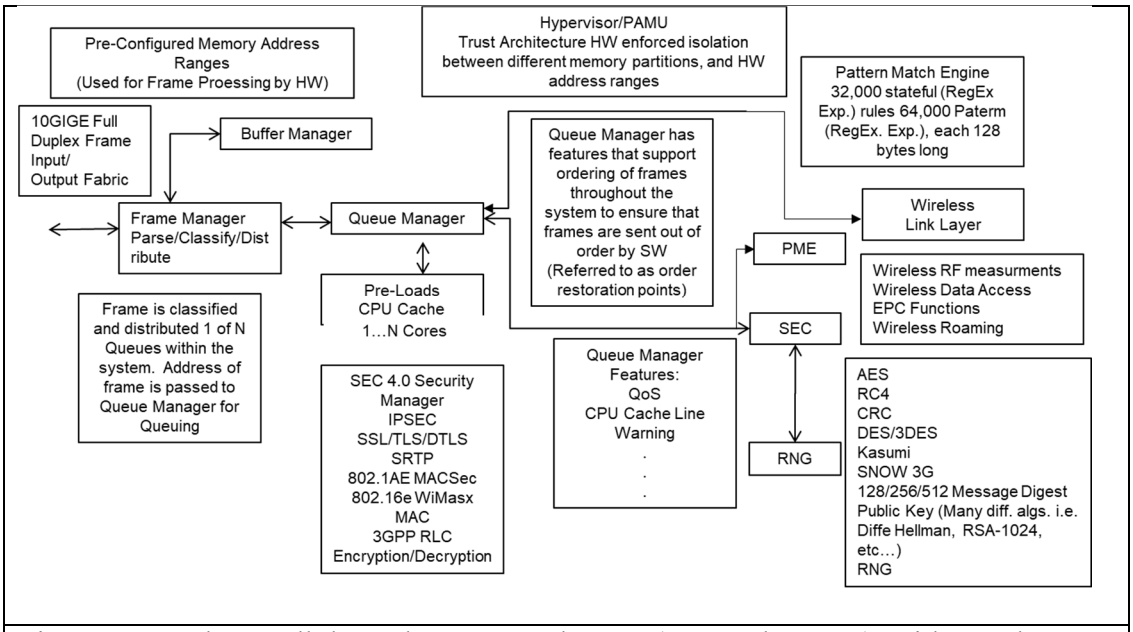

Figure 94. Packet Walkthrough on Example SoC,(Freescale, 2014) With Newly Proposed/Designed Wireless Link Layer Capability

The HW state machine described above require their own Direct Memory Address (DMA) engines to read and write data to and from memory as required during frame processing through a memory gasket and memory controller. Such a configuration would require a GPP to provide configuration and management of the HW during its configuration and boot cycles [this is sometimes referred to as the control plane]. In addition, it would require a slow speed peripheral memory bus so that configuration registers on the HW could be modified during configuration. A GPP would also be required to handle exceptional conditions that occur during frame processing such as error frames and could be helpful in handling conditions that were not perceived during HW design.

Since both configurations require frame processing, additional aspects of the design need to be considered. What is the queue latency of frame processing? For instance, must frame be processed strictly in the order they are received or can some frames be processed in parallel. For performance reasons, if multiple channels are required, frames should be allowed to be multiplexed to different dedicated HW blocks at the same time. However, this implies that the adaptive properties of each channel must be maintained by all dedicated HW IP blocks. These properties would have to be stored in memory and then retrieved from memory as different blocks receive frames that require different adaptive properties. Therefore, a cache is required to ensure unnecessary memory fetches were not required by the DMA engine prior to processing a frame. In order to determine which adaptive properties are required to be loaded by the HW block requires classification of network and wireless frames as they are received. Additional dedicated HW is required to handle frame classification and queuing logic. These HW state machines would communicate to each other via private, HW dedicated buses between the frame processor, the queue processor, and the link layer encryption HW IP blocks. The GPP core(s) would provide the ability to configure the HW registers in each of these blocks via a peripheral memory bus. The peripheral memory bus would also be used for monitoring, dynamic reconfiguration, error conditions, and management (thru a network interface). In this approach, memory transactions are limited to the frame processor and link layer encryption blocks. HW blocks utilize a private bus for communication and the GPP only accesses memory a very small percentage of time mostly for monitoring and management functions. Additional provisions can be provided that force received frames to be stored on memory aligned pages thereby reducing non-aligned memory transactions

to a very small percentage of overall memory transactions. HW would generate memory transactions to access adaptive properties stored on a per channel basis.

A key component of the HW data path is the wireless MAC engine. This programmable engine bridges wireless frames to the wired interface, decrypts/encrypts wireless link layer data & management frames, performs RF measurements of mobile devices, implements wireless roaming between base stations, provides network proxy ARP (if required) for mobile devices, provides per device instruction execution, and monitors the state of the mobile device at all times. As depicted in Figure 57, the wireless MAC engine uses information such as instructions, VLAN tag info, 802.11 or cellular MAC template (used to modify frames to and from the mobile device), and reserved memory that is used by the engine in real-time to modify and/or bridge wireless frames.

Hardware Design And Verification

The most important step in hardware design is to ensure the requirements are well defined and understood. In particular functions that implement features such as the wireless link layer MAC subsystem I described earlier in this paper must be implemented with a thorough knowledge of the protocols so the proper functional decomposition can be accomplished between software and hardware. In particular, standards in the wireless area are changing all the time; the portions of the system that have a high degree of volatility should be implemented in software. However, after many years the data path for these technologies continues to converge toward IP based protocol services. The LTE EPC now is moving all traffic (even voice) to IP based data frames. This commonality

aids in the development of hardware to support the data path. This ensures that even the latest technology can benefit from the development of this type of hardware technology.

However, even functions that are implemented in software still require hardware support. Often this aspect is overlooked during the system design phase. For instance, how does software interact with the hardware to redirect its data path to a new base station? As discussed earlier, this requires a hardware synchronized ability to perform an atomic operation while the data path is still active. Interruption of the data path would cause delay in frame transmissions to a device and reduce its perceived performance. In this case hardware must enable the ability to be updated on a per user basis without mobile devices losing their connectivity and network access. In order to implement this new hardware feature, a systematic review of all 802.11 and cellular specifications would be required to determine what features requirements would be required to achieve the end goal of having all data and voice packets from wireless technology to be handled fully in hardware (e.g. data path acceleration architecture).

Once the requirements have been completed and fully understood, the hardware interface requirements with other subsystems within the SoC must be evaluated to determine if they will impede the wireless subsystem from achieving its functional or performance requirements. All electrical interfaces have to be evaluated to ensure that they meet the performance bench marks and that there is sufficient electrical interface support for system level interfaces required from other subsystems.

During Verilog development there should be well defined interfaces between the functional hardware blocks. This is important at the very beginning because too often functions are duplicated or require too many additional wires of communication between the blocks which increases the die size, increases complexity, and increase the likelihood of failure particularly when implementing large designs. Implementation of combinatorial logic blocks should be consistent throughout the design to reduce complexity as an example when many personnel work on the same project. Once sufficient subsystems have been implemented, software should be written to interact with the test hardware simulation interfaces as early and often as possible so that problems can be spotted as early as possible. Figure 95 depicts such an environment where Linux executes on a simulation of the processor instruction set and the software drivers are written within this environment to interact directly with the Verilog co-simulation environment through the use of SystemC adapters. The SystemC co-simulation adapters are provided by companies such as Virtutech (processor/system simulator and SystemC adapter) and Cadence tools (Verilog/SystemC adapters and simulator). Software engineers can implement software and test against the actual hardware during the hardware development cycle prior to hardware synthesis. In addition, randomized hardware simulations should run continuously (with hardware simulation probes) to catch timing problems and error signals that are caught during execution. When a random simulation fails, it is important to reproduce the failure; the hardware test co-simulation software should record parametric configuration information captured before each test. In only this way will test be reproduced and problems resolved efficiently.

Once all electrical interfaces have been defined, then these interfaces and their descriptions and definitions go into a requirements verification test matrix (RVTM), unit level test benches are created that imitate the electrical interfaces from other subsystems as well as connect all electrical interfaces to hardware signal sources. This enables the unit level tests to randomize patterns and clock edges across these electrical interfaces so that problems can be identified early and often. These tests then would feed into a larger collection of tests that are executed by system level test execution.

Hardware Simulation And Verification

In order to design the hardware and verify the function of a hardware subsystem, a hardware co-simulation environment is required. This foundation for this environment is comprised of Verilog simulation using tools such as those developed by Cadence. Layered above this foundation are the Verilog hardware finite state machines that must be tested. In addition, software libraries built with the SystemC library are also used to drive bus functional models to test the hardware. The Cadence co-simulation library provides SystemC adapters for their simulation environment that allow a SystemC model to connect digital logic to hardware connector names. Typically this is done through what is referred to as a "bus functional model". Such a model supports the ability to test individual hardware subsystems. Hardware subsystems interact with each other through the use of logic signals and buses. Assuming no transitional change of clock domains, all hardware subsystems are clocked with the same clock source; however, there are clock delays through different components used in a Verilog model such as combinatorial and sequential logic. Testing of individual subsystems entail the use of randomization of

clock signals and data bits across all data buses and should include the variance of the clock signals within the specified operational range. As with all logic signals, these signals will vary temporarily (within a range) as a function of temperature and variances in the silicon and randomization of the skew of the clock signal is crucial to identify problems before synthesis. Building upon these subsystem tests, the subsystems are then connected together. New Bus Functional Models (BFM) are built that represent the new or combination of the new digital interfaces. As the tests include more and more logic blocks that must be simulated, the hardware test (SystemC) library needs to ensure that it is built as optimally as possible. The model must reduce unnecessary events (such as per pin events on a clock edge as an example), but be based upon a concept referred to as Transaction Level Modeling (TLM). This approach focuses on functional block events instead of events produced on each individual clock edge. When developing BFMs to connect to subsystems under test, it is important to base the event structure on TLM concepts. This approach still provides a very accurate digital signal timing display while the model runs at a very high rate of speed. As shown Figure 95, hardware models of IP within a SoC can be in a near cycle accurate way, with very acceptable performance, using the TLM based transaction model approach. In this example (Figure 95), a Linux operating system is executing on a simulation of the Power Architecture instruction set while executing a Linux kernel module that actually runs against the real hardware simulation using a shared (shared between the processor simulation) and the SystemC adapter that drives the logic pins on the Verilog model. The Verilog model actually executed and reacted as if it were already synthesized as part of the SoC. This testing would ensure that the Wireless Link Layer Subsystem hardware IP will execute as

expected in real platform environments and ensure early testing of software can occur prior to tape-out of hardware.

Hardware tests are executed at the intended simulated clock speed of the hardware and are executed using a simulated clock signal at the programmed clock speed. An example of tests that are executed include the ability to skew the input and output digital signals in a random way to ensure the finite state machines are robust enough to handle differences found in silicon after SoC synthesis has occurred. Other tests include functionality tests to ensure that functions within the hardware Intellectual Property (IP) works as intended. Other tests include the random ordering of memory transactions to and from the hardware IP as well as negative testing. This simulation test software executes quickly because a very lightweight threading model is used to drive the hardware state machines. All hardware state machines are executed in simulation as they would in hardware. Each independently clocked state machine is another thread that executes in a round robin fashion to ensure that all clock dependencies are enforced.

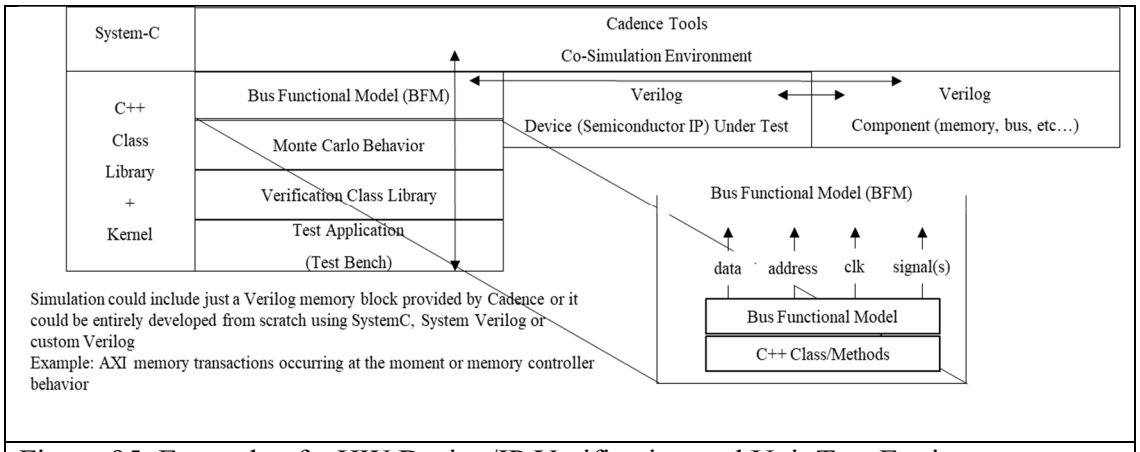

Figure 95. Example of a HW Design/IP Verification and Unit Test Environment

This same model can then be applied to a real synthesized SoC. Instead of the peripheral and memory buses being simulated virtual memory of a test processor running our memory simulation model, we use real system memory and write to real peripheral bus memory interfaces. Thus no changes to the actual tests need occur, just simply modify the memory adapters in the model so they map directly to SoC memory, not simulation memory. An example of this is depicted in Figure 96.

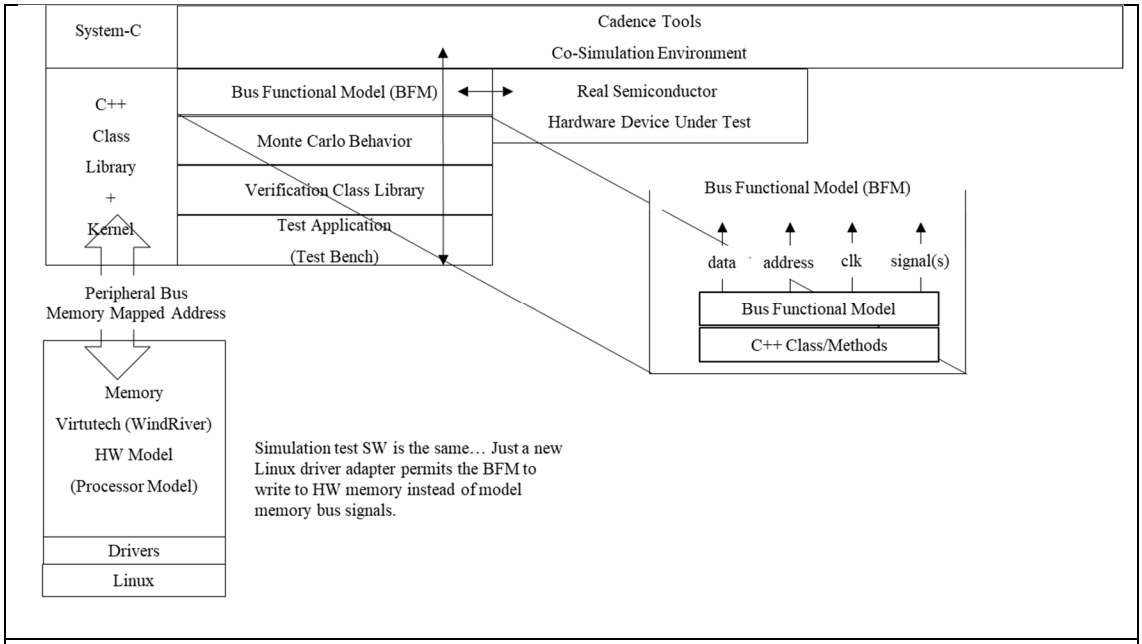

Figure 96. Unit Co-Simulation Test Environment Ported to Real Silicon

Note how the Linux kernel modules (e.g. drivers) are used to provide the mapping between application simulation memory and real system memory. The hardware only understand hardware addresses, so all memory translations must occur between the co-simulation application and the real hardware memory map. Thus, the memory writes all occur (not across a simulated bus to simulated memory) to real system memory.

Randomization of clock gitter has been especially helpful in finding bugs that may have escaped our testing prior to developeing this functional verification, validation, and performance testing software tools and libraries.

Hardware Performance Simulation

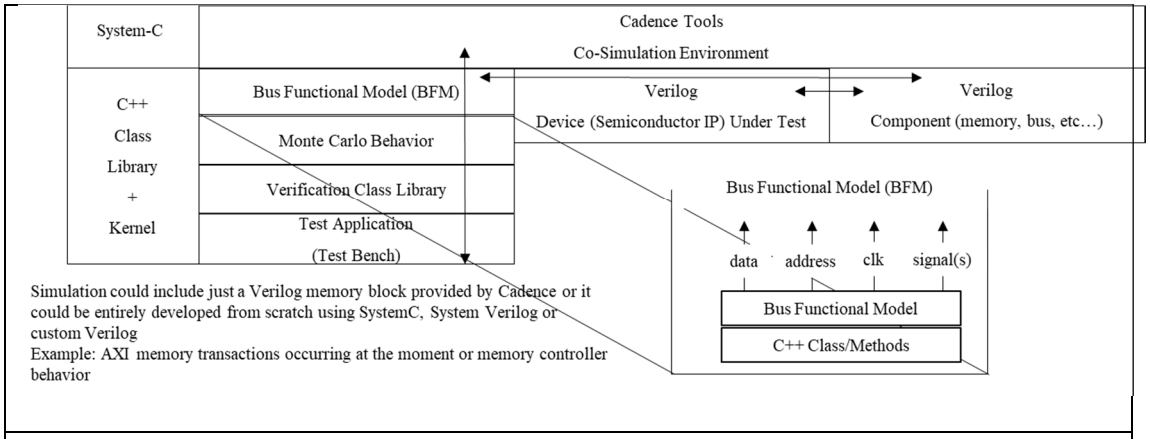

Figure 97. HW Co-Simulation Environment that can be used to test HW Performance

Using the Cadence co-simulation environment with a simulated memory gasket and a robust SystemC test class library, unit level tests can be executed at the simulated clock rate that the target hardware will execute. By measuring simulation time, number of hardware clocks, and unit of time (e.g. seconds), hardware IP designers can ascertain if the design meets the required performance specifications. In addition to running the design as a cycle-accurate simulation, this environment can support executing the design at higher than planned clock rates to determine how performance can be improved in the future. This environment also includes randomization of the address ranges utilized so that an accurate model can be measured as it relates to real-world memory latency due to system memory collisions (e.g. heavy utilization). HW performance is not based upon

raw bus rates, it based upon the ability of the hardware to reach a rate of speed that meets the minimum performance specifications. For example, a memory gasket can perform at 6.4GB/sec; however, it can never reach that because it can only support 3 memory transactions at one time. This is because the memory bus interface being used will only be used for a large number of relatively short memory transactions, not one large transaction. Therefore, though the raw performance of the bus is impressive, it does not meet the requirements because with only 3 transactions allowed in parallel, we are limited to only a very small fraction of the maximum bandwidth.

This does not replace the testing of subsystems that interact with the hardware IP under test. Connected subsystems must meet their performance specification and must be tested to ensure their committed performance target is met when used as intended by the end product user. Hardware can be designed to meet a performance specification, but the preconditions and post conditions are important. If the only way the hardware is going to meet its performance target is to use it in a way that would never occur in its actual use, it should be considered compliant with the requirements.

CHAPTER 7

5G SYSTEM PERFORMANCE ENHANCEMENTS

The final research focused on proposed improvements to accommodate 5G communication systems. I focused on three areas: Beamforming, voice communication and wireless roaming performance. These areas were chosen because of their consequential impact to 5G wireless performance. This research starts out with a short, abbreviated introduction of the recent 3GPP specification changes as it relates to 5G. Following this short introduction, I described proposed improvements in adaptive beamforming, directing energy towards end users. Next, I describe a proposed improvement in voice communication related to the well-known Levinson-Durbin algorithm. Lastly, an improvement in wireless roaming is proposed that reduces the number of interactions required by the mobile device as well as fewer 3GPP state machine operations on the 5G UE.

5G Introduction

The 3GPP new radio (NR) in release 15 provides both a non-standalone operation (used in concert with existing LTE network technology) and a full release for the standalone version which was scheduled for September 2018. The 5G capabilities include some of the following attributes:

1. Network can support both LTE and 5G NR, including dual connectivity where devices connected to both LTE and 5G NR which is referred to as dual connectivity (DC).
2. Carrier aggregation up to 32 carrier components (CC) with 16 CCs in 5G NR.

3. Massive MIMO and beamforming

4. FDD and TDD support for 5G NR frequency bands.

5. Forward error correction utilizes computationally more efficient Low Density Parity Codes (LDPC) are used in place of Turbo Codes at higher data rates.

6. Polar codes are used on the enhanced Mobile Broad Band (eMBB) control channels for the 5G NR interface.

7. Cloud RAN support replaces LTE PDCP and radio link layer (RLC) protocol layers.

8. Lower latency time intervals

9. QoS support using a new model (see user based QoS)

10. Co-existence with LTE in the same radio channels

Policy and charging rules function (PCRF) are not depicted (see **Figure 56**). The following diagram is the cutout for the 4G portion of the design depicted in **Figure 56**). Note that both 3G and 4G utilize a P-GW subsystem for network address translation (NAT) toward the rest of the network (RoN).

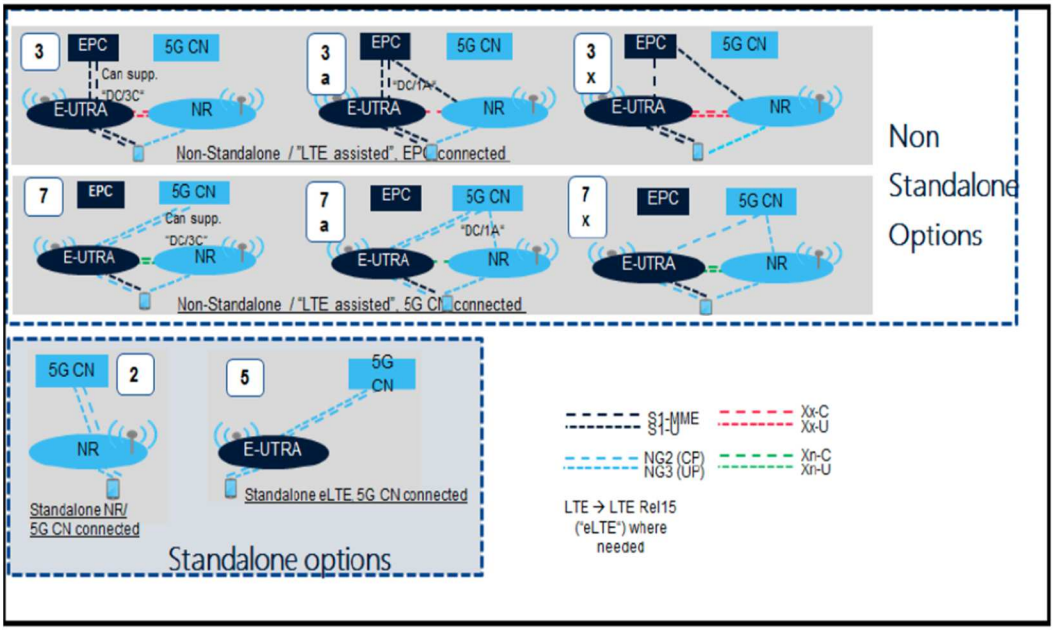

Figure 98 4G / 5G Integration (Release 15)

The 3GPP specification committee is specifying the first phase of 5G in Release 15. To enable wireless operators to deploy 5G quicker, the committee divided release 15 into two parts. The first set of requirements define how a 5G Radio Access Network (RAN) can integrate with an LTE network, this is called a non-standalone option. Such 5G deployments rely upon an existing LTE network in both the RAN and the EPC.

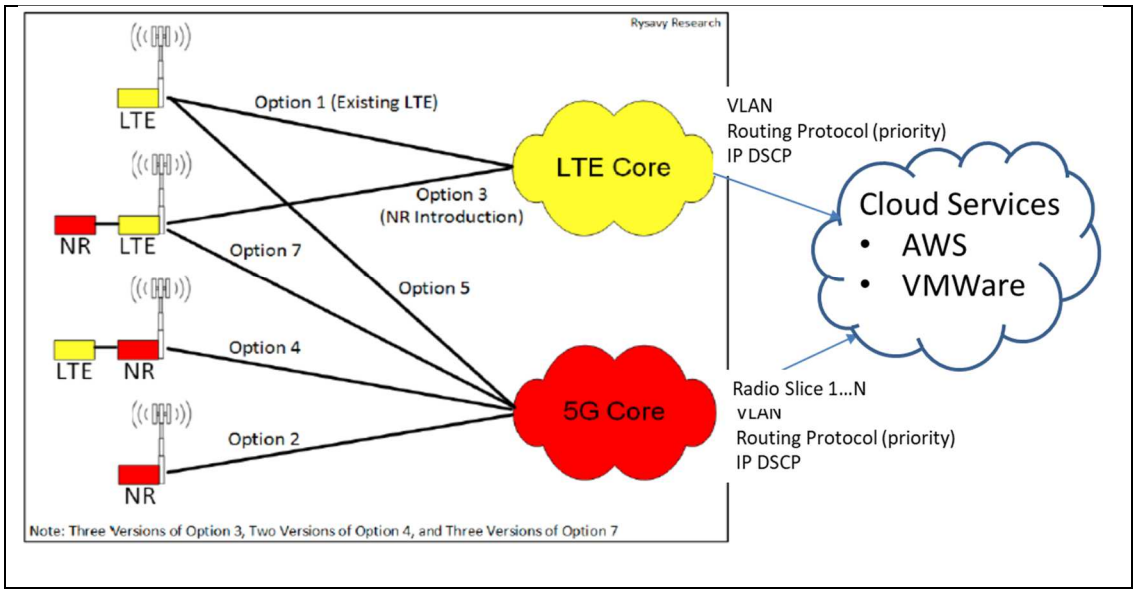

Figure 99 5G Cloud Service Integration (High Level) Options (Modified 3GPP)

The 5G release has been split into two releases: Release 15, which corresponds to NR phase 1, and release 16, which corresponds to NR phase 2. The table below describes 3GPP release 15 NR phase 1 which has put forth some requirements for 5G that focus on fulfilling three key performance indicates (KPIs):

- Greater than 10Gbs peak data rates for the enhanced mobile broadband (eMBB)
- Greater than 1M/km^2 connections for massive machine-type communications
- Less than 1msec latency for low-latency communications (URLLC)

Previously, 3GPP and IEEE committees have defined RAT types such as LTE (E-UTRA) and the WLAN 802.11 family of standards that are in wide use for cellular and wireless access. The new 5G RAT in 3GPP releases 14,15 and 16 which also includes Internet of Things (IoT) machine to machine communication access methods.

	LTE	NR
Frequency of Operation	Up to 6 GHz	Up to 6 GHz, ~28 GHz, ~39 GHz, other mmWave bands (Upto 52 GHz)
Carrier Bandwidth	Max: 20 MHz	Max: 100 MHz (at <6 GHz) Max: 1 GHz (at >6 GHz)
Carrier Aggregation	Up to 32	Up to 16
Analog Beamforming (dynamic)	Not Supported	Supported
Digital Beamforming	Up to 8 Layers	Up to 12 Layers
Channel Coding	Data: Turbo Coding Control: Convolutional Coding	Data: LDPC Coding Control: Polar Coding
Subcarrier Spacing	15 kHz	15 kHz, 30 kHz, 60 kHz, 120 kHz, 240 kHz
Self-Contained Subframe	Not Supported	Can Be Implemented
Spectrum Occupancy	90% of Channel BW	Up to 98% of Channel BW

Figure 100 LTE to 5G NR Comparison (Ref: 3GPP)

Carrier aggregation (CA) was introduced in LTE release 10, providing up to five 20MHz channels for a total bandwidth of 100MHz. Release 13 has increased this to 32 channels for a total of 640MHz of bandwidth. 5G new radio (NR) specification supports up to 16 contiguous or non-contiguous component carriers (CC) for up to 1GHz spectrum.

Due to the massive new hardware an expense related to 5G, 3GPP release 15 provides a phased approach to roll-out of 5G NR. A non-standalone (NSA) version that will use the LTE core and a standalone (SA) version that will use the 5G NR core that will operate completely independent of the LTE core network.

Table 11
New terminology (Ref. 3GPP specification release 15)

LTE eNB	Device that can connect to the Evolved Packet Core (EPC) for the current LTE core network
eLTE eNB	Evolution of the LTE eNodeB tht connect to the EPC and 5G NextGen core
gNodeB	5G NR equivalent to the LTE eNodeB
NG	Interface between the 5G NextGen core and the gNodeB
NG2	Control plane interface between the network core and RAN (S1-C in LTE)
NG3	User plane interface between the network core and RAN (S1-U in LTE)
* Reference 3GPP TR 38.804 (draft v0.4) shows the proposed deployment scenarios for 5G NR	

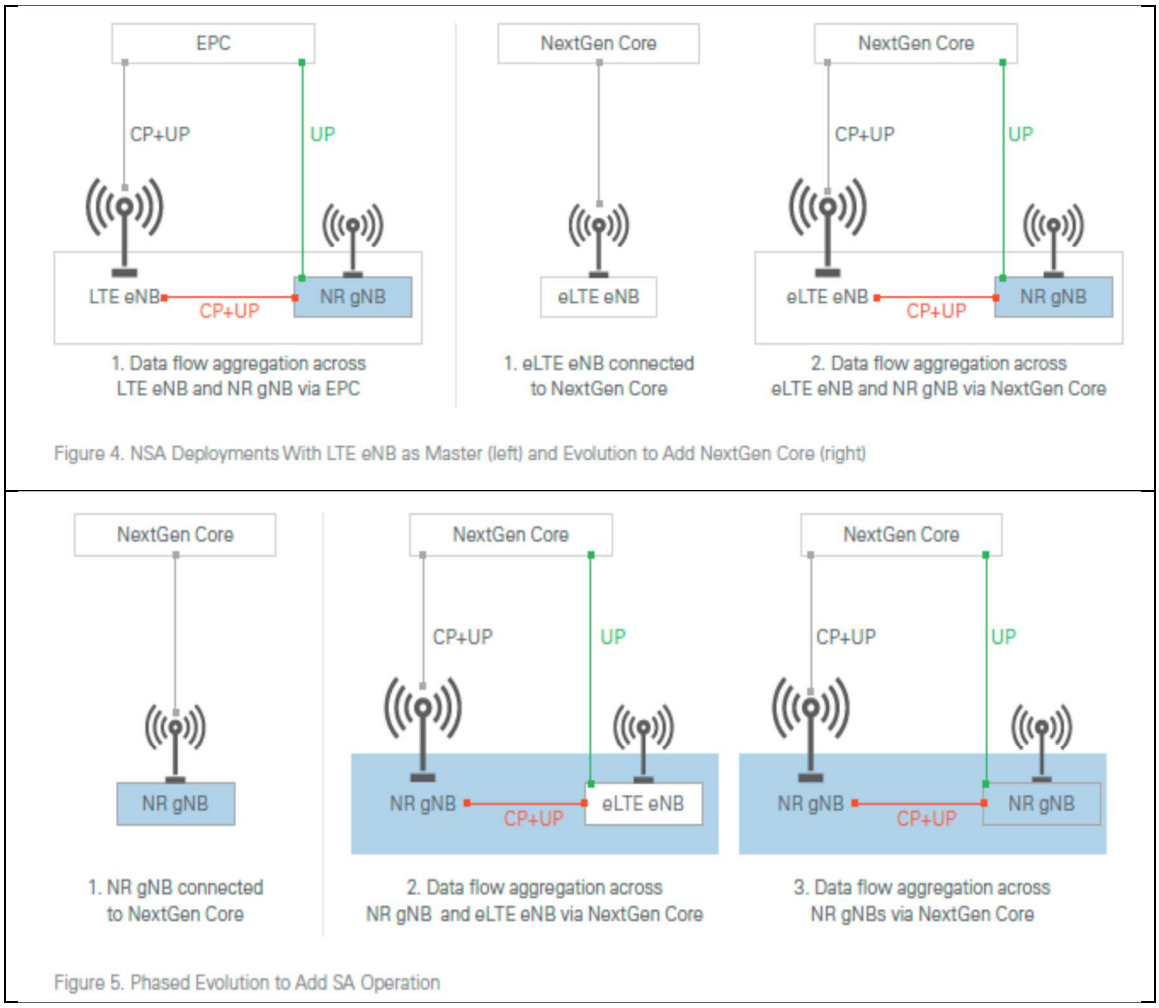

Figure 101 Release 15, Supported 4G and 5G Integration Use Cases

For non-stand alone operation, a frequency plan is proposed between LTE and the 5G NR for dual connectivity. The following table from 3GPP release 15 specifies the how LTE bands correspond to proposed 5G NR frequency ranges.

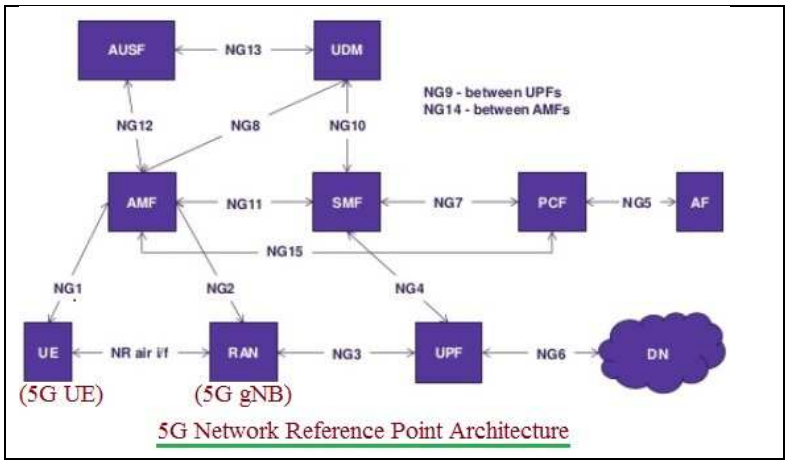

Figure 102 New 5G NR Proposed Core (Ref: 3GPP)

5G Downlink

To define this quantitatively, we will briefly describe the 5G communication channels in more detail. A description of the stacks will be described followed by a representation of the improvements to increase performance in the following areas: Beam Forming, Voice Communication and data transport. To provide proper context, a brief introductory description of the downlink stack followed by the uplink stack will follow.

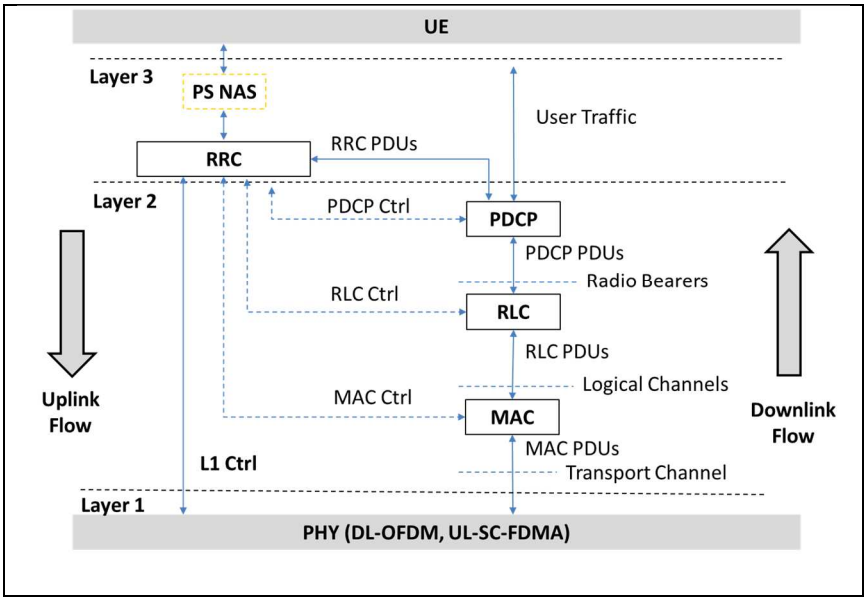

Figure 103 5G Uplink/Downlink Stack

The lowest level of the protocol stack is the physical layer (PHY) that includes the physical modulation orthogonal frequency division modulation (OFDM) with M-ARY subcarrier modulation. The transport block, delivered from the PHY to the media access (MAC) layer, it contains data from the previous radio subframe. It may contain multiple or partial packets, depending on scheduling and modulation. The MAC level functions is responsible for transport block (see Figure 104) retransmission, referred to as hybrid automatic repeat-request (HARQ) implemented as layer 2 transmission retry.

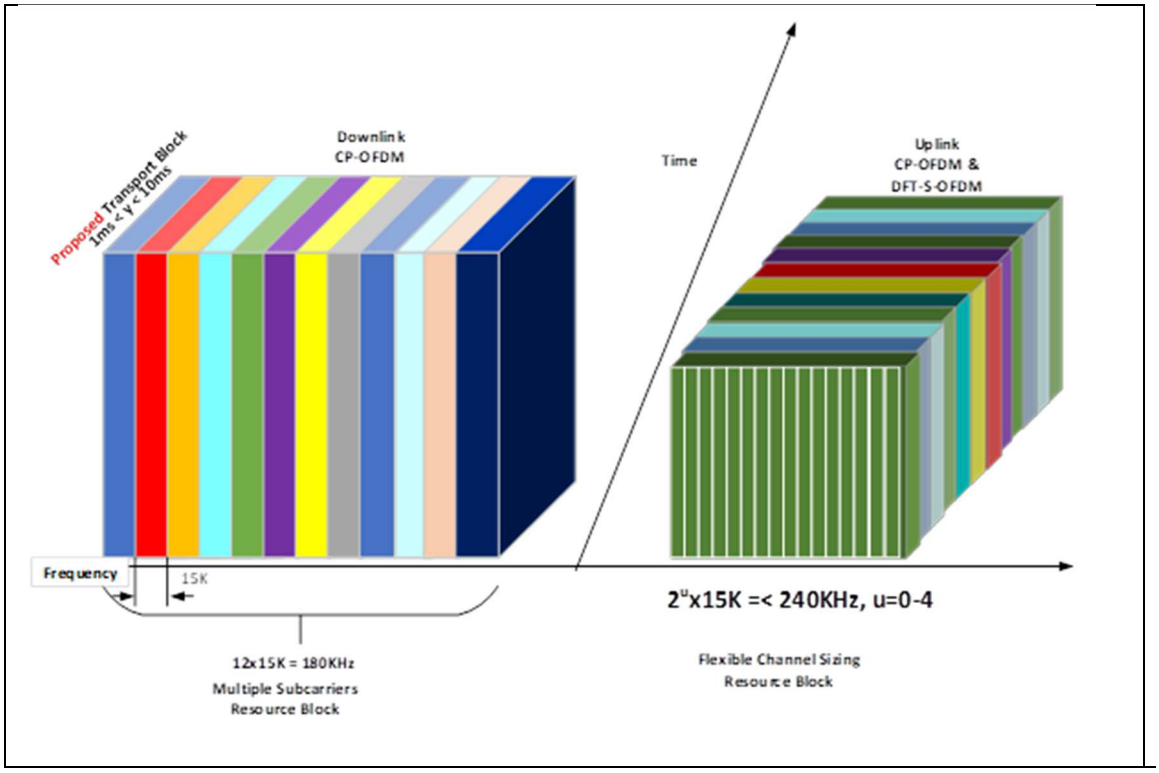

Figure 104 Exemplar: 4G Model – Next changes to model (5G Specification is Not Final)

The mapping of the MAC logical to physical channels follows in the diagram below. The control channel in the lower portion of the picture is used for scheduling, signaling and other low-level functions. The downlink shared channel contains both a transport

channel for paging and for the downlink of data. The physical broadcast channel flows all the way through for broadcast.

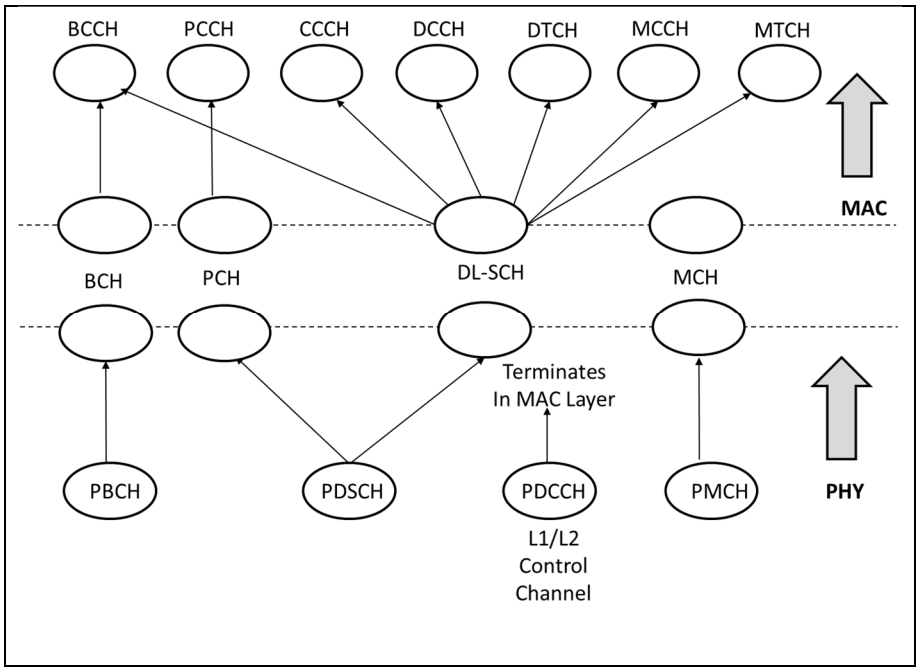

Figure 105 MAC Downlink Mapping (Unchanged in 5G)

The transport channels above user different modulations and coding. Paging and broadcast channels must be received everywhere in the cell, so they must use robust modulation. The DL-SCH can be optimized by the UE.

- Dedicated Control Channel (DCCH): A point-to-point bi-directional channel that transmits dedicated information between a UE and the network.
- Paging Control Channel (PCCH): A downlink channel that transfers paging information. This channel is used when the network does not know the location cell of the UE.

- Common Control Channel (CCCH): Uplink channel for transmitting control information between UE and network. This channel is used by the UE having no RRC connection with the network.
- Dedicated Traffic Channel (DTCH): A point-to-point channel, dedicated to one UE for the transfer of user information. A DTCH can exist in both uplink and downlink.
- Broadcast Control Channel (BCCH): A downlink channel for broadcasting system control information.
- Multicast Control Channel (MCCH): A downlink channel for multicast system control information
- Multicast Traffic Channel (MTCH): A downlink channel for multicast traffic

The UE interprets the transport format field in the downlink MAC which provides the Modulation Coding Scheme (MCS) for the next transport block; the MCS changes dynamically. The MAC also coordinates measures from the local PHY to the RRC regarding local status and conditions, and RRC reports back to the eNodeB using control messages. From the eNodeB to the RRC, the RRC controls modulation and configuration settings. MAC measurements support downlink scheduling based upon Bit Error Rates (BER) and radio conditions at the UE. Buffer status reports are conveyed via the RRC to ensure flow control is maintained between UE and eNodeB.

The Radio Link Control (RLC) performs segmentation and reassembly. The RLC operates in three modes: transparent, unacknowledged, and acknowledged. The RLC provides in-sequence and duplicate detection. The segmentation process involves unpacking an RLC PDU into RLC SDU (or portions of SDUs). The RLC PDU size is

not a fixed because it depends upon the conditions of the channel, it is based on the transport block (TB) size. The condition of the channel varies due to bandwidth requirements, distance, power levels and modulation scheme.

The Packet Data Convergence Protocol (PDCP) layer in the user plane is used for packet data bearers, circuit switched bearers, performs decryption, ROHC header decompression, sequence numbering and duplicate removal. In the control plane, it is used for decryption, integrity protection, sequence numbering and duplicate removal. The ROHC is defined in IETF RFC3095, RFC4815 and RFC3843.

5G Uplink

In 4G LTE and 5G the processes on the uplink side are similar to processes on the downlink side. In 4G the peak data rate is half that of downlink; access is granted by the eNodeB; there are changes in logical channels and transport channels; and random access is used for initial transmissions. The 4G PHY uses SC-FDMA for the uplink because it has a lower peak-average ratio, which allows a more power-efficient transmitter in the UE. In 5G NR the uplink modulation is DFT-S-OFDM and CP-OFDM; however, the uplink performance is approximately the same between 4G and 5G.

Synchronization signals (SS) and system information transmit basic information to all user equipment. Timing information is shared with all devices the transmitter and receiver can synchronize, the receiver can perform synchronous detection and demodulation of the transmitted information from the UE. This is accomplished using

the synchronization signal block (SSB) through the physical broadcast channel (PBCH). LTE 4G has only one pattern of SSB transmission in time domain (see diagram below).

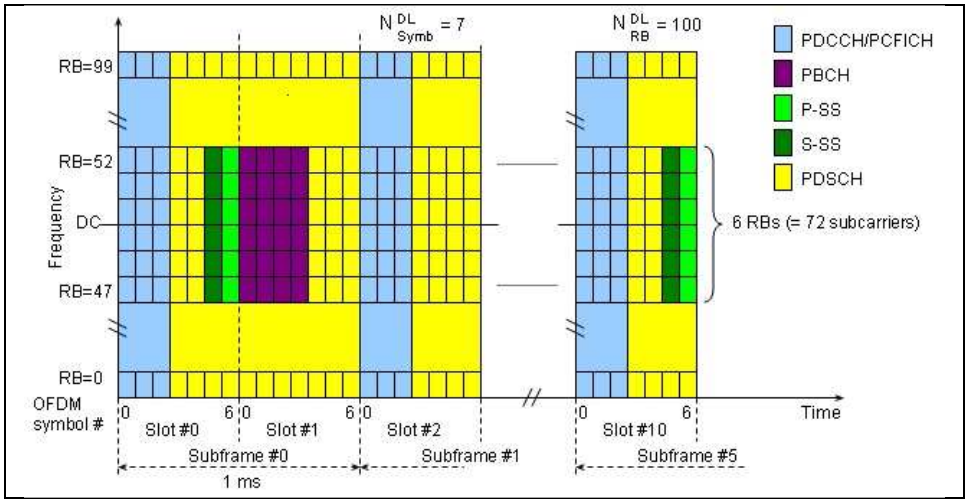

Figure 106 4G PBCH, FDD Normal CP, 20MHz (Ref:3GPP)

Time Domain transmission pattern of SS Block in 5G NR is more complicated than LTE SS Block (see Figure 106) In 4G LTE, the subframe number and the OFDM symbol number are within the subframe is always the same. In 5G NR, there are many different cases of Time Domain pattern of SSB Transmission as illustrated below (see Figure 107).

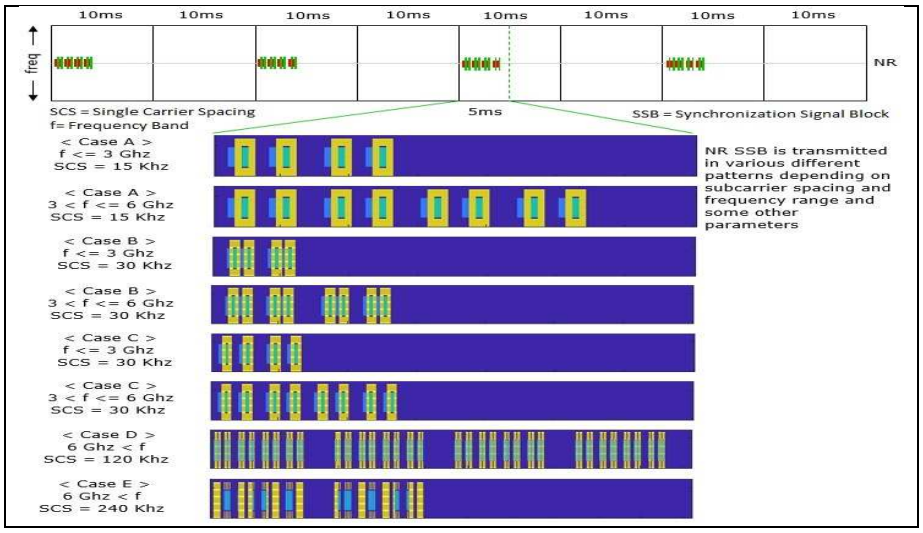

Figure 107 5G PBCH, Changes, Normal CP, FDD 20MHz (Ref: 3GPP)

In order for data to be transmitted the FFT processor of the IFFT is combined into a time domain composite signal which is used to reduce the number of FFT streams required to support the communication of information across 1024 subcarriers, utilizing a linear modulation, such as QPSK as an example, the complex symbol amplitude and phase is modulated according to the associated I/Q constellation and is then multiplied with the individual subcarriers to convey the information on the downlink. This means 1200 resource elements carrying 1200 different complex symbols over 1200 subcarriers. Each subcarrier is assigned to different users. Utilizing the IFFT function, these subcarriers are combined into samples of a composite time domain signal. These time domain samples are then transmitted as the downlink where users pull out the information allocated for them. As a function of the reception of by the handheld devices, a waveform windowing function is used to reduce the inter-user interference due to non-zero out-of-band emission.

Performance Improvements

The following performance improvements in the areas of adaptive beamforming, voice modeling, and roaming performance. Each improvement will be quantified and described in detail. An additional improvement, is in microwave component design. 5G NR requirements inform us of our receiver design and specifically our microwave component design that enables the performance of the receive and transmit chains. The channel spacing below is defined as 15KHz and defines the required phase noise and receiver sensitivity required. Since 5G has higher path loss, signal to noise ratio (SNR) is important, therefore, receiver sensitivity is even more important than was previously the case. The following equation, derived from equation 14, defines our phase noise requirements:

Assuming that carrier power (C) and interference power (I) are the same, to achieve 50dB of adjacent channel rejection, we must achieve a phase noise (L) of the following:

$$L := -50dB - 10\,log_{10}(18KHz) = -92dBc/Hz \tag{159}$$

The channel structure defined below requires -92dBc/Hz of phase noise offset from the tuned frequency of the receiver. In order to reduce the peak to average ration and increase the efficiency of the power amplifier and save battery life, the uplink is different for both 4G and 5G LTE. As depicted in the diagram (see **Figure 104**), the uplink signal has a very short symbol duration and sends the same data over multiple subcarriers, while the CP-OFDM downlink utilizes long symbol durations of 66.7usec duration. In a 20MHz bandwidth, the highest frequency is 9MHz and therefore requires 18Msps Nyquist based sampling or 1200 samples per symbol. For backwards compatibility with UMTS sampling rate of 3.84Msps, LTE 4G and 5G utilize 30.72Msps, a multiple of the

3.84Msps, for a 20MHz bandwidth providing 2048 samples per symbol. To improve latency, a change to the original OFDM modulation scheme has been proposed to add a scalable modulation framework by adding different time slots of 1, 2, 4, 8, 16 or 32. This thereby reduces the minimum transport block size to $\frac{1e3}{32} = 31.25usec$.

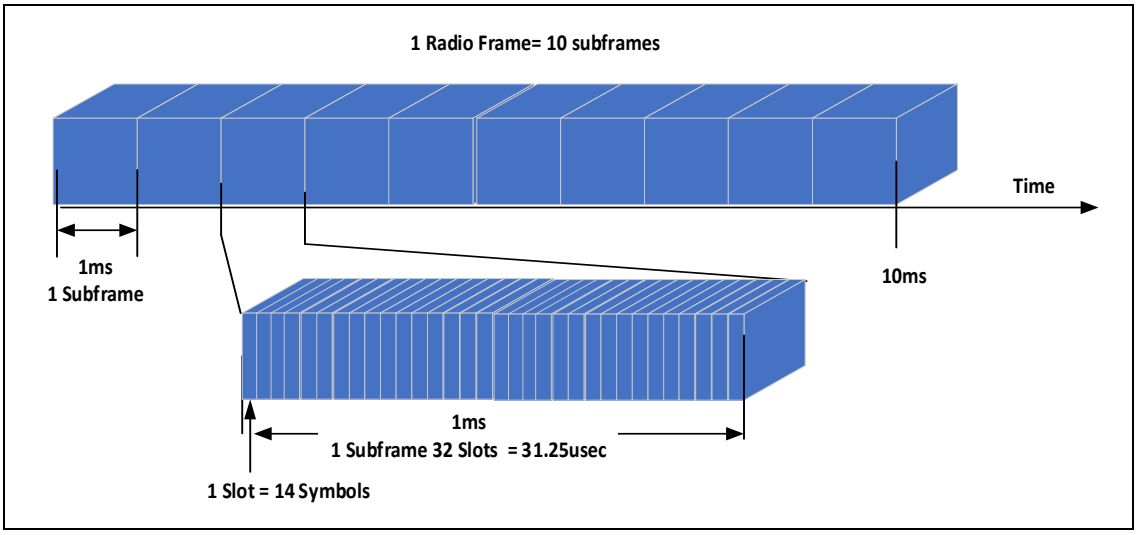

Figure 108 Proposed Change to Reduce Latency to 1msec (Ref: 3GPP)

5G downlink utilized CP-OFDM which is also used by 4G LTE. 5G has changed the uplink frequency to a factor of 2:

$$480KHz = 2^{u}(15e3)Hz, where\ u = 0 - 5 \tag{160}$$

Adaptive Beam Forming

LTE has been a continuous evolution of spatially diverse, multi-antenna transmission encompassed in spatial multiplexing (SU-MIMO) and SDMA (MU-MIMO). Multiple Input, multiple output (MIMO) becomes an even more important component of the 5GNR RAT. The 5G NodeB has two TxRus per polarization, which are connected to cross polarized Tx antenna panels. The 5G NodeB selects one analog beam on each

antenna panel polarization for the downlink MIMO transmission. The UE must be able to measure multiple Tx beams swept on different time units on each panel polarization and select which Tx beam is the best beam. For higher frequencies, beamforming is a necessity due to increased path loss.

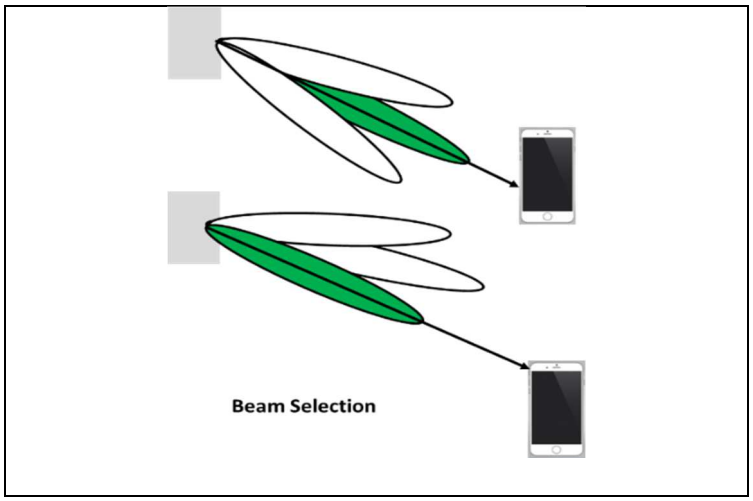

Figure 109 High Frequency Beamforming Necessary to increase Directivity towards Mobile Devices

The following frequency ranges related to mm-Wave are only proposed at this time and are not intended to be final specifications:

		LTE Band													
		1	2	3	5	7	8	19	20	21	25	26	28	39	41	66
NR Freq. Range	3.3 GHz–4.2 GHz	YES		YES	YES	YES	YES	YES	YES	YES		YES	YES	YES	YES	
	4.4 G Hz–4.99 GHz	YES		YES	YES		YES	YES		YES		YES	YES	YES	YES	
	24.25 GHz–29.5 GHz	YES		YES	YES	YES	YES	YES	YES	YES		YES	YES	YES	YES	YES
	31.8 GHz–33.4 GHz			YES		YES			YES				YES			
	37 GHz–40 GHz															YES
	Band 7			YES			YES		YES							
	Band 28			YES		YES			YES							
	Band 41	YES	YES	YES	YES						YES	YES			YES	

Table 3. Release 15 LTE-NR Band Combinations (Source: RP-170847, RP-170826, R4-1702504 [DCM])

Figure 110 5G Frequency Coverage Plan (Ref: 3GPP)

The initial access procedure for all user equipment is provided by a beam sweep to all user equipment (UE) is accomplished through a user beam transmit sweep. Timing synchronization information is provided to all devices. For high frequency applications, the beam is highly directional and therefore requires multiple transmissions in the following manner:

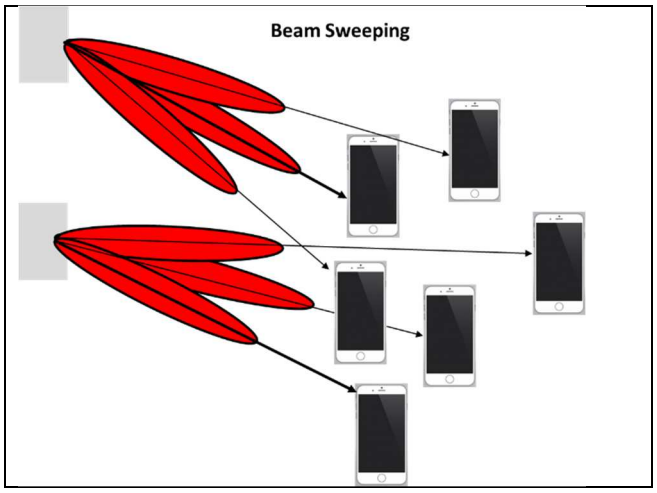

Figure 111 Beam Sweeping provides basic information to UE's

Beamforming and MIMO

Wireless Technologies such as Wi-Fi and Cellular are converging in the market place. This convergence promotes a need for a different link layer protocol stack technology that better facilitates the convergence of these technologies both from the radio frequency (RF) modulation adaptation perspective as well as from the link layer protocol perspective. This convergence has also driven a desire to increase bandwidth, reduce symmetrically Gaussian noise, reduce insertion loss and increase carrier signal frequency. These performance improvements are addressed utilizing microwave component design, digital signal processing (DSP) and aperture [material and structural] design; both

aperture and digital signal processing are required for 'smart' antenna system design. This paper will introduce the use of a new vector antenna technology to improve the performance of modern communication signal sets in concert with massive MIMO, such as those proposed in 5G communication proposals, in concert with a patented link layer routing protocol stack concept.

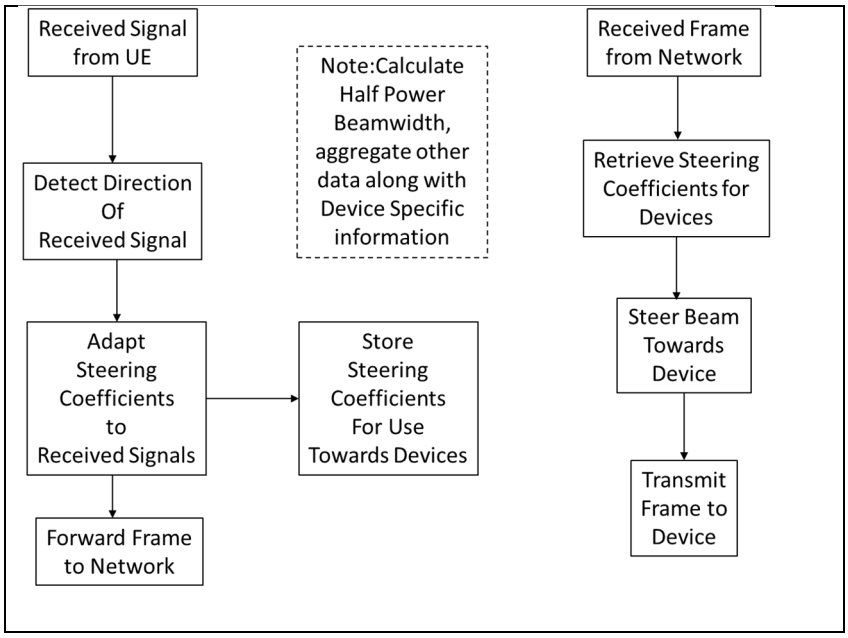

Figure 112 Process of Receiving Energy from UE and Redirecting a Response to that Device

We will define the use spatial and vector arrays in a cellular system. Algorithms will be utilized to receive and beam form energy towards individual devices with in the cell being serviced by the wireless base station. According to the specifications, 1M/km2 connections must be supported for device-to-device communication support and is based upon the following mathematical model:

$$\theta_{\pm} = sin^{-1}\left(\frac{1}{kd}\left(\frac{\pm 2.782}{N} - \delta\right)\right), Half\ Power\ Beam\ Width\ (HPBW) = |\theta_{+} - \theta_{-}| \tag{161}$$

$$\delta = -kd\ sin(\theta_0), where\ \theta_0 = Steering\ Angle \quad (162)$$

Spatial Arrays

A spatial array utilizes spatial diversity with spacing relative to $\frac{\lambda}{2}$ so that angles of arrival can be estimated. Spacing of $< \frac{\lambda}{2}$ removes grating lobes and improves aperture cross-section efficiency. Spatial arrays are used in an adaptive way to service numerous sensors at once in a network scenario. In such a configuration, a device responds to the PRACH channel of the wireless base station. Timing synchronization messages are broadcast by the wireless base station. The PBCH channel sends the physical cell ID (PCI) which contains the cell group id and the cell id. The user equipment (UE) response impinges on the following array elements:

Two spatial array approaches were analyzed to determine the algorithm execution required to determine the direction of propagation such that an adequate response is possible in the correct direction to the received signal. Since a-priori knowledge of the received signal is determined through the broadcast channel (PBCH), and assuming a digital beam former (DBF), the weights of the received signal are determined and the direction of arrival (DOA) is computed in the following manner:

We will assume digital beam forming with an analog band pass filter along with a low noise amplifier (LNA), that sets the noise figure of the receiver, which provides the analog bandwidth that is digitally sampled. Signals are received through a spatial array which has an array manifold; the array manifold vector is also referred to as the array steering vector:

$$a(\theta) = [1 \quad e^{j(kd\sin(\theta)+\Delta)} \quad \dots \quad e^{(N-1)(kd\sin(\theta)+\Delta)}] \tag{163}$$

$$k = \frac{2\pi}{\lambda}, d = Element\ spacing, N = \#\ of\ elements$$
$$\Delta = Electrical\ Phase\ Difference\ between\ two\ adjacent\ elements$$

$$\begin{bmatrix} X_0[k] \\ X_1[k] \\ X_2[k] \\ X_3[k] \end{bmatrix} = \begin{bmatrix} a_0(\theta_0) & \cdots & a_0(\theta_{r-1}) \\ a_1(\theta_0) & \cdots & a_1(\theta_{r-1}) \\ a_2(\theta_0) & \cdots & a_2(\theta_{r-1}) \\ a_{N-1}(\theta_0) & \cdots & a_{N-1}(\theta_{r-1}) \end{bmatrix} \begin{bmatrix} S_0[k] \\ S_1[k] \\ S_2[k] \\ S_{r-1}[k] \end{bmatrix} + \begin{bmatrix} R_0[k] \\ R_1[k] \\ R_2[k] \\ R_{N-1}[k] \end{bmatrix} \tag{164}$$

The matrix $a_n(\theta)$ is a vandermonde matrix structure referred to as matrix **A**. But what do we do when N is very large? It is no longer practical to execute a matrix operation that could handle large > 100 element matrices.

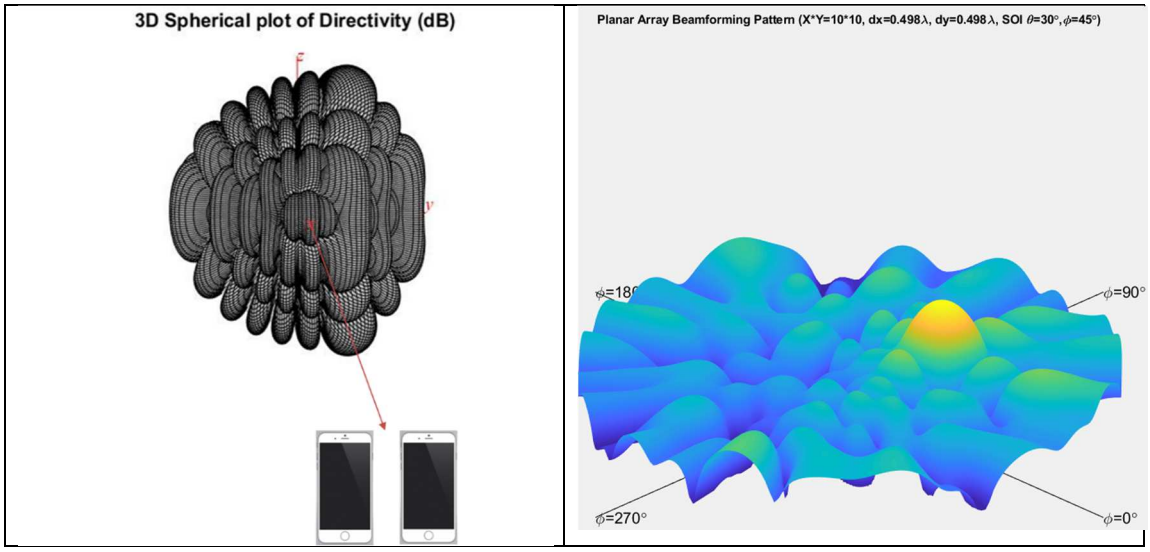

Figure 113 Uniform Pattern 10x10 Panel $\theta = 30, \phi = 45$

As depicted the diagram above, the uniform array is symmetric. The major lobes exist above and below the horizontal because of the array symmetry. The array has a major lobe and 30 degrees as well as at 120 degrees symmetric around 90 degrees at broadside.

The algorithm will be defined to cover a large number of elements and how the algorithm will scale according to these large number of elements. We will describe how MIMO is used in concert with beamforming to improve communications with individual user devices.

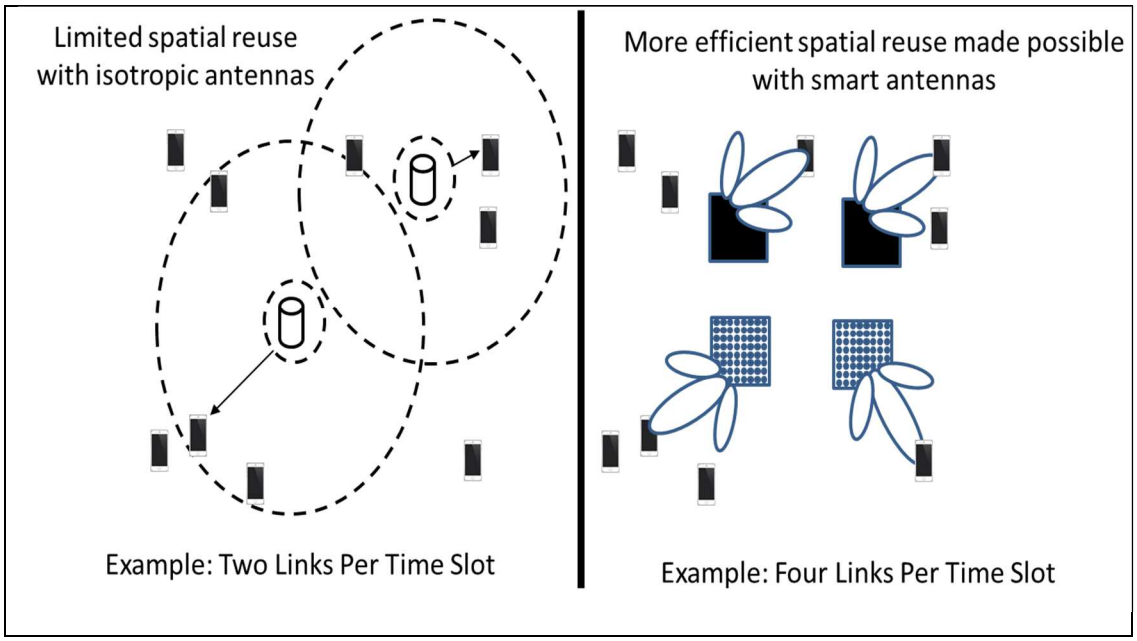

Figure 114 Adaptive Beam Forming Increases the number of devices serviced simultaneously

Beam selection is comprised of a large number of antennas which can be comprised of a uniform, Dolph-Tschebyscheff or binomial planar array. Planar arrays can be rectangular, circular or an irregular shape. Irregular shapes are used to address spatial ambiguity for a variety of apertures when wider frequency band coverage is required for DOA analysis and beamforming where avoiding grating lobes is important; as the frequencies change, the $\frac{\lambda}{2}$ relationship changes. While the uniform array yields the best (smallest) half-power beamwidth, superior side lobe performance is provided by the binomial array. Due to the large number of elements required for 5G communication,

binomial arrays are not practical because of the wide variations of amplitudes required across the array. Uniform arrays have the best directivity and their manufacturability makes them the best choice for 5G communication.

A beamforming array is steered towards an azimuth and elevation through a set of weights that are expressed through the array manifold or steering vector. Signals are received through a spatial array which has an array manifold; the array manifold vector is also referred to as the array steering vector:

$$a(\theta) = [1 \quad e^{j(kd\,sin(\theta)+\Delta)} \quad \dots \quad e^{(N-1)(kd\,sin(\theta)+\Delta)}] \tag{165}$$

$$k = \frac{2\pi}{\lambda}, d = Element\ spacing, N = \#\ of\ elements$$

$$\Delta = Electrical\ Phase\ Difference\ between\ two\ adjacent\ elements$$

The steering is performed by changing the electrical phase Δ on each element. Normally, these values are pre-constructed towards a pre-defined set of angles that have been calibrated per frequency and beam angle.

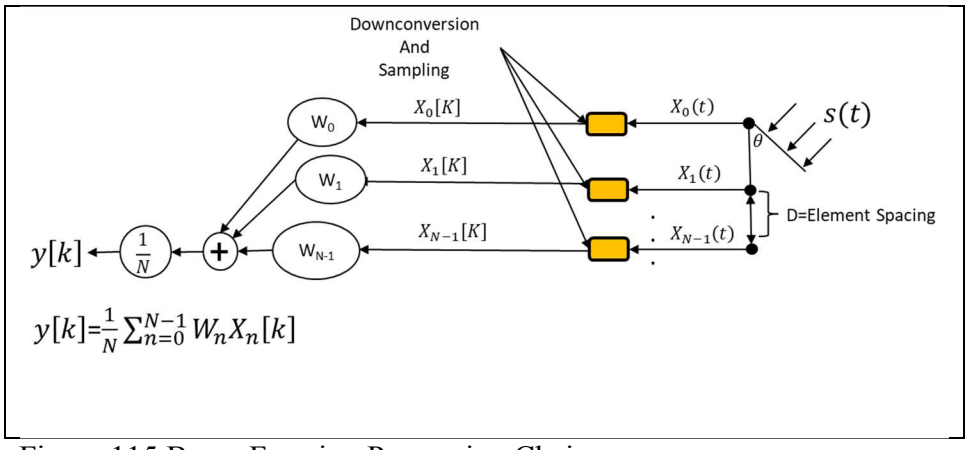

Figure 115 Beam Forming Processing Chain

A beamformer is a weighted sum of sampled baseband signals. By adapting complex weights, we can define the beam pattern. A beamformer in a uniform linear array is analogous to finite impulse response (FIR) filter design by windows. Window functions such as Hanning reduce the side lobe level of beam steering angles. The diagram below describes the beam forming process. The weights in the diagram below are complex weights (real and imaginary).

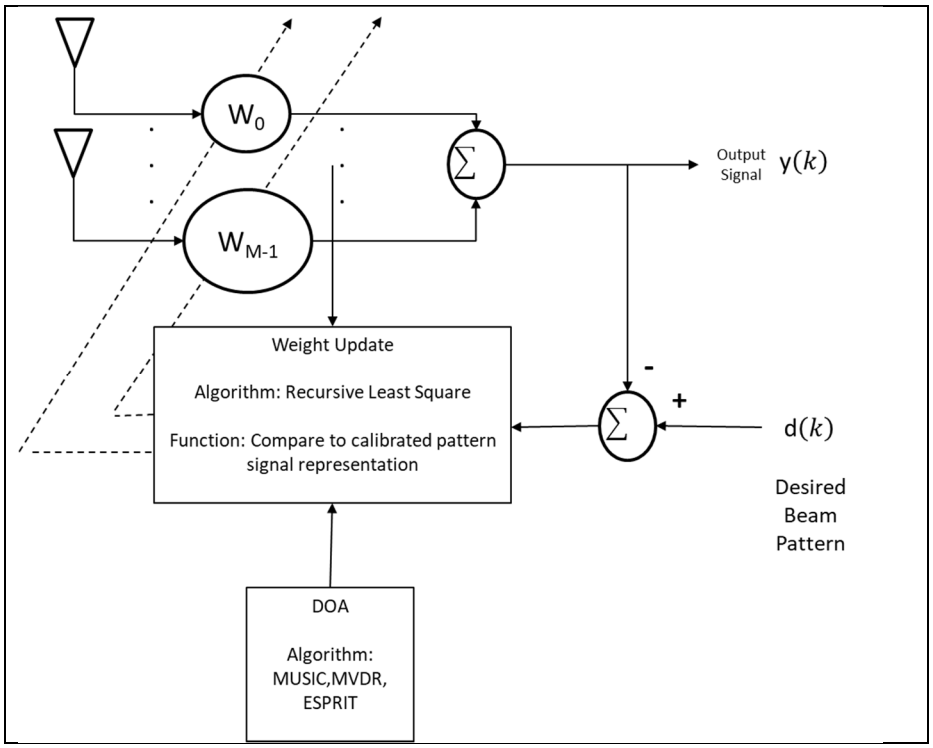

Figure 116 Adaptive Antenna Sensor Weights Updated Dynamically

Two algorithms were evaluated to determine the best in adapting the beam pattern based upon a wireless device accessing the base station. The beam is adapting as signals of interest are received so the beam will steer towards the device of interest during communication.

The 1st algorithm evaluated was the Least Mean Square (LMS) algorithm. The following equation describes this algorithm process:

$$W_{k+1} = W_k + 2\mu X_k(d_k - X_k^T W_k) \tag{166}$$

The 2nd algorithm evaluated was the Recursive Least Square (RLS) algorithm. The following equation describes this algorithm process:

$$K_{n+1} = \frac{\beta^{-1} R_{xx}^{-1}(n) x_{n+1}}{1 + \beta^{-1} x_{n+1}^T R_{xx}^{-1}(n) x_{n+1}} \tag{167}$$

$$\hat{e}_{n+1} = d_{n+1} - b^T(n) x_{n+1} \tag{168}$$

$$b_{n+1} = b_n + K_{n+1}\hat{e}_{n+1} \tag{169}$$

$$R_{xx}^{-1}(n+1) = \beta^{-1} R_{xx}^{-1}(n) - \beta^{-1} K_{n+1} x_{n+1}^T R_{xx}^{-1}(n) \tag{170}$$

The following performance was observed. As the graphs depict, the RLS algorithm does converge more quickly than the LMS algorithm providing an improvement of approximately 10dB in mean square error (MSE). Since beam steering events are frequent and numerous, the convergence time improves performance of the wireless communication link during communication events with a large number of wireless devices.

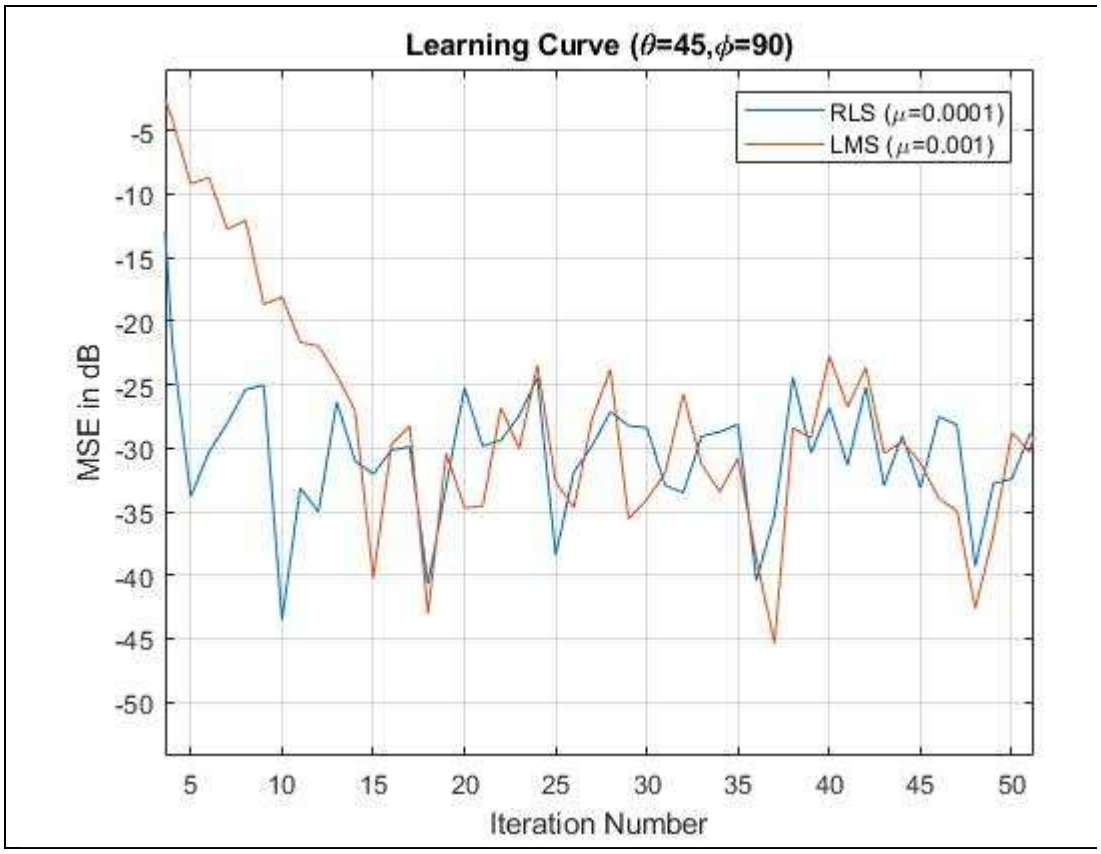

Figure 117 Beam Forming Weight Convergence Performance Improved by RLS Algorithm

Based upon a savings of 15 iterations per wireless beam forming steer event, for a worst case of approximately 1M/km^2 devices.

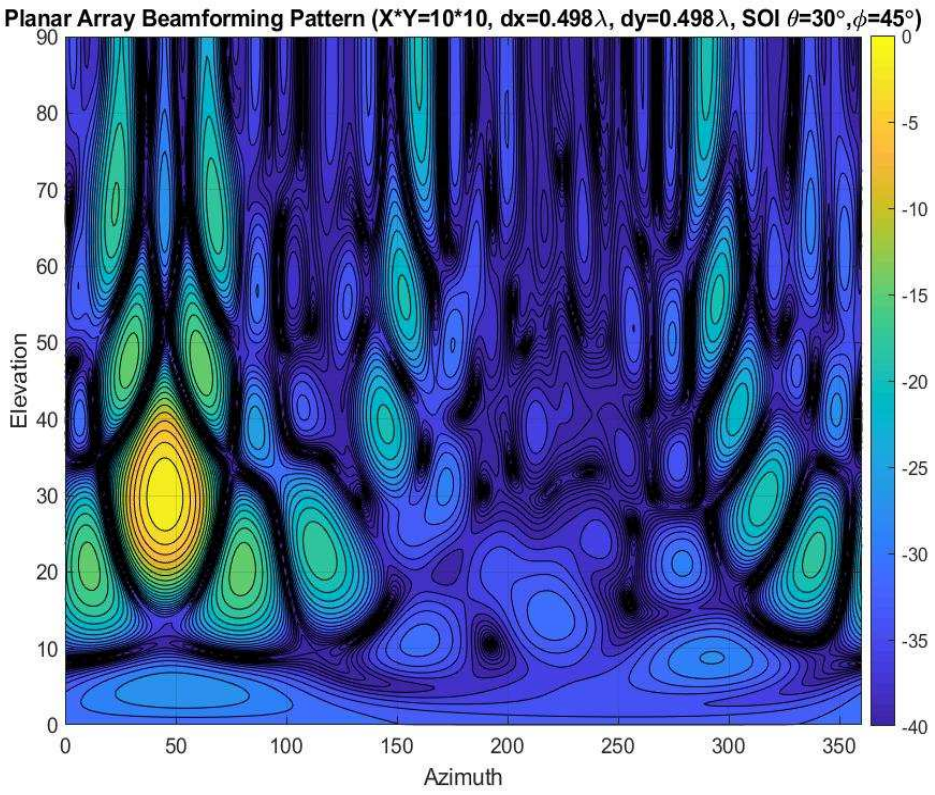

Figure 118 Uniform Pattern $\theta = 30, \phi = 45$

Table 12
Performance Estimates of Spatial Diversity Aperture (RLS)

Array Size Performance (10x10) (MATLAB)	RLS (MATLAB) Measured Performance (usec)	Samples
$\Omega(10) = 2.15(10)^{-4}$	$12928 + \Omega$	1000
$\Omega(10) = 2.15(10)^{-4}$	$12826 + \Omega$	2000
$\Omega(10) = 2.15(10)^{-4}$	$12864 + \Omega$	4000

Table 13
Performance Estimates of Spatial Diversity Aperture (LMS)

Array Size Performance (10x10) (MATLAB)	LMS (MATLAB) Measured Performance (usec)	Samples
$\Omega(10) = 2.15(10)^{-4}$	$4672 + \Omega$	1000
$\Omega(10) = 2.15(10)^{-4}$	$1589.5 + \Omega$	2000
$\Omega(10) = 2.15(10)^{-4}$	$742.5 + \Omega$	4000

Two approaches were investigated along with algorithms to compare the overall performance of each approach: spatial arrays, vector arrays. This work focused on using antenna arrays or smart antennas to increase capacity of the network. The signal processing algorithms that are important in these applications are direction of arrival estimators and adaptive beamformers. The following will describe the attributes associated with arrival estimators and adaptive beamforming algorithms.

A broad category of arrival estimators can be addressed by evaluating two categories of estimators. Those estimators using spatial diversity and those using a vector aperture. The first category will be spatial arrays followed by vector aperture arrays. This will be covered in the context of establish a 5G communication channel at a high frequency.

To address the use of increased matrix sizes (see Figure 120 for performance factor) based upon additional MIMO and aperture interfaces, we utilize the Matrix inversion lemma to reduce the complexity of matrix inverse operations.

The fully configured 5G bandwidth is sampled digitally, the following spatial covariance matrix is created:

$$R_{xx} = \frac{1}{K}\sum_{n=0}^{K-1} X_n X_n^H \tag{171}$$
$$K = Number\ of\ Samples$$

The signal observed at element m at time k is expressed through the following equation, where r is the number of signals:

$$X_m[K] = \sum_{i=0}^{r-1} S_i[k]e^{-jm\omega_i} + R_m[k] \tag{172}$$

This equation can be viewed as the equation for a time domain signal consisting of complex sinusoids in noise if m is interpreted as a discrete time index. Therefore, spectral analysis could be used to computing direction of arrivals (DOA's). In frequency estimation, w_i are the parameters of interest In DOA estimation, the w_i is estimated and the θ_i is computed using the following equation:

$$w_i = 2\pi d\ sin(\theta) \tag{173}$$

The matrix $\boldsymbol{A}$ above is a vandermonde matrix structure. Spectral estimation algorithms such as iterative FFT's can be used to perform DOA. Instead, since we are using a uniform planar array or vector aperture, we will use the super resolution spectral algorithm ESPRIT and MUSIC to calculate the DOA.

The columns of the vandermonde matrix **A** are the steering vectors corresponding to the (r) signals $S_0(k) \ldots S_{r-1}(k)$. X_k is the data vector snapshot at time k.

$$R_{ss} = E[S_K S_K^H], where\ R_{xx} = AR_{ss}A^H + \sigma^2 I \tag{174}$$

The matrix properties in regard to orthogonality of eigenvectors can now be used to separate the signal from the noise. This is used by multiple signal classification (MUSIC) to obtain high resolution spectral estimates and hence angles of arrival.

Vector Arrays

A vector array is a six-axis aperture, each element represents the $E(\theta, \phi, r)$ and $H(\theta, \phi, r)$. The calculation in regard to deriving Direction of Arrival (DOA) is now discussed. Super resolution DOA algorithms are used both for spatial and vector apertures. This means algorithms such as MUSIC, MVDR and ESPRIT can be used. The difference with a vector antenna are the following:

1. A vector antenna requires little to no directionality. Therefore, signal gain is not possible as is the case with spatial arrays. The vector aperture cannot achieve gain and is more susceptible to path loss than spatial arrays.
2. A vector antenna is wideband; however, when in the presence of high frequencies, the size of the vector antenna must be reduced due to resonance on each element due to the size of the wavelength impinging on the array elements.

The $E(\theta, \phi, r)$ portion of the vector antenna elements can be thought of as three dipoles. Due to the cyclical nature of the signals that impinge on these elements, the current standing wave pattern of an element longer that λ undergoes 180^0 phase shifts between adjoining half cycles. Therefore the current in all parts of the element do not have the same phase. As a result, the fields radiated by some parts of the element will not

reinforce those of the others causing significant interference and cancelling effects. Therefore the size of the vector elements must be reduced as a function of very small wavelengths λ.

The vector aperture DOA performance was compared to the uniform planar array. The performance was the following:

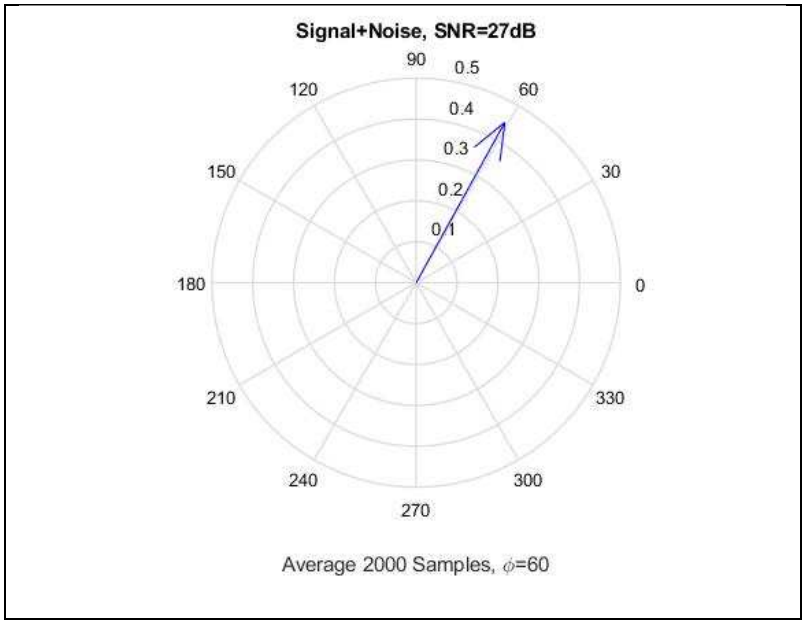

Figure 119 Vector Antenna Performance Using Cross Product DF

This result was achieved by only calculated the cross-product of the received vectors on a vector aperture. This results in a very short equation and fewer instructions are required than using a super-resolution direction finding technique such as MUSIC or MVDR:

$$K = \begin{bmatrix} k_x \\ k_y \\ k_z \end{bmatrix} = \frac{\bar{e} \times \bar{h}}{\|\bar{e}\| \cdot \|\bar{h}\|} = \begin{bmatrix} sin\,\theta\,cos\,\phi \\ sin\,\theta\,cos\,\phi \\ cos\,\theta \end{bmatrix} \tag{175}$$

$$\theta = cos^{-1}(k_z) = sin^{-1}\left(\sqrt{k_x^2 + k_y^2}\right) \tag{176}$$

$$\phi = tan^{-1}\left(\frac{k_y}{k_x}\right) \tag{177}$$

Therefore, the direction of propagation for beamforming can be easily calculated based upon the following estimates:

Table 14
DOA Performance Estimates of Vector Aperture

Array Size Performance (6) (MATLAB)	MATLAB Measured Performance (usec)	Samples
$\Omega(6) = 0.5(10)^{-4}$	$422.5 + \Omega$	1000
$\Omega(6) = 0.5(10)^{-4}$	$649 + \Omega$	2000
$\Omega(6) = 0.5(10)^{-4}$	$1359.5 + \Omega$	4000

As compared to the vector aperture, the uniform planar array must compensate for spatial ambiguity, create a signal covariance and utilize a minimal ESPRIT calculation to derive the DOA with twice the number of elements to maintain polarization discrimination between multiple, co-located devices. I used the same array size as that used by the vector array; however, in reality the spatial array must have twice more elements (i.e. 18 elements) and require additional processing.

Table 15
DOA Performance Estimates of Uniform Planar Array (3x3) array

Array Size Performance (9) (MATLAB)	MATLAB Measured Performance (usec)	Samples
$\Omega(9) = 0.5(10)^{-4}$	$59052 + \Omega$	1000

$\Omega(9) = 0.5(10)^{-4}$	$215947 + \Omega$	2000
$\Omega(9) = 0.5(10)^{-4}$	$822244 + \Omega$	4000

The following is the Array Size impact on the use of matrices across the systems when performing beamforming calculations:

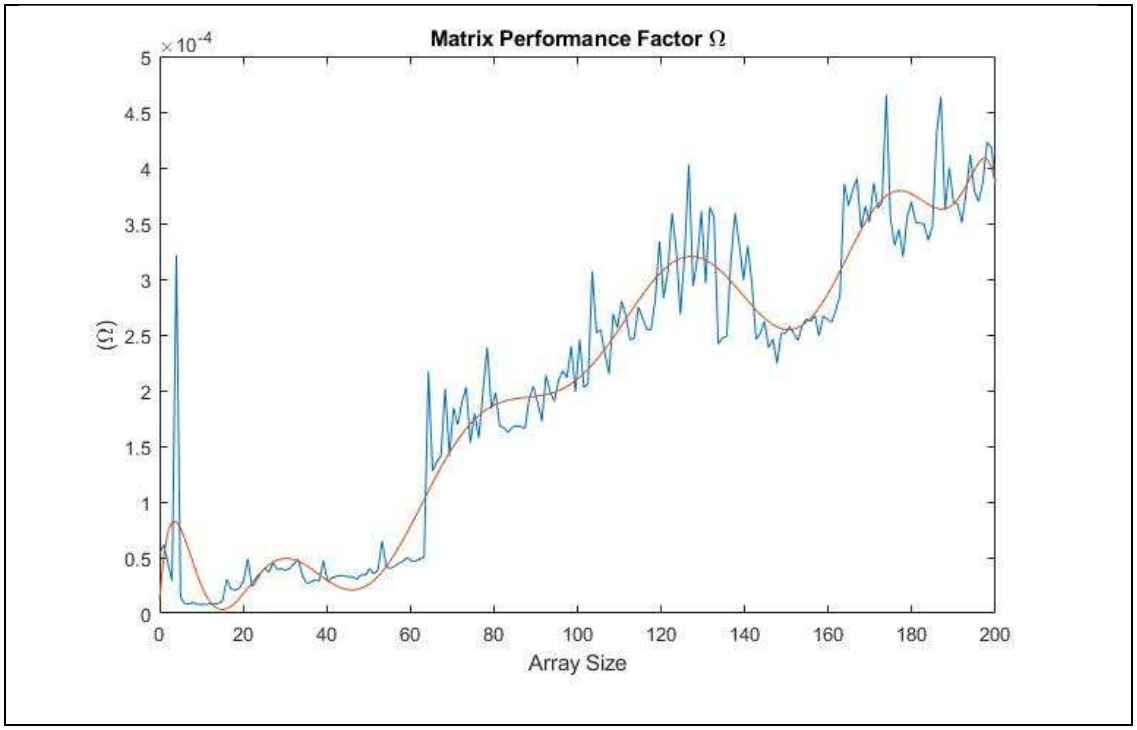

Figure 120 Matrix Math Performance as a Function of Aperture Array Size (Elements vs $\boldsymbol{\Omega}$)

The RLS versus LMS performance results were a bit surprising to me. Though the RLS algorithm did, generally, converge more quickly and provide an initial ~20dB better convergence performance, the approach appeared to be outweighed by the additional matrix math required to implement the algorithm; further research is required to determine performance comparisons using a floating point engine such as provided by a DSP or GPU. The performance results demonstrate that the Vector aperture is far

superior than any other aperture type when determining beamforming patterns and directing energy towards those beams. These algorithms were used to set beam weights that demonstrate apply nulls in the direction of the interfering signals; however, I only used one interfering signal because that analysis was beyond the scope of this project.

Linear Prediction Voice Algorithm

Voice communications performance is achieved by improving upon using a linear prediction whose coefficients are solved using the Levinson-Durbin algorithm. Linear prediction performance can also be improved using the RLS algorithm. The Linear prediction algorithm reduces the symbol rates required over a wireless communication link to support voice communication; only the model coefficients are transmitted. The following is an example of the Levinson-Durbin algorithm performance. The following overview is followed by a derivation for the Levinson-Durbin algorithm for forward linear prediction follows:

In general, we may express this predicted value as a function of the given P past samples:

$$\check{x}(xn|n-1,\ n-2,\ ...,\ n-P) = \Psi(x(n-1),\ x(n-2),\ ...,\ x(n-p)) \quad (178)$$

Now, if this function Ψ is a linear function of the variables: x(n − 1), x(n −2), ..., x(n − P) , we say that the prediction is linear. In a M dimensional space spanned by x(n-1), x(n-2), ..., x(n-P). Hence, we can write:

$$\check{x}\,(n|n-1, n-2, \ldots, n-P) = \sum_{k=1}^{P} a_k(n-k) \quad (179)$$

Based upon the following diagram:

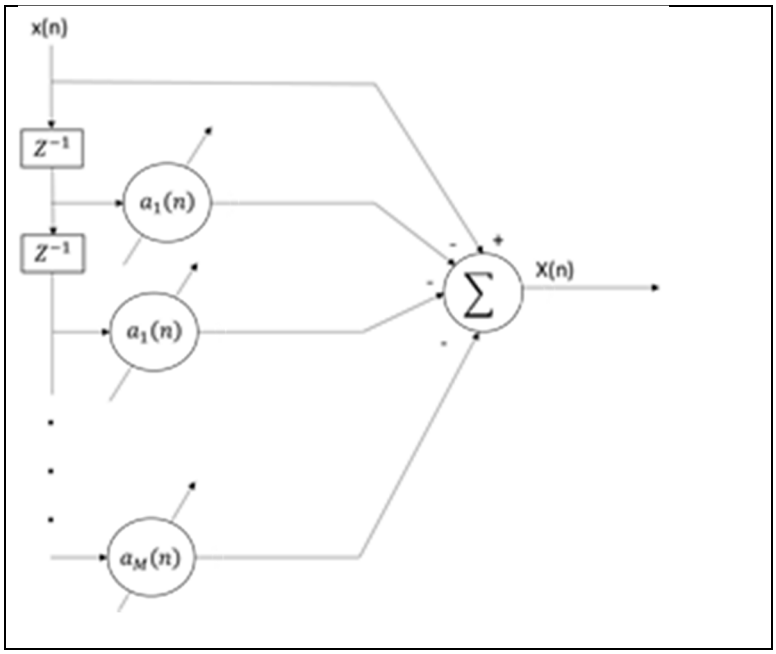

Figure 121 Forward Linear Prediction for the Levinson-Durbin Voice Algorithm

$f_P = x(n) - \tilde{x}\,(n|n-1, n-2, \ldots, n-P) = \sum_{k=1}^{P} a_k(n-k)$: P represents the number of past samples used to predict the next sample. We will now derive the Levinson-Durbin algorithm:

$$r_{m+1} = [(1) \quad (2) \cdots r(m) \quad r(m+1)]^T = \begin{bmatrix} r_m \\ r(m+1) \end{bmatrix} \tag{180}$$

$$R_{m+1} = \begin{bmatrix} R_m & r_m^B \\ (r_m^B)^T r(0) \end{bmatrix} = \begin{bmatrix} r(0)\, r_m^T \\ r_m \;\; R_m \end{bmatrix} \tag{181}$$

$$\psi = \begin{bmatrix} a_{m-1} \\ 0 \end{bmatrix} - \frac{\Delta_{m-1}}{P_{m-1}} \begin{bmatrix} 0 \\ a_{m-1}^B \end{bmatrix} \quad \Delta_{m-1} = r_m^T a_{m-1}^B = a_{m-1}^T r_m^B \tag{182}$$

$$= r(m) + \sum_{k=1}^{m-1} a_{m-1} r(m-k)$$

$$Multiplying\ on\ the\ right\ side\ by\ R_{m+1} = \begin{bmatrix} R_m & r_m^B \\ (r_m^B)^T r(0) \end{bmatrix} = \begin{bmatrix} r(0)\, r_m^T \\ r_m \;\; R_m \end{bmatrix}$$

$$R_{m+1}\psi = R_{m+1}\left\{\begin{bmatrix} a_{m-1} \\ 0 \end{bmatrix} - \frac{\Delta_m}{P_{m-1}}\begin{bmatrix} 0 \\ a_{m-1}^B \end{bmatrix}\right\} \tag{183}$$

$$= \begin{bmatrix} R_m & r_m^B \\ (r_m^B)^T & r(0) \end{bmatrix}\begin{bmatrix} a_{m-1} \\ 0 \end{bmatrix} - \frac{\Delta_{m-1}}{P_{m-1}}\begin{bmatrix} r(0) & r_m^T \\ r_m & R_m \end{bmatrix}\begin{bmatrix} 0 \\ a_{m-1}^B \end{bmatrix}$$

$$= \begin{bmatrix} R_m a_{m-1} \\ (r_m^B)^T a_{m-1} \end{bmatrix} - \frac{\Delta_{m-1}}{P_{m-1}}\begin{bmatrix} r_m^T a_{m-1}^B \\ R_m a_{m-1}^B \end{bmatrix}$$

$$= \begin{bmatrix} R_m a_{m-1} \\ \Delta_{m-1} \end{bmatrix} - \frac{\Delta_{m-1}}{P_{m-1}}\begin{bmatrix} \Delta_{m-1} \\ R_m a_{m-1}^B \end{bmatrix} = \begin{bmatrix} P_{m-1} \\ O_{m-1} \\ \Delta_{m-1} \end{bmatrix} - \frac{\Delta_{m-1}}{P_{m-1}}\begin{bmatrix} \Delta_{m-1} \\ O_{m-1} \\ P_{m-1} \end{bmatrix}$$

$$\begin{bmatrix} P_{m-1} - \frac{\Delta_{m-1}^2}{P_{m-1}} \\ O_{m-1} \\ \Delta_{m-1} - \Delta_{m-1} \end{bmatrix} = \begin{bmatrix} P_{m-1} - \frac{\Delta_{m-1}^2}{P_{m-1}} \\ O_m \end{bmatrix} \tag{184}$$

…Augmented Wiener-Hopf Equation: $R_{m+1}a_m = \begin{bmatrix} P_M \\ 0 \end{bmatrix}$

$$R_{m+1}\psi = \begin{bmatrix} P_{m-1} - \frac{\Delta_{m-1}^2}{P_{m-1}} \\ O_m \end{bmatrix} \ldots \psi(1) = a_{m-1,0} = 1 \ , \tag{185}$$

Since R_m is nonsingular, the unique solution above provides the optimal detector $a_m = \psi$; the following recursion and optimal error power is the following:

$$P_m = P_{m-1} - \frac{\Delta_{m-1}^2}{P_{m-1}} = P_{m-1}\left(1 - \frac{\Delta_{m-1}^2}{P_{m-1}}\right) = P_{m-1}(1 - r_m^2) \ldots r_m = -\frac{\Delta_{m-1}}{P_{m-1}} \tag{186}$$

Finally, the following Levinson-Durbin Recursive Equations now follow:

$$a_m = \begin{bmatrix} a_{m-1} \\ 0 \end{bmatrix} + r_m \begin{bmatrix} 0 \\ a_{m-1}^B \end{bmatrix} \ = \text{Vector Form of Levinson Durbin} \tag{187}$$

$a_{m,k} = a_{m-1,k} + r_m a_{m-1.m-k} \quad k = 0,1, \dots, m$ = Scalar form of Levinson Durbin (188)

$$\Delta_{m-1} = a_{m-1}^T r_m^B = r(m) + \sum_{k=1}^{m-1} a_{m-1,k} r(m-k) \tag{189}$$

$$r_m = -\frac{\Delta_{m-1}}{P_{m-1}} \qquad P_{m-1}(1 - r_m^2) \tag{190}$$

In such a model, we assume the signal can be represented as a time series where the digital filter is excited by white noise. The digital filter parameters are estimated during recording the voice information. We utilize Auto Regressive (AR) method for parametric estimation:

$$s(n) = b_0 w(n) - \sum_{k=1}^{P} a_k s(n-k) \tag{191}$$

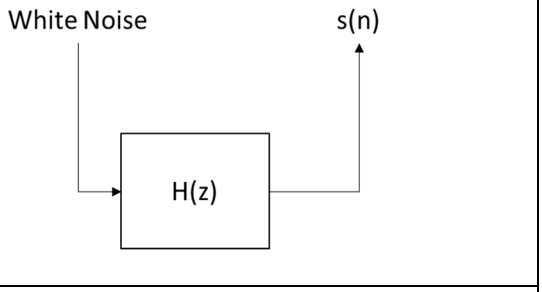

Figure 122 Filter Excited by White Noise

The following frequency domain representation describes the AR process that is based upon the IIR (all-pole) model where coefficients are calculated using linear prediction:

$$s(n) = \sigma_w^2 \left| \frac{1}{A(e^{j\Omega})} \right|^2 \tag{192}$$

The AR parameters are used to represent the signal through autocorrelation equations which are called AR Yule-Walker equations:

$$r_{ss}(k) = \sigma_w^2 \delta(k) + \sum_{i=1}^{P} a_i r_{ss}(k-i) \tag{193}$$

Represented in matrix form as the following:

$$\begin{bmatrix} r_{ss}(1) \\ r_{ss}(2) \\ \cdots \\ r_{ss}(P) \end{bmatrix} = \begin{bmatrix} r_{ss}(0) & r_{ss}(-1) & r_{ss}(1-P) \\ r_{ss}(1) & r_{ss}(0) & \ddots\ r_{ss}(2-P) \\ \cdots & \cdots & \cdots \\ r_{ss}(P-1) & r_{ss}(P-2) & r_{ss}(0) \end{bmatrix} \begin{bmatrix} a_1 \\ a_2 \\ \cdots \\ a_P \end{bmatrix} \tag{194}$$

In order to solve for matrix coefficients $\bar{a}_{1-P}$, the autocorrelation matrix must be inverted. This is performed utilizing the Levinson-Durbin algorithm. The following is an example speech wave form that was modeled using the Linear Prediction and the Levinson Durbin algorithms:

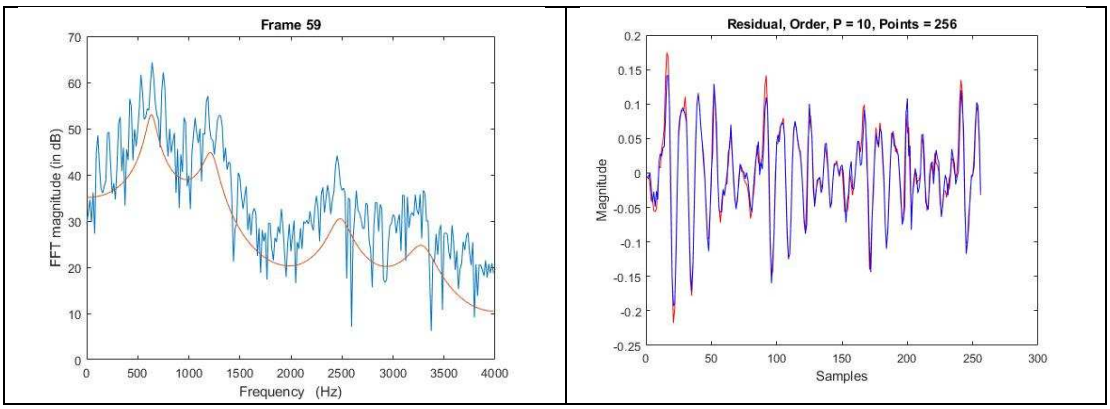

Figure 123 Example speech frame 1

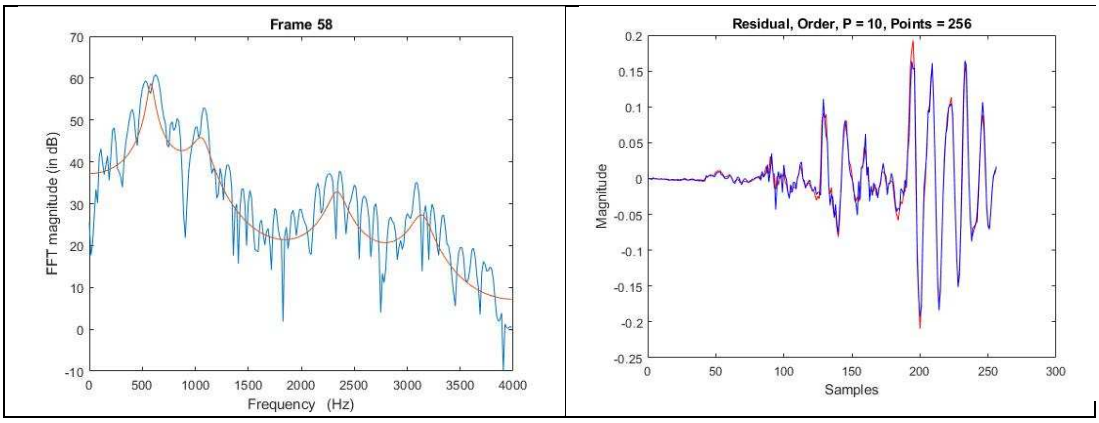

Figure 124 Example speech frame 2

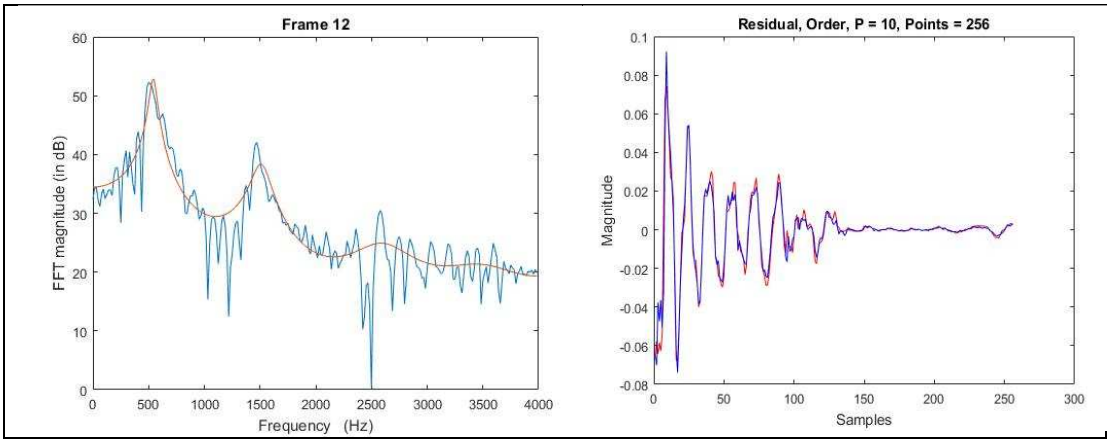

Figure 125 Example Speech Frame 3

These plots represent the frequency spectrum of the 256, 16 bit frame sample with the frequency response overlay on the same graph. Using the Levinson-Durbin algorithm (implemented, in this case, using the lpc MATLAB function). To the right of these plots are the residual (estimation error) calculated using the coefficients calculated using the Levinson-Durbin algorithm. In regard to the frequency plots, you will see peaks and valleys. The peaks represent poles while the valleys represent zeros. Since this algorithm calculates all-pole coefficients, sharp transitions to zeros cannot be represented well. The order of the algorithm specifies the obtainable performance. This algorithm

demonstrates that signals can be reconstructed using the all-pole $1/A(z)$ coefficient estimates derived using the Levinson-Durbin algorithm. As an example, by transmitting only these all-pole coefficients across a wireless communication channel, a white noise source [on a cell phone] can be used in conjunction with these coefficients to reconstruct the transmitted voice signal. In so doing, this reduces the symbol rates required over a wireless communication link to support voice communication; only the model coefficients are transmitted providing the following performance improvements over the wireless channel:

Table 16
Exemplar: Order P = 10, Levinson-Durbin Voice Communication Performance Improvement (Higher order will have higher accuracy, but less reduction performance)

Voice Sample Bits	Model Bits	Reduction Performance Improvement
4096	160	96.1%

If the input sound on the audio device does not detect a magnitude of 9dB or higher above the noise floor, further reduction in bits can be achieved. In such a model, when people converse, there are times of no sound; during these times, no analog input above 10dB is detected and therefore no data should be transmitted during this time. Assuming an average conservative model of ~6% idle pause in speaking (~200ms Ref: Stephen Levinson, Max Planck Institute for Psycholinguistics), the following further improvement is achieved:

Table 17
Example Voice Communication Improvement (32,000 UEs/16 sample, Order P =10), Higher Order will have greater improvement

Voice Sample Bits (~8KHz Rate)	Model Bits	Reduction Performance Improvement	Reduction After Proposed Improvement	Additional Performance Improvement	Final Rate After Improvement
~4,096,000 Kbs	~160,000 Kbs	~96.1%	96.33%	~9,600 Kbs	~150,400 Kbs

Additional improvements in the performance of the linear predictor utilizing the RLS algorithm are possible. The RLS/LMS comparison was discussed in other sections of this document: Beamforming and MIMO (spatial and vector apertures), Channel Equalization and Use of Parallel Correlators.

Roaming Performance

The proposed approach is for software programmed, hardware accelerated state machines to receive the measurement reports from mobile users. Upon receipt of these reports, the hardware accelerated state machines roam devices (from the network side) based upon RF performance and/or load distribution. This section will describe three roaming conditions followed by quantitative numbers in regard to expected performance based upon a hardware accelerated data path that supports load sharing and roaming. Two types of inter-RAT handover algorithms and a 4G handover were evaluated. The first case was the Inter-RAT (WCDMA RAN to GSM) based upon the Inter-RAT handover algorithm. The following are the measurement report attributes:

- The UE monitors the Downlink CPICH Ec/No and CPICH RSCP. The UE informs (in uplink) the connection quality (i.e. DL:Ec/No, DL:Rscp) the RNC monitors this report along with UL power quality (RSCP: received signal code power)
- The Uplink UE Tx power is monitor by the RNC
- When at least one of these measurements drops below a threshold, a IRAT GSM handover (HO) is requested, if improvement is detected once request is made, HO is aborted

Note: WCDMA RAN allows different thresholds to be set.

- If conditions remain unchanged, the HO to WCDMA completes.

A handover (HO) from WCDMA RAN to GSM can also occur when load sharing is required by sending Radio Access Bearer (RAB) assignment reject messages with 'directed retry' as the cause for speech only calls. The call network (CN) will redirect the call to the GSM cellular network.

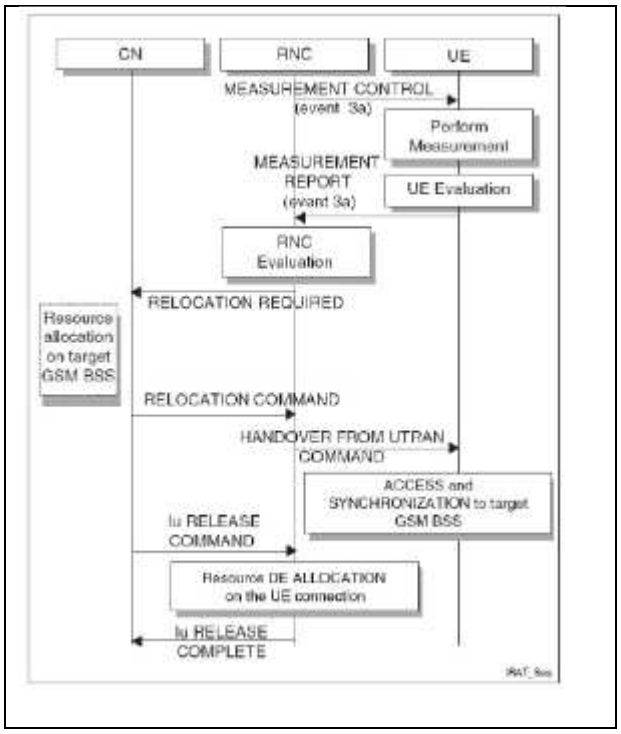

Figure 126 WCDMA to GSM Handover
(Ref: TechNote 2009)

One that performs the Inter-RAT (GSM to WCDMA) based upon the Traffic Channel (TCH) is below the percentage of idle TCH is below the is hand over level (ISHOLEV) and the Ec/No in the Common Pilot Channel (CPICH) is greater than the Mobile Relay Station Level (MRSL)

Note: 2G/GSM to 3G/WCDMA can occur because UTRAN is the preferred network.

- Under these conditions, when a UE is connected to a packet-switch (ps) network, a Cell change & reselection function is activated

Note: Inter-RAT handover enables resources on the target cell while Inter-RAT Cell Change requires no resources reserved in the target cell before hand

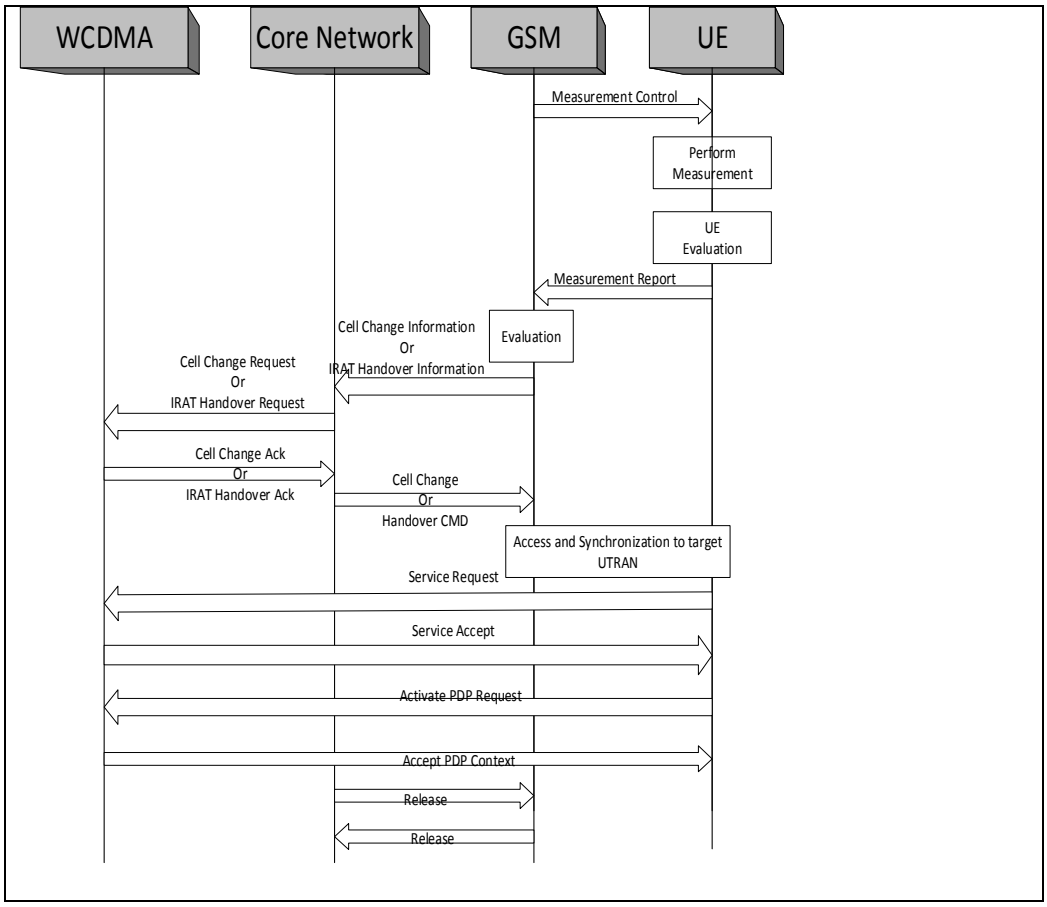

Figure 127 GSM to WCDMA Handover Sequence

- The following parameters are evaluated during the GSM to WCDMA handover.

The following must be true:

- TCH <= ISHOLEV
- CPICH Ec/No > MRSL and CPICH Ec/No > FDDQMIN
- CPICH RSCP > RLA (serving + neighboring GSM cells) + FDDQOFF
- Note: FDDQOFF is the key parameter: it defines an offset between signal quality

of WCDMA and GSM cells. Lower values of FDDQOFF ould be used to off-load the GSM system. Higher values of FDDQOFF could used to keep multi-RATE MS in the

GSM system, example: if a WCDMA to GSM off-load priority setting is applied in the WCDMA system.

4G/5G Handover

The case that requires a new serving gateway (SGW) is required was the only case evaluated since the proposed change to the design would have to work even when the new node is part of a different cell which requires a different IP address domain such that a new SGW would be required.

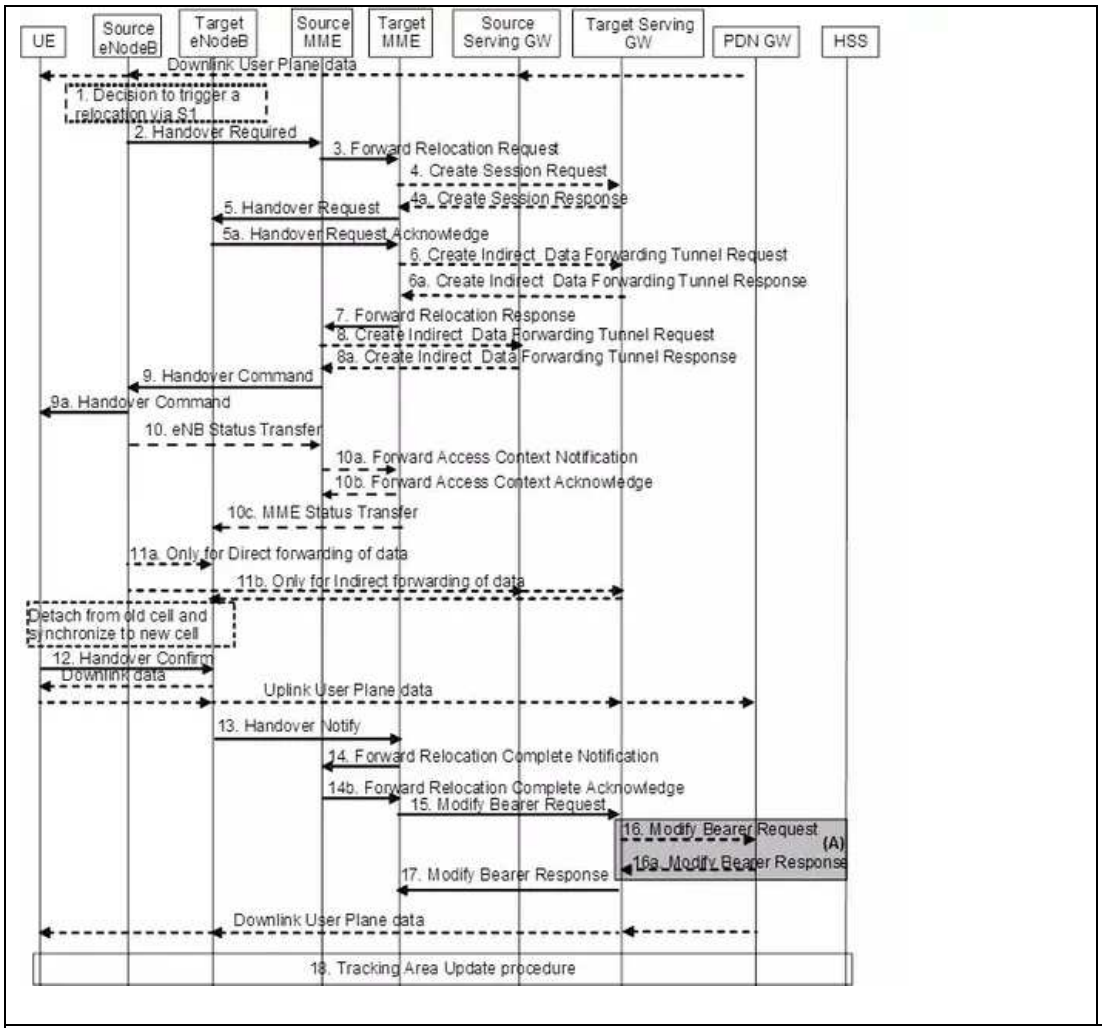

Figure 128 4G Handover Sequence

Improved Roaming Performance

The architecture depicted below describes the physical dimensions (i.e. 25.4mm per 4 analog isolated channels) to support a RF configuration that provides greater than 60dB per channel receive and transmit isolation for frequencies up to 6GHz. At higher millimeter wave (mm-wave) frequencies, due to their smaller λ size, the analog signals are more dense and harder to isolate; in the architecture above, the analog portion of the design is separated from the digital side to provide a method of isolating and scaling the analog portion to these higher frequencies. Further research is planned in the use of special fabrication & integration techniques such as the use of Polystrata material where the interposer could be 3D air substrates separating the individual components thereby providing improved isolation at mm-wave frequencies for large aperture arrays.

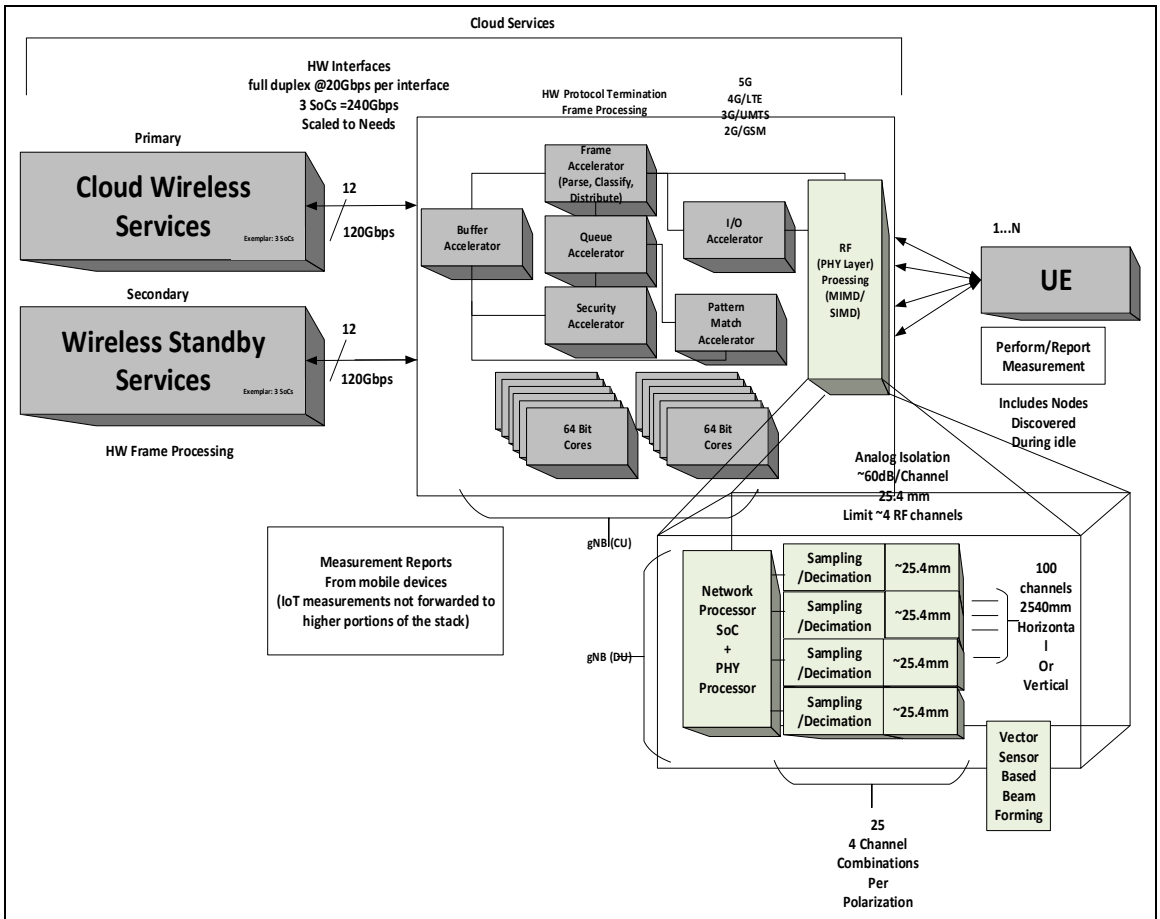

Figure 129 Exemplar Freescale/Cavium Hardware Protocol Termination (up to 6GHz) with a Uniform Planar Array of 10x10, Circularly Polarized

The architecture is a version of an access independent architecture that describes ~12, 64 bit von Neumann processor utilizing 14nm FinFET 3-dimensional System on Chip (SoC) CMOS technology; while on the physical layer processing, a Multiple/Single Instruction Multiple Data (MIMD/SIMD) architecture implemented using either a Harvard or Vector processor design, so classified by Flynn's taxonomy, is depicted. For RF processing, it is estimated that, given a density of 1M/Km^2. For network frame processing, it provides hardware accelerated protocol termination where user traffic flows directly through the 14nm FinFET hardware state machines without intervention by the SoC GPP cores. On

the 10Gbps links, hardware managed buffering is provided by the buffer accelerator; based upon RFC 3439, average buffering is calculated as follows for N flows:

$$L_B = \frac{(RTT)(10^9)}{\sqrt[2]{N}}, where\ RTT = 250usec, C = Link\ speed, N = \#\ of\ flows \quad (195)$$

Due to the density of devices 1M/Km^2 , the IPv6 addresses must be used so that all devices can be accommodated with assigned IP addresses. At a minimum, the following IPv6 address range is required with a 108 bit prefix: [fe80:0000:0000:0000:9999:999x:xxxx] to [fe80:0000:0000:0000:9999:999f:ffff] to permit greater than 1M addresses. Since IPv6 mobility is integrated into the IPv6 protocol, no special accommodations are required to support roaming between nodes in the network. The concept of the design depicted above is to reduce the network transactions required when roaming is necessary due to loss of RF visibility.

The roaming diagrams above depict the sequence of transactions required for a device to hand off to another base station. This transaction sequence can occur with less UE interaction. The cloud service in the diagram above can detect the loss of link based upon the measurement report which can include the device location. The combination of the device location and the measurement report provides the cell controller with the information required to command the device. In this scenario the SGSN GW and possibly the target SGSN GW is in the cellular cloud service layer. Therefore, the IPv6 address is managed internally through memory interfaces. Additionally, since an IP tunnel can exist between geographically dispersed cloud services, target GW's are managed in a similar manner. This more centralized cloud service approach reduces the

number of network protocol transactions, the following performance improvement is provided as an estimate:

Table 18
Performance Estimates

Performance	Existing Roam Transaction Model	Proposed Model	Rationale
Interface Speeds (/transaction) Roaming events/ MME Transactions/ GW Transactions)	10Gbs	Network=40Gbps (SoC) HW FSM=51.2Gbps (DDR3)	Src,Tgt: MME same SoC Src,Tgt: GW same SoC Src,Tgt: gNB (CU) same SoC HW FSM = Finite State Machine (Internal Performance = 104Gbs=52Gbps
Interface Latency	0.416usec	13.93ns	Existing Model: 10Gbs DDR3/3 L=1866MT/s 64 (bits)*1.866(10^9)=104.5 (10^9)=104Gbs
Reduced Network Transaction Savings Roam Event (see Figure 128)	N/A	6.175usec	Src,Tgt: MME same SoC Src,Tgt: GW same SoC Src,Tgt: gNB (CU) same SoC 3 MME Interactions (IMIX -576B) 2 GW Interactions (IMIX - 576B) $4.608(10^4)$ = Total Transactions $4.608(10^{-6}) + 5((.416)10^{-6})$=Existing $4.41(10^{-7}) + 5\left((13.93)10^{-9}\right) = New$
gNB (DU) Full Line Rate	10Gbps	40Gbps	Upgraded Network Processor SoC

Transactions speeds were calculated based upon the assumption that the 5G model is based upon interface rates related to 10Gb Ethernet technology for most transaction interfaces. The proposed model processes transactions with SW programmed HW state machines that utilize memory interfaces. Using the Freescale T4240 as an example, the transaction speeds are equivalent 104Gbs.

Moore's Law has slowed, and semiconductor vendors are forced to provide value in new ways to enhance their capabilities to generate new sales. This is forcing greater integration of specialized capabilities to be integrated into their products. The exemplars above represent network processing chips where specialized network frame processing capabilities continue to be integrated.

User-Based Technology

5G NR technology utilizes user-based performance which implements user-based quality of service (QoS). During negotiation of the cellular session established by the user equipment (UE) through the Radio Access Technology (RAT) protocol, which permits communication with individual UE, UE identifiers are extracted from protocol field elements. 5G RAT is comprised of the enhanced LTE RAT technology + new RAT technology. Enhanced LTE RAT technology provide enhancements to the orthogonal frequency division multiple access (OFDMA) carriers which permit different uses of subcarrier implementations which were previously focused on single carrier (SC) OFDMA communication in the reverse direction from the UE to the network. In some

cases, more (or less) carriers can be assigned to an individual UE based upon QoS classification related to the device type.

At the protocol level, 5G NR enables user-based technology that provides QoS and routing that changes the previous network QoS paradigm of routing classification via IP address, IP protocol, IP port numbers, and type of service (ToS) or differentiated services code point (DSCP). Instead, 5G enables user groups with differing levels of service. Device information is extracted during the initial device entry into the network. During the initial attach procedure, Device queues are configured so that QoS can be implemented for traffic to/from the rest of the network (RoN). The following is an example of queues set up for device groups:

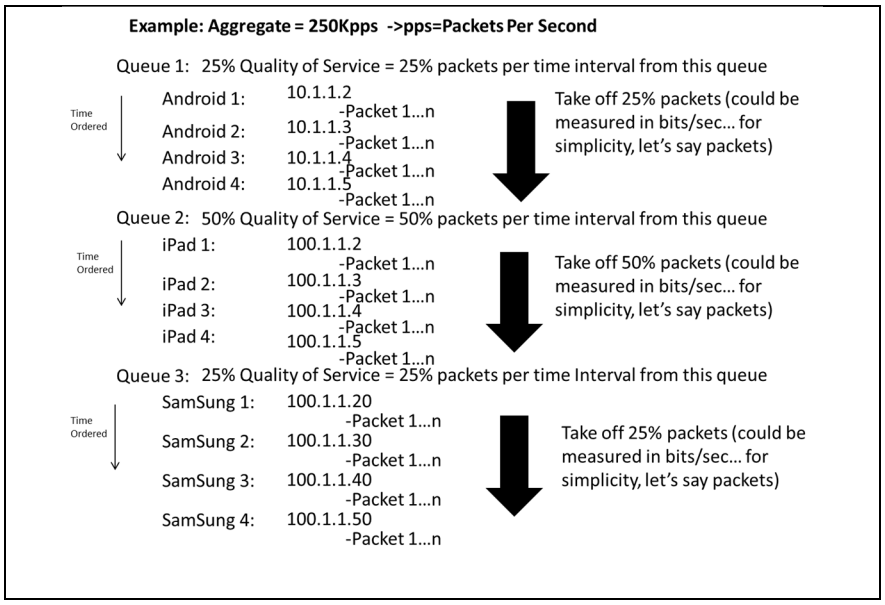

Figure 130 Example User Based Packet Queue (HW Synthesis Provides 40Gbps Stream)

These user groups provide characterization that supports the network slicing architecture defined by the new 5G NR specification. The 5G NR slicing architecture provides the

ability to provide different performance characteristics where each slice operates as an independent, virtualized version of the network. For the application, the network slice is the only network it sees; other, unsubscribed, slices are not visible to the application. The concept is that each slice targets a different user group, one slice could target low-throughput IoT sensors, another autonomous vehicles, while another provides enhanced broadband. The proposed concept supplements this capability by enabling QoS differentiated services within the same network topology using hardware state machines to implement the LLQ or WFQ schemes. These QoS hardware services can then be integrated with existing network infrastructure directly to cloud services which utilize both 802.1pq, layer 3 switching and IP based differentiated services as part of the software defined network (SDN) created as part of the cloud network service layer. QoS management of user-based queues is based upon several algorithms such as:

- Weighted Random Early Detect (WRED)

A hardware accelerator would implement a weighted average by maintaining the length of the output queue; if the output queue length is less than a minimum threshold min_{th} when a packet arrives, the packet is admitted to the queue. If the queue is full or the average queue length is greater than a max threshold max_{th}, the packet is dropped. If the average queue length is in the interval [min_{th}, max_{th}] when the packet arrives, it is dropped. Used as a congestion avoidance algorithm that drops packets that are marked with a certain probability which depends on weight and queue length for data frame exchanges for each user group.

- Low Latency Qeueing (LLQ)

The hardware accelerator would provide strict priority frame queueing similar to the concept described above except the queue is managed on strict priority basis such that jitter and latency are constant for voice and video data exchange for each user group. These algorithms are then used to provide input into Dijkstra's algorithm; the example below can be compute optimized by using an enhanced queueing methodology where a priority queue (see Brodal queue or Fibonacci heap (Fredman & Tarjan 1984)) is implemented using an abstract data type and data structure:

```
function Dijkstra():
N' = {U}//N' is subset of nodes, v is in N' if the least-cost path
       //from the source to v is definitely known
for all nodes v
     if v is adjacent to u
      then D(v) = c(u,v)  // where c(u,v) is the cost from u to v
     else
        D(v) = INFINITY
      end
end

for all nodes in N'
    find w not in N' such at D(w) is a minimum
    add w to N'
    update D(v) for all adjacent to w and not in N':
    D(v)=min(D(v),D(w)+c(w,v))
    // new cost to v is either old cost to v or known shortest path
    // cost to w plus cost from w to v */
end
end // function Dijkstra ()
```

Figure 131 Example Dijkstra's Algorithm deriving Link-State (LS) Routing (Computer Networking, Kurose Ross, 5th Edition)

User based prioritization prioritizes data toward the rest of network (RoN) by translating priority to network protocol fields in the following virtualized cloud service protocol

examples: IP DSCP (ToS), 802.1pq, Routing Protocols: MPLS, RIP, OSPF and EIGRP; at the core of these protocols are the complementary Dijkstra's (LS) and Distance-Vector (DV) algorithms. In the opposite direction, user-based prioritization prioritizes wireless data from RoN to wireless user equipment (UE) at the RAT level, through user based QoS queues and with protocol prioritization. In 5G the notion of QoS network slicing was presented where virtual access is provided only to specific users within a group who have differentiated service access.

As wireless and backhaul communication rates increase (such as over FioS as one example), frame processing will continue to transition to HW acceleration without SW intervention due to the inability of software frame processing to keep up with the required frame processing rates. As defined by the Flynn taxonomy, wireless technology appears to be implementing a mix of Von Neumann and hyperscale processing technology using Xilinx FPGAs that enable processing of complex data sets. Presently, the Von Neumann bottleneck has only gotten worse over time, as the disparity between processor speed and memory access throughput speed has widened. Other hyperscale processing solutions for complex data sets are under evaluation to include GPU's provided by Nvidia and AMD. Future silicon implementing massively parallel MIMD processing architectures include PicoChip (now part of Intel) and Coherent Logix. Bandwidths are increasing, forcing 5G base stations to transition to more capable processors that provide hardware accelerated data frame processing and enhanced security protections. Examples of such architectures are the network processors provided by Intel (IXP2800), Freescale QorIQ (T4240), Broadcomm (BCM5871X), Nokia (FP3/FP4) and Qualcomm (X50) to name a few. Such

architectures terminate and route L2 andL3 based data path protocols used over wireless links to eNodeB without SW intervention. Specialized SoC's such as these provide software defined network (SDN) control over frame processing while hardware state machines accelerate frame processing beyond the speeds possible using SW.

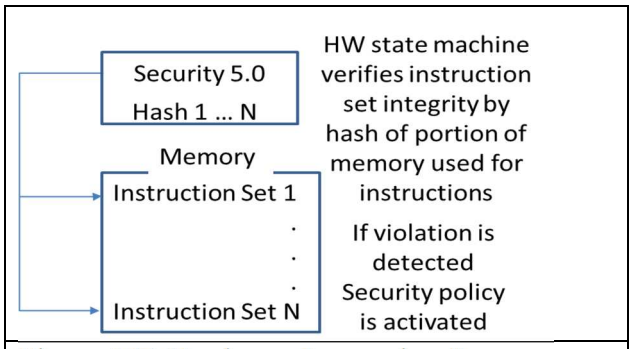

Figure 132 Hardware Instruction Set Verification

In addition to network processing capabilities, semiconductor vendors are integrating improved security features into their SoCs. The security chain of trust starts at the beginning by the use of anti-tamper and anti-clone technology; these are implemented using Physical Uncloneable Function (PUF) technology in concert with such protections as zeroizable fuses that deactivate the chip upon power up or upon security violation detection. SRAM PUF leverages inherent manufacturing variations to create identifiers that are more unique that the human fingerprint. Further, HW trust architectures maintain chain of trust by providing hardware protection engines: I/O isolation, secure boot, hypervisors, pattern match, entropy sources and block/stream based cryptographic algorithms (such as elliptical and RSA) that protect against cyber threats. Security hardware engines verify SW instructions from the beginning using secure boot, HW I/O isolation using hypervisors and peripheral management units (PAMU). Instruction memory is continually protected against cyber threat manipulation by continually

verifying portions of the processor memories used for instruction sets; if any instructions are modified, a security violation is detected and the security policy is implemented. Network data is routed (by hardware state machines -without SW intervention) to real-time HW engines to detect patterns (in some cases millions of pattern combinations are evaluated to detect cyber threats). In such architectures, SW is not trusted to access raw key material; no unencrypted key material is present on any external bus including the memory bus, any and all keys provided to SW are encrypted using cryptographic algorithms such as AES-256 CCM using random entropy. The processors include cryptographic engines with 32- and 64-bit entropy sources (e.g. Random Number Generators (RNG)) that can be configured to add random content on a per cryptographic frame basis at rates exceeding 40Gbsec (>40Gbsec/chip). The architecture assumes a "bump in the wire" cryptography in HW managed frame processing.

Most cellular devices have HW implemented entropy sources (such as RNG) to provide random input to the Levinson-Durbin algorithm used to reconstruct voice information over challenged links. Such entropy sources can also be used to provide random entropy for secure communications.

Control, management and exception frames are routed to the central processing unit to be handled by SW, though hardware must be used to verify security key material since SW is not a trusted source for key material on such an architecture.

The following are the published 3GPP specifications for the 5G protocol stack, though there is misleading information due to differences between published literature and the actual 3GPP specification under document control and further leaks of coming 3GPP specification releases.

Table 19
LTE Resource Blocks (Ref. 3GPP specification)

Channel BW (MHz)	1.4	3	5	10	15	20
Resource Blocks	6	15	25	50	75	100

Table 20
5G NR Resource Blocks (Ref. 3GPP specification)

μ	Min. Downlink Resource Blocks	Max. Downlink Resource Blocks	Min. Upllink Resource Blocks	Max. Uplink Resource Blocks
0	24	275	24	275
1	24	275	24	275
2	24	275	24	275
3	24	275	24	275
4	24	138	24	138

Table 21
5G NR Single Carrier UE and gNB Bandwidth Requirement (Ref. 3GPP specification)

μ	Min. Resource Blocks	Max. Resource Blocks	Sub. Carrier Spacing (KHz)	Freq. BW Minimum (MHz)	Freq. BW Maximum (MHz)
0	24	275	15	4.32	49.5
1	24	275	30	8.64	99
2	24	275	60	17.28	198
3	24	275	120	34.56	396
4	24	138	240	69.12	397.44

Table 22
5G NR Channel Spacing Requirement (Ref. 3GPP specification)

μ	Subcarrier Spacing	Cyclic Prefix	Supported for Data (PDSCH,PUSCH)	Supported for Sync. (PSS,SSS,PBCH)	PRACH
N/A	1.25		No	No	Long Preamble
N/A	5		No	No	Long Preamble
0	15	Normal	Yes	Yes	Short Preamble
1	30	Normal	Yes	Yes	Short Preamble
2	60	Normal, Extended	Yes	No	Short Preamble
3	120	Normal	Yes	Yes	Short Preamble
4	240	Normal	No	Yes	Short Preamble

Table 23
5G NR OFDM Symbol Durations (Ref. 3GPP specification)

μ Numerology	0	1	2	3	4
Carrier Spacing (KHz)	15	30	60	120	240
Symbol Duration (us)	66.67	33.33	16.67	8.33	4.17
Prefix Duration (us)	4.69	2.34	1.17	0.57	0.29
Symbol including CP (us)	71.35	35.68	17.84	8.92	4.46

$$D_{rate} = (10)^{-6} \sum_{c=1}^{C} \left(N_{ant}^{(c)} \left(M_{ary}^{(c)} \right) \left(f^{(c)} \right) (U_{max}) \left(\frac{N_{PRB}^{BW(c)} (N_c)}{T_s^{\mu}} \right) \left(1 - OH^{(c)} \right) \right) \quad (196)$$

$U_{max} = Channel\ Quality\ Indicator, 64{:}\ QAM = \frac{873}{1024}, 256{:}\ QAM = \frac{948}{1024}$

$C = \#\ of\ Aggregated\ Component\ Carriers$

$OH^{(c)} = Overhead - assumed\ equal\ on\ all\ channels = 25\%$

$\mu = Numerology\ (0-5)$, release 15 = (0-4)

$f^{(c)} = Freq.\ scaling\ factor\ (0.75)$

$T_s^{\mu} = \frac{10^{-3}}{14(2^u)}, avg.\ OFDM\ symbol\ duration\ in\ a\ subframe\ for\ numerology\ \mu$

$N_{PRB}^{BW(c)}$ = is the max. resource block (RB) for numerology μ.

$BW(c) = $ Max. BW supported by the UE

$M_{ary}^{(c)} = $ Modulation Order

N_c = # of subcarriers = 12
N_{ant} = # of Antennas
(Ref: 3GPP performance estimation algorithm -Easily reproduced/derived utilizing digital communication algorithms)

Table 24
5G NR Projected Performance Calculations (reduced to release 14)

μ	Channel Spacing KHz	Max Nbr of Resource Blocks	Max. Downlink Performance	**Max. Uplink Performance
0	15	270	1.16Gbps	620Mbps
1	30	273	2.34Gbps	1.25Gbps
2	60	135	2.31Gbps	1.235Gbps
**Note: Reduced to only 2 Antennas on uplink				

Though 5G has identified 8x4 MIMO (8 spatial layers down, 4 spatial layers up), I have assumed the numbers above represent the predominate number of mobile users who will only have 2 spatially diverse antennas available for the reverse direction.

Chapter 8

CONCLUSION

Summary of Results

Based upon the performance results described in the sections above, I focused on three areas: Beamforming, voice communication and wireless roaming performance. These areas were chosen because of their consequential impact to 5G wireless performance. The following research describes proposed improvements in adaptive beamforming (utilizing machine learning) to direct energy towards end users. Next, a proposed improvement in voice communication building up the well-known Levinson-Durbin algorithm. Lastly, an improvement in wireless roaming is proposed that reduces the number of interactions required between the base station and the 5G user equipment (UE) as well as the state machine transitions on the UE. An important aspect of the design is to ensure microwave components meet the requirements of the waveform. One aspect of the design relates to the channel spacing requirement for 4G & early 5G systems which utilize 15KHz channel spacing. Based upon this narrow band requirement, receivers must meet the following phase noise requirements to enable adequate demodulation of these new, large M-ary linear modulation constellations. Assuming carrier and interference power is approximately the same, in order to achieve ~50dB of adjacent channel rejection (i.e. selectivity), the following the following phase noise requirement is described:

$$\mathrm{L} := -50\mathrm{dB} - 10\log_{10}(15\mathrm{KHz}) = -\frac{92\mathrm{dBc}}{\mathrm{Hz}} @ \sim 15\mathrm{KHz\ Offset} \quad (197)$$

(

The first investigation focused on the practical aspects of beamforming and the use of a superior co-channel and co-direction interference mitigation performance of a new type of vector sensor that can be used in conjunction with spatially diverse arrays used to identify beam directionality. This design showed great promise due to its exceptional Direction of Arrival (DOA) performance achieved through a lower computational overhead. This performance translates into greater transaction rates and responses:

Table 25
Superior Performance of the Vector Aperture (Beamforming Energy Detection)

Technique	Samples	Latency + Ω	Accuracy (deg.)	Best Performance
Poynting	1000	422.5	<2	90% over spatial array
Poynting	2000	649	0.5	41% over spatial array
ESPRIT	1000	4672	1	Susceptible to correlated noise
ESPRIT	2000	1589.5	0.2	Susceptible to correlated noise

For beamforming performance, being able to detect energy so that beams can be formed at the appropriate angle was discussed earlier. For this purpose, based upon the half power beam width in horizontal & vertical directions at 6GHz, the Poynting Vector cross product provided the most economic processing solution for a sufficient resolution to be used for dynamically beam forming.

The next research investigation built upon the Levinson-Durbin algorithm as a basis for evaluating voice communication performance. As demonstrated by the results of the Levinson-Durbin test results, the algorithm performance demonstrates impressive voice modeling performance. As part of my research I proposed an algorithm modification to

further reduce voice traffic bandwidth and thereby increase bandwidth as shown in the following table:

Table 26
Example Voice Communication Improvement (32,000 UEs/16 sample), Model Order P=10, Higher Model Order will Yield Additional Performance Improvement

Voice Sample Bits (~8KHz Rate)	Model Bits	Reduction Performance Improvement	Reduction After Proposed Improvement	Additional Performance Improvement	Final Rate After Improvement
~4,096,000 Kbs	~160,000 Kbs	~96.1%	~96.33%	~9,600 Kbs	~150,400 Kbs

This improvement takes advantage of the periodic nature of voice conversations. Lastly, I described a new link layer communication system design that manages and routes wireless communication frame traffic to and from wireless devices that decreases latency and increases performance as defined in the following table:

Table 27
Performance Estimates

Performance	**Existing Roam Transaction Model**	**Proposed Model**	**Rationale**
Interface Speeds (/transaction) Roaming events/ MME Transactions/ GW Transactions)	10Gbs	Network=40Gbps (SoC) HW FSM=59.7Gbps (DDR3)	Src,Tgt: MME same SoC Src,Tgt: GW same SoC Src,Tgt: gNB (CU) same SoC HW FSM = Finite State Machine (Internal Performance = 119Gbs~=60Gbps
Interface Latency	0.416us	13.93ns	Existing Model: 10Gbs DDR3/3 L=1866MT/s 64 (bits)*1.866(10^9)~=119.4Gbs

Reduced Network Transaction Savings Roam Event (see Figure 128)	N/A	6.175usec	Src,Tgt: MME same SoC Src,Tgt: GW same SoC Src,Tgt: gNB (CU) same SoC 3 MME Interactions (IMIX -576B) 2 GW Interactions (IMIX -576B) $4.608(10^{4})$ = Total Transactions $4.608(10^{-6}) +$ $5((.416)10^{-6})$=Existing $4.43(10^{-7}) +$ $5\left((13.93)10^{-9}\right) = \text{New}$
gNB (DU) Full Line Rate	10Gbps	40Gbps	Upgraded Network Processor SoC (IMIX) Existing: 9 cores ~=250,000pps (limited by 8K instructions/packet @ 2GHz) Existing: 40Gbs ~=36 cores New: 40Gbs ~=8,389,261pps Ref: Freescale T4240

This research focused on the requirements and algorithms required to improve beamforming performance with a larger number of antenna elements, an improvement in the use of the Levinson-Durbin voice communication algorithm and the use of hardware acceleration on the network base station side to improve wireless network performance. From the tables above, I have derived the following performance numbers assuming a realistic population of only 250K (Ref: Deployment of 5G Olympics, 2020) concurrent active mobile users within the total 5G population of 1M/Km^2.

Table 28
Performance Enhancements

Performance	Before Algorithm Improvement	After Algorithm Improvement	Total Savings
Increase in Mobile Communication Bandwidth (Voice)	1.25Gbs	1.175Gbs	75Mbs, Higher Efficiency Assumed (IoT)
Beamforming Coefficient Calculations Using Vector Aperture	4672usec	422.5usec	As much as 91% reduction in latency Reduction=0.91(new beam caused by user access)
Frame Processing	500Kpps	2Mpps	*Based upon HW acceleration performance measurements per 10G interface, 4K instructions per frame @2GHz

Beam steering, improved RF efficiency and higher performance network processing will become much more important in 5G architecture and this paper focused on additional design considerations and approaches to provide superior co-channel and co-direction interference mitigation performance by using a new type of vector sensor that can be used in conjunction with a new link layer communication design that manages and routes wireless communication frame traffic to and from wireless devices. The vector sensor provided superior beam forming performance and sufficient DOA accuracy which is estimated by the half power beam width, at 6GHz requires ≤ ~2 degrees, at 24GHz ≤ ~1 degree is sufficient beam forming accuracy. Further research is planned in the area of MIMO concepts such as the use of Alamouti STBC to increase the achievable gain in the millimeter frequency ranges using a uniform planar array (ULA); however, Maximmal Ratio Combining (MRC) has proven to be more effective. I evaluated the performance

between LMS and RLS algorithms in the use of beam forming and discovered that, though the RLS algorithm converges more quickly, it required a greater number of instructions to execute. Further research is necessary to fully evaluate the convergence performance with a larger set of interfering signals. This research concluded with the beginning of an overall hardware architecture that depicts an approach to distribute RF bandwidth and network processing required to exceed the goals of 5G. This architecture depicts the advantage of centralized processing subsystems that have now evolved into cloud services and where the gNB (DU) has turned into RF ports as I depicted in my earlier work patented work in wireless communication. It appears my approach described in our earlier, patented, work and the 5G strategy are converging.

Future Research Directions

The research presented in this dissertation offers a multitude of interesting future directions to further advance user-based link QoS in 5G wireless communications applications. One direction is to closely examine the QoS at the link level by adapting admission control and traffic policing mechanisms (Kozat, et al., 2004; Lai et al, 2009; Reisslein, et al., 1998, 1999) to the approaches presented in this dissertation. With admission control and traffic policing, 5G networks can support general low latency communications (Jiang, et al., 2019; Nasrallah, et al., 2019), which is needed for a wide range of 5G communications services, as well as support popular bandwidth-demanding applications, e.g., video streaming (Reisslein & Ross, 1998; Wang, Chen et al., 2013; Wang, Kwon, et al., 2013). Another future research direction is to expand this research to

future communications paradigms, e.g., cognitive communications and networking (Amjad, et al., 2017; Kakalou, 2017; Tseng, 2015).

The user-based link QoS mechanisms developed in this dissertation research exploit SDN mechanisms (Amin et al., 2018; Jagadeesan & Krishnamachari, 2014; Kellerer et al., 2019; Yang et al., 2015) for the adaptive control of the user QoS. Future research can examine specifically the time scales and performance characteristics of transient adaptations in the proposed 5G communication system. Also, it may be interesting to examine the role of SDN gateway nodes (Thyagaturu et al., 2016; Vilalta et al., 2016) and specifically controlled SDN-based routing (Davoli et al., 2015; Guck et al., 2018) for providing QoS on large 5G networks that incorporate large aggregated network domains. A closely related future research topic is to examine network virtualization (Blenk, et al., 2016; Roozbeh, et al., 2018; Yang, et al., 2018) in the context of the examined link QoS mechanisms.

The emerging multi-access edge computing (MEC) paradigm, which is also referred to as mobile edge computing or fog computing (Bi, et al., 2018; Blanco et al., 2017; Shantharama et al., 2018; Xiang, et al., 2019) presents interesting novel trade-offs in conducting service computing for 5G communications functions in local hardware or software nodes, or in MEC hardware or software nodes (Hsieh, et al., 2018; Van Kempen, et al., 2017; Zanni, et al., 2017). Future research could examine the trade-offs in performance and cost between executing portions of the computing for the proposed link-level QoS mechanisms in local or MEC nodes.

Finally, network coding (Farooqi, et al., 2014; Gabriel et al., 2018; Lucani, et al., 2018; Naeem, et al., 2017; Taghouti, et al., 2019; Wang, et al., 2016) has recently emerged as an attractive coding paradigm for large-scale networks that suffer from unreliable wireless links. An important future research direction is to examine the infusion of network coding into the link-layer QoS scheme developed in this dissertation. Network coding may be able to enhance the overall network throughput, both for unicast and multicast transmissions, and can play an important role in further enhancing 5G communication systems (Patil, et al., 2019; Tsimbalo, et al., 2018; Vukobratovic, et al., 2018).

REFERENCES

Barton, B. (2012, March 30). eUTRAN to UTRAN (4G to 3G). Retrieved March 20, 2014, from LTE and BEYOND: http://www.lteandbeyond.com/2012/03/few-last-articles-were-about-handover.html

Wikipedia. (2014, February 24). Cellular data communication protocol. Retrieved March 15, 2014, From Wikipedia, the free encyclopedia: https://en.wikipedia.org/wiki/Cellular_data_communication_protocol

Freescale. (2014, March 15). T4240/P4080: QorIQ T4240/P4080/P4040/P4081 Communications Processors with Data Path. Retrieved March 15, 2014, From Freescale Semiconductor: http://www.freescale.com/

Airstream. (2014, April 3). ACK Timeouts and the effects on distance. Retrieved March 1, 2014, From Airstream: http://www.air-stream.org/technical/ack-timeouts-and-effects-distance-links

ShareTechnote. (2013, September 4). Handover LTE. Retrieved February 28, 2014, From ShareTechnote: http://www.sharetechnote.com/html/Handover_LTE.html

Peter McGuiggan. (2004). GPRS in Practice. West Sussex, England: John Wiley & Sons.

James F. Kurose, Keith W. Ross. (2010). Computer Networking, Fifth Edition. Boston: Pearson.

Steven M. Kay. (2010). Fundamentals of Statistical Signal Processing (Estimation Theory). Hamilton in Castleton: Prentice-Hall.

Steven M. Kay. (2008). Fundamentals of Statistical Signal Processing (Detection Theory). Troy: Prentice-Hall.

Douglas C. Montgomery. (2013). Design and Analysis of Experiments, Eighth Edition. Hoboken: John Wiley & Sons.

Reisslein, M., & James, F. (2017). U.S. Patent No. 9,717,088. Washington, DC: U.S. Patent and Trademark Office, Multi-Nodal Wireless Communication Systems and Methods

Torla, M. J., James, F. L., Tkacik, T. E., & Millman, S. D. (2012). U.S. Patent No. 9158499. Washington, DC: U.S. Patent and Trademark Office. Cryptographic processing with random number generator checking

Cover, T. (1972). Admissibility properties of Gilbert's encoding for unknown source probabilities. IEEE Transactions on Information Theory, 18:216–217.
Krichevsky, R. (1998). Laplace's law of succession and universal encoding. IEEE Transactions on Information Theory, 44:296–303.

McDiarmid, C. (1989). On the method of bounded differences. In Surveys in Combinatorics, pages 148–188. Cambridge University Press.

Miller, G. (1955). Note on the bias of information estimates. In Information theory in psychology II-B, pages 95–100.

Nemenman, I., Shafee, F., and Bialek, W. (2002). Entropy and inference, revisited. NIPS, 14.

Paninski, L. (2003). Estimation of entropy and mutual information. Neural Computation, 15:1191–1253.

Paninski, L. (2004). Estimating entropy on m bins given fewer than m samples. IEEE Transactions on Information Theory, 50:2200–2203.

Paninski, L. (2005). Variational minimax estimation of discrete distributions under KL loss. Advances in Neural Information Processing Systems, 17.

Paninski, L. (2008). A coincidence-based test for uniformity given very sparsely-sampled discrete data. IEEE Transactions on Information Theory, 54:4750–4755.

Paninski, L. and Yajima, M. (2008). Undersmoothed kernel entropy estimators. IEEE Transactions on Information Theory, 54:4384–4388.

NIST. (2001, May 1) FIPS PUB 140-2. Security Requirements for Cryptographic Modules. Federal Information Processing Standards Publication. Category: Security. Subcategory: Cryptography.

NIST. (2012, February 16) Annex C: Approved Random Number Generators for FIPS PUB 140-2, Security Requirements for Cryptographic Modules.

Rodgers Corporation. “Rodgers Corporation: RO3000 Series High Frequency Circuit Materials”, Data Sheet 1.3000, Publication #92-130, 3/2005.
Rod Waterhouse, “Printed Antennas for Wireless Communications”, 1st Edition, John Wiley & Sons, Inc., New York, 01/02/2008, ISBN-13: 9780470510698.

D. M. Pozar, “Microwave Engineering,” 3rd Edition, John Wiley & Sons, Inc., New York, 2005.

Guo Yichao, Guo Jianmin, Lv Pin, Huan Hao, Tao Ran, “A Code Doppler Compensation Algorithm in Acquisition for High Dynamic Spread Spectrum Signals,”, IEEE Signal Processing, Communications and Computing (ICSPCC), 2016 Digital Object Identifier (DOI): 10.1109/ICSPCC.2016.7753594.

Dr. Andreas Spanias, “Adaptive Filtering, Chapter 9” in Digital Signal Processing An Interactive Approach, 2nd ed. Tempe, Az.

B. Widrow et al, Adaptive noise cancelling: Principles and applications, Proc. IEEE, Vol. 63(12), Jan. 1976.

B. Widrow, S. Stearns, Adaptive Signal Processing, Prentice Hall, 1985.

Gross, Frank B. Smart Antennas with MATLAB, , 2nd Edition, McGraw Hill, 2015.

Douglas, S.C. “Introduction to Adaptive Filters” Digital Signal Processing Handbook Ed. Vijay K. Madisetti and Douglas B. Williams Boca Raton: CRC Press LLC, 1999

Block implementation of adaptive digital filters,Clark, G.; Mitra, S.; Parker, S.;Circuits and Systems, IEEE Transactions on Volume: 28 , Issue: 6, Digital Object Identifier:10.1109/TCS.1981.1085018, Publication Year: 1981 , Page(s): 584 – 592

Fast implementations of LMS adaptive filters Ferrara,E.; Acoustics, Speech and Signal Processing, IEEE Transactions onVolume:28,Issue:4Digital Object Identifier (DOI): 10.1109/TASSP.1980.1163432 Publication Year: 1980 , Page(s): 474 – 475

Comparison of several frequency-domain LMS algorithms Mikhael,W.;Spanias,A.; Circuits and Systems, IEEE Transactions on Volume:34,Issue:5, Digital Object Identifier (DOI): 10.1109/TCS.1987.1086164, Publication Year: 1987 , Page(s): 586 - 588

Johan Duplouy, Christophe Morlaas, Hervé Aubert, Philippe Pouliguen, Patrick Potier, et al.. Reconfigurable Grounded Vector Antenna for 3D Electromagnetic Direction Finding Applications. IEEE Antennas and Wireless Propagation Letters, Institute of Electrical and Electronics Engineers, December, 2017.

Van Trees, Harry L., Optimum Array Processing. Part IV of Detection, Estimation, and Modulation Theory, John Wiley & Sons, Inc., New York, Copyright 2002

Hart, Ted, Birke, Paul V., The Poynting Vector Antenna, 1st Edition, 2016.

Nehorai, A, and Paldi, E, Vector-sensor array processing for electromagnetic source localization, IEEE Trans, on Signal Processing, SP-42, 376-398, Feb, 1994

Nehorai, A, and Paldi, E., Vector sensor processing for electromagnetic source location, Proc, 25th Asilomar Conf. Signals, Syst, Comput., Pacific Grove, Ca, Nov 1991, 566-572

SchWartz, M, Bennett, W. R, and Stein, S, Communication Systems and Techniques McGraw-Hill, New York, 1966.

Keiser, B.E., Broadband Coding, Modulation, and Transmission Engineering, Prentice-Hall, Englewood Cliffs, New Jersey, 1989.

Stoica, P. and Nehorai, A., Performance study of conditional and unconditional direction-of-arrival estiamte, IEEE Trans. Acoust, Speech, Signal Processing, ASSP-38, 1783-1795, Oct. 1990.

Ottersten, B., Viberg, M. and Kailath, T., Analysis of subspace fitting and ML techniques for paraeter estsimate for sensor array data, IEEE Trans. Signal Processing, SP-40, 90-600, March 1992.

Schmidt, R.O., A signal subspace approach to multiple emitter location and spectral estimation Ph.D, Dissertation, Stanford University, Standford, Ca. Nov 1981.

Ferrara, Jr., E.R. and Parks, T.M., Direction finding with an array of antennas having diverse polarization, IEEE Trans, Antennas Propagat., AP-31, 231-236, March 1983

Ziskind, I. and Wax, M., Maximum Likelihood location of diversely polarized sources byt simualted annealing, IEEE Trans. Antennas Progagat. AP-38, 1111-1114, July 1990.

Li, J. and Compution, R.T., JR., Angle and polarization estimation using ESPRIT with a polarization sensitive array, IEEE Trans., Antennas Progat., AP-39, 1376-1383, Sept. 1991

Weiss, A.J. and Friedlander, B., Performance analysis of diversely polarized antenna arrays, IEEE Trans, Signal Processing, SP-39, 1589-1603, July 1991.

Means, J.D., Use of three-dimensional covariance matrix in analyzing the polarization properties of plane waves, J. Geophys, Res., 77, 5551-5559, Oct. 1972

Hatke, G.F., Performance analysis of the SuperCART antenna array, Project Report No. AST-22, Lincoln Laboratory, Massachusetts Institute of Technology, Lexington, Ma, March 1992.

Ferrara, E., Fast LMS implementation of adaptive filters, (Volume:28, Issue:4), IEEE Transactions Digital Identifier (DOI): 10.1109/TASSP.1980.1163432 Publication Year: 1980 , Page(s): 474 – 475

Comparison of several frequency-domain LMS algorithms Mikhael,W.;Spanias,A.; Circuits and Systems, IEEE[20] Spanias, Dr. Andreas Digital Signal Processing An Interactive Approach, 2nd ed. Tempe, Az.: Copyright 2007

Kanda, M., An electrogmatnic near-field sensor for simultaneous electric and magnetic-field measurements, IEEE Trans. on Electromagnetic Compatibility, 26(1), 102-110, Aug. 1984

Clark, G.; Mitra, S.; Parker, S, Block implementation of adaptive digital filters,.;Circuits and Systems, IEEE Transactions on Volume: 28 , Issue: 6, Digital Object Identifier: 10.1109/TCS.1981.1085018, Publication Year: 1981 , Page(s): 584 – 592

Cox, Christopher (2014, John Wiley and Sons), An Introduction to LTE: LTE, LTE-Advanced, SAE, VoLTE and 4G Mobile Communications, 2nd Edition

Rodriquez, Jonathan (2015, John Wiley and Sons), Fundamentals of 5G Mobile Networks

Liyanage, Madhusanka (2015, John Wiley and Sons), Software Defined Mobile Networks

Holler, Jan; Tsiatsis, Vlasios (2014, Elsevier Ltd.) From Machine-to-Machine to the Internet of Things

Barton, B. (2012, March 30). eUTRAN to UTRAN (4G to 3G). Retrieved March 20, 2014, from LTE and BEYOND: http://www.lteandbeyond.com/2012/03/few-last-articles-were-about-handover.html

Wikipedia. (2014, February 24). Cellular data communication protocol. Retrieved March 15, 2014, From Wikipedia, the free encyclopedia: https://en.wikipedia.org/wiki/Cellular_data_communication_protocol

Airstream. (2014, April 3). ACK Timeouts and the effects on distance. Retrieved March 1, 2014, From Airstream: http://www.air-stream.org/technical/ack-timeouts-and-effects-distance-links

ShareTechnote. (2013, September 4). Handover LTE. Retrieved February 28, 2014, From ShareTechnote: http://www.sharetechnote.com/html/Handover_LTE.html

McGuiggan, Pete. (2004). GPRS in Practice. West Sussex, England: John Wiley & Sons.

Kay, Steven M. (2010). Fundamentals of Statistical Signal Processing (Estimation Theory). Hamilton in Castleton: Prentice-Hall.

Kay, Steven M. (2008). Fundamentals of Statistical Signal Processing (Detection Theory). Troy: Prentice-Hall.

Montgomery, Douglas C. (2013). Design and Analysis of Experiments, Eighth Edition. Hoboken: John Wiley & Sons.

Cover, T. (1972). Admissibility properties of Gilbert's encoding for unknown source probabilities. IEEE Transactions on Information Theory, 18:216–217.

Krichevsky, R. (1998). Laplace's law of succession and universal encoding. IEEE Transactions on Information Theory, 44:296–303.

McDiarmid, C. (1989). On the method of bounded differences. In Surveys in Combinatorics, pages 148–188. Cambridge University Press.

Spanias, Andreas (2014). Digital Signal Processing; An Interactive Approach, Second Edition. Tempe, Az.

Balanis, Constantine (2005). Antenna Theory, Third Edition. Hoboken: John Wiley & Sons.

James, Tsui (2004). Digital Techniques for Wideband Receivers. Raleigh: SciTech Publishing.

Kay, Stephen (2006). Intuitive Probability and Random Processes using MATLAB. Springeronline.com.

Miller, G. (1955). Note on the bias of information estimates. In Information theory in psychology II-B, pages 95–100.

Nemenman, I., Shafee, F., and Bialek, W. (2002). Entropy and inference, revisited. NIPS, 14.

Paninski, L. (2003). Estimation of entropy and mutual information. Neural Computation, 15:1191–1253.

Paninski, L. (2004). Estimating entropy on m bins given fewer than m samples. IEEE Transactions on Information Theory, 50:2200–2203.

Paninski, L. (2005). Variational minimax estimation of discrete distributions under KL loss. Advances in Neural Information Processing Systems, 17.

Paninski, L. (2008). A coincidence-based test for uniformity given very sparsely-sampled discrete data. IEEE Transactions on Information Theory, 54:4750–4755.

Paninski, L. and Yajima, M. (2008). Under smoothed kernel entropy estimators. IEEE Transactions on Information Theory, 54:4384–4388.

NIST. (2001, May 1) FIPS PUB 140-2. Security Requirements for Cryptographic Modules. Federal Information Processing Standards Publication. Category: Security. Subcategory: Cryptography.

NIST. (2012, February 16) Annex C: Approved Random Number Generators for FIPS PUB 140-2, Security Requirements for Cryptographic Modules.

Freescale. (2014, March 15). P4080: QorIQ P4080/P4040/P4081 Communications Processors with Data Path. Retrieved March 15, 2014, From Freescale Semiconductor: http://www.freescale.com/webapp/sps/site/prod_summary.jsp?code=P4080

James F. Kurose, Keith W. Ross. (2010). Computer Networking, Fifth Edition. Boston: Pearson.

Allen, J. L., Diamond, B. L. (1966), "Mutual Coupling in Array Antennas", Lincoln Laboratory, Massachusetts Institute of Technology (MIT), Lexington, Massachusetts

Garrity, Doug, EEE 627, Lecture Notes Fall 2016, "Oversampling Sigma-Delta Data Converters"

Miller, Matt, IEEE CICC Ed Session 2004: Introduction to Sigma-Delta Data Converters, Freescale Semiconductor

Guo Yichao, Guo Jianmin, Lv Pin, Huan Hao, Tao Ran, "A Code Doppler Compensation Algorithm in Acquisition for High Dynamic Spread Spectrum Signals,", IEEE Signal Processing, Communications and Computing (ICSPCC), 2016 Digital Object Identifier (DOI): 10.1109/ICSPCC.2016.7753594.

Dr. Andreas Spanias, "Adaptive Filtering, Chapter 9" in Digital Signal Processing An Interactive Approach, 2nd ed. Tempe, Az., 2009.

B. Widrow et al, Adaptive noise cancelling: Principles and applications, Proc. IEEE, Vol. 63(12), Jan. 1976.

B. Widrow, S. Stearns, Adaptive Signal Processing, Prentice Hall, 1985.

Douglas, S.C. "Introduction to Adaptive Filters" Digital Signal Processing Handbook Ed. Vijay K. Madisetti and Douglas B. Williams Boca Raton: CRC Press LLC, 1999

Clark, G.; Mitra, S.; Parker, S. “Block implementation of adaptive digital filters”; Circuits and Systems, IEEE Transactions on Volume: 28, Issue: 6, Digital Object Identifier: 10.1109/TCS.1981.1085018, Publication Year: 1981 , Page(s): 584 – 592

Ferrara,E.;”Fast implementations of LMS adaptive filters. Acoustics, Speech and Signal Processing”, IEEE Transactions onVolume:28,Issue:4, Digital Object Identifier (DOI): 10.1109/TASSP.1980.1163432 Publication Year: 1980 , Page(s): 474 – 475

Mikhael,W.;Spanias,A.; “Comparison of several frequency-domain LMS algorithms” Circuits and Systems, IEEE Transactions on Volume:34,Issue:5, Digital Object Identifier (DOI): 10.1109/TCS.1987.1086164, Publication Year: 1987 , Page(s): 586 - 588

Nehorai, A, and Paldi, E, Vector-sensor array processing for electromagnetic source localization, IEEE Trans, on Signal Processing, SP-42, 376-398, Feb, 1994

Nehorai, A, and Paldi, E., Vector sensor processing for electromagnetic source location, Proc, 25th Asilomar Conf. Signals, Syst, Comput., Pacific Grove, Ca, Nov 1991, 566-572.

Kozat, U. C., Koutsopoulos, I., and Tassiulas, L., A framework for cross-layer design of energy-efficient communication with QoS provisioning in multi-hop wireless networks, In Proc. IEEE INFOCOM 2004, vol. 2, pp. 1446-1456. 2004.

Lai, C.-C., R.-G. Lee, C.-C. Hsiao, H.-S. Liu, and C.-C. Chen, A H-QoS-demand personalized home physiological monitoring system over a wireless multi-hop relay network for mobile home healthcare applications, Journal of Network and Computer Applications, 32(6):1229-1241, 2009.

Reisslein, M., Ross, K.W. and Rajagopal, S., Guaranteeing statistical QoS to regulated traffic: The single node case. In Proc. IEEE INFOCOM, vol. 3, pp. 1061-1072, 1999

Reisslein, M., Ross, K.W. and Rajagopal, S., Guaranteeing statistical QoS to regulated traffic: The multiple node case. In Proc. IEEE Conference on Decision and Control, vol. 1, pp. 531-538, 1998.

Jiang, X., Shokri-Ghadikolaei, H., Fodor, G., Modiano, E., Pang, Z., Zorzi, M. and Fischione, C., Low-latency networking: Where latency lurks and how to tame it. Proceedings of the IEEE, 107(2):280-306, 2019.

Nasrallah, A., Thyagaturu, A., Alharbi, Z., Wang, C., Shao, X., Reisslein, M. and El Bakoury, H., Ultra-low latency (ULL) networks: The IEEE TSN and IETF DetNet standards and related 5G ULL research, IEEE Communications Surveys & Tutorials, 21(1):88–145, 2019.

Reisslein, M., and Ross, K.W., High-performance prefetching protocols for VBR prerecorded video, IEEE Network, 12(6):46-55, 1998.

Wang, X., Kwon, T., Choi, Y., Wang, H. and Liu, J., Cloud-assisted adaptive video streaming and social-aware video prefetching for mobile users, IEEE Wireless Communications, 20(3):72-79, 2013.

Wang, X., M. Chen, T. T. Kwon, L. T Yang, and V. CM. Leung. AMES-cloud: A framework of adaptive mobile video streaming and efficient social video sharing in the clouds, IEEE Transactions on Multimedia, 15(4):811-820, 2013.

Amjad, M., F. Akhtar, M. H. Rehmani, M. Reisslein, and T. Umer, Full-duplex communication in cognitive radio networks: A survey, IEEE Communications Surveys & Tutorials, 19(4):2158-2191, 2017.

Kakalou, I., Psannis, K.E., Krawiec, P. and Badea, R., Cognitive radio network and network service chaining toward 5G: Challenges and requirements. IEEE Communications Magazine, 55(11):145-151, 2017.

Tseng, F.H., Chao, H.C. and Wang, J., Ultra-dense small cell planning using cognitive radio network toward 5G. IEEE Wireless Communications, 22(6):76-83, 2015.

Amin, R., Reisslein, M. and Shah, N., Hybrid SDN networks: A survey of existing approaches. IEEE Communications Surveys & Tutorials, 20(4):3259-3306, 2018.

Jagadeesan, N.A. and Krishnamachari, B., Software-Defined Networking Paradigms in Wireless Networks: A Survey, ACM Comput. Surv., 47(2):27-1—27-12, 2014.

Kellerer, W., Kalmbach, P., Blenk, A., Basta, A., Reisslein, M. and Schmid, S., Adaptable and Data-Driven Softwarized Networks: Review, Opportunities, and Challenges, Proceedings of the IEEE, in print, 2019.

Yang, M., Li, Y., Jin, D., Zeng, L., Wu, X. and Vasilakos, A.V., Software-defined and virtualized future mobile and wireless networks: A survey. Mobile Networks and Applications, 20(1):4-18, 2015.

Thyagaturu, A.S., Dashti, Y. and Reisslein, M., SDN-based smart gateways (Sm-GWs) for multi-operator small cell network management. IEEE Transactions on Network and Service Management, 13(4):740-753, 2016.

Vilalta, R., Mayoral, A., Pubill, D., Casellas, R., Martínez, R., Serra, J., Verikoukis, C. and Muñoz, R., End-to-End SDN orchestration of IoT services using an SDN/NFV-enabled edge node. In Proc. IEEE/OSA Optical Fiber Communications Conference and Exhibition (OFC) (pp. 1-3), 2016.

Davoli, L., Veltri, L., Ventre, P.L., Siracusano, G. and Salsano, S., Traffic engineering with segment routing: SDN-based architectural design and open source implementation. In Proc. IEEE European Workshop on Software Defined Networks (pp. 111-112), 2015.

Guck, J.W., Van Bemten, A., Reisslein, M. and Kellerer, W., Unicast QoS routing algorithms for SDN: A comprehensive survey and performance evaluation. IEEE Communications Surveys & Tutorials, 20(1):388-415, 2018.

Blenk, A., Basta, A., Zerwas, J., Reisslein, M. and Kellerer, W., Control plane latency with SDN network hypervisors: The cost of virtualization. IEEE Transactions on Network and Service Management, 13(3):366-380, 2016.

Roozbeh, A., Soares, J., Maguire, G.Q., Wuhib, F., Padala, C., Mahloo, M., Turull, D., Yadhav, V. and Kostić, D., Software-Defined “Hardware” Infrastructures: A Survey on

Enabling Technologies and Open Research Directions. IEEE Communications Surveys & Tutorials, 20(3):2454-2485, 2018.

Yang, G., Yu, B.Y., Kim, S.M. and Yoo, C., LiteVisor: A Network Hypervisor to Support Flow Aggregation and Seamless Network Reconfiguration for VM Migration in Virtualized Software-Defined Networks. IEEE Access, 6:65945-65959, 2018.

Bi, Y., Han, G., Lin, C., Deng, Q., Guo, L. and Li, F., Mobility support for fog computing: An SDN approach. IEEE Communications Magazine, 56(5):53-59, 2018.

Blanco, B., Fajardo, J.O., Giannoulakis, I., Kafetzakis, E., Peng, S., Pérez-Romero, J., Trajkovska, I., Khodashenas, P.S., Goratti, L., Paolino, M. and Sfakianakis, E., Technology pillars in the architecture of future 5G mobile networks: NFV, MEC and SDN. Computer Standards & Interfaces, 54:216-228, 2017.

Shantharama, P., Thyagaturu, A.S., Karakoc, N., Ferrari, L., Reisslein, M. and Scaglione, A., LayBack: SDN Management of Multi-Access Edge Computing (MEC) for Network Access Services and Radio Resource Sharing. IEEE Access, 6:57545-57561, 2018.

Xiang, Z., Gabriel, F., Perez, E.U., Nguyen, G.T., Reisslein, M., and Fitzek, F.H.P., Reducing Latency in Virtual Machines Enabling Tactile Internet for Human Machine Co-working, IEEE Journal on Selected Areas in Communications, in print, 2019.

Hsieh, H.C., Lee, C.S. and Chen, J.L., Mobile edge computing platform with container-based virtualization technology for IoT applications. Wireless Personal Communications, 102(1):527-542, 2018.

Van Kempen, A., Crivat, T., Trubert, B., Roy, D. and Pierre, G., MEC-ConPaaS: An experimental single-board based mobile edge cloud. In Proc. IEEE Int. Conf. on Mobile Cloud Computing, Services, and Eng. (MobileCloud) (pp. 17-24), 2017.

Zanni, A., Yu, S.Y., Bellavista, P., Langar, R. and Secci, S., Automated selection of offloadable tasks for mobile computation offloading in edge computing. In Proc. IEEE Int. Conf. on Network and Service Management (CNSM) (pp. 1-5), 2017.

Farooqi, M.Z., Tabassum, S.M., Rehmani, M.H. and Saleem, Y., A survey on network coding: From traditional wireless networks to emerging cognitive radio networks, Journal of Network and Computer Applications, 46:166-181, 2014.

Gabriel, F., Wunderlich, S., Pandi, S., Fitzek, F.H. and Reisslein, M., Caterpillar RLNC with feedback (CRLNC-FB): Reducing delay in selective repeat ARQ through coding. IEEE Access, 6:44787-44802, 2018.

Lucani, D.E., Pedersen, M.V., Ruano, D., Sørensen, C.W., Fitzek, F.H., Heide, J., Geil, O., Nguyen, V. and Reisslein, M., Fulcrum: Flexible Network Coding for Heterogeneous Devices. IEEE Access, 6:77890-77910, 2018.

Naeem, A., Rehmani, M.H., Saleem, Y., Rashid, I. and Crespi, N., Network coding in cognitive radio networks: A comprehensive survey, IEEE Communications Surveys & Tutorials, 19(3):1945-1973, 2017.

Taghouti, M., Lucani, D.E., Cabrera, J.A., Reisslein, M., Pedersen, M.V. and Fitzek, F.H., Reduction of Padding Overhead for RLNC Media Distribution With Variable Size Packets, IEEE Transactions on Broadcasting, in print, 2019.

Wang, X., Mei, Q. and Yao, X., The Techniques of Network Coding Applied in the Physical-Layer of the Wireless Communication Systems: A Survey. In Proc. Conference of Spacecraft TT&C Technology in China (pp. 531-541). Springer, Singapore, 2016.

Patil, V., Gupta, S. and Keshavamurthy, C., S-RLNC Multi-generation Mixing Assisted MAC Optimization for Multimedia Multicast over LTE-A. In Cognitive Informatics and Soft Computing (pp. 505-524). Springer, Singapore, 2019.

Tsimbalo, E., Tassi, A. and Piechocki, R.J., Reliability of multicast under random linear network coding. IEEE Transactions on Communications, 66(6):2547-2559, 2018.

Vukobratovic, D., Tassi, A., Delic, S. and Khirallah, C., 2018. Random linear network coding for 5G mobile video delivery. Information, 9(4-72):1-20, 2018.

APPENDIX A

MATLAB PROGRAM AMPLITUDE/PHASE/FREQUENCY ESTIMATOR

```
%
%   Amplitude & Phase & Frequency unknown.
%  -Must estimate frequency using periodogram.
%  -Must estimate amplitude.
%  -Must estimate phase.

samples = 1000;
N = 5;
u0 = 0;
phi = .25 *(2*pi);
f0 = 0.25;
A = 2;
var0 =1;

%all_known_pd=zeros(samples,1);
%all_known_pfa=zeros(samples,1);
%energy_noise=zeros(samples,1);

%A_unknown_pd=zeros(samples,1);
%A_unknown_pfa=zeros(samples,1);

%A_phi_unknown_pd=zeros(samples,1);
%A_phi_unknown_pfa=zeros(samples,1);

all_unknown_pd=zeros(samples,1);
all_unknown_pfa=zeros(samples,1);

wgn = zeros(samples,1);
x0=zeros(samples,1);
x1=zeros(samples,1);
x=zeros(samples,1);
freq_est=zeros(samples,1);
phase_est=zeros(samples,1);
a_est=zeros(samples,1);

for iter=1:samples;

   wgn = u0 + (sqrt(var0)*randn(samples,1));
   x0 = wgn;

   for sig_iter=1:samples;
      x1(sig_iter) = wgn(sig_iter) + cos((2*pi*f0*sig_iter)+phi);
   end;
```

```
index = 1;
sfreq=.005;
efreq=.495;
incfreq=.005;

i_freq = zeros(((efreq-sfreq)/incfreq)+2,1);

for freq=sfreq:incfreq:efreq;

   x_cos = 0;
   x_sin = 0;
   for icnt=1:N;
      x_cos = x_cos + x1(icnt)*cos(2*pi*freq*icnt);
      x_sin = x_sin + x1(icnt)*sin(2*pi*freq*icnt);
   end;
   i_freq(index) = (2/N * (x_cos^2 + x_sin^2));
   index = index + 1;
end;

[value,indice] = max(i_freq);
freq_est(iter) = (sfreq + ((indice-1)*incfreq));

x_cos = 0;
x_sin = 0;
for icnt=1:N;
   x_cos = x_cos + x1(icnt)*cos(2*pi*freq_est(iter)*icnt);
   x_sin = x_sin + x1(icnt)*sin(2*pi*freq_est(iter)*icnt);
end;

a_est(iter) = (2/N)*sqrt(x_cos^2 + x_sin^2);

dphase = 0;
nphase = 0;
for icnt=1:N;
   nphase = nphase + x1(icnt)*sin(2*pi*freq_est(iter)*icnt);
   dphase = dphase + x1(icnt)*cos(2*pi*freq_est(iter)*icnt);
end;

phase_est(iter) = abs(atan(-nphase/dphase));

tx1_var0 = 0;
tx1_var1 = 0;
for tx1=1:N
```

```
      tx1_var0 =  tx1_var0 + abs(
x1(tx1)*a_est(iter)*(cos(2*pi*freq_est(iter)*tx1)+phase_est(iter)) );
      tx1_var1 =  tx1_var1 + abs(
x1(tx1)*a_est(iter)*(sin(2*pi*freq_est(iter)*tx1)+phase_est(iter)) );
   end;
   all_unknown_pd(iter) = 1/(4*var0)*( ((2/N)*tx1_var0)^2 + ((2/N)*tx1_var1)^2 );

end;

tx_pd = sort(all_unknown_pd);

% Derived from sort()
total_cnt=samples;

range = 20;

incr = range/100;
size = range/incr;

%Monte Carlo Solution
pd_y=zeros(range/incr,7);
engy_x=zeros(range/incr,7);

var_pd = var(all_unknown_pd);

pfa = 10^-1;
for nplots=1:7;

index = 1;
for iter=0: incr : range-.2;

  pd_cnt=0;

  nA = sqrt( ((2*var0)/N)*(10^(iter/10)) );
  gamma = nA*(1/2)*chi2cdf((1-pfa),2);

  for n=1:samples;
    if (all_unknown_pd(n) > gamma)
       pd_cnt = pd_cnt + 1;
    end;
  end;

  pd_y(index,nplots) = pd_cnt/total_cnt;
  engy_x(index,nplots) = (range-.2) - iter;
```

```
   index = index + 1;
end;

pfa = pfa*10^-1;
end;

plot(engy_x,pd_y);
```

APPENDIX B

MATLAB PROGRAM BURG PSD ESTIMATOR

```
%
%
%  Burg PSD Estimator
%
%
%  With & Without Noise
%
%
Fs=64;%  Samples/sec
F01 = 10; %Hz
F02 = 11; %Hz
F03 = 25; %Hz
T1 = 1/F01;
T2 = 1/F02;
T3 = 1/F03;
UnitAmplitude = 1;
duration = 2; %length of simulation (sec)

samples = duration*Fs;
t=(1/Fs:1/Fs:duration)';
N = duration * Fs;

T = 1/Fs; %Sampling Interval

DBM = 0;

s1 = UnitAmplitude*sin(2*pi*F01*t);%Pure Signal
s2 = UnitAmplitude*sin(2*pi*F02*t);%Pure Signal
s3 = UnitAmplitude*sin(2*pi*F03*t);%Pure Signal

noise = rand(1,samples)';%noise added to signal

S = s1 + s2 + s3;   %Combined Signals Without Noise

x1 = awgn(s1,0);%add WGN 0db SNR
x2 = awgn(s2,0);%add WGN 0db SNR
x3 = awgn(s3,0);%add WGN 0db SNR

X = x1 + x2 + x3;   %Combined Signals With Noise

%plot (t,s3,t,x3);  %Test Only
%plot(t,s3); %Test Only
for nextPlot = 1: 6
```

```
    if (nextPlot < 4)
       x=S; %Data Set 1

       if (nextPlot == 1)
          modelOrder = 5;
       elseif (nextPlot == 2)
          modelOrder = 15;
       else
          modelOrder = 30;
       end;

    else
       x=X; %Data Set 2
       if (nextPlot == 4)
          modelOrder = 5;
       elseif (nextPlot == 5)
          modelOrder = 15;
       else
          modelOrder = 30;
       end;
    end;

freqPlot = (0:.0078125:31.9921875)';
f = freqPlot;

P = modelOrder;

Pxx = pburg(x,P,f,Fs);

F;
if (DBM == 0)
    plot(freqPlot,Pxx);
    %plot(freqPlot,psdEst);
else
    plot(freqPlot,10*log10(Pxx));  %dB/Hz
    %plot(freqPlot,psdEst);
end;

if (nextPlot < 4)
    title(['Signal, No Noise, Burg, Model Order = ' int2str(modelOrder)]);
else
    title(['Signal + Noise, Burg, Model Order = ' int2str(modelOrder)]);
end;
xlim([0 32]);
```

```
xlabel('Frequency (Hz)');
if (DBM == 0)
   ylabel('PSD Magnitude');
else
   ylabel('PSD Magnitude (dB)');
end;

testPoint = 0; %For debug purposes

end;

%
%
%
%
```

APPENDIX C

MATLAB PROGRAM BLACKMAN-TUKEY PSD ESTIMATOR

```
%
%  Blackman-Tukey PSD Estimator
%
%
%  With & Without Noise
%
%

Fs=64;%  Samples/sec
F01 = 10; %Hz
F02 = 11; %Hz
F03 = 25; %Hz
T1 = 1/F01;
T2 = 1/F02;
T3 = 1/F03;
UnitAmplitude = 1;
duration = 2; %length of simulation (sec)

samples = duration*Fs;
t=(1/Fs:1/Fs:duration)';
N = duration * Fs;

T = 1/Fs; %Sampling Interval

s1 = UnitAmplitude*sin(2*pi*F01*t);%Pure Signal
s2 = UnitAmplitude*sin(2*pi*F02*t);%Pure Signal
s3 = UnitAmplitude*sin(2*pi*F03*t);%Pure Signal

noise = rand(1,samples)';%noise added to signal

S = s1 + s2 + s3;   %Combined Signals Without Noise

x1 = awgn(s1,0);%add WGN 0db SNR
x2 = awgn(s2,0);%add WGN 0db SNR
x3 = awgn(s3,0);%add WGN 0db SNR

X = x1 + x2 + x3;   %Combined Signals With Noise

%plot (t,s3,t,x3);  %Test Only
%plot(t,s3); %Test Only


for nextPlot = 1: 6
```

```
if (nextPlot < 4)
   x = S; %Without Noise
   if (nextPlot == 1)
      Lag = 10; %Without Noise -All Freq. Components visible
   elseif (nextPlot == 2)
      Lag = 20;
   else
      Lag = 70;
   end;
   M = Lag;
else
   x = X;  %With Noise
   if (nextPlot == 4)
      Lag = 10; %Without Noise -All Freq. Components visible
   elseif (nextPlot == 5)
      Lag = 20;
   else
      Lag = 70;
   end;
   M = Lag;
end;

Rxx2 = xcorr(x,x,M,'unbiased');
hammingW = hamming(2*M,'periodic');
%hammingW = hamming(2*M);

freq=0;
psdEst=zeros(1,300);
for k=1: 300  % 30Hz band in a .1 Hz interval
    realM = -M;
    for m=1: 2*M
        psdEst(k) = psdEst(k) + (hammingW(m)*Rxx2(m)*exp(-1i*2*pi*T*realM*freq));
        realM = realM + 1;
    end;
    psdEst(k) = T * psdEst(k);
    freq = freq + .1;
end;

freqPlot = (0:.1:29.9)';

figure;
plot(freqPlot,real(psdEst));
%plot(freqPlot,10*log10(real(psdEst)));  %dB/Hz
```

```
if (nextPlot < 4)
title(['Signal, no noise, Blackman-Tukey Plot Lag = ' int2str(Lag)]);
else
title(['Signal + noise, Blackman-Tukey Plot Lag = ' int2str(Lag)]);
end;

xlabel('Frequency (Hz)');
ylabel('PSD Magnitude');

end;
testPoint = 0; %For debug purposes
```

APPENDIX D

MATLAB PROGRAM COVARIANCE PSD ESTIMATOR

```
%
%
%
%  Covariance PSD Estimator
%
%
%  With & Without Noise
%
%

Fs=64;%  Samples/sec
F01 = 10; %Hz
F02 = 11; %Hz
F03 = 25; %Hz
T1 = 1/F01;
T2 = 1/F02;
T3 = 1/F03;
UnitAmplitude = 1;
duration = 2; %length of simulation (sec)

samples = duration*Fs;
t=(1/Fs:1/Fs:duration)';
N = duration * Fs;

T = 1/Fs; %Sampling Interval

s1 = UnitAmplitude*sin(2*pi*F01*t);%Pure Signal
s2 = UnitAmplitude*sin(2*pi*F02*t);%Pure Signal
s3 = UnitAmplitude*sin(2*pi*F03*t);%Pure Signal

noise = rand(1,samples)';%noise added to signal

S = s1 + s2 + s3;   %Combined Signals Without Noise

x1 = awgn(s1,0);%add WGN 0db SNR
x2 = awgn(s2,0);%add WGN 0db SNR
x3 = awgn(s3,0);%add WGN 0db SNR

X = x1 + x2 + x3;   %Combined Signals With Noise

%plot (t,s3,t,x3);  %Test Only
%plot(t,s3); %Test Only
DBM = 0;
```

```
for nextPlot = 1: 6

   if (nextPlot < 4)
      x=S; %Data Set 1

      if (nextPlot == 1)
         modelOrder = 5;
      elseif (nextPlot == 2)
         modelOrder = 16;
      else
         modelOrder = 30;
      end;

   else
      x=X; %Data Set 2
      if (nextPlot == 4)
         modelOrder = 5;
      elseif (nextPlot == 5)
         modelOrder = 15;
      else
         modelOrder = 30;
      end;
   end;


freqPlot = (0:.0078125:31.9921875)';
f = freqPlot;

P = modelOrder;

%Covariance PSD
Pxx = pcov(x,P,f,Fs);


figure;
if (DBM == 0)
   plot(freqPlot,Pxx);
   %plot(freqPlot,psdEst);
else
   plot(freqPlot,10*log10(Pxx));  %dB/Hz
   %plot(freqPlot,psdEst);
end;
xlim([0 32]);
```

```
if (nextPlot < 4)
   title(['Signal, No Noise, Covariance, Model Order = ' int2str(modelOrder)]);
else
   title(['Signal + Noise, Covariance, Model Order = ' int2str(modelOrder)]);
end;

xlabel('Frequency (Hz)');
if (DBM == 0)
   ylabel('PSD Magnitude');
else
   ylabel('PSD Magnitude (dB)');
end;


testPoint = 0; %For debug purposes

end;
```

APPENDIX E

MATLAB PROGRAM MODIFIED COVARIANCE PSD ESTIMATOR

```
%
%
%  Modified Covariance PSD Estimator
%
%
%  With & Without Noise
%
%

Fs=64;%  Samples/sec
F01 = 10; %Hz
F02 = 11; %Hz
F03 = 25; %Hz
T1 = 1/F01;
T2 = 1/F02;
T3 = 1/F03;
UnitAmplitude = 1;
duration = 2; %length of simulation (sec)

samples = duration*Fs;
t=(1/Fs:1/Fs:duration)';
N = duration * Fs;

T = 1/Fs; %Sampling Interval

s1 = UnitAmplitude*sin(2*pi*F01*t);%Pure Signal
s2 = UnitAmplitude*sin(2*pi*F02*t);%Pure Signal
s3 = UnitAmplitude*sin(2*pi*F03*t);%Pure Signal

noise = rand(1,samples)';%noise added to signal

S = s1 + s2 + s3;   %Combined Signals Without Noise

x1 = awgn(s1,0);%add WGN 0db SNR
x2 = awgn(s2,0);%add WGN 0db SNR
x3 = awgn(s3,0);%add WGN 0db SNR

X = x1 + x2 + x3;   %Combined Signals With Noise

%plot (t,s3,t,x3);  %Test Only
%plot(t,s3); %Test Only
DBM = 0;
```

```
for nextPlot = 1: 6

   if (nextPlot < 4)
      x=S; %Data Set 1

      if (nextPlot == 1)
         modelOrder = 5;
      elseif (nextPlot == 2)
         modelOrder = 15;
      else
         modelOrder = 30;
      end;

   else
      x=X; %Data Set 2
      if (nextPlot == 4)
         modelOrder = 5;
      elseif (nextPlot == 5)
         modelOrder = 15;
      else
         modelOrder = 30;
      end;
   end;

freqPlot = (0:.0078125:31.9921875)';
f = freqPlot;

P = modelOrder;

%Modified Covariance PSD
Pxx = pmcov(x,P,f,Fs);

figure;
if (DBM == 0)
   plot(freqPlot,Pxx);
   %plot(freqPlot,psdEst);
else
   plot(freqPlot,10*log10(Pxx));  %dB/Hz
   %plot(freqPlot,psdEst);
end;

if (nextPlot < 4)
   title(['Signal, No Noise, Modified Covariance, Model Order = ' int2str(modelOrder)]);
else
   title(['Signal + Noise, Modified Covariance, Model Order = ' int2str(modelOrder)]);
```

```
end;
xlabel('Frequency (Hz)');
xlim([0 32]);

if (DBM == 0)
   ylabel('PSD Magnitude');
else
   ylabel('PSD Magnitude (dB)');
end;
testPoint = 0; %For debug purposes

end;
```

APPENDIX F

MATLAB PROGRAM MUSIC ESTIMATOR

```
%
%
%
%
%  MUSIC PSD Estimator
%
%
%  With & Without Noise
%
%

Fs=64;%  Samples/sec
F01 = 10; %Hz
F02 = 11; %Hz
F03 = 25; %Hz
T1 = 1/F01;
T2 = 1/F02;
T3 = 1/F03;
UnitAmplitude = 1;
duration = 2; %length of simulation (sec)

samples = duration*Fs;
t=(1/Fs:1/Fs:duration)';
N = duration * Fs;

T = 1/Fs; %Sampling Interval

s1 = UnitAmplitude*sin(2*pi*F01*t);%Pure Signal
s2 = UnitAmplitude*sin(2*pi*F02*t);%Pure Signal
s3 = UnitAmplitude*sin(2*pi*F03*t);%Pure Signal

noise = rand(1,samples)';%noise added to signal

S = s1 + s2 + s3;   %Combined Signals Without Noise

x1 = awgn(s1,0);%add WGN 0db SNR
x2 = awgn(s2,0);%add WGN 0db SNR
x3 = awgn(s3,0);%add WGN 0db SNR

X = x1 + x2 + x3;   %Combined Signals With Noise

%plot (t,s3,t,x3);  %Test Only
%plot(t,s3); %Test Only
```

```
DBM = 0;

for nextPlot = 1: 6

   if (nextPlot < 4)
      x=S; %Data Set 1

      if (nextPlot == 1)
         modelOrder = 5;
      elseif (nextPlot == 2)
         modelOrder = 15;
      else
         modelOrder = 30;
      end;

   else
      x=X; %Data Set 2
      if (nextPlot == 4)
         modelOrder = 5;
      elseif (nextPlot == 5)
         modelOrder = 15;
      else
         modelOrder = 30;
      end;
   end;


freqPlot = (0:.0078125:31.9921875)';
f = freqPlot;

P = modelOrder;

% Multiple Signal Classification (MUSIC)
% Returns the pseudospectrum in the vector x computed at the
% frequencies specified in vector f

Pxx = pmusic(x,P,f,Fs);

figure;
if (DBM == 0)
   plot(freqPlot,Pxx);
   %plot(freqPlot,psdEst);
else
   plot(freqPlot,10*log10(Pxx));  %dB/Hz
   %plot(freqPlot,psdEst);
```

```
end;

if (nextPlot < 4)
   title(['Signal, No Noise, Multiple Signal Classification (MUSIC), Model Order = '
int2str(modelOrder)]);
else
   title(['Signal + Noise, Multiple Signal Classification (MUSIC), Model Order = '
int2str(modelOrder)]);
end;
xlabel('Frequency (Hz)');
if (DBM == 0)
   ylabel('PSD Magnitude');
else
   ylabel('PSD Magnitude (dB)');
end;

testPoint = 0; %For debug purposes

end;
```

APPENDIX G

MATLAB PROGRAM MUSIC ALGORITHM

```
%
% Calculates the MUSIC pseudo-spectrum
% Also provides an example of the Root version
% of the MUSIC AOA algorithm for a M element
% array with noise variance = 1
% 1st calculate regular MUSIC algorithm,
% 2nd calculate polynomial coefficients for root-MUSIC
% Plots the two methods.
%

M=4; % Number of Antenna Elements
% D = 2;  % number of signals
D = 1;
sig1=1;
%sig2=.3
th1=-4*pi/180;
%th2=8*pi/180;

ii=1:M;
s1=exp(1j*(ii-1)*pi*sin(th1));
% s2=exp(1j*(ii-1)*pi*sin(th2));
% A=[s1.' s2.'];

A=[s1.'];

N=600
s=sqrt(sig1)*sign(randn(D,N));

% calculate the N time samples of the signals for the
% 'D' signal directions

Rss=s*s'/N;

n=sqrt(sig2)*randn(M,N);
% calculate the N noise samples for the M array
% elements

% Calculate the correlation matrices
% Noise
Rnn=(n*n')/N;        % calculate the noise correlation matrix (which is no longer
diagonal)
% Noise & Signal correlations
Rns=(n*s')/N;
```

```
Rsn=(s*n')/N;
% Array correlation matrix
Rrr=A*Rss*A'+A*Rsn+Rns*A'+Rnn;

% Determine the eigenvalues
[V,Diag1]=eig(Rrr);
% Sort eigenvalues from smallest to largest
[Z,idx]=sort(diag(Diag1));
% Determine noise subspace
En=V(:,idx(1:M-D));

% Determine signal eigenvectors
Es=V(:,idx(M-D+1:M));
for k=1:360;
  %theta(k)=-pi/12+pi*k/(6*360);  % 2nd signal
   theta(k)=-pi/6+pi*k/(3*360);
   clear s;
   s=exp(1j*(ii-1)*pi*sin(theta(k)));
   s=s.';
   Pmu(k)=1/abs(s'*En*En'*s);
end

% Calculate the noise matrix A
A=En*En';

%  Now determine the polynomial coefficients
%  for the root-MUSIC polynomial
%  Based on M elements
for kk=-M+1:M-1
   a(kk+M) = sum(diag(A,kk));
end

% Now determine the polynomial
% roots (should be 2* (M-1)
rts=roots(a);

% Calculate the angle(s) w/ these roots
angs=-asin(angle(rts)/pi)*180/pi;
figure;
% plot z plane (imaginery & real parts)
zplane(rts)
figure;
plot(th*180/pi,Pmu/max(Pmu),'k',angs,abs(rts),'kX','markersize',10)
grid on
xlabel('Angle')
```

```
ylabel('|P(\theta)|')
axis([-10 20 0 2])
```

APPENDIX H

MATLAB PROGRAM WELCH PSD ESTIMATOR

```
%
%
%
%  Welch PSD Estimator
%
%
%  With & Without Noise
%
%

Fs=64;%  Samples/sec
F01 = 10; %Hz
F02 = 11; %Hz
F03 = 25; %Hz
T1 = 1/F01;
T2 = 1/F02;
T3 = 1/F03;
UnitAmplitude = 1;
duration = 2; %length of simulation (sec)

samples = duration*Fs;
t=(1/Fs:1/Fs:duration)';
N = duration * Fs;

T = 1/Fs; %Sampling Interval

s1 = UnitAmplitude*sin(2*pi*F01*t);%Pure Signal
s2 = UnitAmplitude*sin(2*pi*F02*t);%Pure Signal
s3 = UnitAmplitude*sin(2*pi*F03*t);%Pure Signal

noise = rand(1,samples)';%noise added to signal

S = s1 + s2 + s3;   %Combined Signals Without Noise

x1 = awgn(s1,0);%add WGN 0db SNR
x2 = awgn(s2,0);%add WGN 0db SNR
x3 = awgn(s3,0);%add WGN 0db SNR

X = x1 + x2 + x3;   %Combined Signals With Noise

%plot (t,s3,t,x3);  %Test Only
%plot(t,s3); %Test Only
```

```
d = 32;
for nextPlot = 1: 6

if (nextPlot < 4)

   x=S; %Data Set 1
   if (nextPlot == 1)
      s = 10;
   elseif (nextPlot  == 2)
      s=20;
   else
      s=30;
   end;

else

   x=X; %Data Set 2
   if (nextPlot == 4)
      s = 10;
   elseif(nextPlot == 5)
      s=20;
   else
      s=30;
   end;

end;

p = nearest((length(t)-d)/(s+1));
hammingW = hamming(d);

xp=zeros(p,d);
shift=0;
for j=1: p
    for jj=1: d;
        xp(j,jj)=xp(j,jj)+ hammingW(jj)*x(jj+(shift*s));
    end;
    shift = shift + 1;
end;

freq=0;
U=0;
for j=1: d;
    U = U + (hammingW(j))^2;
end;
U = T*U;
```

```
psdEst=zeros(1,p);
WelchpsdEst=zeros(1,300);
for kk=1 : 300; % 30Hz band in a .1 Hz interval
   accumPSD=0;
   for k=1: p
      for m=1: d
         psdEst(k) = psdEst(k) + (xp(k,m)*exp(-1i*2*pi*T*m*freq));
      end;
      psdEst(k) = (1/(U*d*T))*(abs((T * psdEst(k))))^2;
      accumPSD = accumPSD + psdEst(k);
   end;
   WelchpsdEst(kk) = accumPSD/p;
   freq = freq + .1;
end;

%pwelch(x,d,d-s,length(x),Fs,'onesided');  %Hamming window

freqPlot = (0:.1:29.9)';

figure;
plot(freqPlot,WelchpsdEst);
%plot(freqPlot,10*log10(WelchpsdEst));  %dB/Hz

if (nextPlot < 4)
   title(['Signal, no noise, Welch Periodogram, sample shift = ' int2str(s)]);
else
   title(['Signal + noise, Welch Periodogram, sample shift = ' int2str(s)]);
end;
xlabel('Frequency (Hz)');
ylabel('PSD Magnitude');

testPoint = 0; %For debug purposes
end;
```

APPENDIX I

MATLAB PROGRAM YULE-WALKER PSD ESTIMATOR

```
%
%
%
%  Yule-Walker PSD Estimator
%
%
%  With & Without Noise
%
%

Fs=64;%  Samples/sec
F01 = 10; %Hz
F02 = 11; %Hz
F03 = 25; %Hz
T1 = 1/F01;
T2 = 1/F02;
T3 = 1/F03;
UnitAmplitude = 1;
duration = 2; %length of simulation (sec)

samples = duration*Fs;
t=(1/Fs:1/Fs:duration)';
N = duration * Fs;

T = 1/Fs; %Sampling Interval

s1 = UnitAmplitude*sin(2*pi*F01*t);%Pure Signal
s2 = UnitAmplitude*sin(2*pi*F02*t);%Pure Signal
s3 = UnitAmplitude*sin(2*pi*F03*t);%Pure Signal

noise = rand(1,samples)';%noise added to signal

S = s1 + s2 + s3;   %Combined Signals Without Noise

x1 = awgn(s1,0);%add WGN 0db SNR
x2 = awgn(s2,0);%add WGN 0db SNR
x3 = awgn(s3,0);%add WGN 0db SNR

X = x1 + x2 + x3;   %Combined Signals With Noise

%plot (t,s3,t,x3);  %Test Only
%plot(t,s3); %Test Only
```

```
%s=3;
%s=10;
s=20;
d=32;

%x=S; %Data Set 1
x=X; %Data Set 2

freqPlot = (0:.1:29.9)';
f = freqPlot;
%modelOrder = 5;
%modelOrder = 15;
%modelOrder = 60;
modelOrder = 30;

T = 1 / Fs;
P = modelOrder;

Rxx = xcorr(x,x,P,'biased');
%Rxx = xcorr(x,x,P,'unbiased');

[ar_coeffs, var] = aryule(x,modelOrder);

rxx = zeros(1,2*P);
for m=2*P: -1 : 1
   for k=1: P
%       rxx(m) = rxx(m) + (ar_coeffs(k)*Rxx(m)) + var;
      rxx(m) = rxx(m) + (ar_coeffs(k)*Rxx(m));
   end;
   rxx(m) = -rxx(m);
end;

freq=0;
psdEst=zeros(1,300);
for k=1: 300  % 30Hz band in a .1 Hz interval
    realM = -P;
  for m=1:2*P
     %  psdEst(k) = psdEst(k) + (rxx (m)*exp(-1i*2*pi*T*realM*freq));
      psdEst(k) = psdEst(k) + (Rxx (m)*exp(-1i*2*pi*T*realM*freq));
      realM = realM + 1;
   end;
     freq = freq + .1;
  psdEst(k) = T * psdEst(k);
end;
```

```
Pxx = pyulear(x,modelOrder,f,Fs);  %-This uses the biased correlation
  % estimate only.
  %-The unbiased correlation estimate can
  % cause unstable solutions (e.g.outside
  % the unit circle

%plot(freqPlot,real(psdEst));
plot(freqPlot,Pxx);

%plot(freqPlot,10*log10(Pxx));  %dB/Hz
title(['Yule-Walker, Biased, Model Order = ' int2str(modelOrder)]);
xlabel('Frequency (Hz)');
ylabel('PSD Magnitude');

testPoint = 0; %For debug purposes

end;
%
```

APPENDIX J

MATLAB PROGRAM RECURSIVE LEAST SQUARE VS LEAST MEAN SQUARE

```
%%%%%%%%%%%%%%%%%%%%%%%%%%%%%%%%%%%%%%%%%%%%%%%%%%
%%%%%%%%%%%%%%%%%%%%%%%%%%%%
%
%  Time Domain Order Recursive RLS & LMS Together (Used for Comparison)
%
% Frank James
%
%%%%%%%%%%%%%%%%%%%%%%%%%%%%%%%%%%%%%%%%%%%%%%%%%%
%%%%%%%%%%%%%%%%%%%%%%%%%%%%
clear;
N=2000;

%White Noise
x=randn(N,1);

%Colored Noise
X=zeros(N,1);
for ii=1:N;
    for jj=1:N
        X(ii)=X(ii)+(x(jj)*exp((-1i*2*pi*jj*ii)/N));
    end
end

% Precompute discrete frequencies
Nf=N;
theta=((2*pi/Nf).*(0:Nf-1));

%L=2; %Order of adaptive filter
%L=4; %Order of adaptive filter
%L=16; %Order of adaptive filter
L=36; %Order of adaptive filter


%mu=0.000001;  % Best
%mu=0.00009; % Ok
mu=0.000001;

% Fixed 'unknown' filter H(z)= MA
b=[1 -1.3435 0.9025];
a=[1 -0.45 0.55];
%b=[ -0.1241 -1.2075 0.7172 1.6302 0.4889 1.0347 0.7269  ...
%    1.4897 1.4090 1.4172 0.6715 -0.3034 0.2939 -0.7873 0.8884 -1.1471];
%a=[1];
```

```
%Compute filter output (excited by white noise)
d=filter(b,a,X);

% Calculate the output & error of the adaptive filter
H=freqz(b,a,theta);


bHat=zeros(L,1);
bHatLMS=zeros(1,L);
FGetFctr=0.9999;
P=eye(L)/mu;

X=X(:);
d=d(:);

ll=1;
iter=1;
for n=L:N

   xx=X(n:-1:n-L+1);

   % Order Recursive RLS vs LMS
   %
   %RLS
   k=FGetFctr^(-1)*P*xx/(1+FGetFctr^(-1)*xx'*P*xx);
   yHat=bHat'*xx;
   e(iter)=d(n)-yHat;
   bHat=bHat+k*conj(e(iter));
   P=FGetFctr^(-1)*P-FGetFctr^(-1)*k*xx'*P;

   %LMS
   %
   yHlms=bHatLMS*xx;
   el(iter)=d(n)-yHlms;
   bHatLMS=bHatLMS+2*mu*el(iter)*xx';


   ll=ll+1;
   if ll==10;
      Hh=freqz(bHat,1,theta);
      Hhl=freqz(bHatLMS,1,theta);
      ll=1;
   end
   iter=iter+1;
```

```
end

figure(1);
%plot(theta,20*log10(abs(Hh)),theta,20*log10(abs(H)));
plot(theta,20*log10(abs(Hh)),theta,20*log10(abs(Hhl)),theta,20*log10(abs(H)));
%plot(theta,20*log10(abs(Hh)));
t = sprintf('RLS-vs-LMS Order, L = %d, mu = %3.7f', L, mu);
title(t);
xlabel('Frequency Index');
ylabel('Magnitude in (dB)');

figure(2);
%plot(10*log10(abs(e(1,L:N)).*abs(e(1,L:N))+1e-8));
plot([1:iter-1],10*log10(abs(e).*abs(e)+1e-8),[1:iter-1], 10*log10(abs(el).*abs(el)+1e-
8));
title(t);
ylabel('MSE (dB)');
xlabel('Iteration');
```

APPENDIX K

MATLAB PROGRAM VECTOR SENSOR CRLB

```
%%%%%%%%%%%%%%%%%%%%%%%%%%%%%%%%%%%%%%%%%%%%%%%%%%%%%%%%%%%%%%%%%%%%%%%%%%%%%%%%
%
% Compute the Cramer-Rao lower bound for a vector sensor
% for a given angle and polarization state
%
%
% (Gross, 2005)
%
% Revised: Frank James
%%%%%%%%%%%%%%%%%%%%%%%%%%%%%%%%%%%%%%%%%%%%%%%%%%%%%%%%%%%%%%%%%%%%%%%%%%%%%%%%

N  = 20;                        % Number of trials
Fc = 10e3;        % Center freq.
Fs = 25e3;       % Sampling freq.
t  = 0:1/Fs:N-1/Fs;                % time axis (s)

theta = 45;                      % elevation (deg) +/-90
phi = -150;                       % azimuth (deg) +/-180

gamma = 75;                        % aux. pol. angle (deg)
eta   = 45;                      % pol. phase diff. (deg)

SNR_dB    = -10:2:20;
SNR       = 10.^(SNR_dB/10);
sigPwr    = ones(1,length(SNR));
noisePwr  = sigPwr./SNR;
noise_std = sigPwr./sqrt(SNR);

nbrAxes = 6;
xyz = [0 0 0];     % relative E & H sensor (x,y,z) positions

NrTrials = 20;     % # of Monte-Carlo trials

%-------------------------------------------------------
%---------- Estimate Arrival Angles Using MUSIC --------
%-------------------------------------------------------
DOAMUSIC_th = zeros(NrTrials,length(SNR));
DOAMUSIC_phi = zeros(NrTrials,length(SNR));

for kk = 1:NrTrials
   for jj = 1:length(SNR)
```

```
        x = zeros(nbrAxes,length(t));

        % Derived from Vector Elements
        ThetaPrime = [cosd(theta).*cosd(phi) -sind(phi);...
                      cosd(theta).*sind(phi)  cosd(phi);...
                      -sind(theta)            0         ;...
                      -sind(phi)             -cosd(theta).*cosd(phi);...
                      cosd(phi)              -cosd(theta).*sind(phi);...
                          0                  sind(theta)         ];

        P = [sind(gamma).*exp(1j*eta*pi/180);cosd(gamma)];

        n = noise_std(jj)*randn(size(x)).*exp(1j*(2*pi*rand(size(x))));
        x = x + kron(ThetaPrime*P,exp(1j*2*pi*Fc*t))+n;

        Rxx = x*x'/size(x,2);

        % Compute MUSIC Pseudo-spectrum over
        % meshgrid of arrival angle
        [Phi,Theta] = meshgrid(sort([linspace(-180,180,361) phi]),...
                               sort([linspace(0,90,91) theta]));
        phi1 = Phi(:);
        theta1 = Theta(:);
        Sxx = zeros(size(theta1,1),1);
        for k = 1:size(theta1,1)
           angle = [phi1(k) theta1(k)];
           Sxx(k,1)= pseudoSpec(angle,xyz,2*pi*Fc,Rxx,'MUSIC');
        end

        % Estimate arrival angle as the peak
        % of the MUSIC pseudo-spectrum

        [~,idx]      = max(Sxx);
        DOAMUSIC_theta(kk,jj) = theta1(idx);
        DOAMUSIC_phi(kk,jj) = phi1(idx);
    end
end

%-------------------------------------------------------
%------- Compute RMS errors for each arrival angle -----
%-------------------------------------------------------

RMS_MUSIC_phi = std(phi-DOAMUSIC_phi,[],1);
RMS_MUSIC_theta = std(theta-DOAMUSIC_theta,[],1);
```

```
%-------------------------------------------------------
%--- Compute Cramer-Rao Lower Bound for the elevation ---
%--- and azimuth arrival angles                      ---
%-------------------------------------------------------
CRLB_theta = zeros(length(SNR),1);
CRLB_phi   = zeros(length(SNR),1);
for i = 1:length(SNR)
   CRLB_theta_phi = VSCRLB_calc_func(theta,phi,gamma,eta, ...
                         sigPwr(i),noisePwr(i),100);
   CRLB_theta(i)  = sqrt(real(CRLB_theta_phi(1,1)));
   CRLB_phi(i)    = sqrt(real(CRLB_theta_phi(2,2)));
end

% Plot Results
figure('Position',[402   104   712   562])
subplot(221),
semilogy(SNR_dB,RMS_MUSIC_th,'g','LineWidth',2),hold on
semilogy(SNR_dB,CRLB_theta*180/pi,'k','LineWidth',2)

%phi = -150;                % azimuth (deg) +/-180
%theta = 45;                % elevation (deg) +/-90
ylabel('\fontsize{8}Angle Estimate Standard Deviation (deg)')
xlabel('\fontsize{8}SNR (dB)')
title('\fontsize{8}Vector Antenna Elevation_{(\theta)} Angle (deg)')
grid on, box on
set(gca,'gridlinestyle','-','fontsize',8,'Yminorgrid','on','minorgridlinestyle','-')

axis tight
xlim([-10 20])
ylim([10^-1 10^2])
legend('MUSIC','{CRLB_{(\theta,\theta)}^{1/2}}')

subplot(222)
semilogy(SNR_dB,RMS_MUSIC_ph,'g','LineWidth',2),hold on
semilogy(SNR_dB,CRLB_phi*180/pi,'k','LineWidth',2)
%
% Combined Plot
%
ylabel('\fontsize{8}Angle Estimate Standard Deviation (deg)')
xlabel('\fontsize{8}SNR (dB)')
title('\fontsize{8}Vector Antenna Azimuth_{(\phi)} Angle (deg)')
grid on,box on
set(gca,'gridlinestyle','-','fontsize',8,'Yminorgrid','on','minorgridlinestyle','-')

axis tight
```

```
xlim([-10 20])
ylim([10^-1 10^2])
legend('MUSIC','{CRLB_{(\phi,\phi)}^{1/2}}')

subplot(223)
semilogy(SNR_dB,(RMS_MUSIC_ph+RMS_MUSIC_th)/2,'g','LineWidth',2),hold on
semilogy(SNR_dB,((CRLB_phi+CRLB_theta)/2)*180/pi,'k','LineWidth',2)

ylabel('\fontsize{8}Angle Estimate Standard Deviation (deg)')
xlabel('\fontsize{8}SNR (dB)')
title('\fontsize{8}Vector Antenna Angular{(\theta,\phi)} Estimation (deg)')
grid on,box on
set(gca,'gridlinestyle','-','fontsize',8,'Yminorgrid','on','minorgridlinestyle','-')

axis tight
xlim([-10 20])
ylim([10^-1 10^2])
legend('MUSIC','{CRLB_{(\theta,\phi)}^{1/2}}')
```

APPENDIX L

MATLAB PROGRAM CALCULATE VECTOR SENSOR PSEUDO SPECTRUM

```
function [Sxx,V] = pseudoSpec(x,xyz,freq,Rxx,type)
%%%%%%%%%%%%%%%%%%%%%%%%%%%%%%%%%%%%%%%%%%%%%%%%%%%%%%%%%%%%%%%%%%%%%%%%
% Evaluates both MUSIC and MVDR pseudo-spectrums
% for a given set of arrival angles for a Vector Sensor
%
% Inputs:
%   x       - (K,2) Angle of Arrival, where K=# of signals
%             Column 1: Azimuth, Column 2: Elevation
%   xyz     - Vector Sensor relative positions of vector sensor antennas [x,y,z]
%   freq    - Frequency (in radians) to determine phase between vector sensors if they are
not co-located along the same x,y,z axis
%   Rxx     - received signal covariance matrix with noise
%   Alg     - 'MVDR' or 'MUSIC'
%
% Outputs:
%   Sxx     - Eigenvectors associated with the pseudo spectrum
%   V       - Eigenvalues associated with the pseudo spectrum
%
% (Gross, 2005)
%
% Created/Revised: Frank James
%%%%%%%%%%%%%%%%%%%%%%%%%%%%%%%%%%%%%%%%%%%%%%%%%%%%%%%%%%%%%%%%%%%%%%%%
c = 3e8;                    % speed of light (m/s)

Sxx = zeros(size(x,1),1);  % Matrix storage for MVDR pseudo-spectrum
for k = 1:size(x,1)

   theta = x(k,2);  % kth elevation
   phi = x(k,1);    % kth azimuth

   % Transformation
   Coord = [ cosd(theta).*cosd(phi)    -sind(phi);...
             cosd(theta).*sind(phi)     cosd(phi);...
            -sind(theta)                0         ;...
            -sind(phi)         -cosd(theta).*cosd(phi);...
             cosd(phi)         -cosd(theta).*sind(phi);...
             0                  sind(theta)         ];

   u = [cosd(phi)*sind(theta);sind(phi)*sind(theta);cosd(theta)]; % direction unit vector
```

```
   q = exp(1j*freq/c*xyz*u);                          % phase delays between vector
sensor elements

   vs_steer = kron(q,Coord);  % steering vector (VS)

   %
   % Setup generalized eigenvalue problem for
   % evaluating MVDR and MUSIC pseudo-spectrums
   %
   switch type
      case 'MVDR'
         G1 = vs_steer'*inv(Rxx)*vs_steer;
     case 'MUSIC'
         [V,D] = eig(Rxx);  % perform eigenvalue decomposition of covariance matrix
         EN = V(:,1:4);     % Extract noise subspace
         G1 = vs_steer'*(EN*EN')*vs_steer; % Identify noise peaks
   end

   G2       = vs_steer'*vs_steer;
   [V,D]    = eig(G2,G1);  % generalized eigenvalue problem
   d        = diag(D);     % associated eigenvalues
   [Sxx(k,1),idx] = max(real(d));% maximum eigenvalue is hypothesis
   v(k,:)       = V(:,idx).';% associated eigenvector of max eigenvalue
end
```

APPENDIX M

MATLAB PROGRAM COMPARISON ROOT-MUSIC VERSUS MUSIC

```
%
%%%%%%%%%%%%%%%%%%%%%%%%%%%%%%%%%%%%%%%%%%%
%%%%%%%%%%%%%%%%%%%%%%%%%%%%%%%%%%%
%
% Root-MUSIC AOA estimation for a M element array with
% noise variance = sig2 use time averages instead of expected
% values by assuming ergodicity of the mean and ergodicity of the correlation.
%
% Calculate regular MUSIC problem, calculate polynomial
% coefficients for Root-MUSIC, and plot the two methods:
% MUSIC, Root-MUSIC
%
% Where M >> D, the number of elements are much larger than the number
% of signals being estimated.
%
%% (Gross, 2005)
%
% Created/Revised: Frank James
%%%%%%%%%%%%%%%%%%%%%%%%%%%%%%%%%%%%%%%%%%%
%%%%%%%%%%%%%%%%%%%%%%%%%%%%%%%%%%%%%%%%%%%
%%%%%%%%%%%%%%%%%%%%%%%%%%%%%%%%%%%%%%%%%%%
%%%%%%%%%%%%%

M=4;
D = 2;  % number of signals
sig1=1;
%sig2=.1;
sig2=.3
th1=-4*pi/180;
th2=8*pi/180;
th1=-5*pi/180;
th2=5*pi/180;

ii=1:M;
  a1=exp(1j*(ii-1)*pi*sin(th1));
  a2=exp(1j*(ii-1)*pi*sin(th2));
A=[a1.' a2.'];
K=300;          % K = length of time samples
K=600
s=sqrt(sig1)*sign(randn(D,K));      % calculate the K time samples of the signals for the
                    % two arriving directions

Rss=s*s'/K;      % source correlation matrix with uncorrelated signals
```

```
n=sqrt(sig2)*randn(M,K);     % calculate the K time samples of the noise for the 6 array
                  % elements
Rnn=(n*n')/K;        % calculate the noise correlation matrix (which is no longer
diagonal)
Rns=(n*s')/K;         % calculate the noise/signal correlation matrix
Rsn=(s*n')/K;         %  calculate the signal/noise correlation matrix
Rrr=A*Rss*A'+A*Rsn+Rns*A'+Rnn       % combine all to get the array correlation
matrix

[V,Dia]=eig(Rrr);
[Y,Index]=sort(diag(Dia));   % sorts the eigenvalues from least to greatest
 EN=V(:,Index(1:M-D));      % calculate the noise subspace matrix of eigenvectors
                  % using the sorting done in the previous line
 ES=V(:,Index(M-D+1:M));       % subspace of signal eigenvectors
for k=1:360;
  %th(k)=-pi/12+pi*k/(6*360);
   th(k)=-pi/6+pi*k/(3*360);
  clear a
   a=exp(1j*(ii-1)*pi*sin(th(k)));
   a=a.';
P(k)=1/abs(a'*EN*EN'*a);
end

C=EN*EN';          % calculate the matrix C

%  Find the coefficients for the root-MUSIC polynomial
for kk=-M+1:M-1
   cc(kk+M) = sum(diag(C,kk));
end
rts=roots(cc);                  % find the roots of the 2*(M-1) polynomial

angs=-asin(angle(rts)/pi)*180/pi     % find the angles associated with these root
figure;zplane(rts)
figure;
plot(th*180/pi,P/max(P),'k',angs,abs(rts),'kX','markersize',10)
grid on
xlabel('Angle')
ylabel('|P(\theta)|')
axis([-10 10 0 1.6])
axis([-30 30 0 1.6])
```

APPENDIX N

MATLAB PROGRAM VECTOR SENSOR ESTIMATE EXAMPLE

```
%%%%%%%%%%%%%%%%%%%%%%%%%%%%%%%%%%%%%%%%%%%%%%%%%%%%%%%%%%%%%%%%%%%%%%%
% Vector Antenna Estimation
% Computed for 100MHz @ 250Msps
%
% Fc = 100MHz
% Fs = 250Msps
%%%%%%%%%%%%%%%%%%%%%%%%%%%%%%%%%%%%%%%%%%%%%%%%%%%%%%%%%%%%%%%%%%%%%%%
clear
close all,

Fc = 100e6;         % Center freq.
rad  = 2*pi*Fc;     % Radian freq.
Fs = 250e6;        % Sampling freq.
t  = (0:100000)/Fs; % Time axis (seconds)
Amp  = 2;           % Amplitude of damped sinusoid (V)
%
% Damping coefficient
%
a  = 315;         % Coeff. 1
b  = 1200;        % Coeff. 2

s  = Amp*sin(rad*t).*(exp(-a*t)-exp(-b*t));  % damped sinusoidal signal s(t)

%------ Steering Vector  --------

theta    =  28;    % Elevation (deg)
phi    = -20;      % Azimuth  (deg)
eta    =  28;      % Polarization phase difference (deg)
gamma =  65;       % Auxilliary polarization angle (deg)

vs_xyz = [0 0 0]; % [x,y,z] position of vector sensor antenna

AzElVecAngle = [ cosd(theta).*cosd(phi) -sind(phi)          ;...
                 cosd(theta).*sind(phi)  cosd(phi)          ;...
                -sind(theta)                 0          ;...
                -sind(phi)          -cosd(theta).*cosd(phi) ;...
                 cosd(phi)          -cosd(theta).*sind(phi) ;...
                     0              sind(theta)          ];

P = [sind(gamma).*exp(1j*eta*pi/180);cosd(gamma)];
```

```
v_vs = AzElVecAngle*P;

rng(1) % set seed on random number generator for repeatability
%noise_std = 0.01;
noise_std = 0.1;
n        = noise_std.*randn(6,length(s)).*exp(1j*rand(6,length(s)));
x        = AzElVecAngle*P*s+n;

%------------ Covariance  -------------
Rxx     = x*x'/size(x,2);
Rxx     = Rxx/trace(Rxx);

%-- Each Azimuth and Elevation --
[Ph,Th] = meshgrid(sort([linspace(-180,180,361) phi]),sort([linspace(0,90,91) theta]));
ph1     = Ph(:);
th1     = Th(:);

Sxx = zeros(size(th1,1),1);
v  = zeros(size(th1,1),2);
for i = 1:size(th1,1)
   % AoA Estimate
   angle        = [ph1(i) th1(i)];
   [Sxx(i,1),v(i,:)] = pseudoSpec(angle,vs_xyz,2*pi*Fc,Rxx,'MUSIC');
   Sxx(i,1)         = 10*log10(Sxx(i,1));
end

%---------- Surface:MUSIC ------------------

Sxx      = reshape(Sxx,size(Th,1),size(Th,2));
Sxx_Norm   = Sxx-max(Sxx(:));

figure,
surf(Ph,Th,Sxx_Norm,'EdgeColor','none'),hold on
axis square,axis tight
colormap(parula),colorbar
view(-30,60)
set(gca,'fontsize',8,'gridlinestyle','-')

zlim([min(Sxx_Norm(:)) 0])
xlabel('\fontsize{8}Azimuth Angle \phi (deg)')
ylabel('\fontsize{8}Elevation Angle \theta (deg)')
zlabel('\fontsize{8}10log_1_0 \lambda (\theta,\phi)')
```

```
str=sprintf('Dampened Input Signal + Noise(%s) = %4.2f Signal Elev(%s)=%d
Az(%s)=%d
Pol(%s,%s)=(%d,%d)','\sigma',noise_std,'\theta',theta,'\phi',phi,'\gamma','\eta',gamma,eta)
title(str)
```

APPENDIX O

MATLAB PROGRAM LEVINSON-DURBIN ESTIMATE EXAMPLE

```
%%%
```

```
      end
   end
   rss(m+1)=rss(m+1)/(length(si)-m);
end

r0=rss(1);
rss=rss(2:P+1,1); % remove r(0) from the matrix
% Now compute the coeff. (here we are using direct matlab inv. function)
%a=inv(R)*rss
% the coefficients
% Levinson-Durbin Recursion to get the coefficients
a(1)=1; % a0 (start)
Pwr=r0; % Power in error
D=rss(1);
thresh=0.04;

index=1:P*nPts;

%while( m <=P && abs(a(m)) > thresh)
m = 0;
while( m < P )

   %index = m*S+1:min((m*S)+2*P,nPts); % indices for the mth frame
   %if (length(index) < (2*P))
   %    index= nPts-(2*P)+1:nPts;
   %end

   %index = m*S+1:((m*S)+S); % indices for the mth frame
   index = m*nPts+1:((m*nPts)+nPts); % indices for the mth frame
   %index = 1:((m*nPts)+nPts); % indices for the mth frame

   m = m + 1;
   Reflect=-D/Pwr; % The reflection coeff. for mth order filter
   %a=[a;0] + Reflect.* conj(flipud([a;0]));  % The coeff. for the pth order
   a=[a;0] + Reflect.*(flipud([a;0]));  % The coeff. for the pth order
                                % filter
   Pwr=Pwr*(1-(abs(Reflect))^2); % Power of the error for mth filter
   if(m+1<=P)
      D=(flipud(rss(1:m+1))')*a; % calculate Delta(D)(m)
   end

   Bze=freqz(1,a,theta1);
   nee(index(1):index(Nf))= ((abs(Fz')-abs(Bze')).^2)./((abs(Fz')).^2);
   neeAvg(m)= (1/Nf)*sum(((abs(Fz')-abs(Bze')).^2)./((abs(Fz')).^2));
   %m = m + 1;
```

```
end
%aa1=-a(2:m-1); % remove the first element of the Prediction-error filter
aa1=-a(2:P+1); % remove the first element of the Prediction-error filter
% coeff. vector (since it is equal to 1 and we do not
% use it here) also we need to put a negative sign
% as the prediction-error-filter has a -ve sign for
% prediction-filter coeff. P


% Now we need to estimate the signal
% Calculate the residual
s=zeros(size(si)); % estimate of x
s(1)=si(1);
for k=2:length(s)
%    for l=1:m-2
   for l=1:P
      if(k-l>=1)
         s(k)=s(k)+aa1(l)*si(k-l);
      end
   end
end %end

%Bze=freqz(1,a,theta1);
%nee(1:nPts)= ((abs(Fz')-abs(Bze')).^2)./((abs(Fz')).^2);
%nee(1:S)= ((abs(Fz')-abs(Bze')).^2)./((abs(Fz')).^2);

Hh=freqz(1,a,theta);

figure(1);
plot(theta,20*log10(abs(Hh)),theta,20*log10(abs(H)));
t = sprintf('Order, P = %d, Points = %d', P, nPts);
title(t);
xlabel('Frequency Index');
ylabel('Magnitude in (dB)');

figure(2);
plot(1:length(si),si,'r-',1:length(s),s,'b-');
t = sprintf('Residual, Order, P = %d, Points = %d', P, nPts);
title(t);
xlabel('Samples');
ylabel('Magnitude');

figure(3);
%plot(1:length(s),abs(fft(s-si)))
```

```
plot(10*log2(nee));
t = sprintf('Order, P = %d, Points = %d', P, nPts);
title(t);
ylabel('All points NEE (dB)');
xlabel('Iteration');

figure(4);
%plot(1:length(s),abs(fft(s-si)))
plot(10*log2(neeAvg));
t = sprintf('Order, P = %d, Points = %d', P, nPts);
title(t);
ylabel('Averaged NEE (dB)');
xlabel('Iteration');
```